Downloaded from orbit.dtu.dk on: May 03, 2024

DTU Library

Influence of tiny concentrations of copper and zinc on the microstructure and intergranular corrosion of Al-Mg- Si alloys

Bartawi, Emad Hasan

Publication date:
2023

Document Version
Publisher's PDF, also known as Version of record

Link back to DTU Orbit

Citation (APA):
Bartawi, E. H. (2023). *Influence of tiny concentrations of copper and zinc on the microstructure and intergranular corrosion of Al-Mg- Si alloys*. Technical University of Denmark.

General rights
Copyright and moral rights for the publications made accessible in the public portal are retained by the authors and/or other copyright owners and it is a condition of accessing publications that users recognise and abide by the legal requirements associated with these rights.

- Users may download and print one copy of any publication from the public portal for the purpose of private study or research.
- You may not further distribute the material or use it for any profit-making activity or commercial gain
- You may freely distribute the URL identifying the publication in the public portal

If you believe that this document breaches copyright please contact us providing details, and we will remove access to the work immediately and investigate your claim.

DTU Civil and Mechanical Engineering
PhD thesis

Influence of tiny concentrations of copper and zinc on the microstructure and intergranular corrosion of Al-Mg-Si alloys

Emad Hasan Bartawi

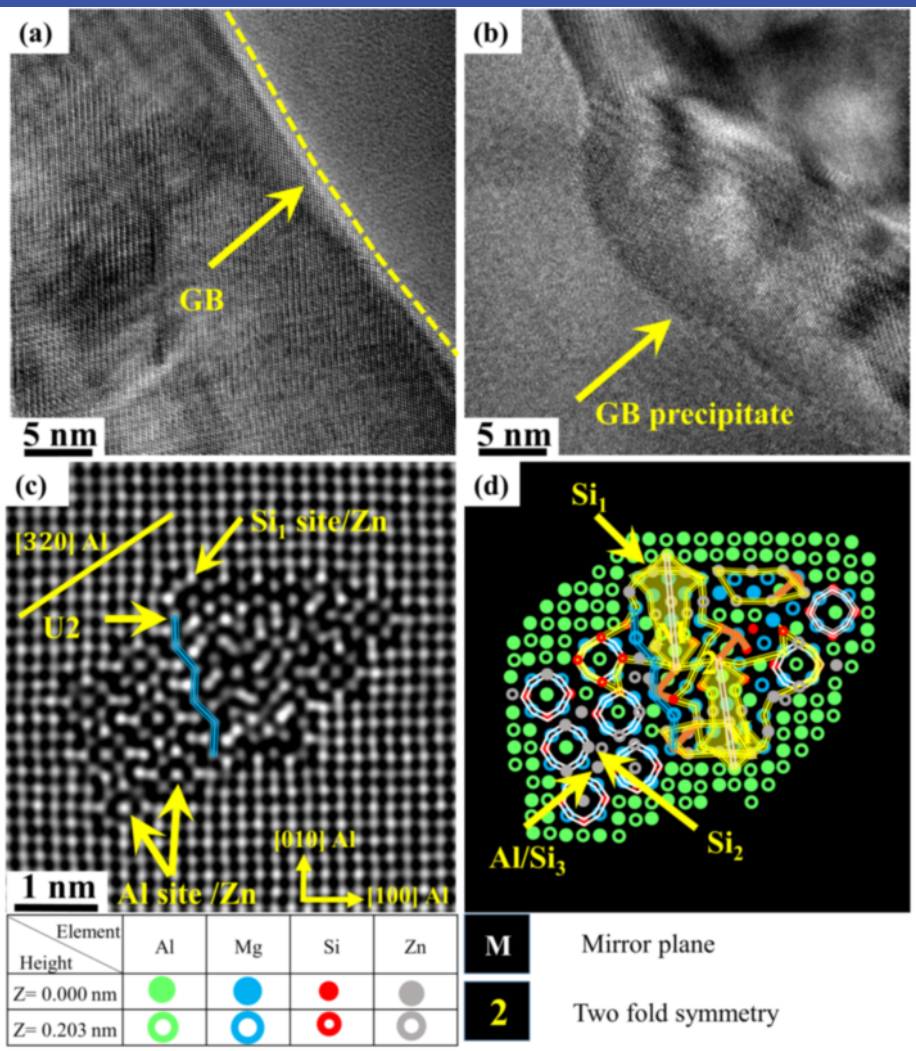

Influence of tiny concentrations of copper and zinc on the microstructure and intergranular corrosion of Al-Mg-Si alloys

A THESIS SUBMITTED TO THE TECHNICAL UNIVERSITY OF DENMARK FOR THE DEGREE OF DOCTOR OF PHILOSOPHY IN THE DEPARTMENT OF CIVIL AND MECHANICAL ENGINEERING

August 2023

By

Emad Hasan Bartawi

Technical University of Denmark

Department of Civil and Mechanical Engineering

Section of Materials and Surface Engineering

Effect of Tiny Concentrations of Copper and Zing on Microstructure and Intergranular Corrosion of Al-Mg-Si Alloys

A doctoral thesis by

Emad Hasan Bartawi
E-Mail: ehaba@dtu.dk
Technical University of Denmark
Department of Civil and Mechanical Engineering - Section of Materials and Surface Engineering
Building 425, room 107
DK-2800 Kgs. Lyngby

Principal Supervisor:

Prof. Rajan Ambat
E-Mail: raam@dtu.dk
Technical University of Denmark
Department of Civil and Mechanical Engineering
Produktionstorvet
Building 425, room 130
DK-2800 Kgs. Lyngby

Co-Supervisors:

Prof. Jesper H. Hattel
E-Mail: jhat@dtu.dk
Technical University of Denmark
Department of Civil and Mechanical Engineering
Produktionstorvet
Building 425, room 228
DK-2800 Kgs. Lyngby

Senior researcher Sankhya Mohanty
E-Mail: samoh@dtu.dk
Technical University of Denmark
Department of Civil Mechanical Engineering
Produktionstorvet
Building 425, room 217
DK-2800 Kgs. Lyngby

Copyright:	Reproduction of this publication in whole or in part must include the customary bibliographic citation, including author attribution,
Published by:	Department of Civil and Mechanical Engineering , Section of Materials and Surface Engineering , Produktionstorvet, Building 425, DK-2800 Kgs. Lyngby

To my beloved parents, Khadija and Hasan,

My adored siblings, Hanna, Wafa, Mervat, Essam and Mohamad,

My wife, Ghada and my lovely daughters Sali and Solar.

Preface

The following doctoral thesis is being submitted as a part of fulfilment of the requirements to obtain the PhD degree at the Department of Civil and Mechanical Engineering at the Technical University of Denmark (DTU). This project was funded by the Independent Research Fund Denmark under grant number 9041-00240A and carried out at the Department of Civil and Mechanical Engineering, Section of Materials and Surface Engineering, during the period from May 1st 2020 to August 14th 2023. The project was supervised by Professor Rajan Ambat, Professor Jesper H. Hattel, and Senior researcher S. Mohanty from the Department of Civil and Mechanical Engineering at the Technical University of Denmark (DTU).

Emad Hasan Bartawi
Kongens Lyngby, Denmark, August 14th, 2023

Abstract

In recycling, scrap composition will determine the amount of scrap that can be added to the recycled products without leading to possible quality degradation in their mechanical properties and/or corrosion resistance. Therefore, this thesis details the research work focused on understanding the influence of a minor amount of Cu and/or Zn (as impurities) on the microstructure, precipitates structures, and intergranular corrosion (IGC) resistance of Al-Mg-Si alloys. The influence of Cu and Zn on the IGC resistance was systematically studied using scanning electron microscopy (SEM), electron backscatter diffraction (EBSD), transmission electron microscopy (TEM), and X-ray computed tomography (CT). Moreover, atomic force microscopy (AFM) coupled with scanning Kelvin probe force microscopy (SKPFM) was conducted to measure the surface potential of the grain boundaries. Furthermore, atom-resolution high-angle annular dark field scanning transmission electron microscopy (HAADF-STEM) was used to study the influence of Cu and Zn on the precipitates structures.

The investigation detailed in this thesis is mainly structured into three parts. The first part focused on the influence of Cu and/or Zn on the microstructure and IGC resistance of Al-Mg-Si alloys in the as-received condition (Chapters 5-8). The second part is focused on the influence of aging time and temperature in the presence of low Cu and/or Zn on the microstructure and IGC resistance of Al-Mg-Si alloys (Chapters 9 and 10). The main focus of the third part of this thesis is to investigate the impact of a minor amount of Cu and/or Zn on the hardening precipitate structures. The detailed results related to the impact of Cu and/or Zn on the microstructure, precipitates structures, and intergranular corrosion of Al-Mg-Si in different aging conditions are presented and thoroughly discussed.

The optical investigation revealed a duplex microstructure compromised of a deformed center layer sandwiched between two recrystallized layers. The EBSD results from the surface layers showed that the fraction of the random high-angle grain boundaries in the explored alloys was ~91 %. It was found that low Cu and/or Zn concentrations can negatively influence the IGC resistance of Al-Mg-Si alloys. The IGC extension and the penetration depth were noticed to increase by increasing the Cu additions. However, Zn addition showed a more noticeable increase in the IGC extension than penetration depth by increasing Zn concentrations. The results also revealed that aging time and temperature can

significantly influence the IGC resistance of Al-Mg-Si alloys. Moreover, the results evidently showed that minor addition of Cu and Zn can significantly influence the precipitate crustal structures. The STEM results indicated the presence of Cu/Zn-rich films along some investigated grain boundaries.

Resumé

I metalgenbrug vil sammensætningen i skrottet metal bestemme den mængde af metalskrot, der kan tilføjes i genanvendte produkter, uden at det fører til en mulig forringelse af deres mekaniske egenskaber og/eller korrosionsbestandighed. Denne afhandling beskriver et forskningsarbejde, der fokuserer på at forstå indflydelsen af mindre mængder Cu og/eller Zn (som urenheder) på mikrostrukturen, præcipitatstrukturerne og modstanden mod inter-granular-korrosion (IGC) i Al-Mg-Si-legeringer. Indflydelsen af Cu og Zn på modstanden mod IGC blev systematisk undersøgt ved hjælp af scanning electron microscopy (SEM), electron backscatter diffraction (EBSD), transmission electron microscopy (TEM), and X-ray computed tomography (CT). Derudover blev atomic force microscopy (AFM) koblet sammen med scanning Kelvin probe force microscopy (SKPFM) for at måle overfladepotentialet for korngrænserne. Desuden blev atom-resolution high-angle annular dark field scanning transmission electron microscopy (HAADF-STEM) brugt til at studere indflydelsen af Cu og Zn på præcipitatstrukturerne.

Undersøgelsen, der er beskrevet i denne afhandling, er struktureret i tre dele. Den første del fokuserer på indflydelsen af Cu og/eller Zn på mikrostrukturen og modstanden mod IGC i Al-Mg-Si-legeringer, i den tilstand legeringen blev modtaget (Kapitler 5-8). Den anden del fokuserer på indflydelsen af aldringstid og temperatur for et lavt Cu og/eller Zn indhold på mikrostrukturen og modstanden mod IGC for Al-Mg-Si-legeringer (Kapitler 9 og 10). Hovedfokus for den tredje del af denne afhandling var at undersøge virkningen af en mindre mængde Cu og/eller Zn på hærdningspræcipitatstrukturerne. Resultaterne relateret til indflydelsen af Cu og/eller Zn på mikrostrukturen, præcipitatstrukturerne og ICG af Al-Mg-Si i forskellige aldringsforhold præsenteres og diskuteres.

Den optiske undersøgelse afslørede en duplex mikrostruktur bestående af et deformationscenterlag, beliggende mellem to rekrystalliserede lag. EBSD-resultaterne fra overfladelagene viste, at andelen af tilfældige high-angle korngrænser i de undersøgte legeringer var ca. 91 %. Studierne viste at meget lave koncentrationer af Cu og/eller Zn kan påvirke IGC-modstanden af Al-Mg-Si-legeringer negativt. Både IGC udbredelsen og penetrationens dybden steg med stigende Cu-tilsætninger. Samtidig viste tilsætning af Zn en mere mærkbar stigning i IGC udbeddelsen end i penetrationens dybden. Resultaterne viste også, at aldringstid og temperatur kan påvirke modstanden mod IGC i Al-Mg-Si-

legeringer markant. Desuden viste resultaterne klart, at mindre tilføjelse af Cu og Zn markant kan påvirke præcipitatkrystalstrukturerne. STEM-resultaterne indikerede en tilstedeværelse af en Cu/Zn-rig film langs nogle af de undersøgte korngrænser.

Acknowledgements

As my three-year journey as a Ph.D. student at DTU comes to an end, here I want to acknowledge all people who helped and supported me to achieve this. The work is the result of many hours and efforts utilizing different advanced techniques, such as atomic force microscope, atom probe tomography, X-ray computed tomography, and scanning transmission electron microscope. With confidence, I can say that many of those hours were dedicated to overcoming all obstacles encountered in the field of transmission electron microscope experiments and spent in a dark room with large TEM microscopes at DTU-CEN, DTU-Risø, and NTNU.

I want to express my sincere gratitude to my primary supervisor Professor Rajan Ambat for giving me the possibility to pursue a Ph.D. degree at DTU and for his support and advice throughout the last three years.

I would like to thank Carsten Gundlach (DTU- Department of Applied Mathematics and Computer Science) for his collaboration regarding X-ray computed tomography. I would like also to thank Oleg Mishin (Department of Civil and Mechanical Engineering) for his support in EBSD experiments. In addition, I extend my thanks to Peter Westermann for helping in acquiring the chemicals needed during my Ph.D. work. Thanks to Flemming Bjerg Grumsen (DTU), and Jens Kling (DTU) for assisting me in the transmission electron microscope. Thanks to Niklas Brinckman and Steffen Munch for their support in sample preparation. Thanks to Jan Halvor Nordlien (Hydro), Robert Ramage (Hydro), and Jonas Kristoffer Sunde (Hydro) for their valuable support and discussions.

Thanks to my colleagues in the sections of Materials and Surface Engineering (DTU) and Manufacturing Engineering (DTU) Feng, Sajjad, Avinash, Anish, Daniel Rio, Konstantin, Kleanny, Daniel, Felix, and Bjarke for their support.

I want to express my heartfelt gratitude to my beloved Ghada Shaban for providing care, unwavering assistance, and demonstrating patience throughout my entire Ph.D. work. I also want to express my deep gratitude to the incredible blessing in my life, *Sali* and *Solar,* for the patience and understanding they displayed.

List of articles and conference contributions

Articles included in this thesis:

1- **Bartawi, E. H.**, Mishin, O. V., Shaban, G., Nordlien, J. H., & Ambat, R. (2022). Electron microscopy analysis of grain boundaries and intergranular corrosion in aged Al-Mg-Si alloy doped with 0.05 wt% Cu. Corrosion Science, 209, 110758. **(Published)**

2- **Bartawi, E. H.**, Mishin, O. V., Shaban, G., Grumsen, F., Nordlien, J. H., & Ambat, R. The effect of trace level copper content on intergranular corrosion of extruded AA6082-T6 alloys. Mater. Chem. Phys. (2023) 128303. **(Published)**

3- **Bartawi, E. H.**, Marioara, C. D., Shaban, G., Rahimi, E., Mishin, O. V., Sunde, J. K., Gonzalez-Garcia, Y., Holmestad, R., & Ambat, R. Toward high intergranular corrosion resistance in recycled 6082 Al-Mg-Si: influence of minor additions of Cu and Zn. **(Ready for submission)**

4- **Bartawi, E. H.**, Marioara, C. D., Rahimi, E., Shaban, G., Mishin, O. V., Sunde, J. K., Gonzalez-Garcia, Y., Holmestad, R., & Ambat, R. Effect of minor addition of Zn on precipitate crystal structures and intergranular corrosion in 6082 Al-Mg-Si alloys. **(Ready for submission)**

5- **Bartawi, E. H.**, Shaban, G., Marioara, C. D., Mishin, O. V., Holmestad, R., & Ambat, R. Effect of aging temperature on microstructure and intergranular corrosion of Al-Mg-Si alloys with low concentrations of Cu and Zn. **(Ready for submission)**

6- **Bartawi, E. H.**, Shaban, G., & Ambat, R. Effect of aging time on microstructure and intergranular corrosion of 6082 Al-Mg-Si alloy with minor additions Cu and Zn. **(Ready for submission)**

7- **Bartawi, E. H.**, Marioara, C. D., Shaban, G., Hatzoglou, C., Holmestad, R., & Ambat, R. Atomic structure of hardening precipitates in Al-Mg-Si alloys: Influence of minor additions of Cu and Zn. **(Ready for submission)**

During the course of the Ph.D., the student has coauthored the following articles that are not included as part of the Ph.D. thesis.

1- Haratian, S., Gupta, K. K., Larsson, A., Abbondanza, G., **Bartawi, E. H.**, Carlà, F., Lundgren, E., & Ambat, R. (2023). Ex-situ synchrotron X-ray diffraction study of CO_2 corrosion-induced surface scales developed in low-alloy steel with different initial microstructure. *Corrosion Science*, 111387. **(Published)**
2- Haratian, S., Gupta, K. K., Larsson, A., **Bartawi, E. H.**, Edvin Lundgren, & Ambat, R. In-situ investigation of the development of the corrosion products/scale during CO_2 corrosion of low-alloy carbon steels using synchrotron X-ray diffraction. **(In preparation)**

Conference contributions:

1- **Bartawi, E. H.**, & Ambat, R. Effect of Cu on the intergranular corrosion behavior of 6082 Aluminium Alloy, EUROCORR 21, virtual event, 20 - 24 September 2021.
2- **Bartawi, E. H.**, Grumsen, F., Nordlien, J. H., & Ambat, R. Microstructure and Intergranular Corrosion of Al-Mg-Si alloy under a trace level copper content, 18th Nordic Corrosion Congress, Åbo Akademi University/ Turku, Finland.
3- **Bartawi, E. H.**, Mishin, O. V., & Ambat, R. Grain boundary characteristics and their correlation to intergranular corrosion of Al-Mg-Si alloy with trace level content of Cu, EUROCORR 22, Berlin/Germany, 28th August - 1st September 2022.
4- Ambat, R., Nordlien, J. H., & **Bartawi, E. H.** Effect of trace level Zn on intergranular corrosion of Al-Mg-Si alloy, 9th ASST Symposium, May 21-25, 2023, Stockholm, Sweden.
5- **Bartawi, E. H.**, Nordlien, J. H., & Ambat, R. Effect of aging time on the intergranular corrosion of Al-Mg-Si alloy with trace level content of Cu and Zn, 9th ASST Symposium, May 21-25, 2023, Stockholm, Sweden.

Table of contents

List of abbreviations and symbols

AA	Aluminium Alloy
IGC	Intergranular Corrosion
GBs	Grain Boundaries
ED	Extrusion Direction
TD	Transverse Direction
ND	Normal Direction
PFZ	Precipitate Free Zone
FIB	Focused Ion Beam
SEM	Scanning Electron Microscopy
SE	Secondary Electron
BSE	Backscattered Electrons
EBSD	Electron Back-Scattered Diffraction
HABs	High Angle Boundaries
LABs	low Angle Boundaries
CSL	Coincidence Site Lattice
TKD	Transmission Kikuchi Diffraction
EDS	Energy-dispersive X-ray spectroscopy
S/TEM	Scanning/Transmission Electron Microscopy
BF	Bright-Field
HAADF	High-Angle Annular Dark-Field
AFM	Atomic Force Microscopy
SKPFM	Scanning Kelvin Probe Force Microscopy
ΔCPD	Contact Potential Difference
E_{Vac}	Vacuum Level
E_F	Fermi Level

$\emptyset_p$	Work Function Energy of Probe
APT	Atom Probe Tomography
XRM	X-ray Microscopy
SSSS	Supersaturated Solid Solution.
SHT	Solution Heat Treatment
WQ	Water-Quenched
UA	Underaged
PA	Peakaged
OA	Overaged
BEVs	Battery Electrical Vehicles

1. Introduction

1.1 Background

Among Aluminium alloys, Al-Mg-Si alloys are the most frequently used family in engineering applications such as automotive, structural, aerospace, and marine applications. This is due to their high strength-to-weight ratio, high thermal and electrical conductivity, and good corrosion resistance [1–3]. The demand for aluminium and aluminium alloys is increasing, and so does the reduction in CO_2 emission. The reported CO_2 emission for producing one ton of aluminium ingot from raw material (bauxite) is between 12 to 17 metric tons. Two-thirds of the emitted CO_2 is due to fossil fuel sources used to produce electricity for the electrolysis process. Lowering these emissions has become inevitable to face their impact on climate change and global warming. From an environmental point of view, recycling lowers energy consumption and, thus, less CO_2 emission. Moreover, aluminium recycling enables a reduction of approximately 95 % of the energy required to produce the same amount of primary aluminium and thus emitting only 5 % of the greenhouse gases compared to primary aluminium [4]. From an economic point of view, recycling offers a considerable advantage due to balancing the payments by reducing imports and the cost required for energy. In addition, only approximately 10 % of the allocated capital needed for producing aluminium in the conventional route (smelting) is required for recycling [5].

Al-Mg-Si alloys are the preferred alloys to be used in automotive applications due to the properties mentioned above, in addition to being corrosion resistance, formable, weldable, and anodizable alloys [6,7]. Within this sector, there is even more tendency to replace steel with aluminum alloys to respond to the weight reduction demands hence reducing the CO_2 emission [8]. Further challenges arise when using aluminium in a component subjected to a corrosive environment or even exposed to elevated temperatures during service. Therefore, focusing on these components' corrosion and mechanical properties requires more understanding of how alloying elements will influence such properties.

The susceptibility to localized corrosion in Al-Mg-Si alloy is reported to be significantly affected by the unbalanced alloying elements and improper heat treatments [9,10]. Susceptibility to IGC is also strongly affected by the quenching rate and the aging

time and temperature [11–13]. water-quenching and air-cooling were investigated with different Cu content. It is reported that Al-Mg-Si alloys (Cu ≤ 0.17 wt%) subjected to water-quenching followed by artificial aging showed good resistance to IGC [10,14]. Moreover, it is documented that susceptibility to IGC generally increases by artificially aging of the alloys to peakaging conditions and then decreases after overaging [9]. Besides quenching rate and unfavorable heat treatment, unbalanced alloying elements significantly influence the IGC of Al-Mg-Si alloys. For instance, Cu is added to Al-Mg-Si alloys to improve their mechanical properties as finer and denser precipitates can be obtained [15]. Yet, Cu additions at relatively high concentrations (≥ 0.12 wt%) negatively influence the corrosion properties of such alloys as Cu will segregate to the grain boundary (GB), resulting in IGC [14,16,17]. In addition, it has also been reported that IGC resistance is greatly affected by different grain boundary types. For instance, low-angle boundaries and coincident site lattice are frequently reported to be less susceptible to IGC than high-angle grain boundaries [18–21].

It has been suggested that the IGC of Al-Mg-Si-Cu alloys is attributed to microgalvanic coupling between Cu- rich film, Cu-containing precipitates (as cathode) and precipitate free zones adjacent to the grain boundaries (as an anode) [22]. Attention has been paid to studying the influence of high Cu concentration on the microstructure and IGC of Al-Mg-Si alloys rather than low concentration as it is claimed that the effect of Cu on the IGC can be avoidable if the Cu is kept below 0.1 wt% [14,23]. Recent studies focused on the role of α-phase [Al(Mn, Fe)Si] on the IGC suggested that such particles will serve as external cathodes promoting the extent of IGC [17,24]. In addition, Q particles (AlMgSiCu), which are common in Al-Mg-Si-Cu artificially aged alloys, are controversial about their contribution to the initiation and propagation of IGC. The first view assumed that Q particles are directly involved in the IGC process serving as a supported cathode accelerating the IGC [9,14,23,25–29]. While on the other hand, the second view claimed that Q particles have no contribution to the initiation and even to the early stage of fissures propagation, suggesting that Q precipitates are inert against reduction and oxidation [17]. To summarize, the previously mentioned studies with Cu ≥ 0.1wt% directly linked the initiation and propagation of IGC in Al-Mg-Si alloys to the Cu-rich film and/or to Cu-containing precipitates. Only one work reported a significant IGC in the presence of 0.06

wt% and 0.04 wt% Zn concluded that the root of observed IGC cannot be decisively explained based on the obtained results [12].

Recently the effect of Zn on the microstructure, mechanical properties, IGC, and precipitate crystal structures of Al-Mg-Si alloys has received increased attention [30–37]. For example, Guo et al. [36] have studied the effect of Zn on the precipitation and IGC of Al-Mg-Si-0.2Cu alloys at different aging conditions. It is claimed that the IGC resistance of the alloy decreased after 1 wt% Zn addition compared to Zn-free alloy due to the formation of coarse grain boundary particles. However, it is also reported that the IGC resistance is improved in the alloys containing high Zn concentration (2-4 wt%) due to the formation of narrower PFZ and Mg-Zn precipitates compared to the low Zn-containing alloys. Furthermore, in a separate work, Saito et al. [37] investigated the influence of Zn addition on the precipitations and IGC of Al-Mg-Si alloys. The results showed that the Zn concentrations up to 0.1wt% have a negligible impact on the precipitate structure and IGC resistance.

The aforementioned background motivated us to systematically investigate the influence of tiny concentrations of Cu/Zn and aging time and temperature on the microstructure, precipitate crystal structure, and IGC of Al-Mg-Si alloys in detail. Such concentrations are expected to be found in recycled aluminium alloys, so it is crucial to understand the sensitivity of Al-Mg-Si alloys to very low Cu and Zn concentrations.

Due to this fact, the overall hypothesis of the current project is that:

- There is a lack in the literature on how tiny concentrations of copper influence intergranular corrosion of Al-Mg-Si alloy and whether the IGC in such low concentration can be linked directly to the copper.
- Whether intergranular corrosion resistance of Al-Mg-Si alloy can be affected by minor addition of Zn and whether the IGC resistance can be improved by careful addition of Cu.
- Lack of understanding of the correlation between grain boundary misorientation and Intergranular corrosion in Al-Mg-Si alloy containing very low Cu concentration.
- Lack of understanding of the influence of treatment parameters (time and temperature) in the presence of trace level of Cu and/or Zn on microstructure and intergranular corrosion of Al-Mg-Si alloys.

1.2 Objectives

The first objective of the present Ph.D. project is to provide a fundamental understanding of the influence of tiny concentrations of copper, zinc, and a combination of copper and zinc on the microstructure, precipitate crystal structures, and intergranular corrosion of Al-Mg-Si alloys in the peakaged (PA) condition. The second objective is to understand the correlation between grain boundary misorientation and the initiation and propagation of intergranular corrosion in Al-Mg-Si-0.05wt% Cu in the PA condition. The third objective of the current work is to investigate the influence of aging time and temperature in the presence of trace levels of Cu and/or Zn on the susceptibility to IGC of Al-Mg-Si alloys. This can be done by understanding the underlying mechanisms causing the IGC with different aging conditions and elemental compositions. This work deals with minor Zn addition, Cu addition, and a combination of Cu and Zn to understand whether such minor addition will affect GB chemistry, GB precipitates, and precipitate crystal structures.

1.3 Structure of the thesis

The current Ph.D. thesis is structured in 14 individual chapters, see Fig. 1.1. Chapter 1 gives a comprehensive introduction to the sensitivity of Al-Mg-Si alloy to copper and zinc as well as introduces the research objective. In Chapter 2, a detailed literature review on Al-Mg-Si alloys, their precipitates, and their susceptibility to intergranular corrosion is reviewed. Material and characterization techniques used in this research are presented in Chapter 3. A summary of the experimental work is presented in Chapter 4. The findings of this study are addressed in Chapters 5-11. Chapter 5 deals with the effect of grain boundary types on the IGC of Al-Mg-Si alloy with 0.05 wt%. Chapters 6 and 7 deal with the influence of minor addition of Cu and Zn on the microstructure and IGC of Al-Mg-Si alloy, respectively. Chapter 8 reports the effect of the combination of Zn and Cu on the IGC and precipitate crystal structures. Chapters 9 and 10 deal with the impact of aging time and temperature on the microstructure and IGC in Al-Mg-Si alloys, respectively. Chapter 11 reports the influence of Cu, Zn, Cu+Zn, and aging temperature of the precipitate structure. Overall discussion and conclusions, along with future work, are presented in Chapters 12, 13, and 14, respectively.

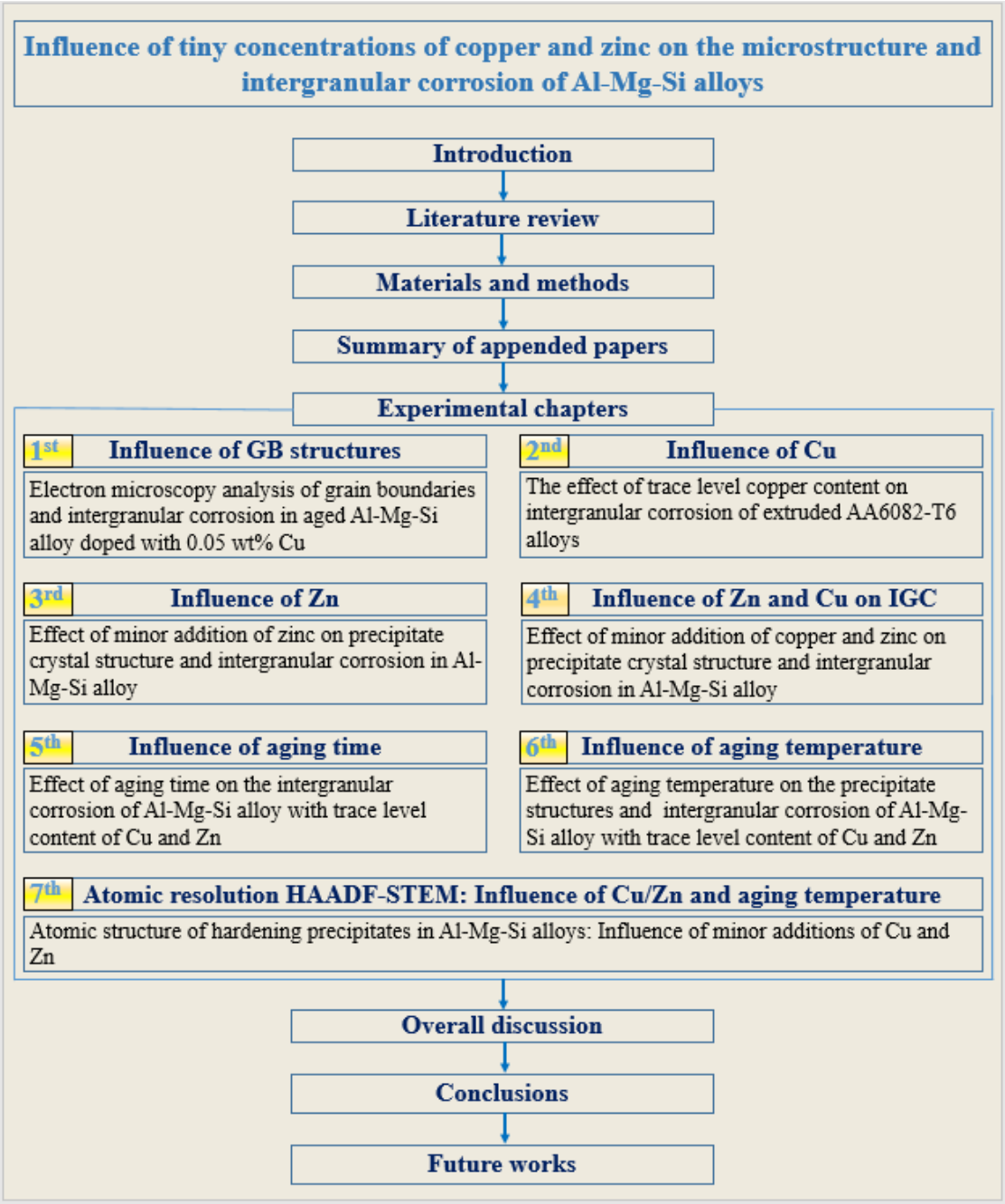

Fig. 1.1. Structure of the Ph.D. dissertation

References

[1] A. Rawal, R. Kumar, H. Saraswat, Reviews on the influences of alloying elements on the microstructure and mechanical properties of aluminum alloys and aluminum alloy composites, Text. Res. J. 82 (2012) 1703–1710.

[2] G. Saevarsdottir, H. Kvande, B.J. Welch, Aluminum production in the times of climate change: The global challenge to reduce the carbon footprint and prevent carbon leakage, Jom. 72 (2020) 296–308.

[3] G.A. Dietrich, Aluminum: technology, applications, and environment, A Profile a Mod. Met. (1998).

[4] J. Gerber, Global aluminium recycling: a cornerstone of sustainable development, International Aluminium Institute, 2006.

[5] S.K. Das, J.A.S. Green, G. Kaufman, Aluminum recycling: Economic and environmental benefits, Light Met. Age. 68 (2010) 42–46.

[6] U.B. Kuruveri, D.B. Panemangalore, S.B. Kuruveri, M. John, P.L. Menezes, Surface modification of 6xxx series aluminum alloys, Coatings. 12 (2022).

[7] D. Altenpohl, Aluminum viewed from within: An introduction into the metallurgy of aluminum fabrication, 1st, Ed. Alum. Dusseld. (1982).

[8] W.S. Miller, L. Zhuang, J. Bottema, A.J. Wittebrood, P. De Smet, A. Haszler, A. Vieregge, Recent development in aluminium alloys for the automotive industry, Mater. Sci. Eng. A. 280 (2000) 37–49.

[9] G. Svenningsen, M.H. Larsen, J.C. Walmsley, J.H. Nordlien, K. Nisancioglu, Effect of artificial aging on intergranular corrosion of extruded AlMgSi alloy with small Cu content, Corros. Sci. 48 (2006) 1528–1543.

[10] G. Svenningsen, M.H. Larsen, J.H. Nordlien, K. Nisancioglu, Effect of thermomechanical history on intergranular corrosion of extruded AlMgSi(Cu) model alloy, Corros. Sci. 48 (2006) 3969–3987.

[11] M.H. Larsen, J.C. Walmsley, O. Lunder, K. Nisancioglu, Effect of excess silicon and small copper content on intergranular corrosion of 6000-series aluminum alloys, J. Electrochem. Soc. 157 (2010) C61.

[12] X. Zhang, X. Zhou, J.O. Nilsson, Corrosion behaviour of AA6082 Al-Mg-Si alloy extrusion: The influence of quench cooling rate, Corros. Sci. 150 (2019) 100–109.

[13] X. Xuehong, Y. Deng, C. Shuiqing, G. Xiaobin, Effect of interrupted ageing treatment on the mechanical properties and intergranular corrosion behavior of Al-Mg-Si alloys, J. Mater. Res. Technol. 9 (2020) 230–241.

[14] G. Svenningsen, J.E. Lein, A. Bjørgum, J.H. Nordlien, Y. Yu, K. Nisancioglu, Effect of low copper content and heat treatment on intergranular corrosion of model AlMgSi alloys, Corros. Sci. 48 (2006) 226–242.

[15] C.D. Marioara, S.J. Andersen, T.N. Stene, H. Hasting, J. Walmsley, A.T.J. Van Helvoort, R. Holmestad, The effect of Cu on precipitation in Al-Mg-Si alloys, Philos. Mag. 87 (2007) 3385–3413.

[16] Y. Zou, Q. Liu, Z. Jia, Y. Xing, L. Ding, X. Wang, The intergranular corrosion behavior of 6000-series alloys with different Mg/Si and Cu content, Appl. Surf. Sci. 405 (2017) 489–496.

[17] S. Kumari, S. Wenner, J.C. Walmsley, O. Lunder, K. Nisancioglu, Progress in understanding initiation of intergranular corrosion on AA6005 aluminum alloy with low copper content, J. Electrochem. Soc. 166 (2019) C3114–C3123.

[18] X. Zhang, Y. Lv, T. Hashimoto, J.O. Nilsson, X. Zhou, Intergranular corrosion of AA6082 Al–Mg–Si alloy extrusion: The influence of trace Cu and grain boundary misorientation, J. Alloys Compd. 853 (2021) 157228.

[19] S.H. Kim, U. Erb, K.T. Aust, G. Palumbo, Grain boundary character distribution and intergranular corrosion behavior in high purity aluminum, Scr. Mater. 44 (2001) 835–839.

[20] T. Minoda, H. Yoshida, Effect of grain boundary characteristics on intergranular corrosion resistance of 6061 aluminum alloy extrusion, Metall. Mater. Trans. A. 33 (2002) 2891–2898.

[21] A. Lervik, S. Wenner, O. Lunder, C.D. Marioara, R. Holmestad, Grain boundary structures and their correlation with intergranular corrosion in an extruded Al-Mg-Si-Cu alloy, Mater. Charact. 170 (2020) 110695.

[22] Z. Wang, H. Li, F. Miao, W. Sun, B. Fang, R. Song, Z. Zheng, Improving the intergranular corrosion resistance of Al–Mg–Si–Cu alloys without strength loss by a two-step aging treatment, Mater. Sci. Eng. A. 590 (2014) 267–273.

[23] H. Zhan, J.M.C. Mol, F. Hannour, L. Zhuang, H. Terryn, J.H.W. De Wit, The influence of copper content on intergranular corrosion of model AlMgSi(Cu) alloys, Mater. Corros. 59 (2008) 670–675.

[24] A. Lervik, T. Danbolt, T. Furu, R. Holmestad, O. Lunder, Comparing intergranular corrosion in Al-Mg-Si-Cu alloys with and without α-Al(Fe,Mn,Cu)Si particles, Mater. Corros. 72 (2021) 575–584.

[25] Y. Zou, Q. Liu, Z. Jia, Y. Xing, L. Ding, X. Wang, The intergranular corrosion behavior of 6000-series alloys with different Mg/Si and Cu content, Appl. Surf. Sci. 405 (2017) 489–496.

[26] S.K. Kairy, T. Alam, P.A. Rometsch, C.H.J. Davies, R. Banerjee, N. Birbilis, Understanding the origins of intergranular corrosion in copper-containing Al-Mg-Si alloys, Metall. Mater. Trans. A Phys. Metall. Mater. Sci. 47 (2016) 985–989.

[27] S.K. Kairy, P.A. Rometsch, C.H.J. Davies, N. Birbilis, On the intergranular corrosion and hardness evolution of 6xxx series Al alloys as a function of Si:Mg ratio, Cu Content, and aging condition, Corrosion. 73 (2017) 1280–1295.

[28] G. Svenningsen, M.H. Larsen, J. Lein, J. Nordlien, K. Nisancioglu, Intergranular corrosion of extruded AA6000-series model alloys, Proc. 9th Int. Conf. Alum. Alloy. (2004) 818–824.

[29] W. Yang, S. Ji, Z. Li, M. Wang, Grain boundary precipitation induced by grain crystallographic misorientations in an extruded Al-Mg-Si-Cu alloy, J. Alloys Compd. 624 (2015) 27–30.

[30] S. Chi, Y. Deng, X. Xu, X. Guo, Influence of minor Zn addition on precipitation behavior and intergranular corrosion properties of Al-Mg-Si alloy, Materials (Basel). 13 (2020) 650.

[31] T. Saito, F.J.H. Ehlers, W. Lefebvre, D. Hernandez-Maldonado, R. Bjørge, C.D. Marioara, S.J. Andersen, R. Holmestad, HAADF-STEM and DFT investigations of the Zn-containing β'' phase in Al-Mg-Si alloys, Acta Mater. 78 (2014) 245–253.

[32] X. Xu, Y. Deng, Q. Pan, X. Guo, Enhancing the intergranular corrosion resistance of the Al–Mg–Si alloy with low Zn content by the interrupted aging treatment, Metall. Mater. Trans. A. 52 (2021) 4907–4921.

[33] A. Lutz, L. Malet, J. Dille, L.H. de Almeida, L. Lapeire, K. Verbeken, S. Godet, H. Terryn, I. De Graeve, Effect of Zn on the grain boundary precipitates and resulting alkaline etching

of recycled Al-Mg-Si-Cu alloys, J. Alloys Compd. 794 (2019) 435–442.

[34] S. Zhu, Z. Li, L. Yan, X. Li, S. Huang, H. Yan, Y. Zhang, B. Xiong, Effects of Zn addition on the age hardening behavior and precipitation evolution of an Al-Mg-Si-Cu alloy, Mater. Charact. 145 (2018) 258–267.

[35] L. Li, S. Ji, Q. Zhu, Y. Wang, X. Dong, W. Yang, S. Midson, Y. Kang, Effect of Zn concentration on the microstructure and mechanical properties of Al-Mg-Si-Zn alloys processed by gravity die casting, Metall. Mater. Trans. A. 49 (2018) 3247–3256.

[36] M.X. Guo, J.Q. Du, C.H. Zheng, J.S. Zhang, L.Z. Zhuang, Influence of Zn contents on precipitation and corrosion of Al-Mg-Si-Cu-Zn alloys for automotive applications, J. Alloys Compd. 778 (2019) 256–270.

[37] T. Saito, S. Wenner, E. Osmundsen, C.D. Marioara, S.J. Andersen, J. Røyset, W. Lefebvre, R. Holmestad, The effect of Zn on precipitation in Al-Mg-Si alloys, Philos. Mag. 94 (2014) 2410–2425.

2. Literature review

2.1 Aluminium alloys

Aluminium is the second most used metal after iron and has become indispensable to our society. Aluminium is extensively used in many applications such as automotive, architecture, electrical transmission, and packaging due to its attractive properties, such as high strength-to-weight ratio, non-toxic, electrical and thermal conductivity, and good corrosion resistance [1]. The demand for Aluminium and its alloy will increase as aluminium consumption is expected to rise by 33.3 Mt for different applications in 2030 compared to 2020, as seen in Fig. 2.1. The transport and electrical applications are expected to take the dominant share of the increased aluminium demand, with an increase of 35 % and 16 %, respectively [2].

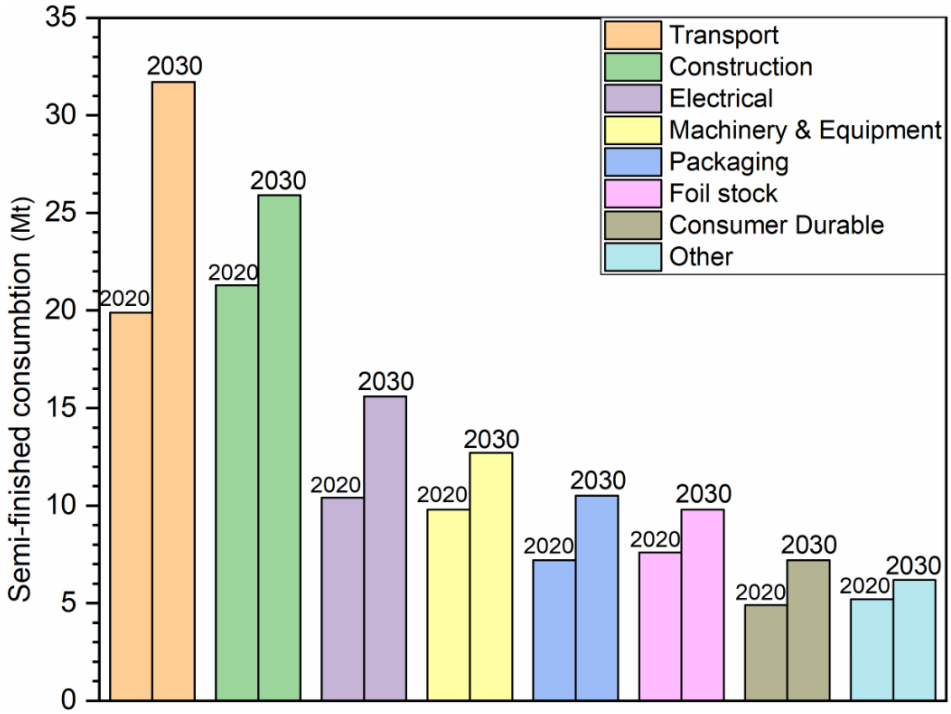

Fig. 2.1. Aluminium semi-finished products consumption forecast in 2030 based on 2020 consumption, modified from [2].

The aluminium-making process involves many steps, including bauxite mining, refining, electrolysis, casting, product manufacturing, etc., as seen in Fig. 2.2. The majority of carbon emission of primary aluminium production comes from electrolysis (consuming a lot of electricity) and the refining process (consuming a lot of heating). The estimated CO_2 emission of both processes is more than 88 % of the whole emission during primary

aluminium production. Due to environmental issues and severe pressure to reduce the amount of CO_2 emission, recycling has become inevitable. Aluminium is recyclable as it can be recycled repeatedly without degrading its mechanical and physical properties. Aluminium recycling can considerably reduce greenhouse gas emissions by more than 90 million tonnes annually by decreasing energy consumption up to 90 % [3,4]. Also, another considerable motivation for recycling Al alloys is the cost reduction due to a noticeable decrease in energy consumption that can be achieved by manufacturing scrap-based Al alloys. Hence it will compete with other structural materials. It is important to mention that the cost of recycled Al alloys is highly influenced by the fraction of pure aluminum added and the amount of energy needed during recycling to keep the impurities within the lower and the upper limits of the standard composition range. However, some other challenges are face in the recycling process, such as collecting the old scrap and removing unwanted components prior to the melting process. Unlike ferrous metals, separating unwanted components requires special technologies to recycle aluminium to ensure recycled metal's high corrosion resistance and mechanical properties [5].

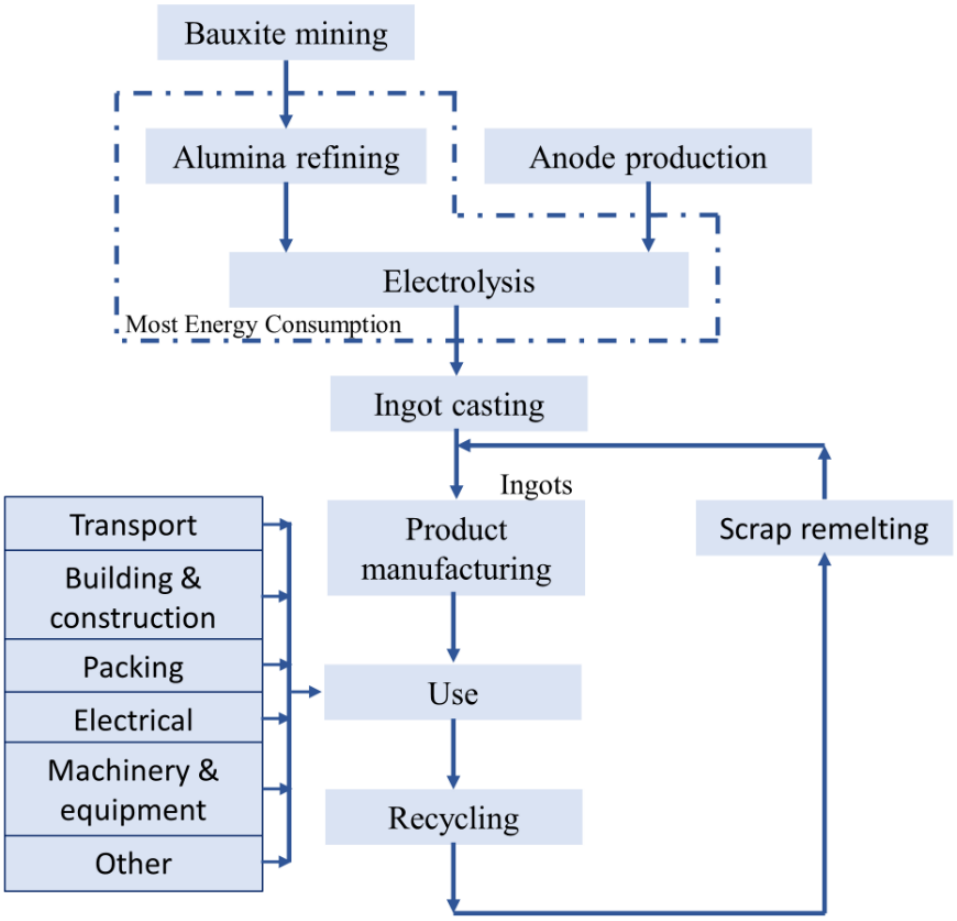

Fig. 2.2. Process flow diagram of aluminium production, modified from [6]

2.2 Aluminium alloy designation

All aluminium alloys fall into two main groups with respect to processing, cast aluminium alloys and wrought aluminium alloys. The wrought aluminium alloys will be considered in this chapter. The designation system of wrought alloys contains four numerical digits, as shown in the Table 2.1. The first digit starts with a number showing the major alloying group. The second digit is related to the variation in a specific series by controlling one or more alloying elements to obtain particular properties. If the second digit is 0, no modification was applied to the original compositions. The third and fourth digits in the 1xxx series refer to the alloy purity level of aluminium used in this alloy. For instance, the designation 1040 refers to the aluminium purity of minimum 99.40 % in this alloy. While in the remaining series from 2xxx to 8xxx, they refer to the specific individual alloy in this group [7–10].

Table 2.1. Wrought aluminium alloys designation system and application.

1xxx	Pure Aluminium Minimum 99.00	Packaging, electronics, and electrical wiring
2xxx	Copper	Aircraft construction & truck frames
3xxx	Manganese	Food and chemical handling, oil tanks, and piping
4xxx	Silicon	Food handling and marine fitting
5xxx	Magnesium	Transportation, pipes and marine applications
6xxx	Magnesium & Silicon	Automotive application, construction, and aircraft applications
7xxx	Zinc	Aerospace applications
8xxx	Other elements (e.g., Lithium, tin or iron)	Aircraft industry

1xxx series alloys: The composition of these alloys is at least 99.00 wt% aluminium. They are exceptionally corrosion-resistant and have high electrical conductivity. However, it has low strength even after strain hardening, hence it is of limited use in engineering applications where mechanical properties are needed. In this system, different intermetallic phases, such as Al_3Fe, Al_5FeSi, and $Al8Fe_2Si$ can be observed in its microstructure when iron and silicon are present as impurities [11].

2xxx series alloys: The main alloying element in this series is copper. This group responds to solution heat treatment due to the high solubility of Cu in aluminium (5.5 wt% at 547 °C) and decreases with temperature decrease. Susceptibility to stress corrosion cracking (SSC) can be improved by heat treatment, but the mechanical properties will decrease. Based on alloy composition and aging parameters, different types of strength-enhancing precipitates can be noticed in its microstructure, e.g., θ phase (Al_2Cu), and it is precursor or S phase (Al_2CuMg) and its precursor [12]. Coarse intermetallic particles, e.g., Al_7Cu_2Fe and Mg_2Si, can also be found [13].

3xxx series alloys: This series is based on manganese and is a non-heat treatable group. Therefore, the improvement in mechanical properties can be obtained by solution strengthening. The solubility of manganese in solid solution at 658 °C is 1.82 wt% and decreases as the temperature decreases. This series is characterized by good formability and good corrosion resistance, thus, it is used, for instance, in heat exchangers, chemical equipment, and radiators. The two major types of intermetallic particles that can be observed in Al-Mn alloys are Al_6 (Fe, Mn) and Al_{12} $(Fe, Mn)_3$ Si. The solidification rate and the alloy composition determine the amount of these particles in its microstructure [14].

4xxx series alloys: Silicon added to this series reduces the melting temperature and enhances fluidity. The silicon solubility in aluminium at 578 °C is 1.65 wt% and decreases at a lower temperature. The alloys containing only silicon are non-heat treatable, but those with copper and/or magnesium, in addition to silicon, are characterized as heat treatable alloys. Aluminium silicon alloys have good corrosion resistance. Al-Si alloys are widely used as wielding filler alloys. Mostly 4xxx series alloys are used as cast alloys. Intermetallic particles such as the AlFeMnSi phase can be found in 4xxx [15].

5xxx series alloys: Magnesium is the primary alloying element in this series as the strength increases via solid solution strengthening. This series is used in structural applications as it has the highest strength among non-heat treatable alloys. Al-Mg alloys are generally used in building and construction. It is also characterized by it is high corrosion resistance. Depending on chemical composition various constituent intermetallic such as Mg_2Si, Al_{12} $(Mn, Fe)_3$ Si, Al_6 (Fe, Mn), or Al_3Fe can be observed in 5xxx alloys [14].

6xxx series alloys: The main two alloying elements in this group are Magnesium and silicon. They are heat treatable alloys with noticeable corrosion resistance, medium strength, and excellent extrudability, making them suitable for architectural and structural applications. Different intermetallic particles can be observed in Al-Mg-Si alloys e.g., $Al_{15}FeSi$, $Al_{15}(FeMn)_3Si$, $AlMn_3Si$ and $Al_{12}Fe_3Si$ [16]. The hardening precipitates in this system are Mg-Si phases.

7xxx series alloys: Zinc is the primary alloying element, usually together with magnesium and copper. The solubility of zinc in aluminium is 31.6 wt% at 275 °C and decreases with decreasing the temperature. Al-Zn-Mg-Cu alloys are heat treatable, providing the highest strength among aluminium alloys. This series has low atmospheric corrosion resistance compared to other alloys. Depending on the chemical composition and heat treatment condition, different particles can be found in 7xxx alloys, e.g., Al_7Cu_2Fe, $(Al, Cu)_6(Fe, Cu)$, and Al_2CuMg [17,18].

8xxx series alloys: The composition varies as it contains one or more of several elements, usually not used as main alloying elements. Some of the Al-Li alloys belong to this category. The mechanical properties of alloys in this group vary depending on the main alloying elements. In the Al-Li alloys, metastable phase δ' (Al_3Li) can be observed in its microstructure. In Cu-containing alloys, T1 (Al_2CuLi), S' (Al_2CuMg), or θ' (Al_2Cu) can be observed [19].

2.3 Corrosion of aluminium alloy

Three possible scenarios can be observed when aluminium is exposed to an aqueous solution: corrosion, passivity, and immunity. The three mentioned scenarios are linked to the acidity or alkalinity level of the environment. The physical and chemical properties of the oxide film's structure formed on the aluminum surface are highly influenced by the environment. For instance, the passive film formed in the air is a thin amorphous layer, while a denser, more compact, and thin amorphous passive film is formed in an aqueous solution [20]. As a general saying, the passive protective film is stable in an aqueous environment with a pH between 4 and 9, while it is soluble in acid and alkaline environments, as seen in Figs. 2.3 and 2.4. However, the aluminium oxide film is highly stable in certain alkaline and acid solutions, such as sodium disilicate and acetic acid, as

seen in Fig. 2.4. Therefore, the corrosivity of the system can also be influenced by the nature of the individual ions present in the solution [21].

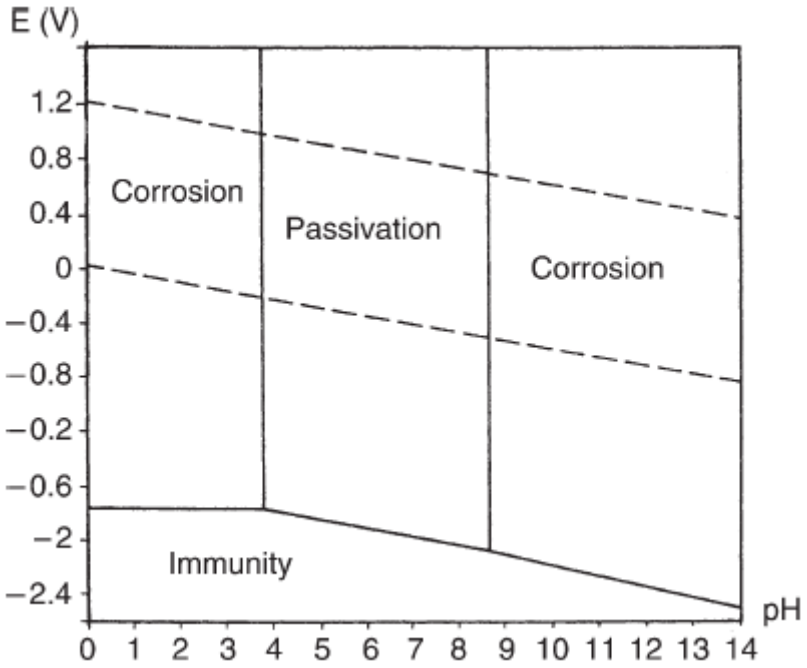

Fig. 2.3. Pourbaix E-pH diagram for aluminium demonstrating the conditions of corrosion, passivation, and immunity [1].

The electrochemical reaction between the alloy and an aqueous phase causes corrosion in aluminium alloys. The oxidation of aluminium occurs according to the following equation:

$$Al \rightarrow Al^{3+} + 3e^{-} \qquad (1)$$

When aluminium is oxidized by losing three electrons, it goes into solution as a cation Al^{+3}, which is balanced by the reduction of the ion present in the solution simultaneously.

The reduction reaction in an aqueous solution depends upon the pH of the solution and other conditions. In general in solutions with varying pH and aerated conditions provide following possibilities for cathodic reduction process. With a pH close to neutral conditions, the reduction reaction equation can be as the follows [1]:

$$3H^{+} + 3e^{-} \rightarrow \tfrac{3}{2} H_2 \qquad (2)$$

At higher potential, hydrogen reduction can occur due to dissociation of water producing protons [1]:

$$H_2O \leftrightarrows H^{+} + OH^{-} \qquad (3)$$

Under neutral or alkaline conditions, dissolved oxygen can contribute to reduction process. Reduction of the dissolved oxygen in neutral or alkaline media is [1]:

$$O_2 + 2H_2O + 4e^- \rightarrow 4OH^- \qquad (4)$$

While oxygen reduction in an acidic solution is [1]:

$$O_2 + 4H^+ + 4e^- \rightarrow 2H_2O \qquad (5)$$

The oxygen solubility in water under atmospheric pressure is influenced by temperature as at 20 °C is 43.4 mg.kg^{-1}, while it becomes no more than 13.8 mg.kg^{-1} at 80 °C.

The corrosion of aluminium is the sum of the oxidation and reduction reactions and is given by the following equations:

$$Al + 3H^+ \rightarrow Al^{3+} + \frac{3}{2}H_2 \qquad (6)$$

Or [1,22]

$$Al + 3\,H_2O \rightarrow Al(OH)_3 + \tfrac{3}{2}H_2 \qquad (7)$$

Al(OH)3, which is insoluble in water and considered as an aluminium corrosion product.

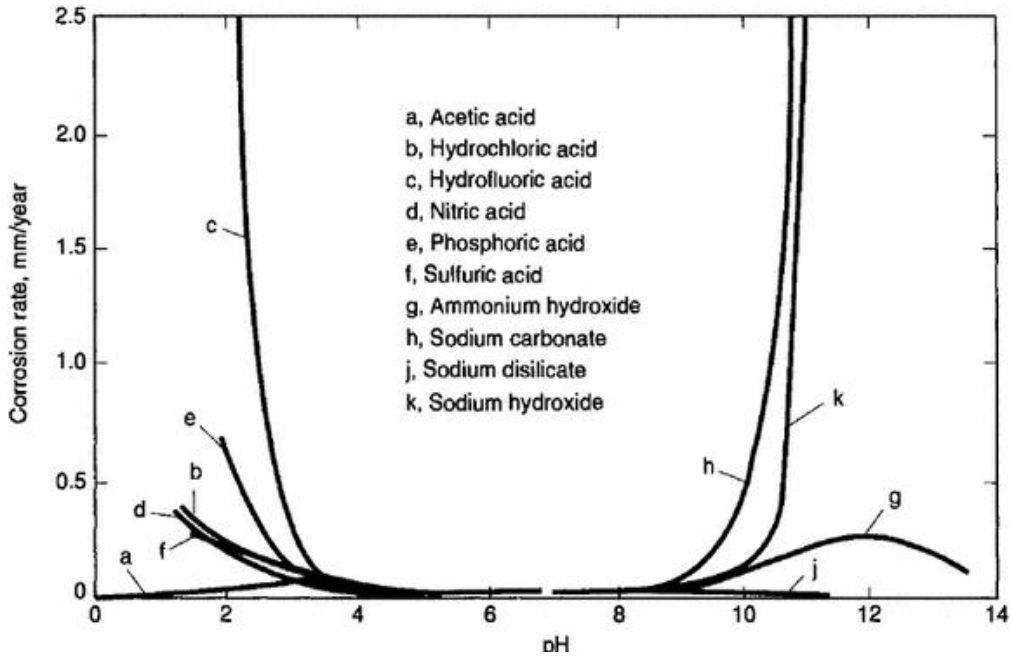

Fig. 2.4. Influence of pH and the nature of acids and bases on the corrosion behavior of 1100-H14 aluminium alloy [21].

2.4 Grain boundary

In polycrystalline materials, the internal interface separating two grains with different crystallographic orientations is called grain boundary (GB) [23]. GBs are considered as 2D defects in the crystal structures and can be found in metallic materials, ceramics, and to a lesser extent, can be observed in organic crystals [24]. Traditionally grain boundaries structure and energy are assumed to be defined by five crystallographic angles. However, it has also recently been found that the atomic density in the grain boundary area can cause GB phase transformation and dramatically modify the GB structure [25]. Three of the five independent macroscopic degrees of freedom (DOFs) specify the misorientation between the adjoined two grains, see Fig. 2.5. One for the rotation angle (θ) between the two crystals, and two of them describing the rotation axis (**o**). The other two DFOs represent the grain boundary's orientation, which is defined by normal vector **n** to the grain boundary plane.

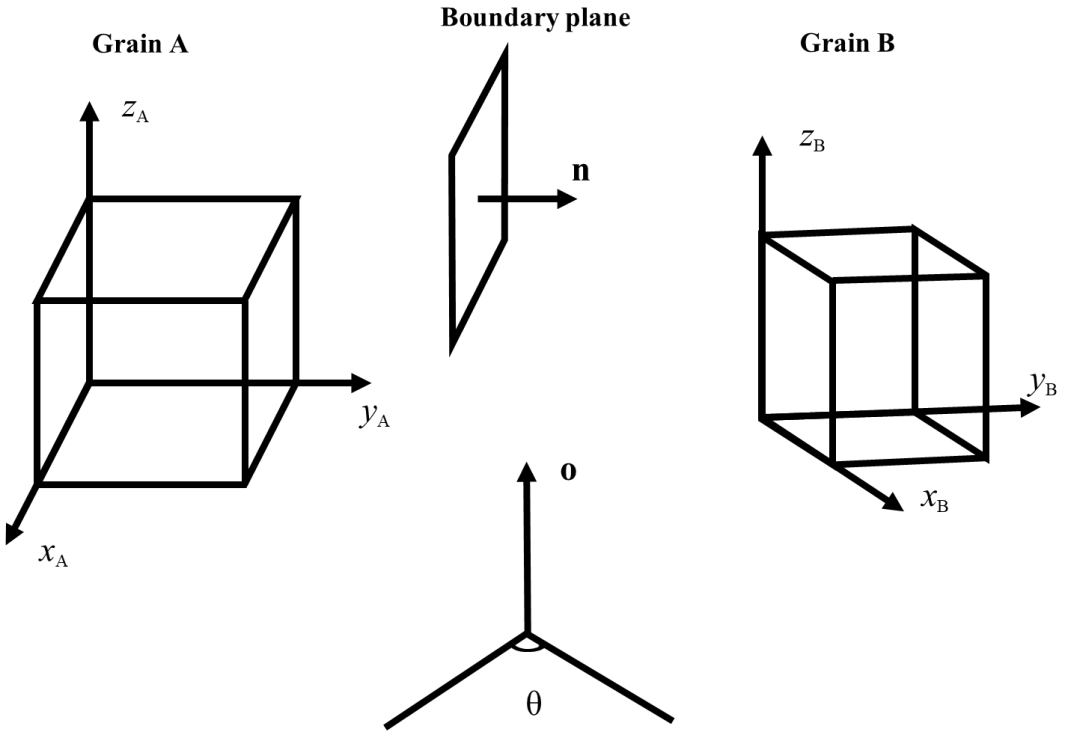

Fig. 2.5. Schematic depiction of factors that define a grain boundary. θ is the misorientation angle, **o is the** rotation axis, and **n** defines the orientation of the boundary plane [26].

The relation between the grain boundary plane normal vector **n** and the rotation axis **o** defines the tilted and twisted grain boundaries. Tilt grain boundaries is formed when the

rotation axis is perpendicular to the normal vector (**o** ⊥ **n**), while in case of twist grain boundaries the rotation axis is parallel to the normal vector (**o** ∥ **n**). Any other GBs that did not fall within this definition are classified as mixed grain boundaries. The pure tilt boundaries can also be divided into symmetric and asymmetric grain boundaries on the basis of their relation to the GB plane. The symmetric tilt grain boundaries are mirrored about the GB plane, while the other type is called asymmetric tilt boundaries [26]. Therefore, the interface plane scheme suggested by Wolf & Lutsko [27] considering the relation between miller indices of contacting planes in a bicrystal and twist angle **φ** is summarized in Table 2.2.

Table 2.2. The four distinguished categories of grain boundaries on the basis of miller indices of grains 1 and 2 and twist angle **φ**.

Symmetrical tilt grain boundary	$\{h1k1l1\} = \{h2k2l2\}$ & $\varphi = 0$
Asymmetric tilt grain boundary	$\{h1k1l1\} \neq \{h2k2l2\}$ & $\varphi = 0$
Twist grain boundary	$\{h1k1l1\} = \{h2k2l2\}$ & $\varphi \neq 0$
Mixed grain boundary	$\{h1k1l1\} \neq \{h2k2l2\}$ & $\varphi \neq 0$

Due to the irregular arrangement of the atoms on the grain boundaries, a higher potential is expected, which is called grain boundary energy. GB energy strongly influences the intergranular corrosion (IGC) resistance and the mechanical properties of the materials. This energy is also influenced by many factors, such as impurities, temperature, and the misorientation angle between the adjacent grains [28–30]. It is convenient to categorize the grain boundaries based on the orientation into high-angle grain boundaries (HAGBs) and low-angle grain boundaries (LAGBs). Low-angle grain boundaries are described by a periodic discrete crystal dislocation. The transition from low-angle to high-angle boundaries is still unknown precisely. Based on the experimental work for investigating the grain boundary energy, it is suggested that the transition angle is near 15° [23,31]. Moreover, in corrosion investigations conducted on aluminium alloys, the coincidence site lattice boundaries have often been used, which are considered as special boundaries, proposed by Kronberg & Wilson [32]. In such boundaries, the grain boundary plane is not taken into consideration [33].

2.5 Segregation in aluminium alloys

Different structures and properties between grain boundaries and grain interior result in different chemical compositions. The chemical partitioning is caused by specific solute segregation, which occurs due to the interaction between grain boundaries and other lattice defects in the grain interior, such as vacancies, dislocations, and foreign atoms [26,34]. The grain boundary segregation is usually closely associated with the formation of the depleted zone, which is called precipitate free zones (PFZs). This phenomenon is attributed to the formation of solute-enriched grain boundaries leading to a vast difference in the concentration of specific solute atoms between the denuded area and unaffected grain interiors [35,36].

The formation of the precipitate free zones is observed along the grain boundaries of aluminium alloys [37–41]. The main mechanisms of segregation through which impurity atoms can reach grain boundaries are vacancy segregation and solute segregation [26,42,43]. The vacancy segregation, also called non-equilibrium segregation, occurred during cooling from solution treatment temperature [26,44]. Quenching aluminium alloys after the heat treatment introduces more point defects to the system (vacancy). During subsequent heat treatment and even as a result of quenching, depending on quenching time and temperature, vacancies migrate toward the grain boundaries as the latter is considered efficient vacancy sinks. At the same time, the vacancy concentrations in the matrix are kept under the supersaturation condition. Depending on the solute-vacancy binding energy, this migration may result in a grain boundary enrichment by specific solute atoms [45]. This implies that the solute-vacancy bindings significantly determine impurity segregation toward grain boundaries. In some cases, strong solute vacancy binding suppresses the segregation of the impurities with a relatively weaker solute vacancy binding [46].

Solute segregations or equilibrium grain boundary segregations happen due to the interaction between chemical defect (foreign atoms), and structure defect (grain boundaries). The driving force for such a process is due to the difference in the free energy between impurity atoms being present at the grain boundaries and the same type of atoms being present in the matrix [26,44]. Segregation phenomena has a significant impact on the corrosion properties, but it also affects other material properties such as strength and strain hardening, and creep [47–55]. Detailed work concerning grain boundary segregations was

conducted on ultrafine-grained aluminium alloys. Segregation of Mg and Si in Al-Mg-Si alloys was documented [56], as well as the segregation of Cu, Mg, and in a limited way, the Zn in Al-Mg-Zn-Cu alloys was also reported [57].

2.6 Thermo-mechanical processing

Most aluminium alloys are subjected to subsequent mechanical working and annealing processing to produce finished or semi-finished aluminum products. Heat treatable alloys are given a precipitation hardening process which includes solutionizing, quenching (e.g., water-quenching or air-cooling), and aging [58,59]. Since the current work is related to Al-Mg-Si alloy, the focus will be paid to discuss the microstructure and IGC resistance of this group. Al-Mg-Si alloys are one of the most popular Al alloys, widely used in automotive and structural applications owing to their attractive properties such as strength-to-weight ratio and good corrosion resistance [60]. Al-Mg-Si alloys are heat treatable and, in many cases, heat treated to T6 condition to achieve adequate strength. The age hardening response of this system is highly influenced by the presence of certain alloying elements, e.g., Sn, Cu, Zn, and Ag [61–66]. The processing route showing the stages for heat treatable alloys is schematically demonstrated in Fig. 2.6.

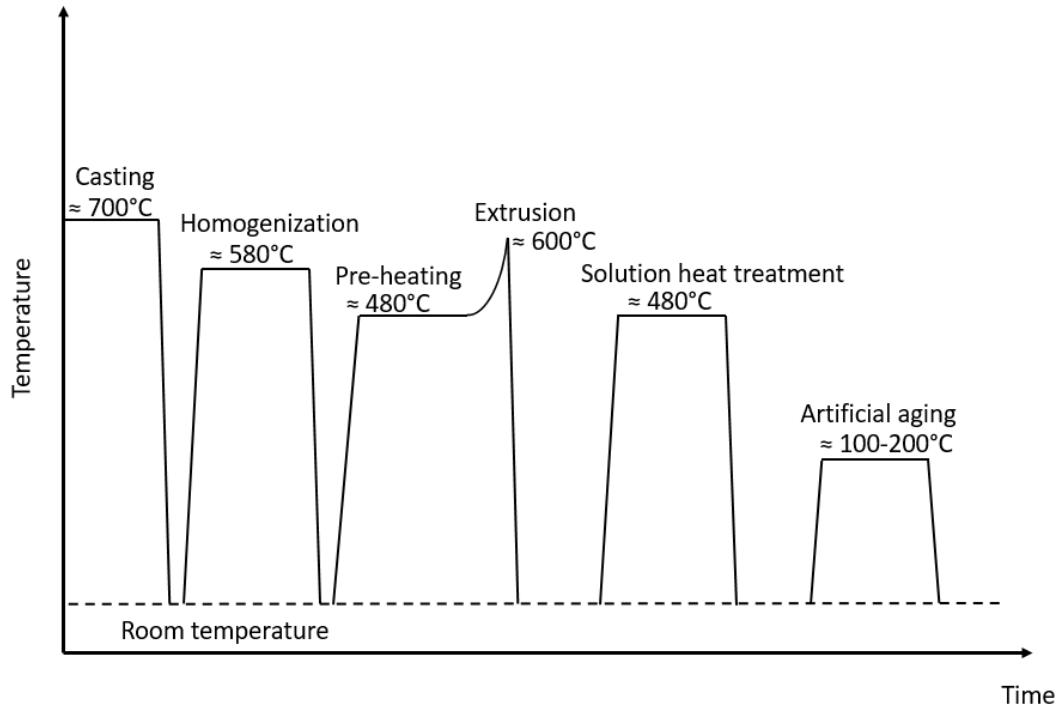

Fig. 2.6. Schematic diagram demonstrating thermo-mechanical processing of aluminium alloys from casting to artificial aging.

As shown in the Fig. 2.6, firstly, alloys are cast into billets. The cast billets' microstructure contains intermetallic compounds formed during the solidification stage. The formation of the Al-Fe-Si phase during billet solidification is influenced by the cooling rate as well as the billet size. A smaller size and more uniform distribution of the Al-Fe-Si phase inside the grains and at the grain boundaries were observed in smaller billets. It is also reported that the grain size in Al-Mg-Si alloys is affected by the size of the casted billets, as the general tendency is, the smaller billets, the smaller the grain size [67]. The homogenization treatment at a temperature near its melting point after casting is performed to transfer β-AlFeSi to α-Al(Fe, Mn)Si, forming nanoscale dispersoid, reducing alloying element segregation, and dissolving Mg_2Si phase formed at the grain boundaries [68–70]. After homogenization heat treatment, the alloys will be further processed by rolling, extrusion, or other forming process [71,72].

Prior to the extrusion, the alloys are carefully preheated to a relatively high temperature to dissolve Mg_2Si precipitates in order to avoid the eutectic melting and thus withstanding a higher temperature before tearing takes place. Increasing the billet's temperature will significantly improve the extrusion speed as well as reduce the required pressure. On the microstructure side, extruded aluminum alloys display two types of structure. The first type consists of the fibrous layer in the center with severely sheared grain along the surface, typically observed in alloys extruded at low temperatures. The second type contains a fibrous layer in the center and recrystallized layer at the surface, generally noted at relatively high-temperature extrusion [73].

Solution heat treatment (SHT) is often required to enhance the mechanical properties of Al-Mg-Si alloys, followed by water-quenching or air-cooling [74,75]. The influence of heat treatment temperature on Al 6082 was documented by Mrówka-Nowotnik et al. [76], who heat treated the alloys within the range from 510 to 580 °C. The results showed that the hardness of the alloys is affected by the heat treatment temperature, as the higher the temperature, the harder the material is. Solution heat treatment procedures are also illustrated in Fig. 2.6 and can be described as follows:

1. Solution heat treatment is performed at an elevated temperature to dissolve the alloying elements in a solid solution. The recommended temperature varies according to the Al alloy type and ranges from 441 to 527 °C. The desired

mechanical properties will not be satisfactory if the alloys are solutionized at low temperatures. On the other hand, if the temperature is too high, the quenching strain will increase as well as the discoloration will promote [77].

2. After solution treatment, the alloys should be quenched to retard or prevent the precipitation, so holding the solid solution and a higher number of vacancies at room temperature [77,78]. A low cooling rate can trigger the formation of precipitates, which will negatively influence the corrosion resistance and mechanical properties [79].
3. The final step is artificial aging, which is usually conducted at temperatures between 100 to 200 °C for 2 to 48 h. In this stage, the supersaturated solid solution obtained after quenching decompose to the meta-stable hardening precipitates in the aluminium alloy matrix [79].

2.7 Precipitation in Al-Mg-Si alloys

Iron containing particles are formed during casting as result of low solid solubility of the iron in molten aluminium (~0.04 wt%) [80]. Several intermetallic particles can be observed in the microstructure of Al-Mg-Si alloys, e.g., $Al_{15}(Fe,Mn)_3Si_2$, Al_5FeSi and $Al_{13}Fe_4$ [80–82]. In the presence of Mn in such alloys, Al_6Mn, $Al_{12}Mn_3Si_2$, α-AlMnSi and α-Al(MnCr)Si (in the presence of Cr) dispersoid particles can be observed [83–86]. The presence of such particles in the microstructure can effectively pin the grain boundaries of Al alloys during the thermomechanical process [87]. After quenching Al-Mg-Si alloys, the alloy 's structure will be supersaturated with Si and Mg. Due to the lower solubility of Si compared to Mg in aluminium, it forms small clusters [88]. The Si-clusters nucleation will occur at temperature as low as -50 °C [76,89]. Therefore, heating or even storing the quenched alloys at a temperature above -50 °C results in the Mg-Si phase as the Mg will diffuse to Si-clusters. During artificial aging and depending on alloy composition, aging time, and temperature, different phases might exist in the matrix. All precipitates in this group are nucleated and grow with a needle, rod, or lath shape aligned along <100> Al directions. The precipitation sequence in Al-Mg-Si alloy during artificial aging, which is generally accepted, is the following [90–93]:

SSSS → atomic cluster → GP zones → β″→ β′, U1, U2, B′ → β, Si
Where SSSS indicates supersaturated solid solution.

Influence of Cu:

Copper is usually added to Al-Mg-Si alloy to improve the age hardening response, increase the number density of precipitates, and enhance these alloys' thermal stability [94–97]. For instance, Xiao et al. [98] investigated the effect of different Cu concentrations (0.5, 1, 2.5, and 4.5 wt%) on the precipitation behavior and age hardening response in Al-Mg-Si alloys. A distinct increase in the hardness as well as in the peakaged (PA) condition was documented by increasing Cu content. In addition, Marioara et al. [99] explored the influence of 0.3 wt% of Cu content on the precipitation behavior of Al-Mg-Si alloy. It is claimed that 0.3 wt% of Cu addition increases the volume fraction of the hardening precipitates, and a finer microstructure can be obtained, resulting in a higher hardness compared to Cu-free alloys. It is also reported that pre- β″ and β″ precipitates found in the PA condition constitute only between 20-30 % of the total number the precipitates, while the rest are L, S, and C precipitates [99]. An overview of precipitation composition, morphology, and crystal structure exists in the Al-Mg-Si-Cu system can be seen in Table 2.3. The precipitation sequence in the presence of Cu ≥ 0.4 wt% shows more complexity and can be stated as:

$$SSSS \rightarrow \text{atomic cluster} \rightarrow \text{GP zones} \rightarrow \beta'' \rightarrow L \rightarrow \beta'_{Cu}, S, Q', C \rightarrow Q, Si$$

Saito et al. [100] investigated the influence of 0.1 wt% Cu addition on the precipitate structures in Al-0.47Mg-0.42Si in the PA condition. The results showed the presence of disordered β″ precipitate in the microstructure of the studied alloy, see Fig. 2.7a. Different sub-unit structures were observed in a disordered β″ phase, e.g., U2, Q′, β'_{Ag}, and C. It was frequently observed that the U2 phase formed in the disordered Cu-free area. Cu was observed at the precipitate/matrix interface in such precipitate and especially in the disordered part.

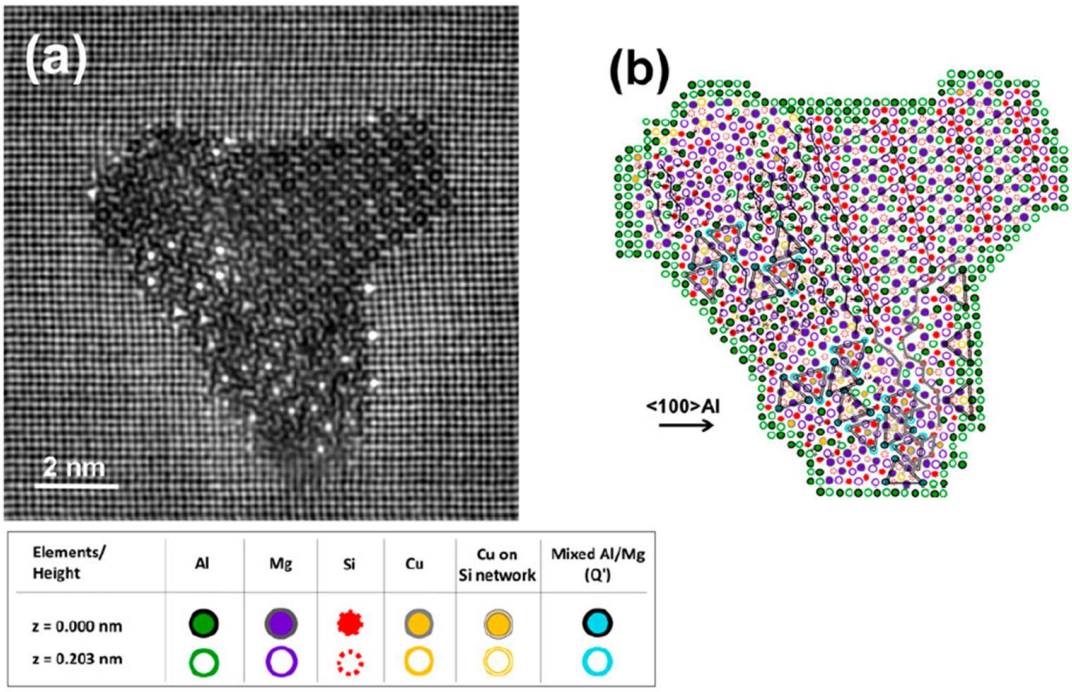

Fig. 2.7. (a) HAADF-HRSTEM images of disordered β″ precipitate found in lean Al-0.47Mg-0.42Si with 0.1wt% Cu aged a t 190 °C for 300 min. (b) Suggested atomic overlay of the disordered β″ precipitate [100].

In a separate work, Sunde et al. [62] studied the influence of different Cu additions (0.03, 0.09, and 0.23 wt%) on the precipitate structures in Al-Mg-Si alloy. The results showed that the majority of the precipitates observed in the microstructure of 0.03 (alloy S) and 0.09 wt% Cu (alloy C) additions in the PA condition were pure β″ precipitates. However, some atomic columns showed higher intensity than other corresponding sites indicating that Cu partially occupied these sites. Moreover, it is reported that the β'_{Cu} was observed in the 0.09 wt% Cu-containing alloy but not in the 0.03 wt% Cu-containing alloy, see Fig. 2.8. The presence of the β'_{Cu} phase in alloy with 0.09 wt% and its absence in alloy with 0.03 wt% was considered an indication of accelerated phase transformation kinetics for the alloy with 0.09 wt% Cu. Further aging of alloys S and C (12 h) showed the presence of unit structures other than β″ such as U2, β'_{Cu}, and Q′.

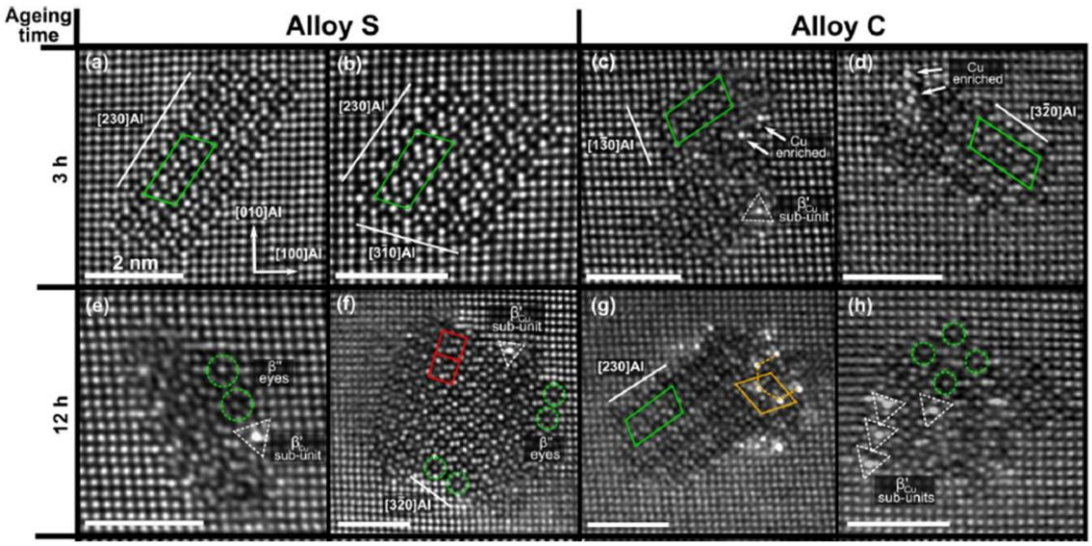

Fig. 2.8. (a, b) HAADF-STEM images of precipitates found in Al-0.72Mg-0.88Si alloy in the peakaged condition with 0.03 wt% (alloy S), (c, d) HAADF-STEM lattice images of precipitates can be found in Al-0.64Mg-0.88Si alloy in the peakaged condition with 0.09 wt% (alloy C), (e, f) HAADF-STEM images observed in alloy S after 12 h aging, and (g, h) HAADF-STEM lattice images observed in alloy C after 12 h aging [62].

Influence of Zn:

Recently, it has been an increasing interest in studying the effect of Zn on the corrosion resistance and mechanical properties of Al-Mg-Si alloys. Several studies showed that Zn addition at relatively high concentrations significantly improves the age hardening response and precipitation kinetics of the artificially aged Al-Mg-Si alloy [64,101–107]. It is claimed that Zn addition ≤ 3 wt% will not affect the precipitation sequences or introduce any precipitates observed in the Al-Mg-Zn system [64,104,106,108]. The primary reported precipitates in the PA condition in Al-Mg-Si-Cu with Zn addition up to 3 wt% are pre-β″, β″, and L phases [106]. However, contradictory results were reported claiming the presence of η′ $MgZn_2$ and/or its precursor in the microstructure of Al-Mg-Si alloy with Zn addition ≥ 2.37 wt% [104,105,107]. In a separate study, Saito et al. [108] studied the influence of Zn addition (≤ 1 wt%) on the precipitate structures in different aging conditions. It is reported that no Mg-Zn precipitates were observed in the microstructure, as most of the observed precipitates are disordered Mg-Si precipitates, see Fig. 2.9. It is also claimed that a regular Si-network was observed in the disordered precipitate structures.

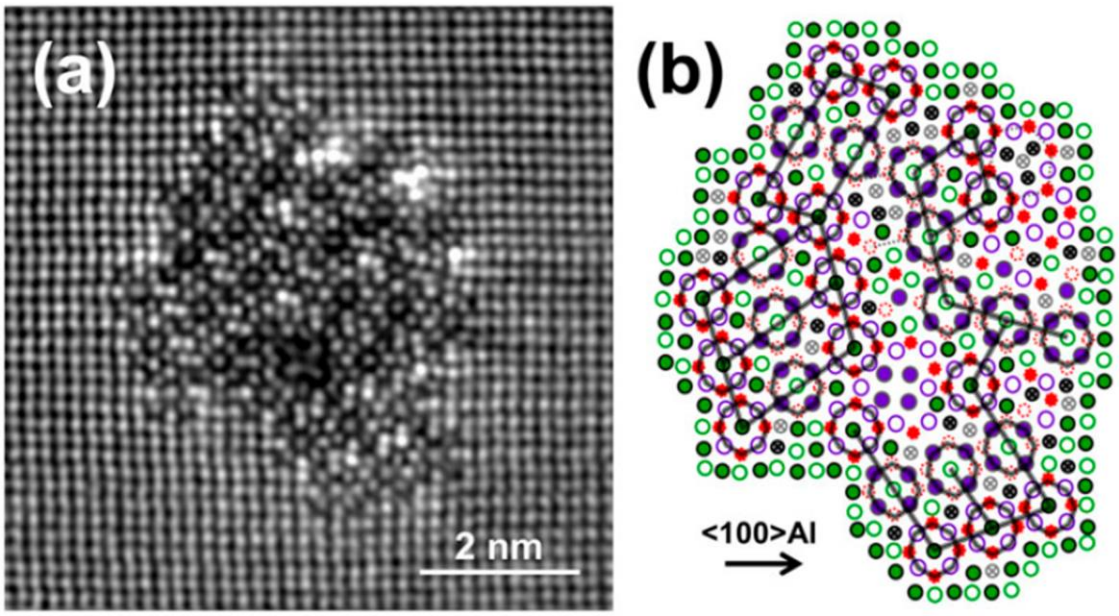

Fig. 2.9. (a) HAADF-STEM images of precipitates found in Al-0.47Mg-0.39Si alloy with 1.02 Zn wt% aged at 185 °C for 12 h and (b) its corresponding suggested atomic overlay [108].

Table 2.3. Overview of different phases documented in Al-Mg-Si-Cu during precipitation hardening.

Phase	Composition	Morphology	Unit cell
GP [109]	$Mg_xAl_{5-x}Si_6$	Spherical/Needles	Primarily monoclinic
β″ [110]	Mg_5Si_6	Needles	Monoclinic
U1 [111]	$MgAl_2$ Si_2	Needles	Trigonal
U2 [112]	MgAlSi	Needles	Orthorhombic
β′ [113]	$Mg_{1.8}Si$	Rods	Hexagonal
B′ [114]	$MgSi_{>1}$	Laths	Hexagonal
L [99]	Variable	Needles	-
S [99]	Variable	Needles	-
C [115]	$AlCu_{0.7}Mg_4Si_{3.3}$	Plates	Monoclinic
Q′ [116]	$Al_4CuMg_6Si_6$	Laths	Hexagonal
Q [117]	$Al_5Cu_2Mg_8Si_6$	Laths	Hexagonal
β [118]	Mg_2Si	Plates	FCC
Si	Si	Plates	Fd-3m

2.8 Intergranular corrosion mechanisms

Intergranular corrosion in Al-Mg-Si alloy is still of great concern as it will affect the lifetime as well as the functionality of the components used in different applications such as automotive and aerospace [21,119]. The driving force for electrochemical corrosion is the presence of an anodic part (depleted zones) and a cathodic part (second-phase particles and segregated elements located along the GBs). It is documented that IGC in Al-Mg-Si-Cu alloys initiates and propagates along grain boundaries due to the micro-galvanic coupling between Q/Q′ precipitates and Cu-rich film located at the GBs acting as a cathode and PFZs serving as an anode [120–126]. Therefore, solid solution composition (matrix/PFZs compositions), the composition of GB regions and the second-phase particles, as well as their number density and distribution, will highly affect the extent and type of the corrosion. In aluminium alloys, the solution potential or matrix potential is defined by the solid solution composition in which the aluminium constitutes the dominant fraction. The second-phase particles will not significantly influence the solution potential as they have different electrochemical potential, which is what cause the localized corrosion [21].

The influence of alloying element on the solution potential measured in a solution containing 53 g/l NaCl and 3 g/l H_2O_2 of binary heat treatment and quenched alloys are shown in Fig. 2.10. The presence of Cu and Zn elements at relatively high concentrations ($\geq$ 1 wt%) will noticeably influence the corrosion potential of the Al alloy. Based on Fig. 2.10, a relatively weak influence ($\sim \pm 10$ mV) on the solution potential in the presence of very low concentrations ($\leq$ 0.1 wt%) of Mn, Cu, Mg, Si, or Zn can be expected. However, a noticeable influence can be expected when the concentration of such elements exceeds 2 wt%, see Fig. 2.10. Since Al-Mg-Si alloys are routinely heat treated to improve their mechanical properties, their microstructure commonly contains different particles such as Fe-rich phases, dispersoids, and hardening precipitates, as described in section 2.7. Therefore, in many cases, some added elements will be heavily consumed by one or more of the particles mentioned above, resulting in a poor influence of such elements on the solution potential of Al-Mg-Si alloy. However, Cu and Zn at relatively high concentrations ($\geq$ 0.1 wt%) tend to segregate toward the grain boundaries in the artificially aged Al-Mg-Si alloys to form a solute-rich film, or Cu/Zn-rich grain boundary particles in the PA and

overaged (OA) conditions [108,127,128]. Therefore, this work will investigate the influence of very low concentrations (≤ 0.06 wt%) of Cu, Zn, and Cu+Zn on the microstructure and IGC resistance of Al-Mg-Si alloys, see section 2.10.

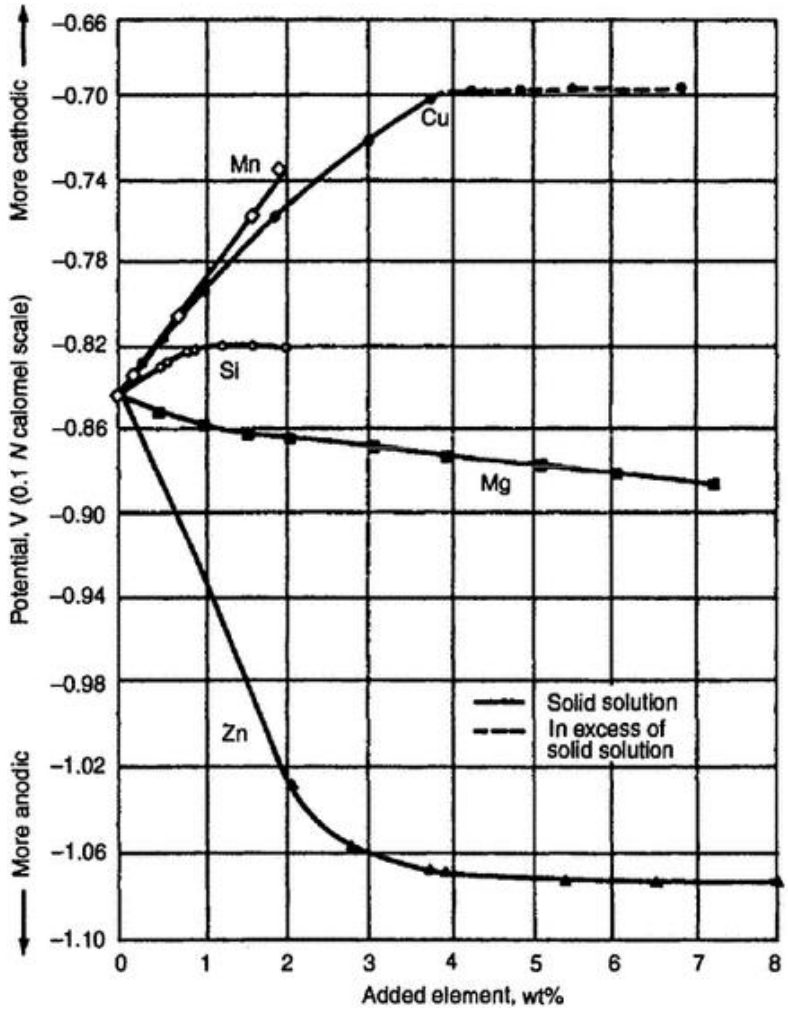

Fig. 2.10. Effect of alloying elements on solution potential of heat treated and quenched high-purity binary aluminium measured at 25 °C [21].

2.8.1 Grain boundary chemistry

The presence of certain alloying elements, such as Cu and Zn in Al-Mg-Si alloys, can negatively influence their IGC resistance due to their segregation toward the grain boundaries. The resistance to IGC can also be affected by quenching rate and aging conditions, as any changes in these conditions might cause considerable changes in IGC resistance [129–132]. This section will focus on the influence of Cu, Zn, heat treatment, and grain boundary misorientation on the IGC resistance in Al-Mg-Si alloys.

Influence of Cu:

Copper is an important element in Al-Mg-Si alloys as it affects the precipitation and age hardening behaviors [62,91,94,133,134]. However, introducing Cu into Al-Mg-Si alloys will reduce their corrosion resistance [135,136]. Intergranular corrosion of Al alloys can be tested in acidified salt solution according to BS ISO 11846 or in sodium chloride and hydrogen peroxide solution according to ASTM G110 [137,138]. It is claimed that IGC caused by Cu can be avoidable if Cu concentration in Al-Mg-Si was held below a critical level of 0.1 wt% [139,140]. Several studies were conducted to investigate the influence of Cu at concentrations higher than 0.1 wt% [121,126,145,146,129,131,132,136,141–144]. The results showed that IGC resistance decreases by increasing Cu concentration. Limited work has been conducted to explore the influence of Cu at a concentration lower than 0.1wt% [123,142,144,147]. For instance, Svenningsen et al. [123,147] studied the influence of a relatively small concentration of Cu on the IGC of Al-Mg-Si-T6 alloy. The results showed no IGC was recorded in alloys with Cu content 0.005 and 0.02 wt%, whereas alloys with 0.12 and 0.17 wt% were susceptible to IGC. It is also suggested that the presence of Q/Q′ phase along the GBs in such alloy plays a critical role in IGC.

However, to our knowledge, only one work has been conducted to understand the influence of quenching rate on IGC in Al-Mg-Si with small Cu and Zn concentrations (0.06 and 0.04 wt%, respectively) [148]. It is claimed that the quenching rate greatly influenced the susceptibility to IGC in the studied alloy. However, the authors stated that the root cause of the IGC in such alloy with low Cu and Zn content was unclear, as no Cu film was detected at the grain boundaries. Moreover, the fraction of Q/Q′ precipitates detected at such a low level of Cu was only 10 % in the water-quenched condition and 5 % in air-cooled condition. The conclusion of the work mentioned above is that explaining the IGC occurs at such low Cu and Zn concentration cannot be explained based on their results.

Influence of Zn:

Recently, there has been an increasing interest in investigating the influence of Zn on the corrosion resistance and mechanical properties in Al-Mg-Si alloys [103,104,106,149–151]. For example, Guo et al. [106] explored the influence of 3 wt% Zn addition in Al-0.9Mg-0.6Si on the precipitation kinetics and age hardening response. It is claimed that a noticeable decrease in the activation energy of β″ precipitates resulted in

considerable improvement in the age hardening response. Very limited work has been performed on the corrosion side to investigate how Zn addition will influence the corrosion resistance of Al-Mg-Si alloys [104,108,149,150]. The results obtained by Guo et al. [104] on understanding the influence of Zn addition (0, 1, 2, 3, and 4 wt%) on the intergranular corrosion of Al-Mg-Si alloy with 0.2 wt% Cu showed that 1 wt% of Zn will improve the IGC resistance. At the same time, further Zn addition (2-4 wt%) lead to a decrease in the IGC resistance of this type of alloy. Contradictory results were documented by Chi et al. [149], who investigated the effect of Zn addition (0.05 and 0.2 wt%) on the IGC resistance of Al-Mg-Si alloys. The results indicated that the susceptibility to IGC increased by increasing Zn content from 0.05 to 0.2 wt%. Therefore, the mechanism of the IGC in the presence of Zn as well as the role that Zn plays in determining the intergranular corrosion resistance of Al-Mg-Si/Al-Mg-Si-Cu alloys in different aging conditions, is still unclear.

In separate work, Saito et al. [108] investigated the influence of Zn additions (≤ 1 wt%) on the microstructure and IGC resistance in Al-0.5Mg-0.4Si alloys in different aging conditions. The results showed no measurable impact on the microstructure and IGC resistance if Zn additions are ≤ 0.1 wt%. It is also reported that a pronounced IGC was observed in alloy with 1 wt% Zn, indicating that the critical Zn level negatively affecting the IGC resistance is between 0.1 and 1 wt%. It is also found that the aging condition can significantly influence the IGC resistance, as the underaged (UA) condition showed higher IGC resistance than the PA and OA conditions. As noticed, the previously mentioned studies paid more attention to relatively high Zn concentrations as no systematic work has been done to understand how tiny concentrations of Zn will affect the IGC and microstructure of Al-Mg-Si alloys.

Influence of grain boundary misorientation:

The effect of grain boundary types on grain boundary chemistry and, thus, on the intergranular corrosion resistance is of great interest [152–154]. It is reported that grain boundary misorientation plays a significant role in determining IGC resistance of Al-Mg-Si alloy system [124,155,156]. High-angle grain boundaries (misorientation angle > 15 °) are found to be more susceptible to IGC than other types of boundaries. Yang et al. [124] investigated the correlation between grain boundary misorientation and IGC resistance. The results showed that high-angle boundaries are more prone to IGC than low-angle

boundaries. This can be explained based on the different diffusion rates for different misorientations resulting in various types of precipitates. It is claimed that low-angle boundaries contain only β (Mg_2Si) precipitates or their precursor, while high-angle boundaries contain Q/Q′ at the same aging condition [124]. Another work was conducted by Lervik et al. [127] to investigate the influence of misorientation on grain boundary particles in Al-Mg-Si-Cu alloy. The results showed that low-angle boundaries are highly decorated with Q/Q′ precipitates with a relatively narrow PFZ compared to high-angle boundaries. The low susceptibility of low-angle boundaries to IGC was explained on the basis of the absence of the Cu-rich film. In contrast, this film, along with the distantly separated Q/Q′ precipitates, were observed along high-angle boundaries.

Influence of heat treatment:

Intergranular corrosion in Al-M-Si alloys is caused due to segregation of Mg, Si, and Cu toward grain boundaries, which during the subsequent aging will form precipitates along grain boundaries along with Cu-rich film in the PA conditions [33,57,120,157]. Thus, it was found that heat treatment parameters significantly affect the grain boundary composition and its adjacent regions. For instance, Zhang et al. [148] studied the influence of cooling rate on the IGC resistance of Al-Mg-Si alloy. It is claimed that the water-quenched alloy followed by artificial aging was more susceptible to IGC compared to the air-cooled alloy subjected to the same aging conditions. However, contradictory results were documented by Svenningsen et al. [147]. Moreover, aging time and temperature highly influence susceptibility to IGC in Al-Mg-Si-Cu alloys. It was claimed that the UA alloys are highly susceptible to intergranular corrosion due to the presence of Cu-rich film and Q/Q′ precipitates at grain boundaries. The susceptibility to IGC slightly decreases by reaching the PA condition. Further aging leads to either suppressing or eliminating IGC in Al-Mg-Si alloy due to the grain boundary particles coarsening and discontinuity as well as the absence of Cu-rich film resulting in pitting corrosion [130,141,158].

2.9 Intergranular corrosion testing methods

Intergranular corrosion can be observed in Al alloy groups such as Al-Cu alloys (2xxx series), Al-Mg alloys (5xxx), Al-Mg-Si alloys (6xxx series), and Al-Zn-Mg alloys (7xxx). A range of test methods and standards are available for investigation and evaluation of the IGC resistance of aluminium alloys, e.g., the International Standard Organization

(ISO) and the American Society for Testing Materials (ASTM) [137,138]. The first method, according to BS ISO 11846 method B, is that the samples are degreased and alkaline etched in NaOH at 55 to 60 °C, followed by dipping the samples in the test solution at room temperature. The test solution consists of 30 g/l sodium chloride and 10 ml ± 1 of concentrated hydrochloric acid [137]. The second method is according to ASTM G110, in which the sample should be etched in a solution containing 50 ml of nitric acid and 5 ml of hydrofluoric acid added to 945 ml of distilled water. After that, the samples should be immersed in a solution containing 57 g of sodium chloride and 10 ml of hydrogen peroxide (30 % H_2O_2) for either 6 or 24 h [138]. The acidified solution is more aggressive than the one containing hydrogen peroxide. Therefore, BS ISO 11846 method B is preferred for testing IGC of Al-Mg-Si alloys [146,156,159], while ASTM G110 is primarily used for testing Al 2xxx and 7xxx series [138,160].

2.10 Overall summery

The main challenge in recycling Al alloys is that large amounts of the available scraps are post-consumer scraps, which contain different alloying elements that can negatively influence the corrosion resistance of the final recycled alloys. Shifting toward sustainability requires recycling the Al scarps, as recycling consumes only approximately 5 % of the energy needed to produce the same amount of primary Al alloys. Scrap-related impurities, e.g., Cr, Mn, Si, Fe, Cu, and Zn, will inevitably be present in the recycled Al alloys if different scrap qualities are considered. Therefore, in the current work, the influence of Cu, Zn, and Cu+Zn on the microstructure and IGC resistance of 6082 Al-Mg-Si alloys will be considered in detail.

- It appears that Cu, Zn, and Cu+Zn have a considerable influence on the microstructure, precipitate structures, and IGC resistance of Al-Mg-Si alloys.
- It seems that grain boundary misorientation influences grain boundary chemistry, hence IGC resistance.
- It is evident that heat treatment parameters can greatly influence the microstructure and IGC resistance of Al-Mg-Si alloys.

However, significant attention has been paid to investigating the influence of relatively high Cu and Zn (≥ 0.1 wt%) on the microstructure and IGC resistance of Al-Mg-Si alloys, as these two elements are usually intentionally added to improve the mechanical

properties. Therefore, there needs to be more systematic work concerning the influence of very low amounts of Cu and Zn, as a result of recycling on the microstructure, precipitate structures, and IGC resistance of Al-Mg-Si alloys in different aging conditions. The main objective of the present Ph.D. study is to comprehensively explore the impact of minor additions of Cu (≤ 0.05 wt%), Zn (≤ 0.06 wt%), and Cu+Zn on the microstructure, precipitate crystal structures, and IGC resistance of Al-Mg-Si alloys in different aging conditions.

References

[1] C. Vargel, Corrosion of Aluminium, 2004. https://doi.org/10.1016/B978-0-08-044495-6.X5000-9.

[2] Z. Aljanabi, J. Carrere, C. Cruz, Opportunities for aluminium in a post-Covid economy, Int. Alum. 3 (2022) 1–8.

[3] G. Liu, C.E. Bangs, D.B. Müller, Stock dynamics and emission pathways of the global aluminium cycle, Nat. Clim. Chang. 3 (2013) 338–342.

[4] International Aluminium Institute, Aluminium Recycling – Home, (n.d.). https://recycling.world-aluminium.org/home/ (accessed April 9, 2023).

[5] N. Arab, The Challenges of Aluminum Recycling From End-of-Life Vehicles, J. Environ. Friendly Mater. 1 (2017) 19–25.

[6] X. Yi, Y. Lu, G. He, H. Li, C. Chen, H. Cui, Global carbon transfer and emissions of aluminum production and consumption, J. Clean. Prod. 362 (2022) 132513.

[7] J.G. Kaufman, Introduction to aluminum alloys and tempers, ASM international, 2000.

[8] S.H. Avner, Introduction to physical metallury: second edition, 1974.

[9] T. Sheppard, Extrusion of aluminium alloys, Springer Science & Business Media, 2013.

[10] J.G. Kaufman, Understanding wrought and cast aluminum alloy designations, Introd. to Alum. Alloy. Tempers. 23–37 (2000).

[11] A.M. Samuel, F.H. Samuel, Modification of iron intermetallics by magnesium and strontium in Al-Si alloys, Int. J. Cast Met. Res. 10 (1997) 147–157. https://doi.org/10.1080/13640461.1997.11819229.

[12] J.F. Nie, Physical metallurgy of light alloys, Fifth Edit, Elsevier, 2014. https://doi.org/10.1016/B978-0-444-53770-6.00020-4.

[13] E.A. Starke, Heat-treatable aluminum alloys, Alum. Alloy. Res. Appl. Contemp. Res. Appl. 31 (2012) 35–63.

[14] R. Sanders, S. Baumann, H. Stumpf, Wrought non–heat-treatable aluminum alloys, Treatise on Materials Science & Technology, 1989. https://doi.org/10.1016/b978-0-12-341831-9.50008-5.

[15] J. Sieniawski, M. Wierzbińska, Morphology prediction of intermetallics formed in 4xxx type of aluminium alloy, Manuf. Eng. 31 (2008) 262–268.

[16] G. Mrówka-Nowotnik, J. Sieniawski, M. Wierzbińska, Analysis of intermetallic particles in AlSi1MgMn aluminium alloy, J. Achiev. Mater. Manuf. Eng. 20 (2007) 7–8.

[17] F. Andreatta, H. Terryn, J.H.W. de Wit, Effect of solution heat treatment on galvanic coupling between intermetallics and matrix in AA7075-T6, Corros. Sci. 45 (2003) 1733–1746. https://doi.org/10.1016/S0010-938X(03)00004-0.

[18] Y. Yoon, R.G. Buchheit, Dissolution behavior of Al2CuMg (S phase) in chloride and chromate conversion coating solutions, J. Electrochem. Soc. 153 (2006) B151.

[19] I.J. Polmear, Wrought aluminium alloys, 1997. https://doi.org/10.1016/b978-075066371-7/50007-4.

[20] Z. Szklarska-Smialowska, Pitting corrosion of aluminum, Corros. Sci. 41 (1999) 1743–1767.

[21] J.R. Davis, Corrosion of aluminum and aluminum alloys, ASM international, 1999.

[22] R.T. Foley, T.H. Nguyen, The chemical nature of aluminum corrosion: V . energy transfer in aluminum dissolution, in: J. Electrochem. Soc., 1982: pp. 464–467. https://doi.org/10.1149/1.2123881.

[23] A.P. Sutton, Interfaces in crystalline materials, Monogr. Physice Chem. Mater. (1995) 414–423.

[24] J. Rivnay, L.H. Jimison, J.E. Northrup, M.F. Toney, R. Noriega, S. Lu, T.J. Marks,

A. Facchetti, A. Salleo, Large modulation of carrier transport by grain-boundary molecular packing and microstructure in organic thin films, Nat. Mater. 8 (2009) 952–958.

[25] J. Hickman, Y. Mishin, Extra variable in grain boundary description, Phys. Rev. Mater. 1 (2017) 1–4. https://doi.org/10.1103/PhysRevMaterials.1.010601.

[26] P. Lejček, Grain boundary segregation in metals, Springer Series in Materials Science, 2010. https://doi.org/10.1007/978-3-642-12505-8_1.

[27] D. Wolf, J.F. Lutsko, On the geometrical relationship between tilt and twist grain boundaries, Zeitschrift Für Krist. Mater. 189 (1989) 239–262.

[28] Z. Huang, F. Chen, Q. Shen, L. Zhang, T.J. Rupert, Combined effects of nonmetallic impurities and planned metallic dopants on grain boundary energy and strength, Acta Mater. 166 (2019) 113–125.

[29] X.R. Qian, Y.T. Chou, Correlation between grain boundary corrosion and grain boundary energy in niobium bicrystals, Philos. Mag. A. 45 (1982) 1075–1079.

[30] K. Wang, W. Zhang, J. Xu, W. Dan, The impact of misorientation on the grain boundary energy in bi-crystal copper: an atomistic simulation study, J. Mol. Model. 28 (2022) 47.

[31] D.G. Brandon, The structure of high-angle grain boundaries, Acta Metall. 14 (1966) 1479–1484.

[32] M.L. Kronberg, u F.H. Wilson, Secondary recrystallization in copper, JOM. 1 (1949) 501–514.

[33] D.L. Engelberg, Intergranular corrosion, in: Shreir's Corros., Elsevier, 2010: pp. 810–827. https://doi.org/10.1016/B978-044452787-5.00032-9.

[34] D. McLean, A. Maradudin, Grain boundaries in metals, Phys. Today. 11 (1958) 35–36. https://doi.org/10.1063/1.3062658.

[35] E. STARKE, The causes and effects of "denuded" or "precipitate-free" zones at grain boundaries in aluminum-base alloys, J Met. 22 (1970) 54–63.

https://doi.org/10.1007/bf03355628.

[36] T. Ogura, S. Hirosawa, A. Cerezo, T. Sato, Atom probe tomography of nanoscale microstructures within precipitate free zones in Al–Zn–Mg(–Ag) alloys, Acta Mater. 58 (2010) 5714–5723. https://doi.org/10.1016/J.ACTAMAT.2010.06.046.

[37] P.N.T. Unwin, G.W. Lorimer, R.B. Nicholson, The origin of the grain boundary precipitate free zone, Acta Metall. 17 (1969) 1363–1377.

[38] A.J. Cornish, M.K.B. Day, Precipitation in the neighbourhood of grainboundaries in an Al – Zn – Mg allo, J Inst Met. 97 (1969) 44–52.

[39] H. Zhao, F. De Geuser, A. Kwiatkowski da Silva, A. Szczepaniak, B. Gault, D. Ponge, D. Raabe, Segregation assisted grain boundary precipitation in a model Al-Zn-Mg-Cu alloy, Acta Mater. 156 (2018) 318–329. https://doi.org/10.1016/j.actamat.2018.07.003.

[40] M. de Haas, S.M. van Scherpenzeel, J.T.M. de Hosson, Grain boundary segregation and precipitation in aluminium alloy AA6061, Mater. Sci. Forum. 519–521 (2006) 467–472. https://doi.org/10.4028/www.scientific.net/msf.519-521.467.

[41] H. JIANG, Modelling of grain boundary segregation, precipitation and precipitate-free zones of high strength aluminium alloys, Loughborough University of Technology, 1994.

[42] J.D. Embury, R.B. Nicholson, The nucleation of precipitates: The system Al-Zn-Mg, Acta Metall. 13 (1965) 403–417. https://doi.org/10.1016/0001-6160(65)90067-2.

[43] G.W. Lorimer, R.B. Nicholson, Further results on the nucleation of precipitates in the AlZnMg system, Acta Metall. 14 (1966) 1009–1013. https://doi.org/10.1016/0001-6160(66)90229-X.

[44] S. Hofmann, P. Leiĉek, Solute segregation at grain boundaries, Interface Sci. 3 (1996) 241–267.

[45] C. Wolverton, Solute-vacancy binding in aluminum, Acta Mater. 55 (2007) 5867–5872. https://doi.org/10.1016/j.actamat.2007.06.039.

[46] H. Kimura, R.K. Hasiguti, Interaction of vacancies with Sn atoms and the rate of G-P zone formation in an Al-Cu-Sn alloy, Acta Metall. 9 (1961) 1076–1078. https://doi.org/10.1016/0001-6160(61)90179-1.

[47] D. Raabe, M. Herbig, S. Sandlöbes, Y. Li, D. Tytko, M. Kuzmina, D. Ponge, P.P. Choi, Grain boundary segregation engineering in metallic alloys: A pathway to the design of interfaces, Curr. Opin. Solid State Mater. Sci. 18 (2014) 253–261. https://doi.org/10.1016/J.COSSMS.2014.06.002.

[48] T. Frolov, S. V Divinski, M. Asta, Y. Mishin, Effect of interface phase transformations on diffusion and segregation in high-angle grain boundaries, Phys. Rev. Lett. 110 (2013) 255502.

[49] J.F. Nie, Y.M. Zhu, J.Z. Liu, X.Y. Fang, Periodic segregation of solute atoms in fully coherent twin boundaries, Science (80-.). 340 (2013) 957–960. https://doi.org/10.1126/science.1229369.

[50] J.P. Buban, K. Matsunaga, J. Chen, N. Shibata, W.Y. Ching, T. Yamamoto, Y. Ikuhara, Grain boundary strengthening in alumina by rare earth impurities, Science (80-.). 311 (2006) 212–215.

[51] R.G. Song, W. Dietzel, B.J. Zhang, W.J. Liu, M.K. Tseng, A. Atrens, Stress corrosion cracking and hydrogen embrittlement of an Al--Zn--Mg--Cu alloy, Acta Mater. 52 (2004) 4727–4743.

[52] R.-G. Song, B.-J. Zhang, M.-K. Tseng, Role of grain boundary segregation in corrosion fatigue process of high strength aluminium alloy, Mater. Chem. Phys. 45 (1996) 84–87.

[53] T. Kawabata, O. Izumi, Ductile fracture in the interior of precipitate free zone in an Al-6.0%Zn-2.6%Mg alloy, Acta Metall. 24 (1976) 817–825. https://doi.org/10.1016/0001-6160(76)90048-1.

[54] J.K. Park, A.J. Ardell, Microchemical analysis of precipitate free zones in 7075-A1 in the T6, T7 and RRA tempers, Acta Metall. Mater. 39 (1991) 591–598. https://doi.org/10.1016/0956-7151(91)90127-M.

[55] T. Ogura, A. Hirose, T. Sato, Effect of PFZ and grain boundary precipitate on mechanical properties and fracture morphologies in Al-Zn-Mg (Ag) Alloys, in: Mater. Sci. Forum, 2010: pp. 297–302.

[56] G. Sha, K. Tugcu, X.Z. Liao, P.W. Trimby, M.Y. Murashkin, R.Z. Valiev, S.P. Ringer, Strength, grain refinement and solute nanostructures of an Al-Mg-Si alloy (AA6060) processed by high-pressure torsion, Acta Mater. 63 (2014) 169–179. https://doi.org/10.1016/j.actamat.2013.10.022.

[57] G. Sha, L. Yao, X. Liao, S.P. Ringer, Z.C. Duan, T.G. Langdon, Segregation of solute elements at grain boundaries in an ultrafine grained Al-Zn-Mg-Cu alloy, Ultramicroscopy. 111 (2011) 500–505. https://doi.org/10.1016/j.ultramic.2010.11.013.

[58] M.A. Zaidi, J.A. WERT, Thermomechanical processing of aluminum alloys, in: Elsevier, 1989: pp. 137–170. https://doi.org/10.1016/b978-0-12-341831-9.50010-3.

[59] R. Ciach, Advanced light alloys and composites, Springer Science & Business Media, 2013.

[60] I. Polmear, Light alloys: from traditional alloys to nanocrystals, Elsevier, 2005.

[61] T. Saito, E.A. Mørtsell, S. Wenner, C.D. Marioara, S.J. Andersen, J. Friis, K. Matsuda, R. Holmestad, Atomic structures of precipitates in Al–Mg–Si alloys with small additions of other elements, Adv. Eng. Mater. 20 (2018) 1800125. https://doi.org/10.1002/adem.201800125.

[62] J.K. Sunde, C.D. Marioara, R. Holmestad, The effect of low Cu additions on precipitate crystal structures in overaged Al-Mg-Si(-Cu) alloys, Mater. Charact. 160 (2020) 110087. https://doi.org/10.1016/j.matchar.2019.110087.

[63] Y. Weng, Z. Jia, L. Ding, Y. Pan, Y. Liu, Q. Liu, Effect of Ag and Cu additions on natural aging and precipitation hardening behavior in Al-Mg-Si alloys, J. Alloys Compd. 695 (2017) 2444–2452. https://doi.org/10.1016/j.jallcom.2016.11.140.

[64] S. Zhu, Z. Li, L. Yan, X. Li, S. Huang, H. Yan, Y. Zhang, B. Xiong, Effects of Zn

addition on the age hardening behavior and precipitation evolution of an Al-Mg-Si-Cu alloy, Mater. Charact. 145 (2018) 258–267. https://doi.org/10.1016/J.MATCHAR.2018.08.051.

[65] G. Lu, B. Sun, J. Wang, Y. Liu, C. Liu, High-temperature age-hardening behavior of Al–Mg–Si alloys with varying Sn contents, J. Mater. Res. Technol. 14 (2021) 2165–2173. https://doi.org/10.1016/J.JMRT.2021.07.122.

[66] W. Tu, J. Tang, Y. Zhang, L. Cao, L. Ma, Q. Zhu, L. Ye, S. Liu, Influence of Sn on the precipitation and hardening response of natural aged Al-0.4Mg-1.0Si alloy artificial aged at different temperatures, Mater. Sci. Eng. A. 765 (2019) 138250. https://doi.org/10.1016/J.MSEA.2019.138250.

[67] S. Zajac, B. Hutchinson, A. Johansson, L.-O. Gullman, Microstructure control and extrudability of Al--Mg--Si alloys microalloyed with manganese, Mater. Sci. Technol. 10 (1994) 323–333.

[68] L. Lodgaard, N. Ryum, Precipitation of dispersoids containing Mn and/or Cr in Al-Mg-Si alloys, Mater. Sci. Eng. A. 283 (2000) 144–152. https://doi.org/10.1016/s0921-5093(00)00734-6.

[69] N.C.W. Kuijpers, F.J. Vermolen, C. Vuik, P.T.G. Koenis, K.E. Nilsen, S. van der Zwaag, The dependence of the β-AlFeSi to α-Al(FeMn)Si transformation kinetics in Al-Mg-Si alloys on the alloying elements, Mater. Sci. Eng. A. 394 (2005) 9–19. https://doi.org/10.1016/j.msea.2004.09.073.

[70] I. Polmear, D. StJohn, J.-F. Nie, M. Qian, Light alloys: metallurgy of the light metals, Butterworth-Heinemann, 2017.

[71] A.L. Dons, The Alstruc homogenization model for industrial aluminum alloys, J. Light Met. 1 (2001) 133–149. https://doi.org/10.1016/S1471-5317(01)00007-4.

[72] K. Zheng, D.J. Politis, L. Wang, J. Lin, A review on forming techniques for manufacturing lightweight complex—shaped aluminium panel components, Int. J. Light. Mater. Manuf. 1 (2018) 55–80. https://doi.org/10.1016/J.IJLMM.2018.03.006.

[73] T. Sheppard, Processing of 6XXX alloys, in: Extrus. Alum. Alloy., Springer US, 1999: pp. 253–322. https://doi.org/10.1007/978-1-4757-3001-2_6.

[74] D.L. Zhang, L.H. Zheng, D.H. StJohn, Effect of a short solution treatment time on microstructure and mechanical properties of modified Al-7wt.%Si-0.3wt.%Mg alloy, J. Light Met. 2 (2002) 27–36. https://doi.org/10.1016/S1471-5317(02)00010-X.

[75] D.K. Dwivedi, R. Sharma, A. Kumar, Influence of silicon content and heat treatment parameters on mechanical properties of cast Al-Si-Mg alloys, Int. J. Cast Met. Res. 19 (2006) 275–282. https://doi.org/10.1179/136404606X153867.

[76] G. Mrówka-Nowotnik, J. Sieniawski, Influence of heat treatment on the microstructure and mechanical properties of 6005 and 6082 aluminium alloys, J. Mater. Process. Technol. 162 (2005) 367–372.

[77] P.E. Semih Genculu, Aluminum alloys and heat treatment, CABWW. 1100 (2000) 87–118.

[78] K.P.S. Chauhan, Influence of heat treatment on the mechanical properties of aluminium alloys (6xxx series): A literature review, Int. J. Eng. Res. 6 (2017) 386–389.

[79] A.K. Dahle, Aluminum alloys, heat treatment of, Encycl. Mater. Sci. Technol. (2011) 111–113.

[80] L.F. Mondolfo, Aluminum alloys: structure and properties, Elsevier, 2013.

[81] L. Lu, A.K. Dahle, Iron-rich intermetallic phases and their role in casting defect formation in hypoeutectic Al-Si alloys, Metall. Mater. Trans. A Phys. Metall. Mater. Sci. 36 (2005) 819–835. https://doi.org/10.1007/s11661-005-1012-4.

[82] B. Trink, I. Weißensteiner, P.J. Uggowitzer, K. Strobel, S. Pogatscher, High Fe content in Al-Mg-Si wrought alloys facilitates excellent mechanical properties, Scr. Mater. 215 (2022) 114701. https://doi.org/10.1016/J.SCRIPTAMAT.2022.114701.

[83] X. Wang, J. Qin, H. Nagaumi, R. Wu, Q. Li, The effect of α -Al(MnCr)Si dispersoids

on activation energy and workability of Al-Mg-Si-Cu alloys during hot deformation, Adv. Mater. Sci. Eng. 2020 (2020). https://doi.org/10.1155/2020/3471410.

[84] C.L. Liu, H. Azizi-Alizamini, N.C. Parson, W.J. Poole, Q. DU, Microstructure evolution during homogenization of Al-Mg-Si-Mn-Fe alloys: Modelling and experimental results, Trans. Nonferrous Met. Soc. China (English Ed. 27 (2017) 747–753. https://doi.org/10.1016/S1003-6326(17)60085-2.

[85] F. Zupanič, S. Žist, M. Albu, I. Letofsky-Papst, J. Burja, M. Vončina, T. Bončina, Dispersoids in Al-Mg-Si Alloy AA 6086 modified by Sc and Y, Materials (Basel). 16 (2023) 2949. https://doi.org/10.3390/ma16082949.

[86] R. Hu, T. Ogura, H. Tezuka, T. Sato, Q. Liu, Dispersoid formation and recrystallization behavior in an Al-Mg-Si-Mn alloy, J. Mater. Sci. Technol. 26 (2010) 237–243. https://doi.org/10.1016/S1005-0302(10)60040-0.

[87] G. Michot, G. Champier, Physical metallurgy of P/M aluminium alloys, Revue de métallurgie, Paris, 1991. https://doi.org/10.1016/b978-0-08-099431-4.00002-6.

[88] G.A. Edwards, K. Stiller, G.L. Dunlop, APFIM investigation of fine-scale precipitation in aluminium alloy 6061, Appl. Surf. Sci. 76–77 (1994) 219–225. https://doi.org/10.1016/0169-4332(94)90346-8.

[89] I. Kovaćs, J. Lendvai, E. Nagy, The mechanism of clustering in supersaturated solid solutions of A1-Mg2Si alloys, Acta Metall. 20 (1972) 975–983. https://doi.org/10.1016/0001-6160(72)90092-2.

[90] G.A. Edwards, K. Stiller, G.L. Dunlop, M.J. Couper, The precipitation sequence in Al–Mg–Si alloys, Acta Mater. 46 (1998) 3893–3904. https://doi.org/10.1016/S1359-6454(98)00059-7.

[91] C.D. Marioara, S.J. Andersen, H.W. Zandbergen, R. Holmestad, The influence of alloy composition on precipitates of the Al-Mg-Si system, Metall. Mater. Trans. A. 36 (2005) 691–702.

[92] S.J. Andersen, C.D. Marioara, R. Vissers, A. Frøseth, H.W. Zandbergen, The structural relation between precipitates in Al–Mg–Si alloys, the Al-matrix and

diamond silicon, with emphasis on the trigonal phase U1-MgAl2Si2, Mater. Sci. Eng. A. 444 (2007) 157–169. https://doi.org/10.1016/J.MSEA.2006.08.084.

[93] R. Vissers, M.A. van Huis, J. Jansen, H.W. Zandbergen, C.D. Marioara, S.J. Andersen, The crystal structure of the β′ phase in Al–Mg–Si alloys, Acta Mater. 55 (2007) 3815–3823. https://doi.org/10.1016/J.ACTAMAT.2007.02.032.

[94] J. Man, L. Jing, S.G. Jie, The effects of Cu addition on the microstructure and thermal stability of an Al–Mg–Si alloy, J. Alloys Compd. 437 (2007) 146–150. https://doi.org/10.1016/J.JALLCOM.2006.07.113.

[95] M. Murayama, K. Hono, W. Miao, D.E. Laughlin, The effect of Cu additions on the precipitation kinetics in an Al-Mg-Si alloy with excess Si, Metall. Mater. Trans. A. 32 (2001) 239–246. https://doi.org/10.1007/s11661-001-0254-z.

[96] M.W. Zandbergen, A. Cerezo, G.D.W. Smith, Study of precipitation in Al–Mg–Si Alloys by atom probe tomography II. Influence of Cu additions, Acta Mater. 101 (2015) 149–158. https://doi.org/10.1016/J.ACTAMAT.2015.08.018.

[97] C.D. Marioara, S.J. Andersen, J. Røyset, O. Reiso, S. Gulbrandsen-Dahl, T.E. Nicolaisen, I.E. Opheim, J.F. Helgaker, R. Holmestad, Improving thermal stability in Cu-containing Al-Mg-Si alloys by precipitate optimization, Metall. Mater. Trans. A. 45 (2014) 2938–2949. https://doi.org/10.1007/s11661-014-2250-0.

[98] Q. Xiao, H. Liu, D. Yi, D. Yin, Y. Chen, Y. Zhang, B. Wang, Effect of Cu content on precipitation and age-hardening behavior in Al-Mg-Si-xCu alloys, J. Alloys Compd. 695 (2017) 1005–1013. https://doi.org/10.1016/J.JALLCOM.2016.10.221.

[99] C.D. Marioara, S.J. Andersen, T.N. Stene, H. Hasting, J. Walmsley, A.T.J. Van Helvoort, R. Holmestad, The effect of Cu on precipitation in Al-Mg-Si alloys, Philos. Mag. 87 (2007) 3385–3413. https://doi.org/10.1080/14786430701287377.

[100] T. Saito, C.D. Marioara, S.J. Andersen, W. Lefebvre, R. Holmestad, Aberration-corrected HAADF-STEM investigations of precipitate structures in Al-Mg-Si alloys with low Cu additions, Philos. Mag. 94 (2014) 520–531. https://doi.org/10.1080/14786435.2013.857051.

[101] S. Zhu, Z. Li, L. Yan, X. Li, S. Huang, H. Yan, Y. Zhang, B. Xiong, Natural aging behavior in pre-aged Al–Mg–Si–Cu alloys with and without Zn addition, J. Alloys Compd. 773 (2019) 496–502. https://doi.org/10.1016/J.JALLCOM.2018.09.244.

[102] L. Yan, Y. Zhang, X. Li, Z. Li, F. Wang, H. Liu, B. Xiong, Effect of Zn addition on microstructure and mechanical properties of an Al–Mg–Si alloy, Prog. Nat. Sci. Mater. Int. 24 (2014) 97–100. https://doi.org/10.1016/J.PNSC.2014.03.003.

[103] M.X. Guo, Y.D. Zhang, G.J. Li, S.B. Jin, G. Sha, J.S. Zhang, L.Z. Zhuang, E.J. Lavernia, Solute clustering in Al-Mg-Si-Cu-(Zn) alloys during aging, J. Alloys Compd. 774 (2019) 347–363. https://doi.org/10.1016/J.JALLCOM.2018.09.309.

[104] M.X. Guo, J.Q. Du, C.H. Zheng, J.S. Zhang, L.Z. Zhuang, Influence of Zn contents on precipitation and corrosion of Al-Mg-Si-Cu-Zn alloys for automotive applications, J. Alloys Compd. 778 (2019) 256–270. https://doi.org/10.1016/j.jallcom.2018.11.146.

[105] L. Li, S. Ji, Q. Zhu, Y. Wang, X. Dong, W. Yang, S. Midson, Y. Kang, Effect of Zn concentration on the microstructure and mechanical properties of Al-Mg-Si-Zn alloys processed by gravity die casting, Metall. Mater. Trans. A. 49 (2018) 3247–3256. https://doi.org/10.1007/s11661-018-4684-2.

[106] M.X. Guo, X.K. Zhang, J.S. Zhang, L.Z. Zhuang, Effect of Zn addition on the precipitation behaviors of Al–Mg–Si–Cu alloys for automotive applications, J. Mater. Sci. 52 (2017) 1390–1404. https://doi.org/10.1007/s10853-016-0433-3.

[107] X.P. Ding, H. Cui, J.X. Zhang, H.X. Li, M.X. Guo, Z. Lin, L.Z. Zhuang, J.S. Zhang, The effect of Zn on the age hardening response in an Al-Mg-Si alloy, Mater. Des. 65 (2015) 1229–1235. https://doi.org/10.1016/j.matdes.2014.09.086.

[108] T. Saito, S. Wenner, E. Osmundsen, C.D. Marioara, S.J. Andersen, J. Røyset, W. Lefebvre, R. Holmestad, The effect of Zn on precipitation in Al-Mg-Si alloys, Philos. Mag. 94 (2014) 2410–2425. https://doi.org/10.1080/14786435.2014.913819.

[109] C.D. Marioara, S.J. Andersen, J. Jansen, H.W. Zandbergen, Atomic model for GP-zones in a 6082 Al-Mg-Si system, Acta Mater. 49 (2001) 321–328.

https://doi.org/10.1016/S1359-6454(00)00302-5.

[110] S.J. Andersen, H.W. Zandbergen, J. Jansen, C. Træholt, U. Tundal, O. Reiso, The crystal structure of the β″ phase in Al-Mg-Si Alloys, Acta Mater. 46 (1998) 3283–3298. https://doi.org/10.1016/S1359-6454(97)00493-X.

[111] K. Matsuda, Y. Sakaguchi, Y. Miyata, Y. Uetani, T. Sato, A. Kamio, S. Ikeno, Precipitation sequence of various kinds of metastable phases in Al-1.0 mass% Mg2Si-0.4 mass% Si alloy, J. Mater. Sci. 35 (2000) 179–189. https://doi.org/10.1023/A:1004769305736.

[112] S.J. Andersen, C.D. Marioara, A. Frøseth, R. Vissers, H.W. Zandbergen, Crystal structure of the orthorhombic U2-Al4Mg4 Si4 precipitate in the Al-Mg-Si alloy system and its relation to the β′ and β″ phases, Mater. Sci. Eng. A. 390 (2005) 127–138. https://doi.org/10.1016/j.msea.2004.09.019.

[113] C. Cayron, P.A. Buffat, Transmission electron microscopy study of the β′ phase (Al-Mg-Si alloys) and QC phase (Al-Cu-Mg-Si alloys): ordering mechanism and crystallographic structure, Acta Mater. 48 (2000) 2639–2653. https://doi.org/10.1016/S1359-6454(00)00057-4.

[114] K. Matsuda, T. Naoi, K. Fujii, Y. Uetani, T. Sato, A. Kamio, S. Ikeno, Crystal structure of the β″ phase in an Al-1.0 mass% Mg2Si-0.4 mass% Si alloy, Mater. Sci. Eng. A. 262 (1999) 232–237. https://doi.org/10.1016/s0921-5093(98)00962-9.

[115] M. Torster, F.J.H. Ehlers, C.D. Marioara, S.J. Andersen, R. Holmestad, Applying precipitate-host lattice coherency for compositional determination of precipitates in Al-Mg-Si-Cu alloys, Philos. Mag. 92 (2012) 3833–3856. https://doi.org/10.1080/14786435.2012.693214.

[116] K. Matsuda, S. Ikeno, Y. Uetani, T. Sato, Metastable phases in an Al-Mg-Si alloy containing copper, Metall. Mater. Trans. A. 32 (2001) 1293–1299.

[117] L. Sagalowicz, G. Lapasset, G. Hug, Transmission electron microscopy study of a precipitate which forms in the Al-Mg-Si system, Philos. Mag. Lett. 74 (1996) 57–66.

[118] K. Matsuda, Y. Ishida, I. Mullerova, L. Frank, S. Ikeno, Cube-phase in excess Mg-type Al-Mg-Si alloy studied by EFTEM, J. Mater. Sci. 41 (2006) 2605–2610.

[119] V. Guillaumin, G. Mankowski, Localized corrosion of 6056 T6 aluminium alloy in chloride media, Corros. Sci. 42 (2000) 105–125. https://doi.org/10.1016/S0010-938X(99)00053-0.

[120] S.K. Kairy, P.A. Rometsch, K. Diao, J.F. Nie, C.H.J. Davies, N. Birbilis, Exploring the electrochemistry of 6xxx series aluminium alloys as a function of Si to Mg ratio, Cu content, ageing conditions and microstructure, Electrochim. Acta. 190 (2016) 92–103. https://doi.org/10.1016/J.ELECTACTA.2015.12.098.

[121] S.K. Kairy, T. Alam, P.A. Rometsch, C.H.J. Davies, R. Banerjee, N. Birbilis, Understanding the origins of intergranular corrosion in copper-containing Al-Mg-Si alloys, Metall. Mater. Trans. A Phys. Metall. Mater. Sci. 47 (2016) 985–989. https://doi.org/10.1007/s11661-015-3296-3.

[122] G. Svenningsen, M.H. Larsen, J.H. Nordlien, K. Nisancioglu, Effect of high temperature heat treatment on intergranular corrosion of AlMgSi(Cu) model alloy, Corros. Sci. 48 (2006) 258–272. https://doi.org/10.1016/j.corsci.2004.12.003.

[123] G. Svenningsen, J.E. Lein, A. Bjørgum, J.H. Nordlien, Y. Yu, K. Nisancioglu, Effect of low copper content and heat treatment on intergranular corrosion of model AlMgSi alloys, Corros. Sci. 48 (2006) 226–242. https://doi.org/10.1016/j.corsci.2004.11.025.

[124] W. Yang, S. Ji, Z. Li, M. Wang, Grain boundary precipitation induced by grain crystallographic misorientations in an extruded Al-Mg-Si-Cu alloy, J. Alloys Compd. 624 (2015) 27–30. https://doi.org/10.1016/j.jallcom.2014.10.206.

[125] M.H. Larsen, J.C. Walmsley, O. Lunder, R.H. Mathiesen, K. Nisancioglu, Intergranular corrosion of copper-containing AA6xxx AlMgSi aluminum alloys, J. Electrochem. Soc. 155 (2008) C550. https://doi.org/10.1149/1.2976774.

[126] T. Minoda, H. Yoshida, Effect of grain boundary characteristics on intergranular corrosion resistance of 6061 aluminum alloy extrusion, Metall. Mater. Trans. A. 33

(2002) 2891–2898. https://doi.org/10.1007/s11661-002-0274-3.

[127] A. Lervik, S. Wenner, O. Lunder, C.D. Marioara, R. Holmestad, Grain boundary structures and their correlation with intergranular corrosion in an extruded Al-Mg-Si-Cu alloy, Mater. Charact. 170 (2020) 110695. https://doi.org/10.1016/j.matchar.2020.110695.

[128] A. Lervik, T. Danbolt, T. Furu, R. Holmestad, O. Lunder, Comparing intergranular corrosion in Al-Mg-Si-Cu alloys with and without α-Al(Fe,Mn,Cu)Si particles, Mater. Corros. 72 (2021) 575–584. https://doi.org/10.1002/maco.202011954.

[129] C. Schnatterer, D. Zander, Influence of the grain boundary chemistry on the intergranular corrosion mechanisms of a high-strength Al-Mg-Si alloy, Surf. Interface Anal. 48 (2016) 750–754. https://doi.org/10.1002/sia.5859.

[130] V. Guillaumin, Influence of overaging treatment on localized corrosion of Al 6056, Corrosion. 56 (2000) 12–23. https://doi.org/10.5006/1.3280517.

[131] H. Zhan, J.M.C. Mol, F. Hannour, L. Zhuang, H. Terryn, J.H.W. De Wit, The influence of copper content on intergranular corrosion of model AlMgSi(Cu) alloys, Mater. Corros. 59 (2008) 670–675. https://doi.org/10.1002/maco.200804110.

[132] G. Svenningsen, M.H. Larsen, J. Lein, J. Nordlien, K. Nisancioglu, Intergranular corrosion of extruded AA6000-series model alloys, Proc. 9th Int. Conf. Alum. Alloy. (2004) 818–824.

[133] S. Esmaeili, D.J. Lloyd, Effect of composition on clustering reactions in AlMgSi(Cu) alloys, Scr. Mater. 50 (2004) 155–158. https://doi.org/10.1016/j.scriptamat.2003.08.030.

[134] S. Esmaeili, D.J. Lloyd, The role of copper in the precipitation kinetics of 6000 series Al alloys, Mater. Sci. Forum. 519–521 (2006) 169–176. https://doi.org/10.4028/www.scientific.net/msf.519-521.169.

[135] C. Schnatterer, D. Zander, Influence of the grain boundary chemistry on the intergranular corrosion mechanisms of a high-strength Al-Mg-Si alloy, Surf.

Interface Anal. 48 (2016) 750–754.

[136] S.K. Kairy, P.A. Rometsch, C.H.J. Davies, N. Birbilis, On the intergranular corrosion and hardness evolution of 6xxx series Al alloys as a function of Si:Mg ratio, Cu Content, and aging condition, Corrosion. 73 (2017) 1280–1295. https://doi.org/10.5006/2506.

[137] E.N. ISO, Corrosion of metals and alloys. Determination of resistance to intergranular corrosion of solution heat-treatable aluminium alloys, Br. Stand. Inst. (2005).

[138] G. ASTM, 110-92:"Practice for evaluating intergranular corrosion resistance of heat-treatable aluminum alloys by immersion in sodium chloride+ hydrogen peroxide solution," Annu. B. ASTM Stand. (2009).

[139] H. Hug, Ueber den einflußgeringer schwermetallgehalte auf die korrosionsbeständigkeit von Al-Mg-Si Legierungen, Aluminium. 23 (1941) 33.

[140] K. Nisancioglu, Ø. Strandmyr, Corrosion of AlMgSi alloys with Cu additions: the effect of Cu content up to 0.9 weight percent, Report no, STF34 A78052, SINTEF, Trondheim, Norw. (1978).

[141] G. Svenningsen, M.H. Larsen, J.C. Walmsley, J.H. Nordlien, K. Nisancioglu, Effect of artificial aging on intergranular corrosion of extruded AlMgSi alloy with small Cu content, Corros. Sci. 48 (2006) 1528–1543. https://doi.org/10.1016/j.corsci.2005.05.045.

[142] M.H. Larsen, J.C. Walmsley, O. Lunder, K. Nisancioglu, Effect of excess silicon and small copper content on intergranular corrosion of 6000-series aluminum alloys, J. Electrochem. Soc. 157 (2010) C61. https://doi.org/10.1149/1.3261804.

[143] W.J. Liang, P.A. Rometsch, L.F. Cao, N. Birbilis, General aspects related to the corrosion of 6xxx series aluminium alloys: Exploring the influence of Mg/Si ratio and Cu, Corros. Sci. 76 (2013) 119–128. https://doi.org/10.1016/J.CORSCI.2013.06.035.

[144] M.H. Larsen, J.C. Walmsley, O. Lunder, R.H. Mathiesen, K. Nisancioglu,

Intergranular corrosion of copper-containing AA6xxx AlMgSi aluminum alloys, J. Electrochem. Soc. 155 (2008) C550. https://doi.org/10.1149/1.2976774.

[145] S. Kumari, S. Wenner, J.C. Walmsley, O. Lunder, K. Nisancioglu, Progress in understanding initiation of intergranular corrosion on AA6005 aluminum alloy with low copper content, J. Electrochem. Soc. 166 (2019) C3114–C3123. https://doi.org/10.1149/2.0211911jes.

[146] C. Schnatterer, A. Bulinger, D. Zander, Evaluating the intergranular corrosion susceptibility of Al-Mg-Si-Cu alloys using electrochemical methods, Mater. Corros. 67 (2016) 1308–1313. https://doi.org/10.1002/maco.201608979.

[147] G. Svenningsen, M.H. Larsen, J.H. Nordlien, K. Nisancioglu, Effect of thermomechanical history on intergranular corrosion of extruded AlMgSi(Cu) model alloy, Corros. Sci. 48 (2006) 3969–3987. https://doi.org/10.1016/j.corsci.2006.03.018.

[148] X. Zhang, X. Zhou, J.O. Nilsson, Corrosion behaviour of AA6082 Al-Mg-Si alloy extrusion: The influence of quench cooling rate, Corros. Sci. 150 (2019) 100–109. https://doi.org/10.1016/j.corsci.2019.01.030.

[149] S. Chi, Y. Deng, X. Xu, X. Guo, Influence of minor Zn addition on precipitation behavior and intergranular corrosion properties of Al-Mg-Si alloy, Materials (Basel). 13 (2020) 650. https://doi.org/10.3390/ma13030650.

[150] X. Xu, Y. Deng, Q. Pan, X. Guo, Enhancing the intergranular corrosion resistance of the Al–Mg–Si alloy with low Zn content by the interrupted aging treatment, Metall. Mater. Trans. A. 52 (2021) 4907–4921. https://doi.org/10.1007/s11661-021-06433-z.

[151] M.X. Guo, G.J. Li, Y.D. Zhang, G. Sha, J.S. Zhang, L.Z. Zhuang, E.J. Lavernia, Influence of Zn on the distribution and composition of heterogeneous solute-rich features in peak aged Al-Mg-Si-Cu alloys, Scr. Mater. 159 (2019) 5–8. https://doi.org/10.1016/j.scriptamat.2018.09.004.

[152] J. Yan, N.M. Heckman, L. Velasco, A.M. Hodge, Improve sensitization and

corrosion resistance of an Al-Mg alloy by optimization of grain boundaries, Sci. Rep. 6 (2016) 1–10. https://doi.org/10.1038/srep26870.

[153] A. Bałkowiec, J. Michalski, H. Matysiak, K.J. Kurzydlowski, Influence of grain boundaries misorientation angle on intergranular corrosion in 2024-T3 aluminium, Mater. Sci. Pol. 29 (2011) 305–311. https://doi.org/10.2478/s13536-011-0050-4.

[154] X. Zhang, Y. Jiao, Y. Yu, B. Liu, T. Hashimoto, H. Liu, Z. Dong, Intergranular corrosion in AA2024-T3 aluminium alloy: The influence of stored energy and prediction, Corros. Sci. 155 (2019) 1–12. https://doi.org/10.1016/j.corsci.2019.04.031.

[155] X. Zhang, Y. Lv, T. Hashimoto, J.O. Nilsson, X. Zhou, Intergranular corrosion of AA6082 Al–Mg–Si alloy extrusion: The influence of trace Cu and grain boundary misorientation, J. Alloys Compd. 853 (2021) 157228. https://doi.org/10.1016/j.jallcom.2020.157228.

[156] X. Zhang, X. Zhou, J.O. Nilsson, Z. Dong, C. Cai, Corrosion behaviour of AA6082 Al-Mg-Si alloy extrusion: Recrystallized and non-recrystallized structures, Corros. Sci. 144 (2018) 163–171. https://doi.org/10.1016/j.corsci.2018.08.047.

[157] A. Shi, B.A. Shaw, E. Sikora, The role of grain boundary regions in the localized corrosion of a copper-free 6111-like aluminum alloy, Corrosion. 61 (2005) 534–547. https://doi.org/10.5006/1.3278189.

[158] H. Li, P. Zhao, Z. Wang, Q. Mao, B. Fang, R. Song, Z. Zheng, The intergranular corrosion susceptibility of a heavily overaged Al-Mg-Si-Cu alloy, Corros. Sci. 107 (2016) 113–122. https://doi.org/10.1016/j.corsci.2016.02.025.

[159] D. Zander, C. Schnatterer, C. Altenbach, V. Chaineux, Microstructural impact on intergranular corrosion and the mechanical properties of industrial drawn 6056 aluminum wires, Mater. Des. 83 (2015) 49–59. https://doi.org/10.1016/J.MATDES.2015.05.079.

[160] M.E. Parker, R.G. Kelly, Improved accelerated testing for localized corrosion susceptibility of high-strength aluminum alloys, in: Mater. Sci. Forum, 2014: pp.

223–228.

3. Materials and methods

This chapter presents an overview of the materials and characterization techniques used in this Ph.D. thesis as part of various investigations reported in different chapters.

3.1 Materials used

The materials used in the current study were 16 variants of Al-Mg-Si 6082 alloys with only difference in the minor additions of Cu and Zn. The 16 profiles with different small additions of Cu (≤ 0.05 wt%) and/or Zn (≤ 0.06 wt%) were model alloys designed for investigations mimicking recycled alloys (see Table 3.1 and Fig. 3.1) by Hydro Aluminium, Norway.

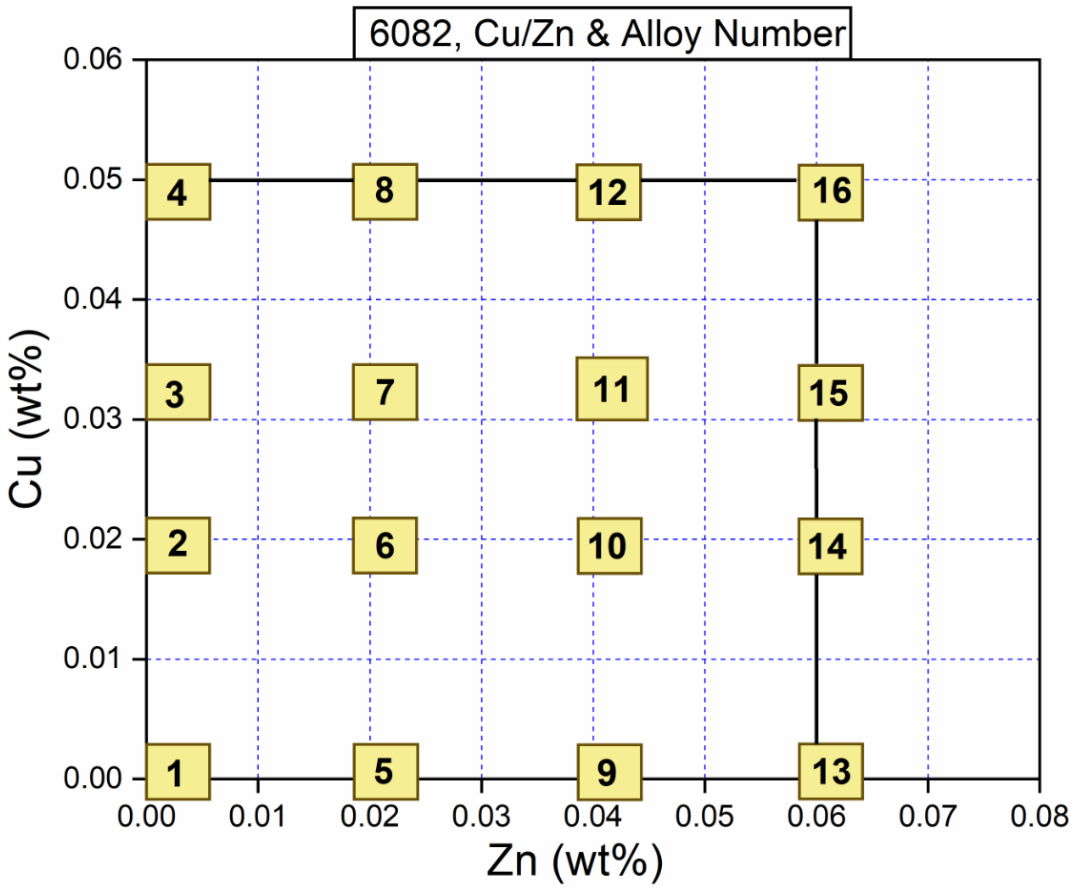

Fig. 3.1. Schematic diagram showing the Cu and Zn concentrations of the 16 studied alloys.

First, the alloys were prepared and cast with diameters of Ø95 mm. The cast billets were homogenized at 575 °C for 135 min and then cooled to room temperature at a cooling rate of 350 °C/h. Afterwards, homogenized billets were hot extruded at a ram speed of 5.6 mm/s and an average billet temperature of approximately 530 °C. Subsequently, the flat

extruded profiles with a cross-section of 4 x 25 mm^2 were water-quenched. The profiles of the water-quenched were stretched 0.5 % and artificially aged to peakaged condition. The aging curve of the as-received condition is illustrated in Fig. 3.2.

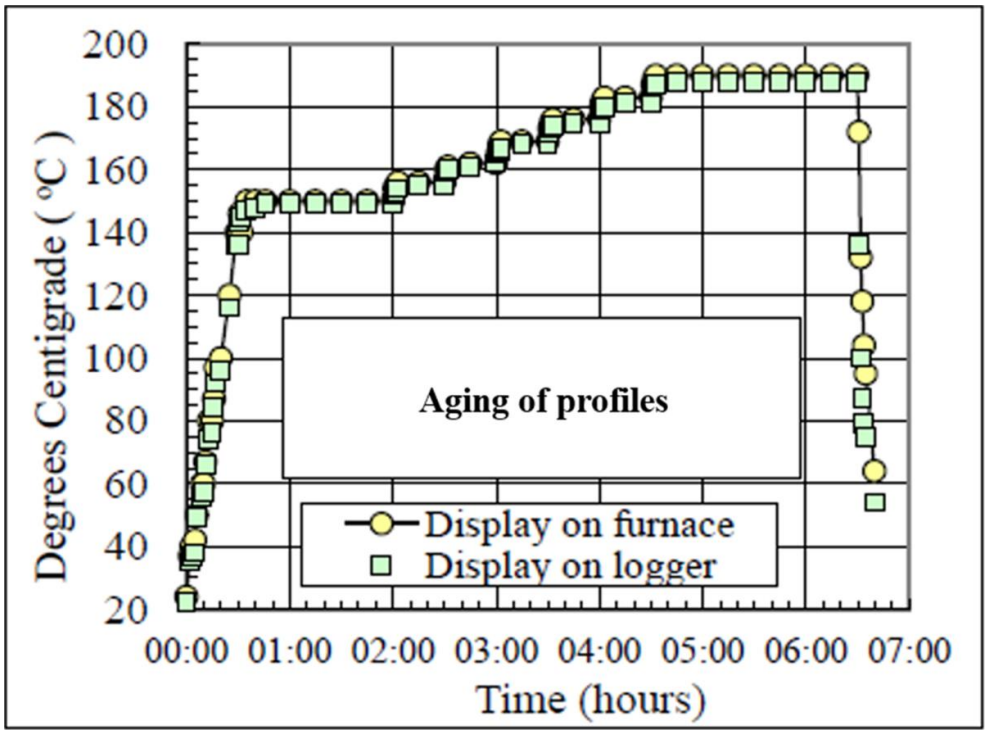

Fig. 3.2. Aging profile shows the temperature vs. time curve of the water-quenched 16 Al-Mg-Si alloys used in this project.

Exploring the impact of trace levels of certain alloying elements (i.e., Cu and Zn), expected to be found in Al-Mg-Si alloys as a result of recycling, on the microstructure and intergranular corrosion performance is the key issue of this Ph.D. study. To ensure that the corrosion performance of the studied alloys is not influenced by varying concentrations of different alloying elements such as Mg, Si, Mn, and Fe, the concentrations of such elements were carefully controlled and kept almost constant, see Table 3.1.

Table 3.1. Chemical composition (wt%) of Al-Mg-Si 6082 alloys investigated in this Ph.D. study.

Alloy ID	Mg	Si	Cu	Zn	Fe	Mn	Al
Al.1	0.647	0.968	0.001	0.003	0.219	0.544	Bal.
Al.2	0.644	0.965	0.017	0.003	0.218	0.545	Bal.
Al.3	0.644	0.968	0.034	0.003	0.220	0.541	Bal.
Al.4	0.639	0.956	0.048	0.003	0.217	0.538	Bal.
Al.5	0.638	0.962	0.001	0.022	0.214	0.554	Bal.
Al.6	0.635	0.933	0.018	0.022	0.210	0.559	Bal.
Al.7	0.634	0.940	0.034	0.022	0.211	0.558	Bal.
Al.8	0.628	0.937	0.050	0.022	0.211	0.554	Bal.
Al.9	0.636	0.941	0.001	0.041	0.210	0.539	Bal.
Al.10	0.636	0.945	0.018	0.041	0.214	0.548	Bal.
Al.11	0.635	0.931	0.034	0.041	0.206	0.555	Bal.
Al.12	0.636	0.942	0.050	0.041	0.216	0.562	Bal.
Al.13	0.634	0.943	0.001	0.059	0.211	0.555	Bal.
Al.14	0.634	0.945	0.018	0.059	0.211	0.560	Bal.
Al.15	0.630	0.949	0.034	0.059	0.207	0.570	Bal.
Al.16	0.627	0.949	0.050	0.059	0.208	0.580	Bal.

Moreover, all extruded profiles showed recrystallized surface layer of a thickness of 380 to 500 µm and a deformed layer in the center, see Fig. 3.3.

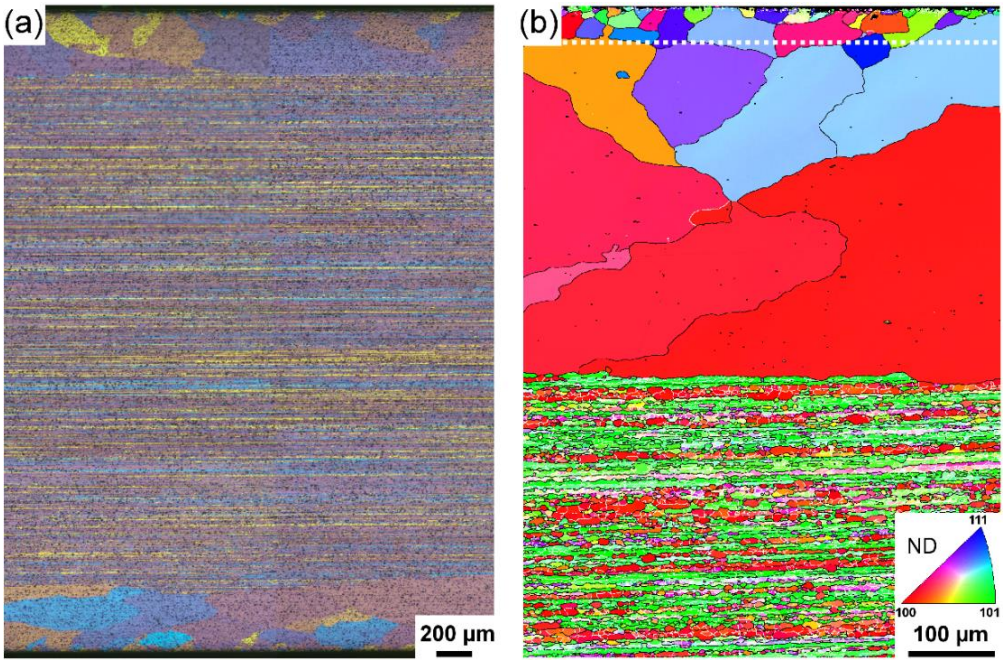

Fig. 3.3. Microstructure of Al.4 alloy at the as received condition: (a) optical image exhibiting the recrystallized surface layer on the top and bottom parts; (b) EBSD images of the recrystallized and deformed layer [1].

The current work also considered the influence of aging parameters in the presence of such very low Cu and Zn additions. The first set of alloys of interest (Al.3, Al.7, and Al.16) were firstly solution heat treated at 540 °C for 30 min, and subsequently, water-quenched. The alloys were then transferred for artificial aging at different aging temperatures (130, 140, 150, 165, 175, 185, 200, 220, and 240 °C) for 5 h, see Fig. 3.4a. The second set of alloys of interest (Al.1, Al.4, Al.13, Al.16, and Al.7) were solution heat treated at 540 °C for 30 min, and then water-quenched. Subsequently, the alloys were subjected to different aging times (1 h, 2 h, 5 h, and 24 h) at 185 °C, Fig. 3.4b. The alloys were selected based on their high/low IGC resistance investigated at the as-received condition. The temperature and the time used during the aging were chosen to consider the various aging conditions of underaged (UA), peakaged (PA), and overaged (OA).

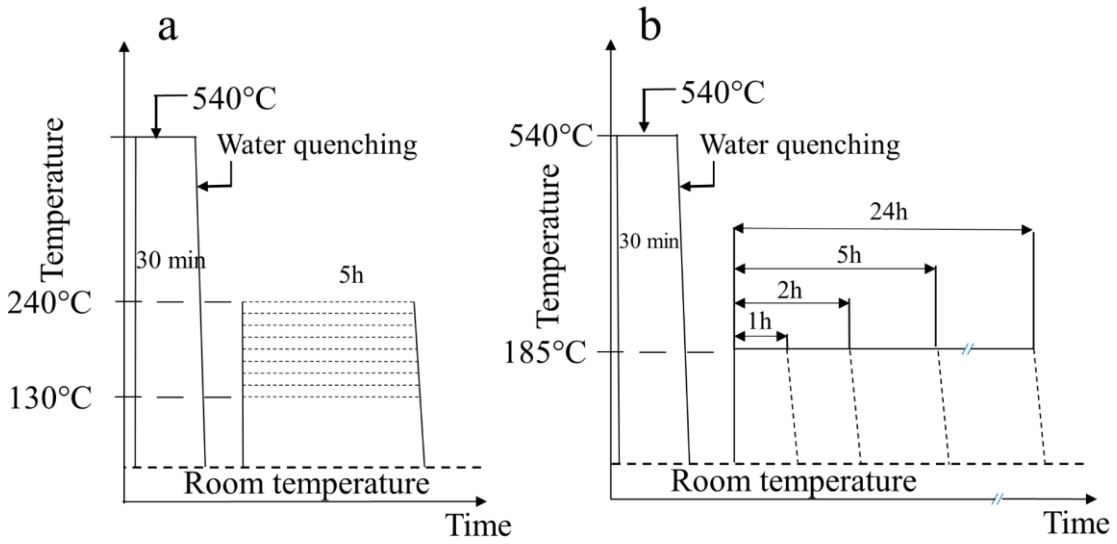

Fig. 3.4. Schematic diagram of (a) solution heat treatment and aging temperature; (b) solution heat treatment and aging time used in the current Ph.D. study.

3.2 Intergranular corrosion testing

Specimens of 25 x 20 x 4 mm^3 were cut from the flat profiles of the received Al-Mg-Si 6082 alloys, see Fig. 3.5. Accelerated corrosion test was carried out according to the standard BS ISO 11846 method B [2]. The test requires surface preparation prior to the immersion test. However, the standard allows a wide variety of parameters in surface preparation and immersion test, which can cause insufficient reliability and reproducibility. Therefore, in the current project, the same parameters were set and adopted for all experiments to adequately compare the alloys with different compositions and heat treatment conditions. The surface preparation involved the subsequent steps of acetone degreasing, etching in 8 wt% NaOH at approximately 56 °C for 5 min, rinsing in distilled water, followed by desmutting in a concentrated nitric acid (HNO_3) for 2 min. Afterward, the specimens were rinsed in distilled water and air dried. Specimens were later immersed in a solution consisting of 10 ml/l concentrated hydrochloric acid (HCl) and 30 g/l sodium chloride (NaCl) at room temperature for 24 h. Prior to the immersion tests, Lacomit varnish was used to coat the sectioned sides of the specimens to avoid any interference between the recrystallized and deformed layers.

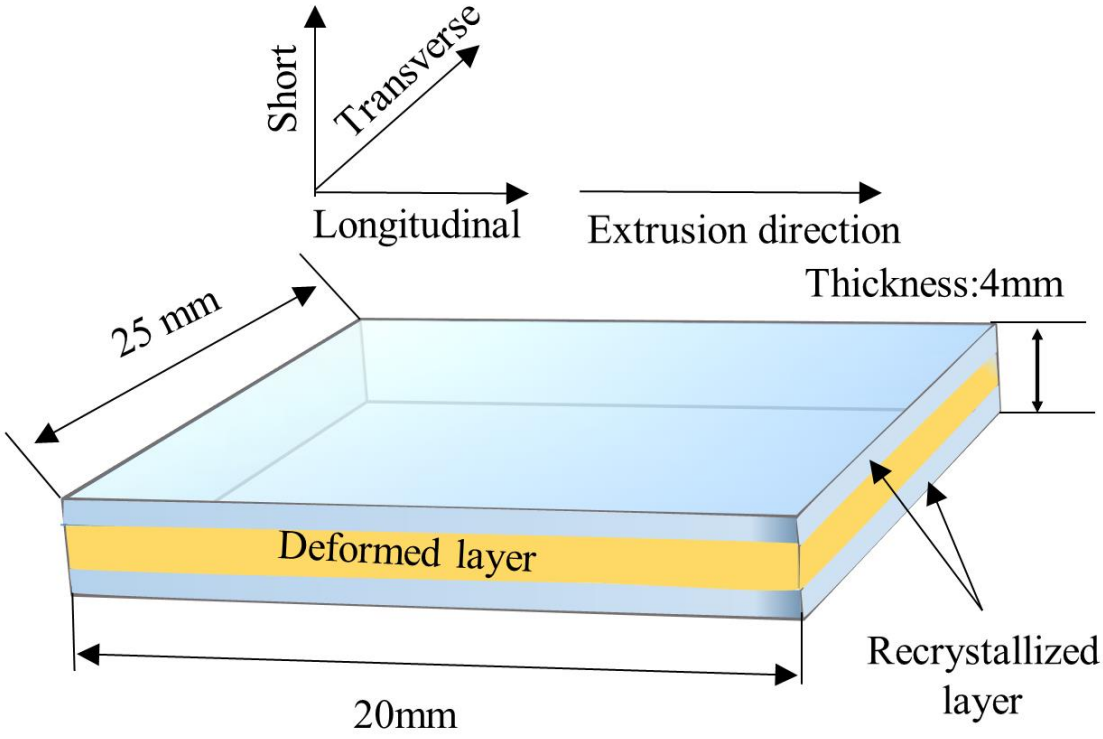

Fig. 3.5. Schematic drawing of the samples used for the intergranular corrosion test.

3.3 Characterization techniques

3.3.1 Scanning Electron Microscopy (SEM) of corroded samples

Scanning electron microscope is one of the most versatile instruments to study specimens' microstructure and elemental composition. In this work, the surface morphology and cross-section morphology of the corroded samples were investigated using high resolution scanning electron microscope AFEG 250 analytical ESEM operated in a high-vacuum. For cross-section investigation, the samples were cold embedded in an epoxy resin, mechanically polished up to 1 µm, rinsed with distilled water, and air dried. To avoid anomalous contrast caused by charging, a thin electrical conducting gold layer of approximately 3 nm was sputtered prior to SEM investigation. Surface information was obtained using secondary electrons detector (SE), while the Z-contrast images were recorded using backscattered electrons (BSE).

3.3.2 Transmission Electron Microscopy (TEM)

Transmission electron microscopy is a powerful technique in which the electrons are transmitted through a very thin sample (approximately 100 nm) and then impact on a detector to generate highly magnified and high-resolution images. In this study, A JEOL

3000F instrument operated at 300 kV in the transmission electron microscope mode was used to investigate the microstructure and grain boundary regions. A Titan Analytical 80-300ST microscope operated at 300 kV in scanning transmission electron microscope (STEM) mode equipped with an X-Max 80TLE detector from Oxford Instruments was employed to study the grain boundary chemistries as well as grain boundary particle compositions. A spherical aberration CS-probe corrected JEOL ARM200F microscope operated at 200 kV in high annular angle dark-field scanning transmission electron microscope (HAAD-STEM) mode was used to investigate the precipitate atomic structures. The HAADF-STEM technique provides atomic number Z contrast enabling to identify the heavier Cu (Z_{Cu}=29) and Zn (Z_{Zn}= 30) columns from those lighter columns containing Al (Z_{Al}= 13), Mg (Z_{Mg}= 12) and Si (Z_{Si}= 14). Therefore, the heavier the element, the greater the intensity of the scattering leading to atomic Z contrast in the acquired images [3].

All TEM specimens studied in this project were prepared from the top recrystallized surface layer by grinding them to approximately 100 µm and punched into Ø3mm disks. Subsequently, the foils were electropolished using a twin-jet Struers TenuPol-5 polishing system. The electrolyte comprises 80 % ethanol, 10 % 2-butoxyethanol, and 10 % perchloric acid 65 %. The electropolishing was carried out at a temperature of approximately -20 °C.

3.3.3 X-ray Computed Tomography (CT)

X-ray computed tomography (CT) is a nondestructive technique that provides unrivaled 3D information on the internal structure of studied objects. Zeiss XRadia 410 Versa X-ray microscope was used to obtain a 3D visualization nondestructively of the internal structure of the corroded samples. Cylindrical specimens with a diameter of 1.9 mm and a height of 4 mm (the thickness of the extruded alloys) were cut from almost the center part of the specimens, see Fig. 3.6. Prior to the CT scan, the specimens were tested in an acidified solution for 72 h according to standard BS ISO 11846 method B described in section 3.2. To ensure that only the flat surface will be exposed to the acidified solution described in section 3.2, a Lacomit was used to cover the side surface of the cylindrical samples. Thereafter, the corroded cylindrical specimens were imaged using X-ray CT to obtain 3D images of the intergranular corrosion attack. The CT instrument was operated at 40 kV and 10 W using a 4x objective and a filter LE3 in front of the X-ray source to remove

the lowest energy. 3201 projections with 25 s acquisition time per projection were adopted, resulting in a total acquisition time of 24:01 h. The images were recorded at a pixel size of 2.1 µm using 2x2 binning. All scans were reconstructed based on a cone algorithm using filtered back projection [4], provided by Zeiss as a software package. Further analysis was performed using Avizo 9.7.0 software.

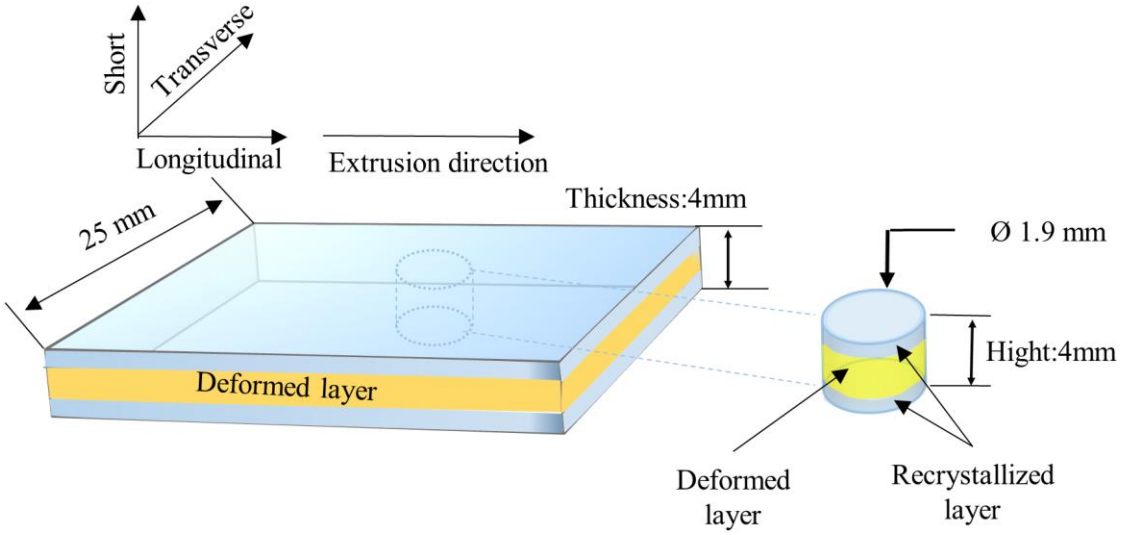

Fig. 3.6. Schematic drawing of the samples used for X-ray computed tomography scan.

3.3.4 Focused Ion Beam (FIB-SEM)

Focused ion beam FEI Helios 5 Hydra UX DualBeam using Xe source was used in this project. FIB technique was used to prepare TEM samples from the grain boundary of the corroded samples and as a sculpting tool to mark the grain boundaries of interest by milling to be scanned later using AFM/SKPFM, see Fig. 3.7.

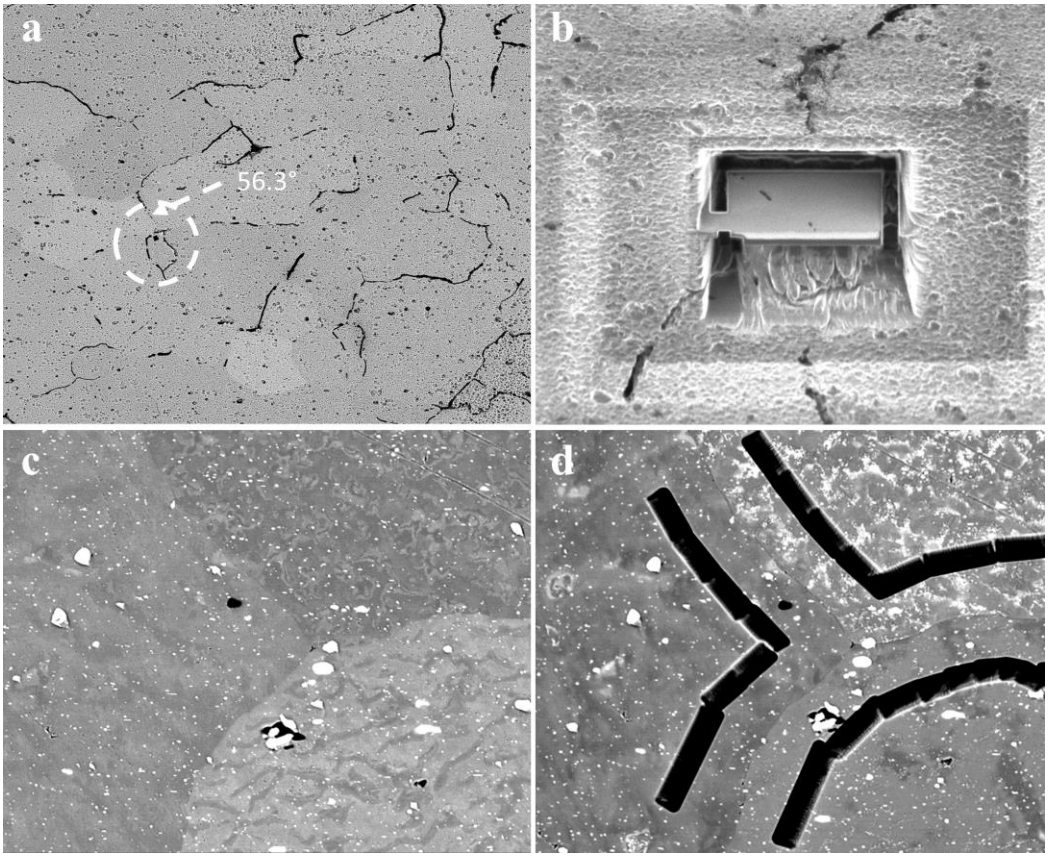

Fig. 3.7. BSE-SEM images showing: (a) grain boundary of interest (high angle grain boundary) for TEM investigation; (b) TEM lamella ready for left out; (c) grain boundaries of interest for AFF/SKPFM investigation; (d) grain boundaries after milling and cleaning ready for AFM/SKPFM analysis.

3.3.5 Atomic Force/Scanning Kelvin Probe Force Microscope (AFM/SKPFM)

To investigate the influence of minor addition of Cu and/or Zn on the grain boundary surface potential, AFM/SKPFM measurements were conducted using Bruker Dimension Edge™ instrument with an SCM-PIT-V2 tip coated with PtIr5. Prior to AFM/SKPFM scanning, the samples were mechanically polished to 0.25 µm, followed by a final OP-S polishing for 30 s. Thereafter, the grain boundaries of interest were marked using Xe source, followed by a 0.3 nA final cleaning step to remove the contamination and materials redeposited during the milling process, see Fig. 3.7(c, d). The topography and grain boundary potential were recorded at room temperature.

3.3.6 Electron Backscatter Diffraction (EBSD-SEM)

Electron backscattered diffraction is an SEM-based technique to investigate the crystal structure and orientation at the specimen surface. The EBSD was used to investigate the grain boundary types, i.e., low angle boundaries (LABs), random high angle boundaries

(HABs), and coincidence site lattice (CSL), as well as the grain boundary misorientation angle. The gran boundary characterizations were carried out using Zeiss Sigma 300 field emission (FE-SEM) equipped with the Oxford C-Nano EBSD detector.

References

[1] E.H. Bartawi, O. V. Mishin, G. Shaban, J.H. Nordlien, R. Ambat, Electron microscopy analysis of grain boundaries and intergranular corrosion in aged Al-Mg-Si alloy doped with 0.05 wt% Cu, Corros. Sci. 209 (2022) 110758.

[2] E.N. ISO, Corrosion of metals and alloys. Determination of resistance to intergranular corrosion of solution heat-treatable aluminium alloys, Br. Stand. Inst. (2005).

[3] P.D. Nellist, S.J. Pennycook, The principles and interpretation of annular dark-field Z-contrast imaging, Adv. Imaging Electron Phys. 113 (2000) 147–203.

[4] L.A. Feldkamp, L.C. Davis, J.W. Kress, Practical cone-beam algorithm, Josa A. 1 (1984) 612–619.

4. Summary of appended papers

This chapter provides a summary of the key finding in the research papers resulting from the current Ph.D. work. Each research paper is presented as an individual chapter (Chapters 5–11). The main objective of the current Ph.D. is to deeply understand the influence of minor addition of Cu (≤ 0.05 wt%) and Zn (≤ 0.06 wt%) on the microstructure and intergranular corrosion resistance of Al-Mg-Si alloys.

4.1 Paper I

Electron microscopy analysis of grain boundaries and intergranular corrosion in aged Al-Mg-Si alloy doped with 0.05 wt% Cu

In this research work, a particular focus was paid to statistically investigating the influence of the different grain boundary (GB) types on the intergranular corrosion resistance (IGC) of 6082 Al-Mg-Si alloy in the peakaged (PA) condition. Random high-angle grain boundaries (HABs) with misorientations $\theta > 15°$, low angle grain boundaries (LABs) with misorientations $\theta = 2° – 15°$ and coincidence site lattice (CSL) low Σ ($3 \leq \Sigma \leq 21$) were considered in this work. The as-received alloy showed a heterogeneous microstructure through the flat profile thickness. The center layer (~3 mm) contains a deformed structure with a notable portion of LABs of ~38 %, which is found between two recrystallized surface layers, see Fig. 4.1.

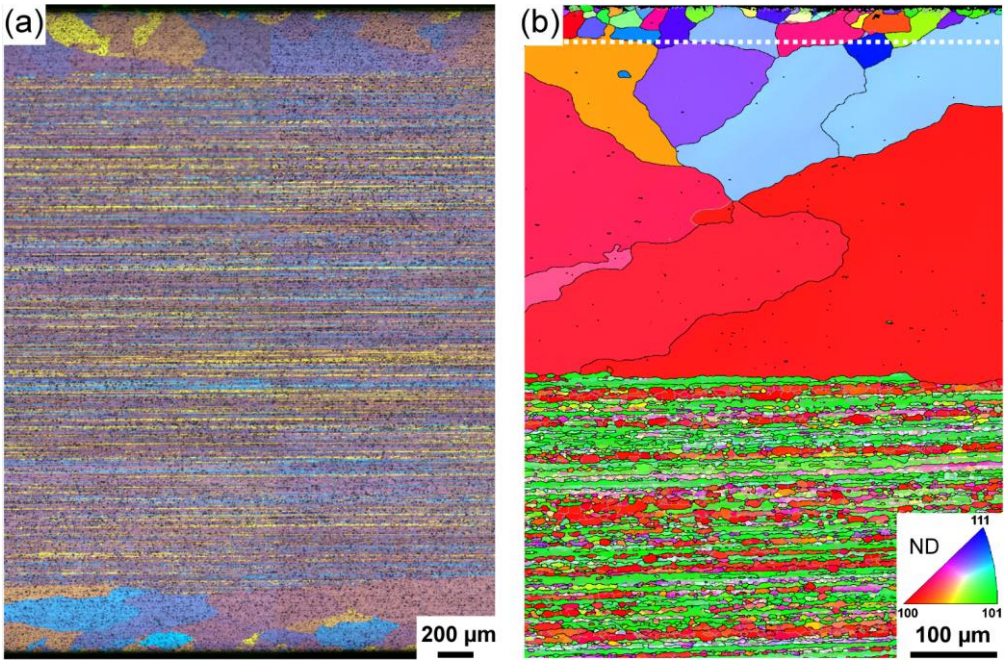

Fig. 4.1. Microstructure of 6082 Al-Mg-Si alloy: (a) optical image showing the entire thickness; (b) EBSD map showing the top surface layer and part of the deformed center layer.

The EBSD results indicated that the HABs are the dominant type in the recrystallized layer of ~82.4 %, while the reminder 9.1 % and 8.5 % are LABs and CSL grain boundaries, respectively. Concerning the IGC, the test was conducted on the recrystallized surface layer. The IGC resistance was investigated as a function of time as follows 90 min to define which GB types corroded first, the 24 h test is the standard one based on ISO 11846 method B, and the 72 h test to determine which GBs can resist such long time experiment.

The IGC test, based on ~2200 investigated GBs, evidently showed that the IGC took place after 90 min of exposure as ~6 % of the investigated GBs were partially or entirely corroded. Most of the affected GBs in the 90 min test were HABs. With increasing the exposure time to 24 h, the fraction of the corroded GBs noticeably increased as ~51 % of the inspected GBs were corroded. The portion of the corroded GBs in the standard test (24 h) within different groups was ~56 %, ~49, and ~10 of HABs, CSL boundaries, and LABs, respectively, see Table 4.1. Interestingly, the results also indicated that the Σ3 boundaries were highly susceptible to IGC, as ~68 % of the inspected boundaries were corroded after 24 h of exposure. After 72 h of exposure, ~99 % of the studied GBs were corroded, see Table 4.1.

Table 4.1. Fractions (%) of the corroded grain boundaries within different types of GBs.

Test duration	LABs	Random HABs	Σ3–Σ21 boundaries	Only Σ3 boundaries	All boundaries
90 min	2.2	6.2	12.8	17.4	6.3
24 h	9.7	56.2	49.3	68.4	50.5
72 h	93.8	100	97.6	100	99.2

4.2 Paper II

The effect of trace level copper content on intergranular corrosion of extruded AA6082-T6 alloys

The influence of minor additions of Cu (0.001, 0.02, 0.03, and 0.05 wt%) on the microstructure and IGC resistance of 6082 Al-Mg-Si alloys have been investigated in this part of study. The EBSD results from the recrystallized surface layer indicated no noticeable difference in the fraction of different GB types between the four studied alloys. Based on EBSD, ~90 of the investigated GBs were HABs, while the remaining 10 % of the GBs were LABs. High-angle annular dark-field scanning transmission electron microscopy (HAAD-STEM) results showed the presence of β-phase and Cu-rich β particles in alloy with 0.05 wt% Cu. Despite low Cu content, Cu-rich films were also observed along some investigated GBs, see Fig. 4.2. The presence of GB particles and Cu films will be the driving force for the IGC to take place. The severity of the IGC highly depends on the continuity of the Cu-films, the type of GB particles, and the density of these particles along the GBs. More severe IGC can be expected with denser GB particles and more continuous Cu-rich film.

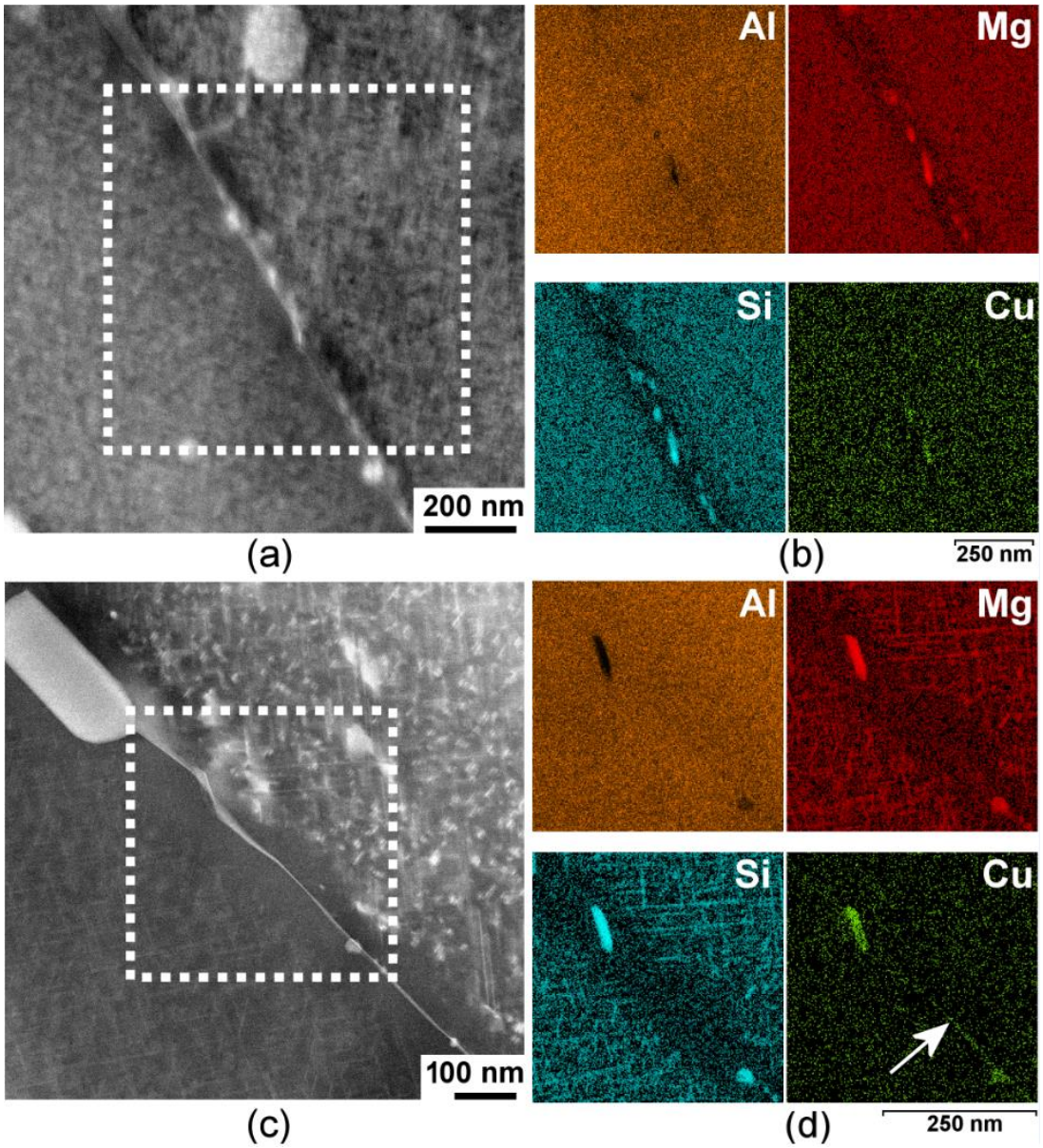

Fig. 4.2. HAAD-STEM images showing the GB of 0.05 wt% Cu containing alloy (a, c) and their corresponding elemental Al, Mg, Si, and Cu maps (b, d).

The IGC influenced small numbers of GBs in the sample with 0.001 wt% Cu, however, the numbers of the affected GBs were increased by increasing the Cu content, see Fig. 4.3. Moreover, the penetration depth of the IGC was raised as a function of Cu content.

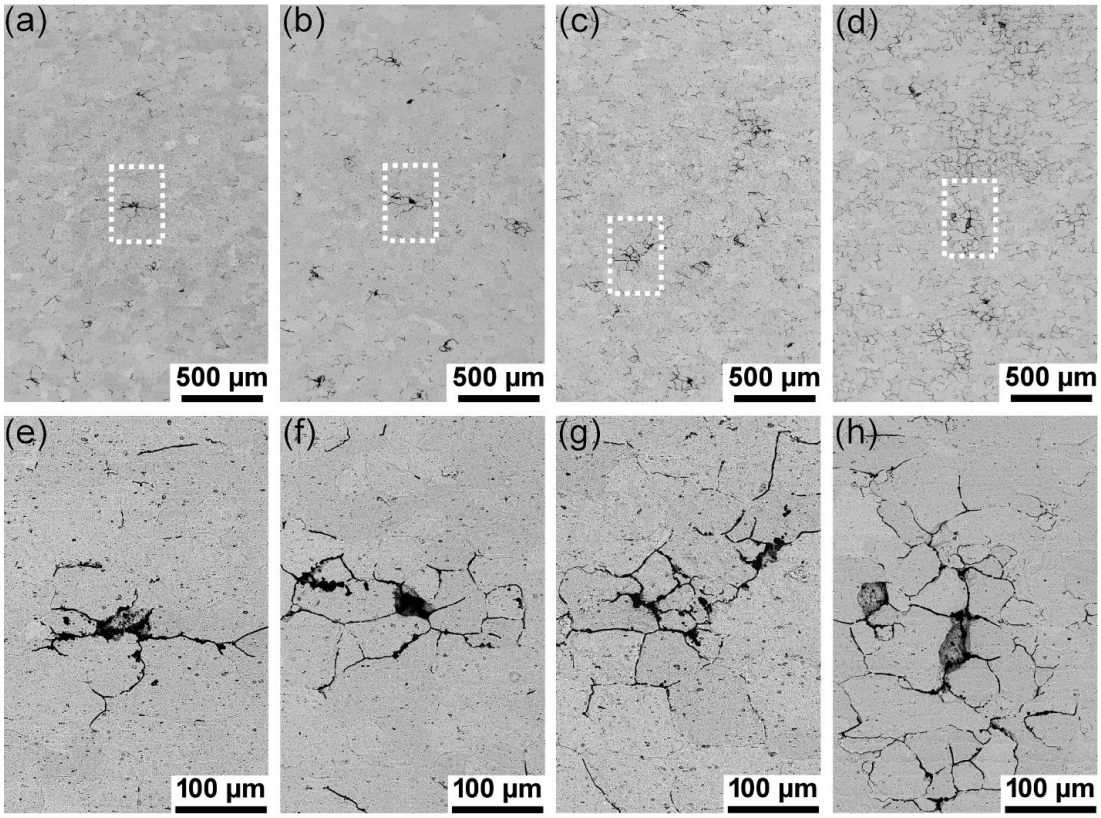

Fig. 4.3. SEM-BSE images showing the surface morphology of the investigated alloys after 24 h corrosion test.

4.3 Paper III

Toward high intergranular corrosion resistance in 6082 Al-Mg-Si alloys: influence of minor additions of Cu and Zn

The influence of minor addition of Zn (0.003 (A1), 0.02 (A2), 0.04 (A3), and 0.06 (A4) wt%) on the microstructure, precipitate structure, and IGC resistance of Al-Mg-Si-(0.05 Cu wt%) has been investigated. The EBSD results showed that the fractions of the random HABs are similar in the studied alloys (~90 %). The TEM results showed a precipitates free zone (PFZ) of ~100 nm detected on either side of all investigated alloys. Furthermore, the STEM results indicated the presence of β, Q/Q′ particles, and Cu-rich film along the GBs in alloy A1. The grain boundaries in A4 revealed the presence of β, Zn-containing Q/Q′ particles, Cu, and Zn-rich films along some investigated GBs. However, not all investigated GBs showed the presence of Cu and Zn-rich films, as some of the inspected GBs displayed either Cu-rich film or clean GBs with Q/Q′ and Zn-containing Q/Q′ particles. Moreover, the atomic resolution HAADF-STEM images indicated that minor addition of Cu and Zn can significantly influence the precipitate crystal structures.

Two Cu sub-unit structures (e.g., Q′/C and β'_{Cu} sub-units) can be detected in the β″ precipitate structures.

The IGC results indicated that IGC invaded the surface of alloy A1, while IGC resistance increased by increasing Zn content, see Fig. 4.4. The numbers of the corrode GBs after 24 h of exposure to the acidified solution were noticeably decreased in alloy A4 with higher Zn content compared to that in alloy A1 with the lowest Zn content. Moreover, some cavities resulting from fallen grain were observed within the IGC network. The number of cavities in alloy A1 with low Zn was higher than in alloy A4 with higher Zn content, see Fig. 4.4(a, d).

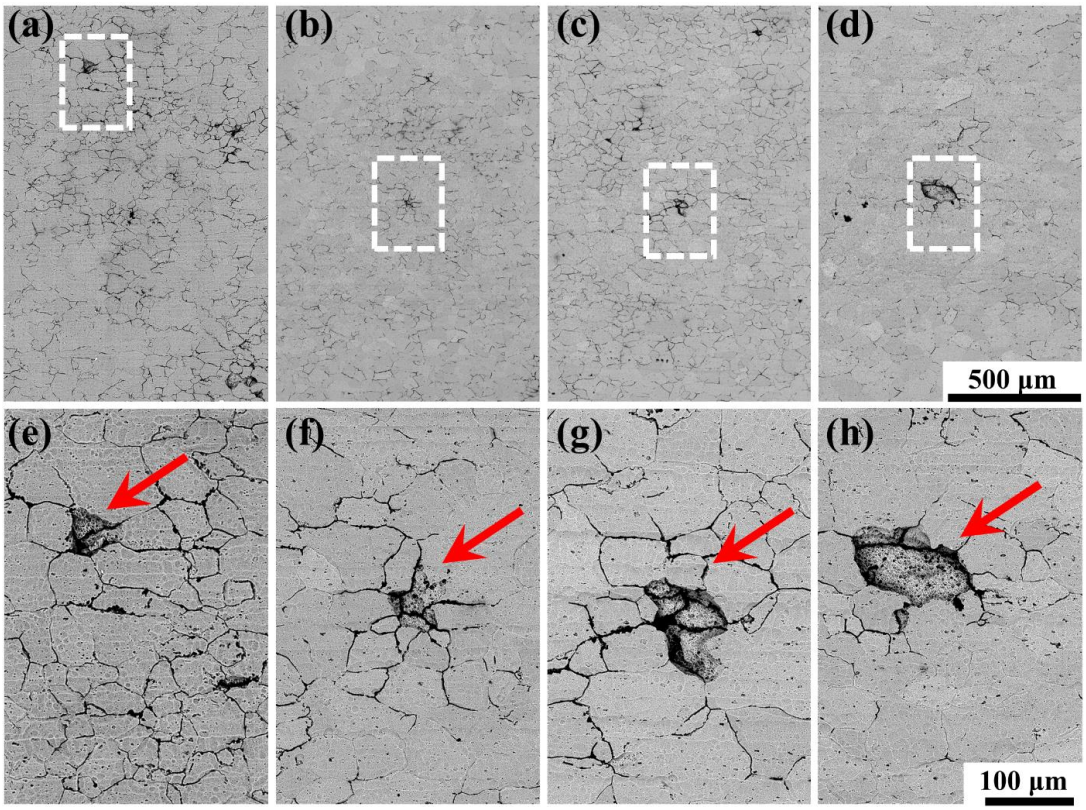

Fig. 4.4. SEM-BSE images showing the surface morphology of the studied alloys with different Zn additions after 24 h IGC test.

4.4 Paper-IV

Effect of minor addition of Zn on precipitate crystal structures and intergranular corrosion in 6082 Al-Mg-Si alloys

This research paper focus on understanding the effect of minor addition of Zn (0.003 (R1), 0.02 (R2), 0.04 (R3), and 0.06 (R4) wt%) in Al-Mg-Si alloys on the microstructure, precipitate structures, and IGC resistance. STEM has been used to

investigate the GB chemistry and precipitate crystal structures. Furthermore, atomic force microscopy (AFM) coupled with scanning Kelvin probe force microscope (SKPFM) was adopted in this paper to elucidate the influence of Zn on the surface potential along the GBs. The STEM results indicated the presence of two groups of GBs in alloy R1; the first group is GBs free from particles, and the second one is GBs that demonstrated the presence of Mg-Si particles. The GBs in alloy R4 showed the presence of Zn-rich Mg-Si particles. In addition, no Zn-rich film was detected in alloys R1 and R4. The atomic resolution HAADF-STEM indicated that low Zn concentration can led to the presence of Q′/C sub unit structure in the β″ precipitate structure, see Fig. 4.5.

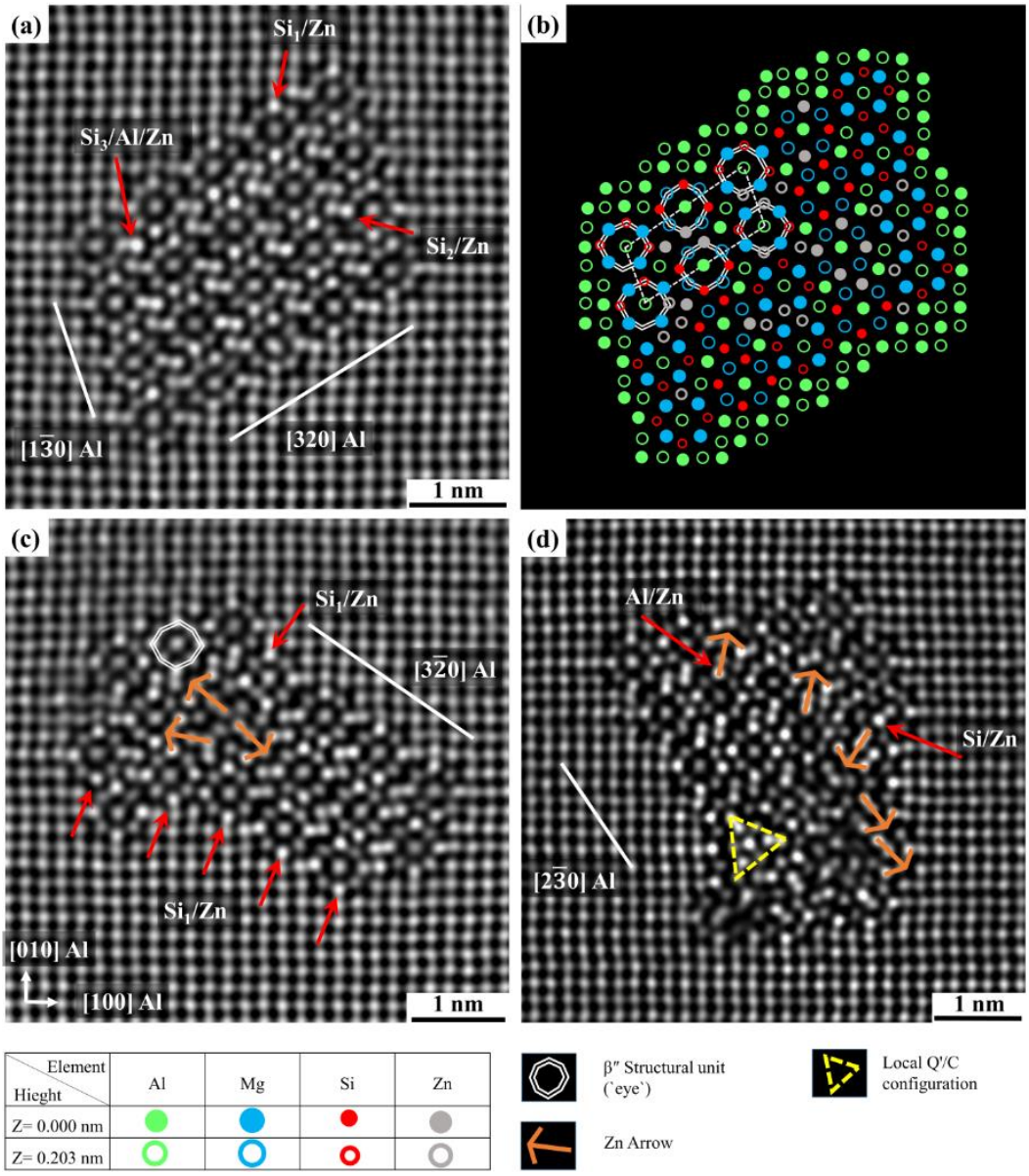

Fig. 4.5. HAADF-STEM images showing the impact of 0.06 wt% Zn on the precipitate structure in Al-Mg-Si alloy in the peakaged condition.

The accelerated IGC tests indicated that alloys R1 and R2 had a relatively high IGC resistance, as a typical localized IGC was observed. However, a transition toward more uniform IGC was noticed by increasing Zn concentrations, hence, a uniform IGC attack was observed in alloy A4. Furthermore, The SKPFM results demonstrated more negative potential measured along the GBs in R4 compared to the adjacent Al matrix, indicating that the GBs, in this case, will act as an anode, while the near Al matrix will serve as a cathode.

4.5 Papers V and VI

Effect of aging temperature on microstructure and intergranular corrosion of Al-Mg-Si alloys with low concentrations of Cu and Zn

In this work, the impact of aging temperature (isochronal) and aging time (isothermal) on the microstructure and IGC of Al-Mg-Si alloy has been investigated. In the isochronal study, three Al-Mg-Si alloys with different Cu and Zn concentrations L1 (0.03 Cu and 0.003 Zn), L2 (0.03 Cu and 0.02 Zn), and L3 (0.05 Cu and 0.06 Zn) in wt% were studied. The alloys were aged at 130, 140, 150, 165, 175, 185, 200, 220, and 240 °C for 5 h. The results revealed the presence of Cu-rich film along some investigated GBs in alloy L3 aged at 140 °C for 5 h. Moreover, the inspected GBs in alloy L3 also showed the presence of closely spaced GBs particles and distinguished PFZ of ~45 nm. Further increasing the aging temperature to 240 °C to reach the overaged (OA) condition in alloy L3, the results revealed coarse GB particles and bulk precipitates. Additionally, no Cu and/or Zn-rich films were observed in alloy L3 in the OA condition and low Cu/Zn concentrations.

The accelerated corrosion test showed that alloys L1 and L3 in the underaged (UA) condition (aged between 130-165 °C) were remarkably susceptible to IGC as a uniform IGC was noted, see Fig. 4.6. The IGC resistance in alloy L1 increased as the aging temperature increased to 185 °C, as more localized IGC could be seen. Moreover, alloy L2 showed relatively high IGC resistance in all aging conditions, though the IGC resistance decreased by increasing the aging temperature to 175 °C, see Fig. 4.6.

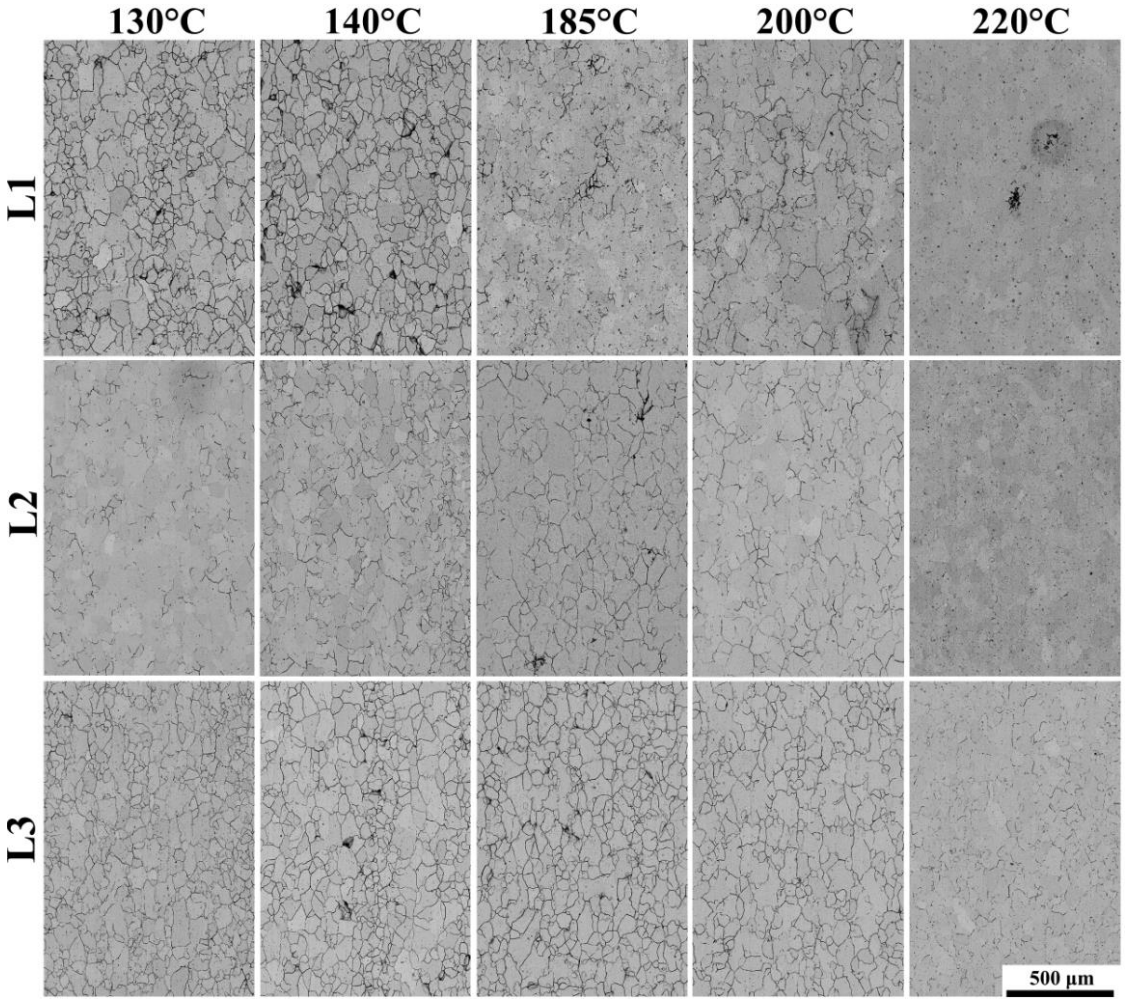

Fig. 4.6. SEM-BSE images showing the surface morphology of the inspected alloys aged at different temperatures (on the top) after 24 h IGC test.

Effect of aging time on microstructure and intergranular corrosion of 6082 Al-Mg-Si alloy with minor additions Cu and Zn

In the isothermal work, five Al-Mg-Si alloys with different Cu and Zn concentrations S1 (0.001 Cu and 0.003 Zn), S2 (0.05 Cu and 0.003 Zn), S3 (0.03 Cu and 0.02 Zn), S4 (0.001 Cu and 0.06 Zn), and S5 (0.05 Cu and 0.06 Zn) in wt% were studied. The alloys were aged for 1, 2, 5, and 24 h at 185 °C. According to the accelerated IGC test, the highest IGC resistance in all aging conditions was observed in alloy S1, see Figs. 4.7 and 4.8. However, the IGC resistance of S1 was decreased in the PA condition. Alloys S2 and S5 exhibited low IGC resistance in the UA and PA conditions, see Fig. 4.8. Furthermore, alloy S3 showed relatively good IGC resistance compared to alloys S2 and S4 as the presence of Cu and Zn in S3 is believed to reduce the electrochemical potential difference between GBs and PFZs.

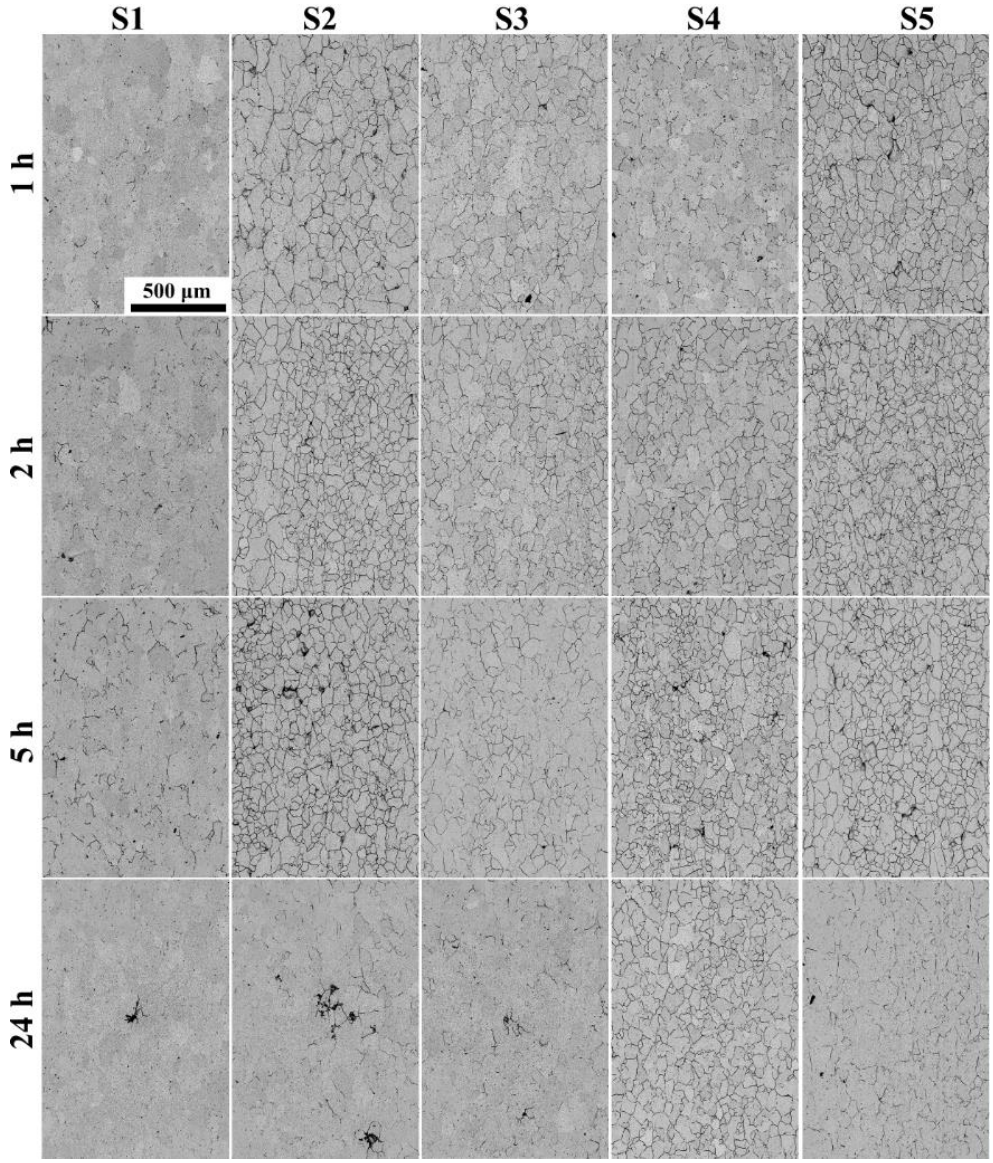

Fig. 4.7. SEM-BSE images demonstrating the surface morphology of the studied alloys aged at different time (on the side) after 24 h IGC test.

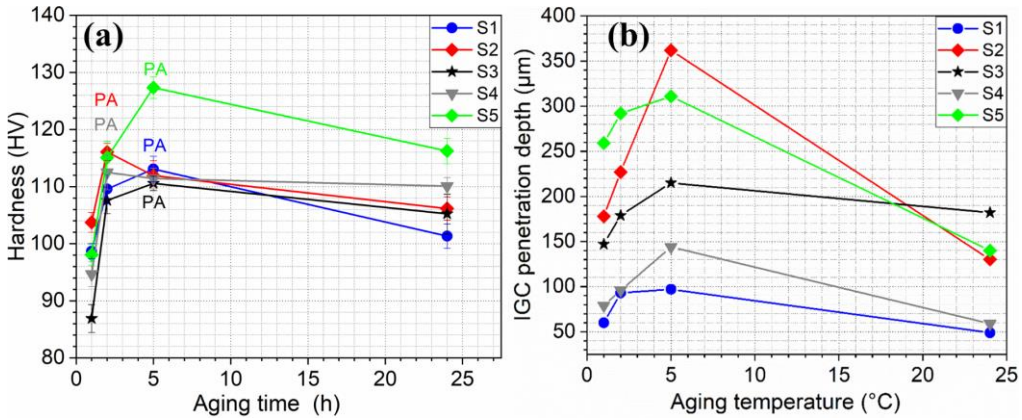

Fig. 4.8. Age hardening curve (a) and the maximum penetration depths (b) for the investigated alloys in different aging conditions.

4.6 Paper VII

Atomic structure of hardening precipitates in Al-Mg-Si alloys: Influence of minor additions of Cu and Zn

In this paper, the influence of Cu (0.05 wt%), Zn (0.06 wt%), and Cu+Zn on the hardening precipitate structure and their compositions in Al-Mg-Si alloy have been investigated using atomic resolution HAADF-STEM and atom probe tomography (APT). The HAADF-STEM results indicated that minor Cu addition could significantly influence the hardening precipitate structures in the PA condition, as ~53 % of the inspected structures were identified as disordered precipitates. Disordered indicates that Cu and/or Zn incorporated into β″ structures and led to the formation of different sub-unit structures, e.g., U1, U2, B′, β'_{Cu}, or Q′/C. Cu atoms were also noticed to occupy the atomic sites inside β″ structure and at the β″/Al matrix interface, see Fig. 4.9.

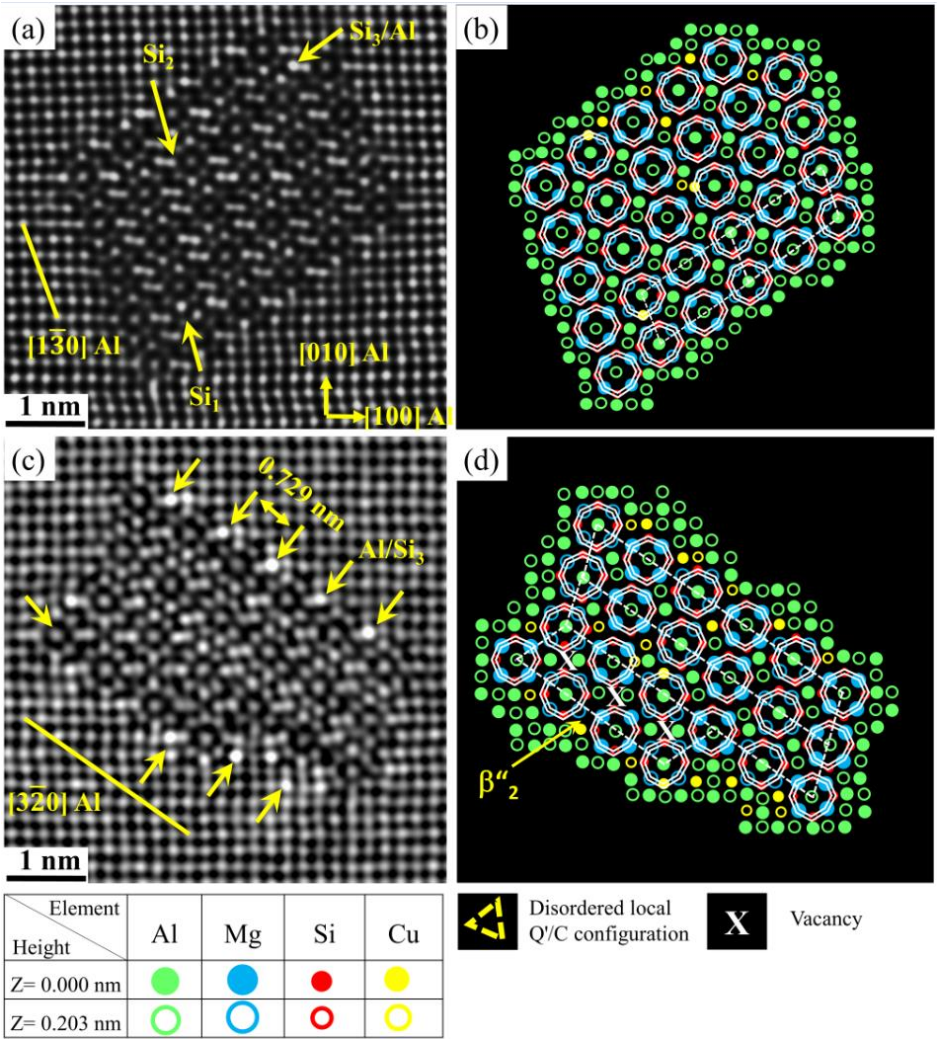

Fig. 4.9. HAADF-STEM images demonstrating the impact of 0.05 wt% Cu on the precipitate structures found in Al-Mg-Si alloy in the peakaged condition.

Concerning the impact of Zn on the precipitate structures, the results showed that ~60 % of the investigated precipitates were identified as disordered structures. Furthermore, the results showed that Zn had a unique impact on the precipitate structures, as two-fold symmetry, mirror symmetry, and arrow configuration were observed, see Fig. 4.10.

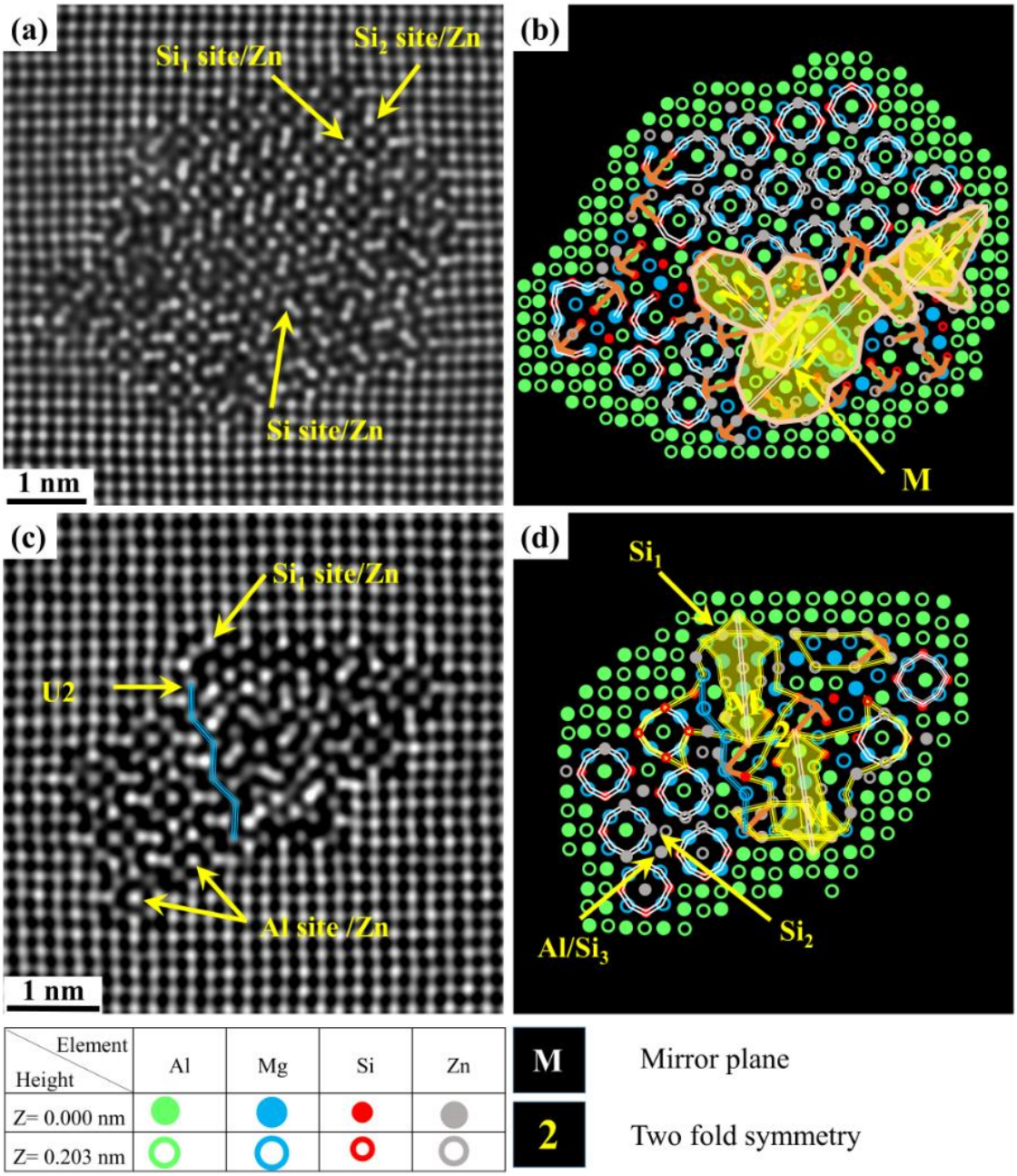

Fig. 4.10. HAADF-STEM images showing the influence of 0.06 wt% Zn on the precipitate structures in the Al-Mg-Si alloy.

Summary of appended papers

5. Paper I

Electron microscopy analysis of grain boundaries and intergranular corrosion in aged Al-Mg-Si alloy doped with 0.05 wt% Cu

Emad H. Bartawi[1,*], Oleg V. Mishin[1], Ghada Shaban[1], Jan H. Nordlien[2], Rajan Ambat[1]

[1] Department of Civil and Mechanical Engineering, Technical University of Denmark, Kgs. Lyngby 2800, Denmark

[2] Hydro, Innovation & Technology, Hydrovegen 160, 4265, Håvik, Norway

[*]Corresponding author: ehaba@mek.dtu.dk

Keywords: Alloy; Aluminium; SEM; STEM; TEM; Intergranular corrosion

Abstract

The microstructure and intergranular corrosion have been studied in an extruded and aged Al-Mg-Si alloy doped with 0.05 wt% Cu after immersing the material in an acidified salt solution. Intergranular corrosion takes place in this alloy despite the low Cu content. Electron microscopy analysis of the surface exposed to the corrosive environment does not reveal any significant difference in the fraction of corroded random and coincident site lattice high angle boundaries. Low angle boundaries with misorientations below 10° are found to be consistently more resistant to intergranular corrosion than any other boundary type.

E.H. Bartawi, O.V. Mishin, G. Shaban, J.H. Nordlien, R. Ambat, Electron microscopy analysis of grain boundaries and intergranular corrosion in aged Al-Mg-Si alloy doped with 0.05wt% Cu, Corr. Sci. 209 (2022) 110758, https://doi.org/10.1016/j.corsci.2022.110758.
The format of the published paper was adapted to match the format of the Ph.D. thesis.

5.1 Introduction

Heat treatable Al-Mg-Si (6xxx series) alloys have a number of attractive properties such as a fairly high strength-to-weight ratio, excellent weldability and formability, which makes them widely used in construction, automotive and other demanding industrial sectors. While corrosion resistance of these alloys is generally high, unbalanced alloying elements/impurities or improper heat treatments can provoke intergranular corrosion (IGC). In particular, additions of Cu above 0.1 wt% can make aged Al-Mg-Si alloys highly susceptible to IGC as the formation of Cu film and particles along grain boundaries (GBs) and participate free zones in regions adjacent to GBs may result in microgalvanic coupling [1–7]. In contrast, Al-Mg-Si alloys with Cu content below 0.1 wt% typically do not demonstrate severe IGC. For example, the presence of 0.0005 wt% Cu and 0.02 wt% Cu in the Al-Mg-Si alloys did not substantially affect their corrosion properties [1–6]. Furthermore, corrosion in an Al-Mg-Si alloy with 0.03 wt% Cu was found insignificant, occurring predominantly in the form of pitting rather than in the form of IGC [3]. On the other hand, an Al-Mg-Si alloy (AA6082-T6) with 0.06 wt% Cu studied by Zhang et al. [8] demonstrated pronounced IGC in the recrystallized microstructure when aging was performed after water-quenching. High frequencies of corroded boundaries were also observed in the deformed microstructure of this alloy [9]. Apparently, concentrations in the range 0.03 wt% < f_{Cu} < 0.06 wt% are critical for defining whether an alloy is susceptible to IGC. Despite its significance, this critical range has not been covered in previous publications on the Al-Mg-Si alloys.

Tiny concentrations of Cu are especially important in products obtained by recycling Al scrap with initially varying compositions. As the production of secondary Al globally increases, verification of the effects of small Cu concentrations on corrosion performance of the Al-Mg-Si system becomes critically important for the lifetime of products manufactured using recycled aluminum. Therefore, the purpose of this work is to study IGC in an Al-Mg-Si alloy with a concentration of Cu in the previously unexplored range. The alloy chosen for this study is AA6082-T6 with 0.05 wt% Cu, in which IGC is evaluated by examining the material surface after immersion tests.

A special focus in this work is on statistical analysis of IGC along different GB types as evidence exists that corrosion along individual boundaries depends on their crystallographic parameters. In particular, random high angle boundaries (HABs) in Al are

frequently reported to be more susceptible to IGC than low angle boundaries (LABs) and some low Σ coincident site lattice (CSL) HABs often described as special boundaries [10–16]. It should be noted that the previous studies of correlations between the GB type and the extent of IGC in the Al-Mg-Si alloys were mostly conducted on samples with fairly high Cu-contents (≥ 0.1 wt%). To our knowledge, only one study of such correlations was performed on the AA6082-T6 alloy with 0.06 wt% Cu, where a deformed microstructure with a high frequency of LABs (~65%) was studied [9]. However, the surface of hot-rolled or extruded Al-Mg-Si plates and profiles is usually recrystallized [1,13,17] with a high frequency of HABs rather than LABs. Therefore, in the present study correlations between the GB type and the extent of IGC are analyzed for the recrystallized surface of a hot-extruded AA6082 profile. To characterize the microstructure, a large variety of electron microscopy techniques are used in this work, which include optical microscopy, several transmission electron microscopy (TEM) based techniques, scanning electron microscopy (SEM), electron backscatter diffraction (EBSD) and transmission Kikuchi diffraction (TKD).

5.2 Experimental

The chemical composition of the AA6082 alloy used in this work is shown in Table 5.1. The as-cast ingot was homogenized at 575°C and then hot extruded into 4-mm-thick flat profiles. After extrusion, the material was water-quenched, then aged at 185 °C and delivered in the T6 temper.

Table 5.1. Chemical composition (wt%) of the Al 6082-T6 alloy used in this study

Cu	Mg	Si	Fe	Zn	Mn	Al
0.048	0.639	0.956	0.217	0.003	0.538	Balance

5.2.1 Optical microscopy, SEM and EBSD/TKD experiments

To establish the presence of through-thickness heterogeneities of the extruded sample, the longitudinal section containing the extrusion direction (ED) and the normal direction (ND) was investigated using both optical microscopy and EBSD. Bulk specimens were at first mechanically polished using a diamond suspension with an average particle size of 1 μm. One of these specimens was then electrochemically etched in the tetrafluoroboric acid for 70 sec, and optical micrographs were taken using a Zeiss Axio Vert.A1 microscope. Another specimen was electropolished for EBSD in the A2 electrolyte

from Struers. EBSD studies were carried out at an accelerating voltage of either 15 kV or 20 kV using a Zeiss Sigma 300 field emission gun SEM equipped with a C-Nano EBSD detector from Oxford Instruments. The microstructure in the ED-ND plane was investigated using an EBSD step size of 0.3 µm. A larger step size, 4 µm, was used for studying the crystallographic texture, covering the entire sample thickness over a distance of 20 mm along the ED.

For the EBSD analysis of the as-received microstructure in the plane containing the ED and the transverse direction (TD), the top surface of the extruded material was mechanically polished and then electropolished following the same procedure as for the ED-ND plane. The thickness of the surface layer removed by polishing was estimated to be ~40 µm. EBSD data from the ED-TD plane were collected in several regions, covering a total area of 2 mm^2 with a step size of 1 µm. Several thin foils from the same plane were investigated using the TKD technique to identify boundaries of specific types to be further analyzed by TEM. The accelerating voltage used for obtaining TKD was 30 kV.

The obtained EBSD data were analyzed using the Channel 5 post-processing software and the MTEX-5.6.0 Toolbox. LABs in the EBSD data were defined as boundaries with misorientations $\theta = 2–15°$, while HABs were defined as boundaries with misorientations $\theta > 15°$. Within the HAB group, low Σ ($3 \leq \Sigma \leq 21$) coincident site lattice (CSL) boundaries were defined as boundaries with misorientations deviated from the corresponding exact CSL misorientations by an angle $\Delta\theta$ less than the maximum allowable deviation $\Delta\theta_m = 15° \Sigma^{-1/2}$ [19]. HABs other than $\Sigma3–\Sigma21$ boundaries were categorized as "random" HABs in this work. Fractions of the different boundary types were calculated as number fractions.

The regions in the bulk specimens studied by EBSD in the ED-TD plane were reexamined in the SEM after the corrosion tests. In total, almost 2200 boundaries were inspected before and after the corrosion tests. In addition, to evaluate the depth of the corrosion attack, the corroded samples were sectioned along the ED-ND plane and several SEM images were taken from this plane after polishing.

5.2.2 TEM experiments

To prepare TEM foils of the as-received material, specimens containing the ED and the TD were at first cut from the top sample surface and mechanically thinned to a thickness

of 0.1 mm. Final electropolishing was then conducted at -25 °C in Struers A2 electrolyte using a TenuPol-5 double-jet polishing system. A JEOL 3000F TEM operated at 300 kV was used for taking bright field images of the microstructure. In addition, a Titan Analytical 80-300ST microscope operated in the scanning transmission (STEM) mode was utilized for both high angle annular dark field (HAADF) imaging and energy dispersive spectroscopy (EDS) using a windowless X-Max 80TLE detector from Oxford Instruments.

5.2.3 IGC tests

IGC tests were conducted on bulk 25 × 20 × 4 mm^3 specimens. In these specimens, the ED-TD plane initially characterized by SEM and EBSD was gently mechanically polished to remove any possible surface contamination introduced during the SEM/EBSD analysis. To ensure that only the ED-TD plane would be exposed to the corrosive environment, the narrow sides of the specimens were coated with Lacomit varnish. The specimens were then immersed in a solution containing 10 ml/l of concentrated HCl (1.19 g/ml) and 30 g/l NaCl for either 90 min, 24 h or 72 h at room temperature. The 90-min test was performed to identify GBs at which IGC would take place first. The 24-h test was the standard test conducted according to the BS ISO 11846 method B [18]. Finally, the 72-h test was carried out to identify boundaries able to withstand more extended exposure to the corrosive environment than in the standard test.

5.3 Results

5.3.1 Through-thickness heterogeneity of the as-received material

The microstructure of the as-received material is strongly heterogeneous through the thickness (see Fig. 5.1). The interior layer contains a hot-deformed microstructure with a large fraction of LABs (f_{LAB}=38 %) sandwiched between two recrystallized layers, where f_{LAB} is only ~9 % (see Table 5.2). The thickness of the recrystallized surface layers is approximately 0.4 mm, and the layer is not uniform; it demonstrates fine recrystallized grains with a size of ~20 μm at the immediate surface, while much coarser grains are seen at larger depths within this layer. The average recrystallized grain size d_{Rex} at the depth exposed to the corrosive solution is 63 μm (see Fig. 5.1b and Table 5.2). The spacing d_{ND} measured by EBSD between all boundaries along the ND in the interior layer is ~3 μm, while the spacing measured between HABs only is 4 μm (Table 5.2). Crystallographic orientations in the interior layers show a combination of the rolling texture components

such as Bs {110}⟨112⟩, S {123}⟨634⟩ and Cu {112}⟨111⟩ with the cube {001}⟨100⟩ texture (see Table 5.2). Compared to the interior layer, the texture in the recrystallized surface layer is generally weaker and contains a pronounced shear {001}⟨110⟩ component.

Table 5.2. Characteristics of microstructure and texture in the 6082-T6 plate analyzed using EBSD. The d_{ND} value in brackets represents the spacing between HABs only.

Layer	d_{Rex} or d_{ND} (μm)	f_{LAB} (%)	Bs {110}⟨112⟩ (%)	S {123}⟨634⟩ (%)	Cu {112}⟨111⟩ (%)	Cube {001}⟨100⟩ (%)	Shear {001}⟨110⟩ (%)
Surface	63	9	0.2	3.9	0.8	0.2	21.1
Interior	3(4)	38	25.8	27.2	4.8	23.1	-

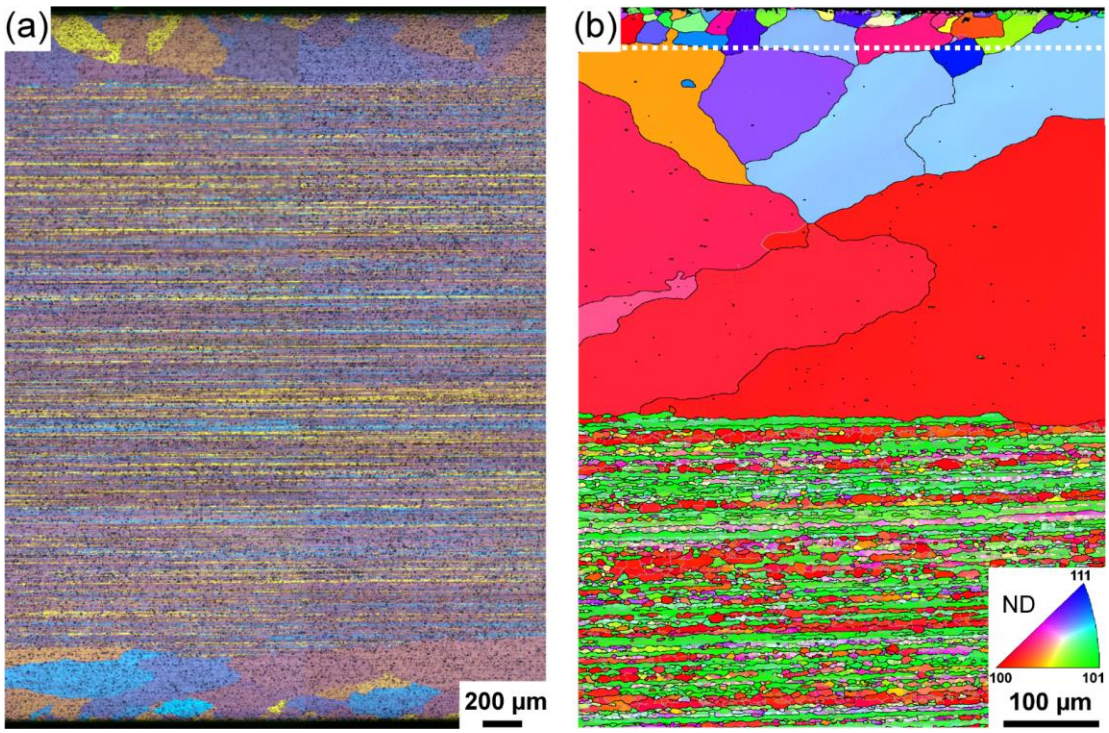

Fig. 5.1. Microstructure in the ED-ND section of the AA6082-T6 plate: (a) optical micrograph showing the microstructure through the entire plate thickness; (b) region investigated using the EBSD technique. The color code for orientations is shown in the inset. Gray and black lines indicate LABs and HABs, respectively. The depth exposed to the corrosive solution after polishing of the top surface is approximately indicated by the dashed line. Note that the thickness of the removed top layer varies slightly from specimen to specimen. The ED is parallel to the scale bar.

5.3.2 TEM analysis of boundary regions

In the following, examples of three boundary types (random HABs, low angle and Σ3 boundaries) are presented. Note that since random HABs were the dominant boundary type in the recrystallized layer of the as-received material, several such boundaries were readily found in the prepared TEM foils. In contrast, Σ3–Σ21 CSL boundaries and LABs were rare in this layer, with only one Σ3 boundary and two LABs observed in the inspected foils.

A bright field TEM image showing a random HAB with a misorientation of 46° ⟨144⟩ and a HAADF image showing another HAB with a misorientation of 54° ⟨313⟩ are presented in Fig. 5.2a and Fig. 5.2b, respectively. In these two images, comparatively coarse particles are observed along the boundaries. Whereas the chemistry of the particles seen in Fig. 5.2a was not analyzed, EDS data were obtained for the particles seen in Fig. 5.2b.

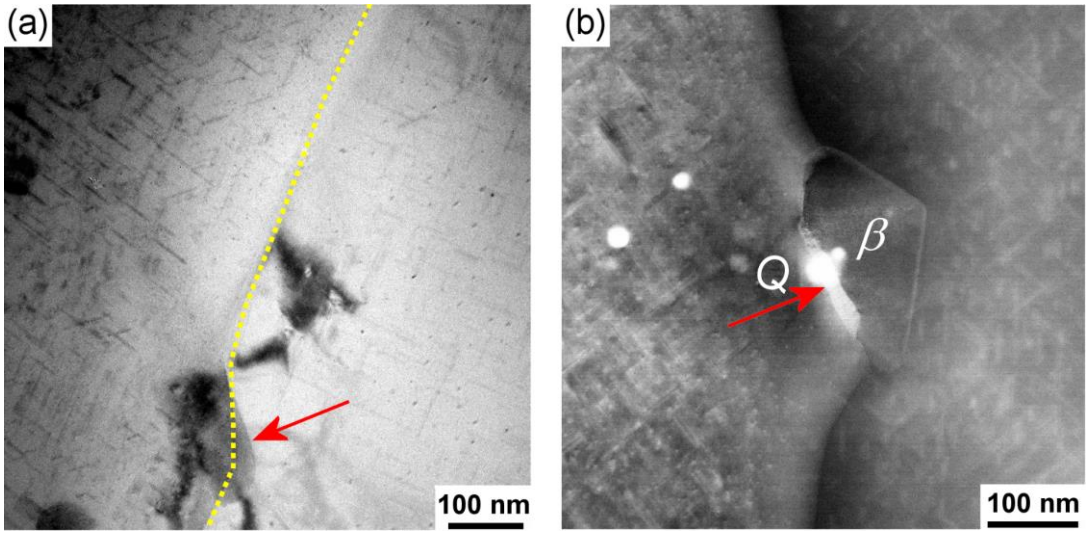

Fig. 5.2. Regions containing random HABs: (a) bright field TEM image where the HAB is marked by the dashed yellow line, while the arrow indicates a comparatively coarse GB particle; (b) HAADF STEM image showing both β and Q particles along the HAB (the *Q* particle is indicated by the arrow). Note a high frequency of fine precipitates present in the grain interiors and the lack of such precipitates in the regions close to the HABs.

Based on these data, one of the particles is identified as Mg_2Si (β-phase particle), and another particle is a Q-phase particle containing high concentrations of Mg, Si, Cu and some Al [1–6]. Furthermore, a large number of characteristic needle-shaped β″ and rod-shaped β′ precipitates are seen in grain interiors, while regions adjacent to these HABs are

free of such precipitates. The width of such precipitate free zones (PFZs) is approximately 0.1 µm. Inspection of several regions in TEM foils indicates that Al(Fe,Mn)Si particles are also present in the microstructure (not seen in Fig. 5.2). Additionally, EDS analysis reveals the presence of thin Cu film along the inspected boundaries (see Fig. 5.3).

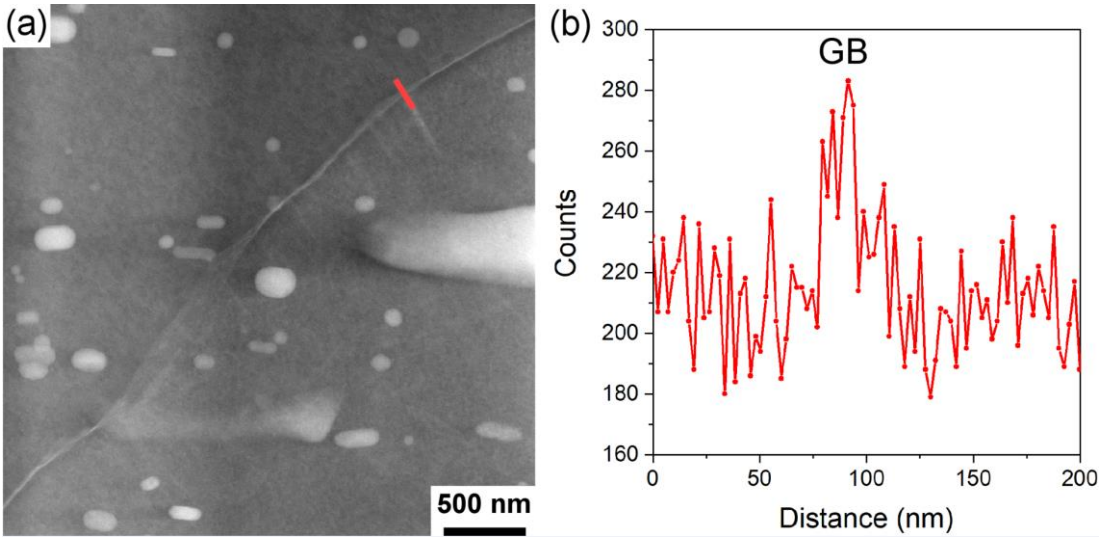

Fig. 5.3. HAADF STEM image (a) and EDS scan data (b) illustrating the presence of Cu film along a grain boundary. Although the exact misorientation across this boundary was not measured, based on variations in the appearance of selected area diffraction patterns observed on both sides across the boundary, this boundary is considered to be a HAB.

Fig. 5.4 shows a HAADF image and elemental maps taken from the Σ3 boundary. The misorientation across this boundary deviates from the exact Σ3 misorientation by 3°. The boundary is slightly curved and contains narrow Q-phase particles as is evident from the EDS analysis. In addition, a Mg_2Si particle was found in a different location along this boundary (not shown in Fig. 5.4). A well-defined PFZ is seen next to this boundary.

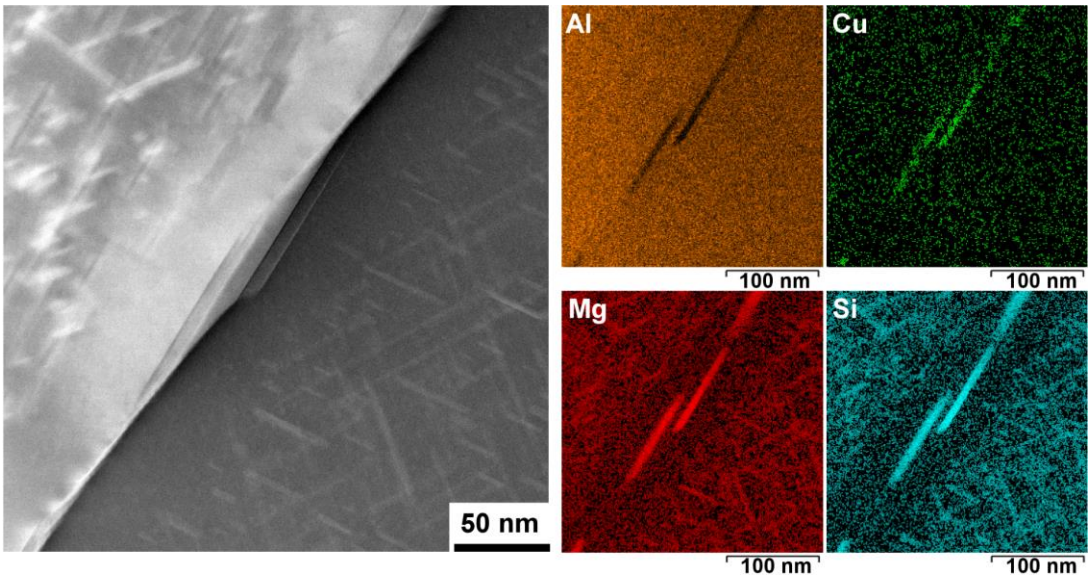

Fig. 5.4. HAADF STEM image and elemental maps taken from a region containing a boundary classified as Σ3. As follows from the elemental maps, several narrow particles along the HAB are *Q* particles. Note the presence of a well-defined PFZ in the vicinity of the boundary.

Finally, HAADF images from two LABs are shown in Fig. 5.5. No GB particles and no PFZ are observed at the LAB with a misorientation angle of 5° (Fig. 5.5a). In contrast, Q-phase and β particles are seen along and in the vicinity of the LAB with a misorientation angle of 12° (Fig. 5.5b). The frequency of β″ and β′ precipitates near this LAB is reduced compared to the frequency of precipitates in the grain interior regions.

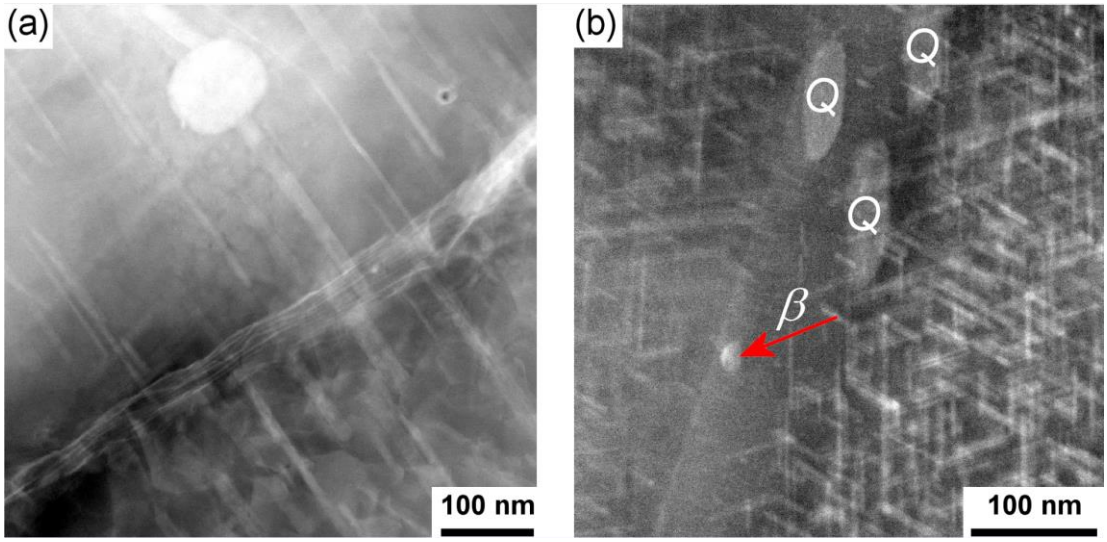

Fig. 5.5. HAADF STEM images of regions containing LABs: (a) boundary with a misorientation angle of 5°; (b) boundary with a misorientation angle of 12° containing several *Q*-phase and β particles.

5.3.3 Statistical SEM-based analysis of intergranular corrosion

To investigate the occurrence of IGC along different boundary types, boundary misorientations in several regions were measured by EBSD and these regions were then inspected after different durations in the corrosive environment. The majority of the boundaries in these regions were random HABs (82.4 %). The remaining 9.1 % and 8.5 % of all boundaries were LABs and Σ3–Σ21 CSL boundaries, respectively.

Example misorientation maps before the corrosion tests and SEM images of the corroded surface are shown in Fig. 5.6. It is seen that most grains in the region presented in Fig. 5.6(a, b) are somewhat smaller than grains in Fig. 5.6(c-f), which suggests that the former region was slightly closer to the immediate surface of the extruded material than the two other regions (see Fig. 5.1). Considering the sample after 90-min exposure to the corrosive solution, only a small number of GBs is affected by IGC (see Fig. 5.6b), and the

depth of IGC attack is limited to ~60 μm (see Fig. 5.7a). A larger number of GBs is found to be corroded after 24 h (Fig. 5.6d).

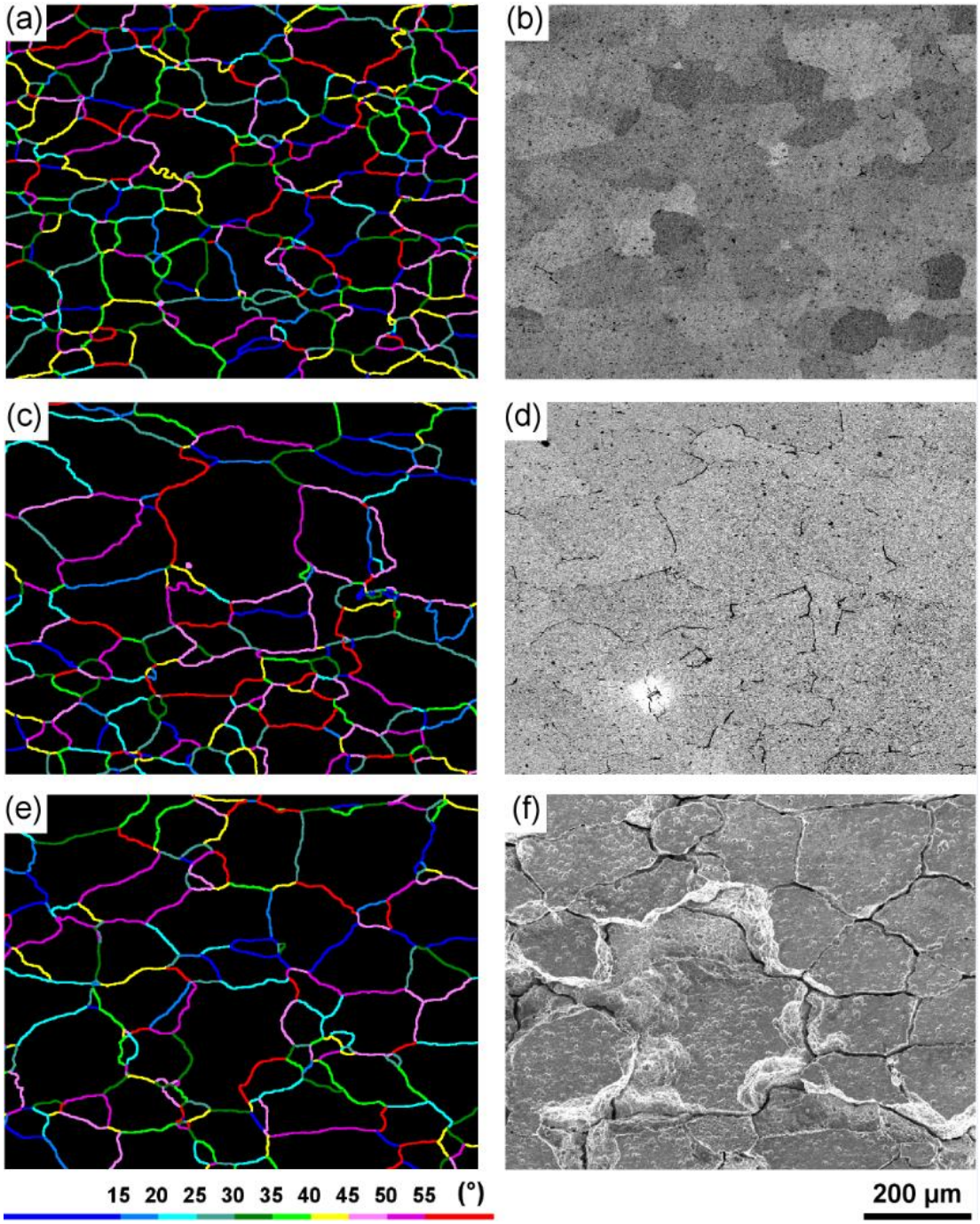

Fig. 5.6. Example regions from the ED-TD plane of the AA6082-T6 plate inspected before and after corrosion tests for different periods of time: (a,b) 90 min; (c,d) 24 h; (e,f) 72 h; (a,c,e) misorientation maps collected using the EBSD technique prior to the corrosion tests. Different colors in these maps correspond to different ranges of misorientation angles shown in the legend;

(b, d, f) BSE images of the same regions after gentle mechanical polishing and exposure to the corrosive solution.

The extent of corrosion along these boundaries is not entirely uniform, with some boundary segments remaining not corroded and other segments being heavily corroded. IGC in this samples is found to propagate to a depth of almost 200 µm (see Fig. 5.7b). Finally, IGC affected almost all GBs in the area investigated after the 72-h exposure. As several grains have fallen out during the 72-h test, the initial specimen surface appears to be drastically modified (cf. Fig. 5.6e and Fig. 5.6f), with boundaries seen below the fallen-out grains in Fig. 5.6f. In some places, the corrosion attack reaches a depth of ~500 µm, i.e. the interior layer. Fig. 5.7c shows that within this layer, IGC propagates predominantly along the ED (see Fig. 5.7c).

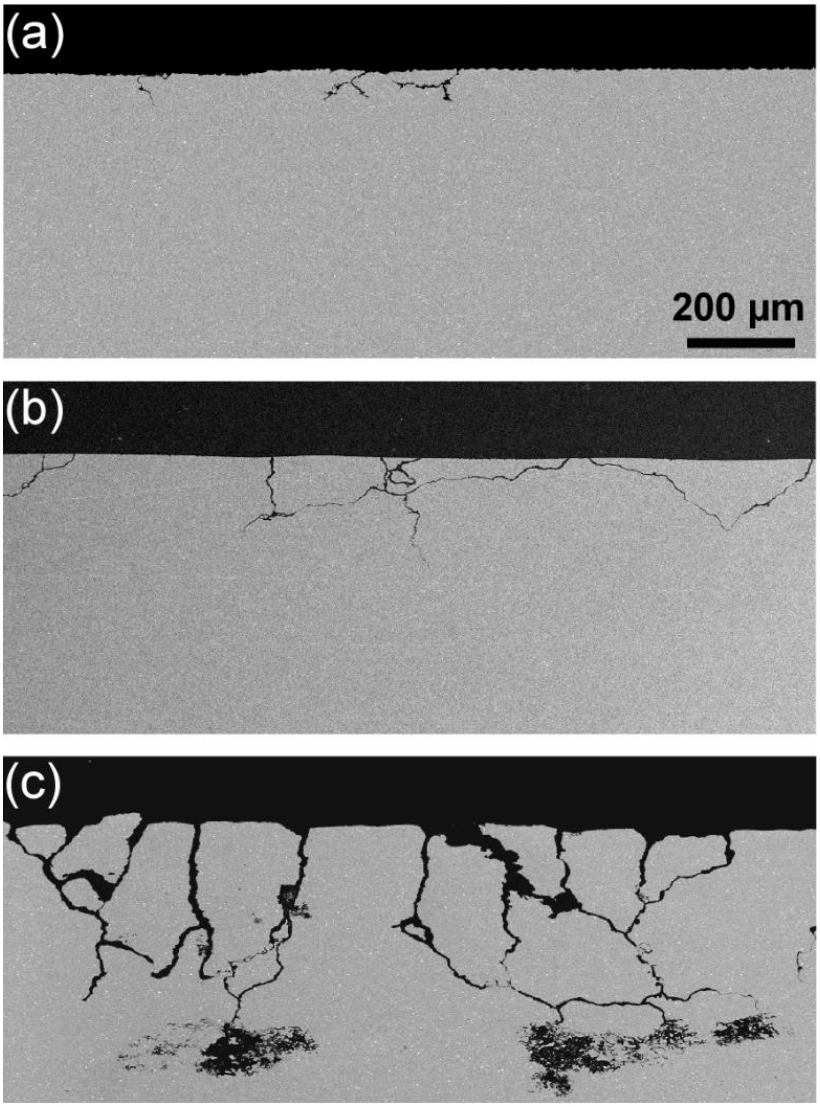

Fig. 5.7. BSE images taken from the ED-ND section of the corroded samples after corrosion tests for different periods of time: (a) 90 min; (b) 24 h; (c) 72 h. The ED is parallel to the scale bar.

Statistical analysis of the GBs affected by IGC during the 90-min test in the corrosive environment indicates that the fraction of corroded boundaries, defined as boundaries with at least one corroded segment, is only ~6 % (Table 5.3). Most of the corroded GBs are random HABs (Fig. 5.8a), with a slightly higher fraction of boundaries having misorientations in the range 45–55° (Fig. 5.8b and Fig. 5.9). As the frequencies of LABs and CSL HABs are rather small in the recrystallized layer, very few such boundaries are affected by IGC in the inspected regions. Comparing fractions of corroded LABs and Σ3–Σ21 CSL boundaries within each group, it is seen that the fraction of corroded LABs is much lower than the fraction of corroded Σ3–Σ21 boundaries (see Table 5.3). Out of 23 Σ3 boundaries in the regions inspected after the 90-min test, 4 boundaries (~17 %) are found to be partially corroded. It should be emphasized that each Σ3 boundary in the present material exhibited some curvature over its length, i.e. these Σ3 boundaries did not demonstrate the characteristic twin morphology.

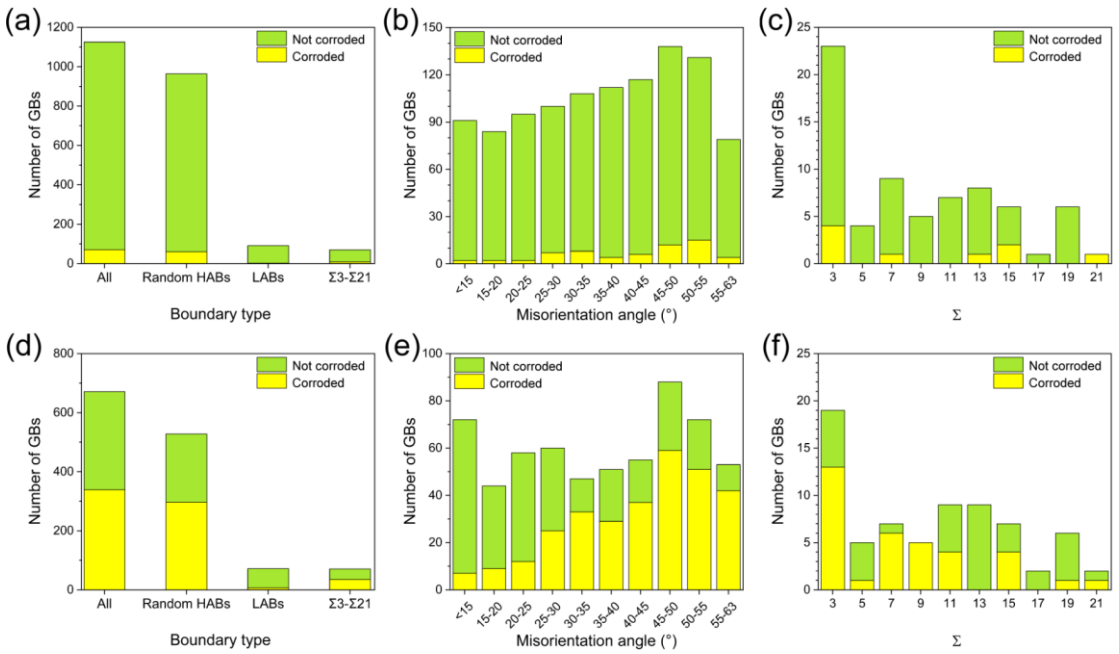

Fig. 5.8. Distributions of corroded and not corroded boundaries in the samples after the 90-min (a, b, c) and 24-h (d, e, f) corrosion tests sorted by the boundary type (a, d), by the misorientation angle (b, e) and by the Σ value (c, f). Note that Σ3–Σ21 boundaries are not included in (b, e).

In the regions inspected after the 24-h test, ~51 % of all GBs are corroded (see Table 5.3). Random HABs appear to be more affected by IGC than the other boundary types (Table 5.3 and Fig. 5.8d). For the random HABs, the fraction of corroded boundaries is 56 %. Within this group of boundaries, the susceptibility to IGC tends to increase rapidly with increasing misorientation angle to 30–35°, after which the fraction of corroded

boundaries levels off (see Fig. 5.8e and Fig. 5.9). Many CSL HABs are also susceptible to IGC, with 49 % of these boundaries being corroded. The most frequently corroded CSL boundary types are Σ3, Σ7 and Σ9, while Σ5, Σ13, Σ17 and Σ19 boundaries are corroded either less frequently or not at all (see Fig. 5.8f). Only 10 % of all LABs are corroded. Thus, LABs are clearly more corrosion resistant than both CSL and random HABs after 24 h in the acidified salt solution. No boundaries with misorientations less than 10° are found to be corroded after the 24-h test.

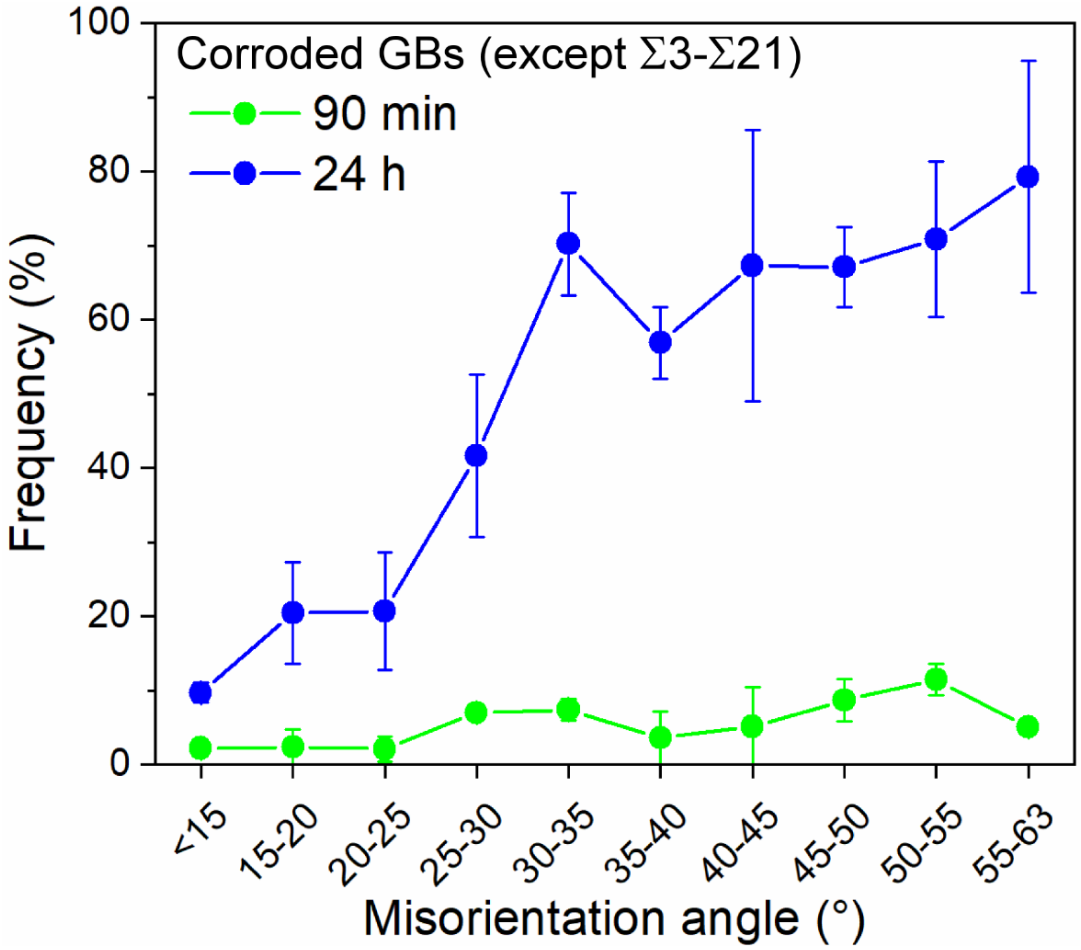

Fig. 5.9. Summed fraction of corroded LABs and random HABs after the 90-min and 24-h corrosion tests as a function of misorientation angle. Error bars correspond to the standard deviation.

The fraction of corroded boundaries after the 72-h test is 99.2 % (see Table 5.3). Out of 359 boundaries analyzed after this test, only two LABs and one Σ13 boundary are not affected by corrosion.

Table 5.3. Fractions (%) of corroded boundaries within different groups of boundaries

Test duration	LABs	Random HABs	Σ3–Σ21 boundaries	Only Σ3 boundaries	All boundaries
90 min	2.2	6.2	12.8	17.4	6.3
24 h	9.7	56.2	49.3	68.4	50.5
72 h	93.8	100	97.6	100	99.2

5.4 Discussion

The microstructure of the surface layer directly exposed to the corrosive environment is of key importance in the present work. As shown in Fig. 5.1, the surface layer is recrystallized, and is thus very different from the interior layer containing the hot-deformed microstructure. Moreover, within the recrystallized layer the grain size increases with increasing distance from the surface. Obviously, the microstructural heterogeneities of the as-received material are caused by a highly non-uniform distribution of strain during deformation [20–23]. During extrusion, layers close to the immediate surface undergo a high shear strain, which decreases with increasing distance from the surface. Thus, the total strain and the stored energy at the surface are much higher compared to those in the interior layers. The high stored energy provides a driving force for recrystallization, which takes place right after extrusion when the material is still hot. The variation in the total strain also affects the frequency of recrystallization nuclei within the surface layer. As the recrystallized grains are much smaller at the immediate surface than at larger depths in the recrystallized layer (see Fig. 5.1), it is concluded that the frequency of recrystallization nuclei was higher near the immediate surface and decreased with increasing depth. The presence of a high shear strain before recrystallization is also substantiated by the observation of the shear $\{001\}\langle 110\rangle$ component in the recrystallization texture of the surface layers (see Table 5.2). It has been shown that even a small fraction of this shear texture component in the deformed material may be sufficient to develop a pronounced $\{001\}\langle 110\rangle$ component during recrystallization [23]. While the fraction of the $\{001\}\langle 110\rangle$ component in the surface layer is significant, 21 % (Table 5.2), the majority of orientations in this layer do not belong to any standard texture components, i.e. a large number of recrystallized grains have random orientations and are surrounded by random HABs.

TEM-based analysis indicates that the random HABs are decorated by Q- and β-phase particles (see Fig. 5.2) and that many inspected boundaries contain Cu film (Fig. 5.3). The latter observation is significant as no Cu film was previously found in the AA6082-T6 alloy with 0.06 wt% Cu investigated by Zhang et al. [8,9]. The presence of the Cu film and particles along such HABs can be attributed to high GB energies promoting segregation of alloying elements. The formation of the film and GB particles causes solute depletion in regions near GBs, which, in combination with vacancy depletion [24], results in PFZs. Since the Cu film and Cu-rich Q particles as well as Si-rich β particles after selective dissolution of Mg are cathodic in respect to PFZs [25,26], microgalvanic coupling is expected to occur, leading to pronounced IGC in the investigated material. This interpretation is consistent with many reports where both Cu film and *Q* particles were considered to provoke IGC [1–5], although there is an alternative view suggesting that *Q* particles unconnected by Cu film act as temporary barriers against IGC propagation [27,28].

As the GB particles and the film are not uniformly distributed along GBs, IGC at individual boundaries may also be not uniform, which results in the presence of partially corroded boundaries (see SEM images in Fig. 5.6). It is interesting that the fraction of boundaries affected by IGC during the 24-h test remains small in the medium angle range (15–25°) and increases with increasing misorientation angle to 35° (Fig. 5.9), which correlates with a general increase in the GB energy in this angular range [29].

Comparing IGC along random and CSL HABs, no significant differences in the fraction of corroded boundaries are observed between these two groups (see Table 5.3). This observation is different from those reported for an Al-Mg alloy, where all $\Sigma \leq 29$ [11] were considered to be more resistant to corrosion attack than other HABs. In the present study, only four CSL types ($\Sigma 5$, $\Sigma 13$, $\Sigma 17$ and $\Sigma 19$) show comparatively good resistance to IGC in the 90-min and 24-h tests. It is possible that some of these CSL boundaries are symmetric tilt boundaries with reduced energies [29,30] and hence with reduced susceptibility to segregate Cu and other alloying elements. The $\Sigma 5$, $\Sigma 13$, $\Sigma 17$ and $\Sigma 19$ boundaries are, however, so rare in the present material (in total, 2.6 % of all boundaries) that they can hardly affect the overall resistance to IGC.

Furthermore, the present study provides clear evidence that boundaries identified as $\Sigma 3$ in our material are not more corrosion resistant than random HABs. It should be noted that the maximum allowable deviation from the exact $\Sigma 3$ relationship defined by the

Brandon criterion is rather broad, $\Delta\theta_m$= 8.66°. Therefore, boundaries classified as Σ3 are not necessarily true twin boundaries. It is indicative that in contrast to twin boundaries characterized by an easily recognizable straight morphology and small deviations $\Delta\theta$ from the exact Σ3 misorientation (typically $\Delta\theta < 2°$) [31], the Σ3 boundary shown in Fig. 5.4 demonstrates some curvature with a considerable deviation $\Delta\theta$=3°. Based on the boundary morphology and the large deviation from the exact Σ3 relationship, it is concluded that this boundary is not a coherent twin boundary. The energy for such non-twin Σ3 boundaries may be similar to that of random HABs, which can result in GB segregation, formation of GB particles and PFZ (see Fig. 5.4), and hence in IGC.

To examine deviations from the exact 60° ⟨111⟩ misorientation in a statistical manner, $\Delta\theta$ was calculated for each Σ3 boundary in the EBSD data from the recrystallized layer. This information is presented in Fig. 5.10a as the distribution of $\Delta\theta$ normalized by the maximum allowable deviation θ_m. It is seen that the distribution is broad and that there is only one boundary with a small deviation from the exact Σ3 misorientation ($\Delta\theta$=1.6° and $\Delta\theta/\theta_m$=0.2). This boundary is curved and is found to be corroded after the 24-h corrosion test (Fig. 5.11). Therefore, a small deviation from the ideal Σ3 misorientation does not guarantee the twin morphology and improved corrosion resistance for the present alloy. The other boundaries classified as Σ3 are characterized by large deviations, with the majority of $\Delta\theta$ in the range 6–8.5°, and are also curved. The fact that most Σ3 boundaries in the investigated alloy demonstrate large deviations from the exact Σ3 misorientation and that they are morphologically different from boundaries of annealing twins suggests that these Σ3 boundaries do not have special properties. It is therefore not surprising that their corrosion resistance is similar to that of random HABs (see Table 5.3).

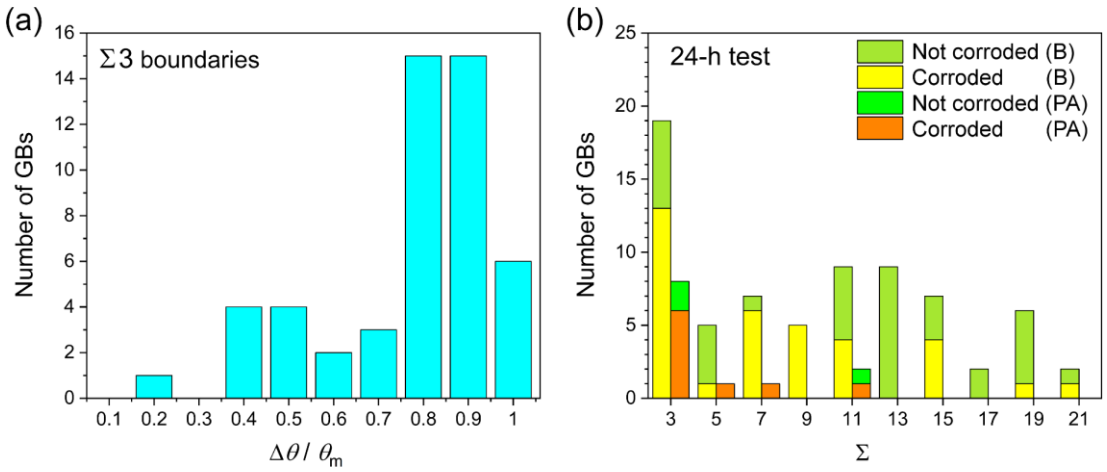

Fig. 5.10. The effect of allowable deviations $\Delta\theta$ from the exact CSL misorientations on the number of CSL boundaries: (a) distribution of normalized deviations from the exact Σ3 relationship for all boundaries classified as Σ3 according to the Brandon criterion; (b) numbers of HABs classified as CSL using either the Brandon (B) criterion or Palumbo-Aust (PA) criterion in the 24-h sample.

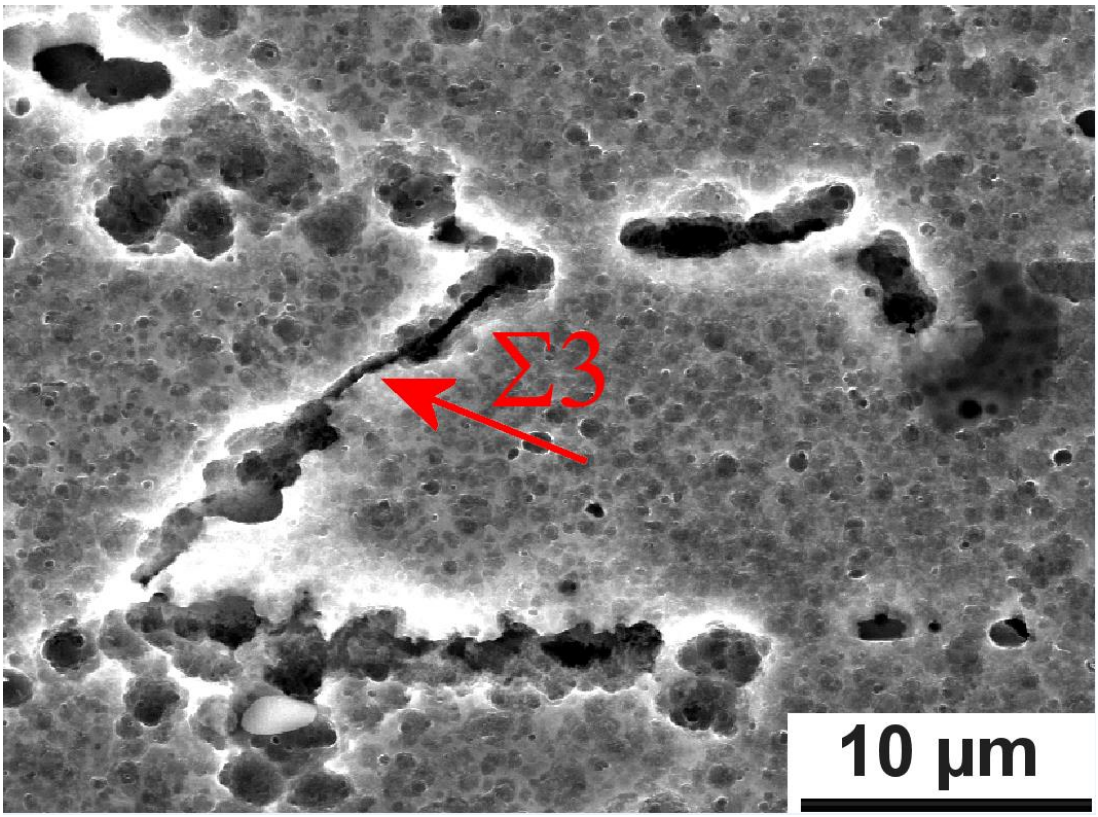

Fig. 5.11. Secondary electron image taken after the 24-h corrosion test from a region containing one boundary with a small deviation ($\Delta\theta = 1.6°$) from the exact Σ3 misorientation. Despite the small deviation, this Σ3 boundary is corroded.

According to Refs. [10,32], a more restrictive criterion $\Delta\theta_m = 15° \Sigma^{-5/6}$ is better suited for identifying corrosion-resistant boundaries in face-centered cubic materials. If this criterion is applied to our data set, the fraction of Σ3–Σ21 boundaries becomes negligibly

small (1.5 %). As an example, numbers of CSL boundaries identified in the 24-h test sample using both the Brandon criterion and the criterion proposed by Palumbo and Aust (PA) [32] are shown in Fig. 5.10b. It is seen that the PA criterion decreases the total number of boundaries classified as CSL. Nevertheless, even this criterion fails to establish a clear correlation between the Σ value and resistance to IGC for our material. This lack of correlation is likely related to the fact that the CSL approach does not take into account the boundary plane orientation, which is also an important parameter in determining the extent of GB precipitation and therefore the extent of IGC [16,33].

For the present material, only one group of boundaries, namely, LABs are found to be consistently more corrosion-resistant than any other boundary type. LABs are low energy boundaries and hence are usually considered less prone to GB segregation than HABs [13]. Even when particles are present along some LABs, such as that shown in Fig. 5.5b, no well-developed PFZ is formed along these LABs. The absence of well-developed PFZs slows down the electrochemical reaction between β particles along LABs and the adjacent regions with a high frequency of β′ and β″ precipitates. However, if Cu-rich *Q* particles (with a more positive corrosion potential) precipitate along LABs, microgalvanic coupling will occur between the cathodic Q particles and adjacent anodic regions, leading to preferential dissoluti½on of the anodic regions. Although no statistical analysis of different types of precipitates along LABs can be provided in this work because of the low frequency of LABs in the recrystallized layer, the fraction of LABs containing particles in the present material is expected to be small. For example, only less than 10 % of all LABs were found to be decorated with particles in the AA6082-T6 alloy with 0.06 wt% Cu [9]. It is also indicative that the percentage of corroded LABs is lower than that of any other boundary type even in the most corroded sample exposed to the test solution for 72 h (see Table 5.3). On the other hand, the observation of pronounced IGC in the interior layer after the 72-h test (Fig. 5.7c) implies that a high LAB fraction alone is not sufficient for good resistance against IGC. In fact, active propagation of IGC in the interior layer can occur along closely spaced HABs despite the high fraction of LABs (Table 5.2).

Based on the results obtained in the present experiment, it is anticipated that heat treatments resulting in surface layers with sufficiently large recrystallized grains and high fractions of LABs prior to aging can be used to effectively improve corrosion resistance of Al-alloys. For instance, high fractions of LABs can be obtained by forming a strong

annealing texture dominated by a single texture component. In particular, strong textures and high frequencies of LABs can be obtained during grain growth in samples with a pronounced recrystallization texture [34,35].

5.5 Conclusions

The microstructure and intergranular corrosion in the acidified salt solution have been studied in an extruded and aged Al-Mg-Si alloy doped with 0.05 wt% Cu. The following conclusions are drawn from this study:

1) EDS analysis shows the presence of Cu film along grain boundaries. Furthermore, comparatively coarse β and Q particles are present along each inspected boundary, except for a LAB with a misorientation angle of 5°. There is no observable change in the frequency of β″ and β′ precipitates in the vicinity of this LAB as compared to the frequency of such precipitates in grain interior regions. In contrast, a reduced frequency of precipitates is observed near a LAB with a misorientation angle of 12°. Well-defined PFZs are seen in the vicinity of the inspected random HABs and Σ3 boundary.
2) Intergranular corrosion takes place in this alloy despite the low Cu content. The surface layer demonstrates evidence of intergranular corrosion already after 90 min of exposure to the corrosive solution, with ~6 % of all analyzed grain boundaries being partially or fully corroded. As the duration of exposure increases to 24 h and 72 h, the fraction of corroded boundaries increases to 51% and 99 %, respectively. Furthermore, the depth of IGC attack increases from ~60 μm to ~500 μm after exposure for 90 min and 72 h, respectively.
3) Comparing IGC along random and CSL HABs, no significant differences in the fraction of corroded boundaries are observed between these two groups though several CSL boundaries (Σ5, Σ13, Σ17 and Σ19) show comparatively good resistance to IGC in the 90-min and 24-h tests. Boundaries classified as Σ3 do not exhibit twin morphology and better corrosion resistance in the present material. Most of these boundaries are characterized by large deviations from the exact Σ3 misorientation. Only LABs with misorientations below 10° are consistently found to be more corrosion-resistant than any other boundary type.

CRediT authorship contribution statement

Emad H. Bartawi: Conceptualization, Methodology, Investigation, Formal analysis, Writing - Original Draft, **Oleg V. Mishin:** Writing - Original Draft, Investigation, Formal analysis, **Ghada Shaban:** Writing - Review & Editing, Formal analysis, **Jan H. Nordlien:** Writing - Review & Editing, **Rajan Ambat:** Conceptualization, Supervision, Writing - Review & Editing, Project administration, Funding acquisition.

Declaration of Competing Interest

The authors declare that they have no known competing financial interests or personal relationships that could have appeared to influence the work reported in this paper.

Acknowledgements

The authors would like to thank Hydro Aluminium, Norway, for providing material. The authors also thank Dr. J. Kling from DTU Nanolab for his technical assistance during STEM experiments and Mr. K.V. Werner for providing a code for calculating number fractions of grain boundaries from EBSD data. EHB and RA acknowledge funding from the Independent Research Fund Denmark (grant number 9041- 00240A).

Data availability

The raw/processed data required to reproduce these findings cannot be shared at this time as the data also forms part of an ongoing study.

References

[1] G. Svenningsen, J. Erik, A. Bjørgum, J. Halvor, Y. Yu, K. Nisancioglu, Effect of low copper content and heat treatment on intergranular corrosion of model AlMgSi alloys, *Corros. Sci.* 48 (2006) 226–242. doi: 10.1016/j.corsci.2004.11.025.

[2] G. Svenningsen, M.H. Larsen, J. Lein, J. Nordlien, K. Nisancioglu, Intergranular Corrosion of Extruded AA6000-Series Model Alloys, *Proc. 9th Int. Conf. Alum. Alloy*. (2004) 818–824.

[3] H. Zhan, J.M.C. Mol, F. Hannour, L. Zhuang, H. Terryn, J.H.W. De Wit, The influence of copper content on intergranular corrosion of model AlMgSi (Cu) alloys, *Mater. Corros.* 59 (2008) 670–675, doi: 10.1002/maco.200804110.

[4] Y. Zou, Q. Liu, Z. Jia, Y. Xing, L. Ding, X. Wang, The intergranular corrosion behavior of 6000-series alloys with different Mg/Si and Cu content, *Appl. Surf. Sci.* 405 (2017) 489–496. doi: 10.1016/j.apsusc.2017.02.045.

[5] G. Svenningsen, M. H. Larsen, J.C Walmsley, J. H. Nordlien, K. Nisancioglu, Effect of artificial aging on intergranular corrosion of extruded AlMgSi alloy with small Cu content, *Corros. Sci*. *48* (2006) 1528–1543, doi: 10.1016/j.corsci.2005.05.045.

[6] G. Svenningsen, M. H. Larsen, J. H. Nordlien, K. Nisancioglu, Effect of thermomechanical history on intergranular corrosion of extruded AlMgSi (Cu) model alloy, *Corros. Sci*. *48* (2006) 3969–3987, doi: 10.1016/j.corsci.2006.03.018.

[7] M.H. Larsen, J.C. Walmsley, O. Lunder, K. Nisancioglu, Effect of excess silicon and small copper content on intergranular corrosion of 6000-series aluminum alloys, ***J. Electrochem. Soc.*** 157 (2010) C61. doi: 10.1149/1.3261804.

[8] X. Zhang, X. Zhou, J.O. Nilsson, Corrosion behaviour of AA6082 Al-Mg-Si alloy extrusion: The influence of quench cooling rate, *Corros. Sci.* 150 (2019) 100–109, doi: 10.1016/j.corsci.2019.01.030.

[9] X. Zhang, Y. Lv, T. Hashimoto, J.-O. Nilsson, X. Zhou, Intergranular corrosion of AA6082 Al–Mg–Si alloy extrusion: The influence of trace Cu and grain boundary misorientation, *J. Alloys Compd.*,853 (2021) 157228, doi:

10.1016/j.jallcom.2020.157228.

[10] S.H. Kim, U. Erb, K.T. Aust, G. Palumbo, Grain boundary character distribution and intergranular corrosion behavior in high purity aluminum, *Scr. Mater*. 44 (2001) 835–839. doi: 10.1016/S1359-6462(00)00682-5.

[11] J. Yan, N.M. Heckman, L. Velasco, A.M. Hodge, Improve sensitization and corrosion resistance of an Al-Mg alloy by optimization of grain boundaries, *Sci. Rep*. 6 (2016) 1–10, doi: 10.1038/srep26870.

[12] L.H. Chan. H. Weiland, S. Cheong, G.S. Rohrer, A. D. Rollett, The correlation between grain boundary character and intergranular corrosion susceptibility of 2124 aluminum alloy, in: *Applications of Texture Analysis*, ed. A.D. Rollett (2008) 261–267, doi: 10.1002/9780470444214.ch28.

[13] T. Minoda, H. Yoshida, Effect of grain boundary characteristics on intergranular corrosion resistance of 6061 aluminum alloy extrusion, *Metall. Mater. Trans. A* 33 (2002) 2891–2898, doi: 10.1007/s11661-002-0274-3.

[14] A. Lervik, S. Wenner, O. Lunder, C.D. Marioara, R. Holmestad, Grain boundary structures and their correlation with intergranular corrosion in an extruded Al-Mg-Si-Cu alloy, *Mater. Charact*. 170 (2020) 110695, doi: 10.1016/j.matchar.2020.110695.

[15] X. Zhang, Y. Lv, T. Hashimoto, J.-O. Nilsson, X. Zhou, Intergranular corrosion of AA6082 Al–Mg–Si alloy extrusion: The influence of trace Cu and grain boundary misorientation, *J. Alloys Compd.* 853 (2021) 157228, doi: 10.1016/j.jallcom.2020.157228.

[16] A.J. Davenport, Y. Yuan, R. Ambat, B.J. Connolly, M. Strangwood, A. Afseth, G.M. Scamans, Intergranular corrosion and stress corrosion cracking of sensitised AA5182, *Mater. Sci. Forum* 519–521 (2006) 641–646, doi: 10.4028/www.scientific.net/MSF.519-521.641.

[17] H.-E. Ekström, T. Furu, O.V. Mishin, T. Pettersen, B. Olsson, Mechanical properties, texture and microstructure of flat AA6063 and AA6082 profiles, *Aluminium* 78

(2002) 930–937.

[18] BS EN ISO 11846:2008, Corrosion of metals and alloys. Determination of resistance to intergranular corrosion of solution heat-treatable aluminium alloys, *British Standards Institution* (2005).

[19] D.G. Brandon, The structure of high-angle grain boundaries, *Acta Metall.* 14 (1966) 1479–1484. doi: 10.1016/0001-6160(66)90168-4.

[20] S.E. Schoenfeld, R.J. Asaro, Through thickness texture gradients in rolled polycrystalline alloys, *Int. J. Mech. Sci.* 38 (1996) 661–683. doi: 10.1016/S0020-7403(96)80008-7.

[21] O. Engler, M.Y. Huh, C.N. Tomé, A study of through-thickness texture gradients in rolled sheets, *Metall. Mater. Trans. A* 31 (2000) 2299–2315, doi: 10.1007/s11661-000-0146-7.

[22] F. Pérocheau, J.H. Driver, Texture gradient simulations for extrusion and reversible rolling of FCC metals, *Int. J. Plast.* 16 (2000) 73–89, doi: 10.1016/S0749-6419(99)00048-0.

[23] L.F. Shuai, T.L. Huang, G.L. Wu, G. Winther, X. Huang, O.V. Mishin, Unusual through-thickness variations of microstructure and texture in heavily rolled and annealed Al–0.3%Cu, *Mater. Charact.* 162 (2020) 661–683, doi: 10.1016/j.matchar.2020.110173.

[24] S.C. Jha, T.H. Sanders Jr., M.A. Dayananda, Grain boundary precipitate free zones in Al-Li alloys. *Acta Metall*. 35 (1987) 473-482, doi: 10.1016/0001-6160(87)90253-7.

[25] F. Eckermann, T. Suter, P.J. Uggowitzer, A. Afseth, P. Schmutz, The influence of MgSi particle reactivity and dissolution processes on corrosion in Al–Mg–Si alloys, *Electrochim. Acta* 54 (2008) 844–855, doi: 10.1016/j.electacta.2008.05.078.

[26] F. Zeng, Z. Wei, J. Li, C. Li, X. Tan, Z. Zhang, Z. Zheng, Corrosion mechanism associated with Mg_2Si and Si particles in Al–Mg–Si alloys, *Trans. Nonferrous Met. Soc. China* 21 (2011) 2559–2567, doi: 10.1016/S1003-6326(11)61092-3.

[27] K. Shimizu, K. Nisancioglu, High resolution SEM investigation of intercrystalline corrosion on 6000-series aluminum alloy with low copper content, *ECS Electrochem. Lett*. (2014) 3 C29, doi: 10.1149/2.0041409eel.

[28] S. Kumari, S. Wenner, J.C. Walmsley, O. Lunder, K. Nisancioglu, Progress in understanding initiation of intergranular corrosion on AA6005 aluminum alloy with low copper content, *J. Electrochem. Soc.* 166 (2019) C3114–C3123, doi: 10.1149/2.0211911jes.

[29] D.L. Olmsted, S.M. Foiles, E.A. Holm, Survey of computed grain boundary properties in face-centered cubic metals: I. Grain boundary energy, *Acta Mater.* 57 (2009) 3694–3703, doi: 10.1016/j.actamat.2009.04.007.

[30] S. Kiyohara, H. Oda, T. Miyata, T. Mizoguchi, Prediction of interface structures and energies via virtual screening, *Sci. Adv.* 2 (2016) e1600746, doi: 10.1126/sciadv.1600746.

[31] O.V. Mishin, X. Huang, TEM study of twin segments in annealed copper, *Mater. Sci. Forum* 294–296 (1999) 401–404, doi: 10.4028/www.scientific.net/MSF.294-296.401.

[32] G. Palumbo, K.T. Aust, Structure-dependence of intergranular corrosion in high purity nickel, *Acta Metall. Mater.* 38, (1990) 2343–2352. doi: 10.1016/0956-7151(90)90101-L.

[33] Y. Zhao, M.N. Polyakov, M. Mecklenburg, M.E. Kassner, A.M. Hodge, The role of grain boundary plane orientation in the β phase precipitation of an Al–Mg alloy, *Scr. Mater.* 89 (2014) 49–52, doi: 10.1016/ j.scriptamat.2014.07.003.

[34] H. Tian, H.L. Suo, O.V. Mishin, Y.B. Zhang, D. Juul Jensen, J.-C. Grivel, Annealing behaviour of a nanostructured Cu–45 at.%Ni alloy, *J. Mater. Sci.* 48 (2013) 4183–4190, doi: 10.1007/s10853-013-7231-y.

[35] H. Tian, H.L. Suo, A.C. Wulff, J.-C. Grivel, O.V. Mishin, D. Juul Jensen, Comparative characterization of Cu–Ni substrates for coated conductors, *J. Alloys Compd.* 601 (2014) 9–13, doi: 10.1016/j.jallcom.2014.02.114.

6. Paper II

The effect of trace level copper content on intergranular corrosion of extruded AA6082-T6 alloys

E.H. Bartawi [1,*], O.V. Mishin [1], G. Shaban [1], F. Grumsen [1], J.H. Nordlien [2], R. Ambat [1]

[1] Department of Civil and Mechanical Engineering, Technical University of Denmark, Kgs. Lyngby 2800, Denmark

[2] Hydro Innovation & Technology, Hydrovegen 160, 4265 Håvik, Norway

[*]Corresponding author: ehaba@dtu.dk

Abstract

The effect of trace level Cu content on intergranular corrosion in an acidified salt solution has been systematically studied in four AA6082-T6 extrusions containing 0.001, 0.02, 0.03 and 0.05 wt% Cu. Although these Cu concentrations are smaller than those expected to directly contribute to intergranular corrosion (IGC) in aged AA6082 alloys, IGC is observed in the present experiment even in alloy with the lowest Cu content. Whereas the extent of IGC is negligibly small in the alloy containing 0.001 wt% Cu, it increases with increasing Cu content. Profound IGC is observed in the alloy containing 0.05 wt% Cu. Microstructural characterization reveals Cu segregations along some grain boundaries in each alloy. There are, however, differences in the size and number density of precipitates as well as in the width of precipitate free zones between the different samples.

E.H. Bartawi, O.V. Mishin, G. Shaban, F. Grumsen, J.H. Nordlien, R. Ambat, The effect of trace level copper content on intergranular corrosion of extruded AA6082-T6 alloys, Mater. Chem. Phys. (2023) 128303, https://doi.org/10.1016/j.matchemphys.2023.128303.
The format of the published paper was adapted to match the format of the Ph.D. thesis.

6.1 Introduction

Heat-treatable Al-Mg-Si (6xxx-series) alloys are extensively used in construction, automotive and aerospace industries due to their high strength-to-weight ratio, good formability and generally good corrosion resistance [1,2]. Copper in these alloys is either intentionally added to improve mechanical properties or can be present as a trace element in recycled aluminum. While Cu increases the mechanical strength of Al-Mg-Si alloys, it may have detrimental effects on their resistance to intergranular corrosion (IGC) [3–11]. These effects strongly depend on the Cu content in the alloy composition. For example, comparing corrosion in several 6xxx alloys with 0.02, 0.18 and 0.7 wt% Cu tested in an acidified salt solution (standard BS ISO 11846(method B) [12]), Larsen et al. [7] found that the alloy with 0.02 wt% Cu was resistant to IGC, whereas samples with higher concentrations of Cu were susceptible to IGC. The IGC in these alloys was provoked by segregation of Cu along grain boundaries (GBs) and by formation of precipitate free zones (PFZs) near GBs, which resulted in microgalvanic coupling between PFZs and cathodic Cu-rich films [7]. Similarly, Svenningsen et al. [8,9] reported that aged Al-Mg-Si alloys with 0.0005 and 0.02 wt% Cu were resistant to IGC, while alloys with 0.12 and 0.17 wt% Cu exhibited IGC in the acidified salt solution. Thermal processing was found to play an important role in controlling IGC of these alloys. In particular, post-extrusion water-quenching of the alloys with 0.12 wt% Cu and 0.17 wt% Cu improved their resistance to IGC compared to air-cooled samples with same Cu content. The poorer IGC resistance in the air-cooled samples was attributed to the presence of Cu-rich films and/or Q-phase particles along GBs [8–10]. The susceptibility to IGC in the air-cooled samples decreased after artificial (peak) aging [10], indicating that in alloys with comparatively high Cu content (> 0.1 wt%) IGC can effectively be controlled through thermomechanical processing. The influence of thermal treatments on the susceptibility to IGC was also considerable in an alloy with 0.004 wt% Cu and an excess amount of Si [11]. In this alloy, no IGC was revealed in a sample naturally aged after solution heat treatment (SHT) followed by water-quenching, whereas all other tested conditions demonstrated some evidence of IGC regardless of the cooling rate [11]. In contrast, Zhang et al. [13] found that AA6082 with 0.06 wt% Cu air-cooled after SHT was more resistant to IGC than a water-quenched condition [13]. Marioara et al. [14] showed that the susceptibility to IGC after water-quenching could vary depending on the aging temperature. These authors also

showed that low-strain rolling prior to aging improved the resistance to IGC of AA6005A due to an increased number of Cu-containing particles precipitated at dislocations, which reduced the amount of Cu segregated at GBs [14].

The concentration of Mg and Si in Al-Mg-Si-(Cu) alloys is another factor affecting their IGC resistance. According to Zou et al. [4], although the concentration of Cu was of primary importance for IGC resistance, the susceptibility to IGC was also affected by the Mg/Si ratio. In particular, for alloys containing 0.14 wt% Cu, a sample with a higher Mg/Si ratio (2.13) showed predominantly pitting corrosion, whereas a sample with a lower Mg/Si ratio (0.55) demonstrated significant IGC [4]. Pronounced IGC along high angle GBs was also observed in aged AA6082 samples with either 0.05 wt% Cu or 0.06 wt% Cu and with Mg/Si ratios of 0.67 and 0.62, respectively [15,16].

Summarizing the previous observations of IGC tested according to the BS ISO 11846 standard [12], it appears that 6xxx-series alloys with copper content of at least 0.05 wt% Cu are generally prone to IGC though the negative effect of copper can be mitigated by appropriate thermomechanical treatments and increased Mg/Si ratios. Al-Mg-Si alloys with Cu ≤ 0.05% wt% are typically reported to be either resistant to IGC or demonstrating insignificant IGC. In one study [17], IGC was observed in aged 6xxx-series alloys with only 0.001 wt% Cu. However, IGC tests in this study were conducted using a different standard [18] utilizing a short exposure to concentrated HNO_3 followed by a long exposure to a salt solution. As no Cu film and no Q-phase particles were observed in the microstructure, IGC in these alloys was attributed to microgalvanic coupling between PFZs and grain boundary Mg_2Si precipitates [17]. In a study of an aged Al-Mg-Si alloy with 0.03 wt% Cu tested using the ASTM G110-92 standard, corrosion was reported to be insignificant and occurred predominantly in the form of pitting [19]. Apparently, the use of different testing procedures can affect the extent of IGC, which is additional factor complicating the comparison of IGC in the 6xxx alloys with small Cu content.

The purpose of the present work is to systematically investigate the effects of Cu in the range 0.001–0.05 wt% on the microstructure and IGC of four AA6082-T6 alloys tested according to Ref.[12]. To ensure that IGC is not affected by varying concentrations of Mg and Si, the Mg/Si ratio is maintained almost constant (~0.67) in the alloys prepared for this study. The microstructure of the as-received samples is investigated in this work using optical microscopy, scanning electron microscopy (SEM), transmission electron microscopy (TEM), energy dispersive spectroscopy (EDS) and the electron backscatter

diffraction (EBSD) technique. The extent and penetration depth of IGC are characterized based on SEM and X-ray microscopy (XRM). Therefore, the analysis of IGC in this work benefits from a combination of 2D and 3D characterization techniques.

6.2 Experimental

6.2.1 Material

Four AA6082 ingots with different concentrations of copper (Table 6.1) were produced to simulate varying compositions of Al-Mg-Si alloys manufactured using recycled aluminum. The as-cast ingots were homogenized at 575°C and cooled to room temperature at a rate of 350°C/h. The material was then hot extruded into 4-mm-thick flat profiles. The extruded material was water-quenched, stretched 0.5 % and artificially peakaged using a two-step aging process. The obtained temper is defined as T6 by Hydro Aluminium.

Table 6.1. Chemical composition (wt%) of AA6082-T6 samples used in this study

Sample	Cu	Mg	Si	Fe	Zn	Mn	Al
1	0.001	0.647	0.968	0.219	0.003	0.544	Bal.
2	0.017	0.644	0.965	0.218	0.003	0.545	Bal.
3	0.034	0.644	0.968	0.219	0.003	0.541	Bal.
4	0.048	0.639	0.956	0.217	0.003	0.538	Bal.

6.2.2 Optical microscopy and electron microscopy-based experiments

Initially, specimens with a size of 25 × 20 × 4 mm^3 were machined from the as-received extrusions. The narrow sides and the surface of these specimens were ground, followed by mechanical polishing and electrochemical etching in the tetrafluoroboric acid for 70 s. Images of the microstructure were then taken from three orthogonal planes using a Zeiss Axio Vert.A1 light optical microscope. The three planes included (i) ED-TD plane containing the extrusion direction (ED) and transverse direction (TD), (ii) ED-ND plane containing the ED and the normal direction (ND) and (iii) TD-ND plane (see Fig.1). Specimens for SEM, EDS and EBSD were prepared in a different manner: their surface (ED-TD plane) was mechanically polished and then electropolished in a Struers A2 solution. The total thickness of the removed surface layer for these specimens was estimated to be ~40 μm.

Backscattered electron (BSE) images from each sample were taken in a Zeiss Sigma 300 field emission gun SEM operated at 20 kV. SEM-based EDS analysis was then conducted on samples 1 and 4 using an Ultim Max 65 silicon drift EDS detector. Both line scans and elemental maps were obtained from several regions in these samples. EBSD data were collected using a C-Nano EBSD detector from Oxford Instruments. In each sample, an area of at least 1 mm^2 was covered with a step size of 1 µm. Low angle boundaries (LABs) in the EBSD data were defined as boundaries with misorientations $\theta = 2–15°$, while high angle boundaries (HABs) were defined as boundaries with misorientations $\theta > 15°$. In addition to the EBSD characterization of bulk specimens, thin foils from sample 4 were investigated using transmission Kikuchi diffraction (TKD) to identify boundaries of specific types which were further analyzed by TEM.

The thin foils were prepared by electropolishing of slices cut from the ED-TD plane. After initial mechanical thinning to 0.1 mm, the foils were produced at –25°C in the Struers A2 electrolyte using a TenuPol-5 double-jet polishing system. A JEOL 3000F microscope operated at 300 kV was used for taking bright field TEM images of the microstructure in the four studied alloys. For samples 1 and 4, high angle annular dark field (HAADF) images and EDS data were obtained in a Titan Analytical 80-300ST microscope operated in the scanning transmission (STEM) mode. This microscope was equipped with a windowless X-Max 80TLE detector.

In addition to the studies of the as-received samples, SEM analysis was also conducted on specimens subjected to IGC tests. For analysis of the surface exposed to the corrosive environment, the tested specimens were rinsed with distilled water and dried in air. SEM inspections of the ED-ND plane of these specimens were made on mechanically polished sections. For each tested specimen and inspection plane, BSE images and secondary electron images were taken at 10 kV.

6.2.3 IGC tests

Several 25 × 20 × 4 mm^3 specimens for standard IGC tests were etched for 5 min in a water-based solution containing 8 wt% NaOH at 56 °C, followed by rinsing in deionized water and air drying. To remove etching products from the surface, the specimens were dismutted in a concentrated nitric acid for 2 min, again rinsed in deionized water and air-dried. The thickness of the removed surface layer due to etching is estimated to be ~15 µm [20]. To ensure that only the ED-TD plane would be exposed to the corrosive environment,

the narrow sides of the specimens were coated with Lacomit varnish. The specimens were tested at room temperature according to the BS ISO 11846 (method B) standard [12], i.e. by immersing them in a solution containing 10 ml/l of concentrated HCl (1.19 g/ml) and 30 g/l NaCl for 24 h.

Specimens to be inspected using X-ray microscopy had a different geometry than those used in the standard tests. These specimens were cylinders with a diameter of ~1.9 mm and a height of 4 mm. The cylindrical surface of the specimens was covered by Lacomit, so that only the flat surfaces were exposed to the corrosive solution. The chemical composition of the solution was identical to that used in the standard tests. The duration of the exposure for these specimens was 72 h. After the exposure, one corroded specimen of each alloy was investigated by XRM and three specimens of each alloy were inspected using SEM.

6.2.4 X-ray microscopy

The corroded cylindrical specimens after the 72-h test described in section 2.3 were characterized using XRM to obtain 3D visualizations of the corrosion attack. Experiments were performed using a Zeiss XRadia 410 Versa X-ray microscope. This microscope was operated at 40 kV and 10 W using a LE3 filter and 4× objective. 3201 projections with an exposure time of 25 s per projection were acquired using 2×2 binning, which resulted in a pixel size of 2.1 μm. Image reconstruction was carried out based on a cone beam algorithm with filtered back-projection [21] implemented in a dedicated software package from Zeiss. Analysis and visualization of the collected data were carried out using the Avizo 9.7.0 software.

6.3 Results

6.3.1 Microstructure of the as-received samples

6.3.1.1 Optical micrographs

Optical micrographs showing the microstructure of the as-received extrusions in three orthogonal planes are presented in Fig. 6.1. It is seen that each sample has recrystallized surface layers and largely non-recrystallized interior layers with lamellar boundaries aligned along the ED. The thickness of the recrystallized layers varies from ~0.4 mm to 0.5 mm in different locations of the extrusions. The average recrystallized grain size

is 20–30 µm at the immediate surface, while much coarser grains are observed closer to the interface between recrystallized and non-recrystallized microstructure, i.e. the recrystallized grain size increases with increasing depth. In the following, only the recrystallized surface layer exposed to the corrosive environment will be considered in this work.

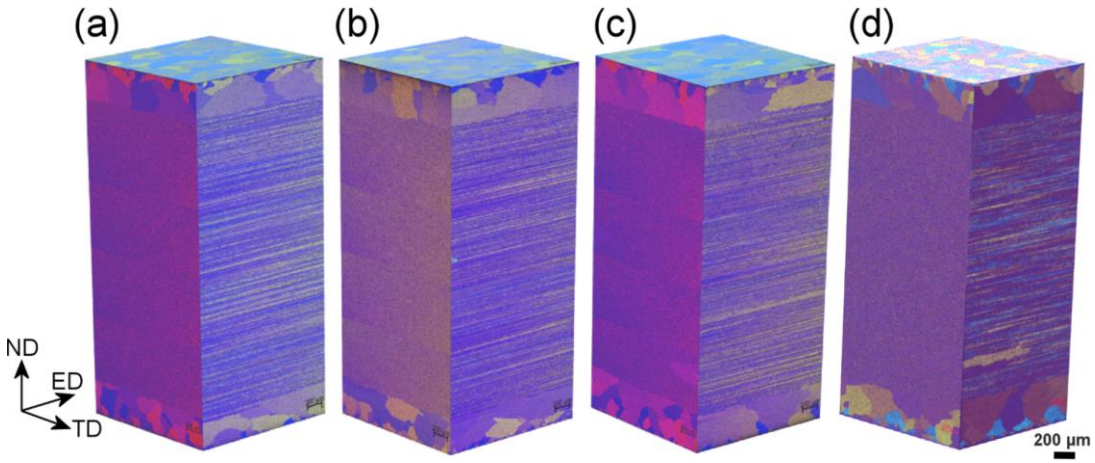

Fig. 6.1. Optical micrographs showing the microstructure of the extruded samples in three orthogonal planes: (a) sample 1; (b) sample 2; (c) sample 3; (d) sample 4.

6.3.1.2 EBSD data and SEM observations

Orientation maps collected using EBSD from the recrystallized layer at a depth of ~40 µm are presented in Fig. 6.2(a, b) for samples 1 and 4. The average grain sizes at this depth are measured to be 50–60 µm in samples 1 and 4, and similar grain sizes are found in samples 2 and 3. Analysis of boundary misorientations indicates that there is no significant difference in fractions of different boundary types between the samples. In each sample, the fractions of LABs and HABs are approximately 10 % and 90 %, respectively. Coincident site lattice HABs are not included in the boundary statistics here because a previous study of sample 4 did not reveal significant differences between IGC along Σ3–Σ21 boundaries and random HABs [15].

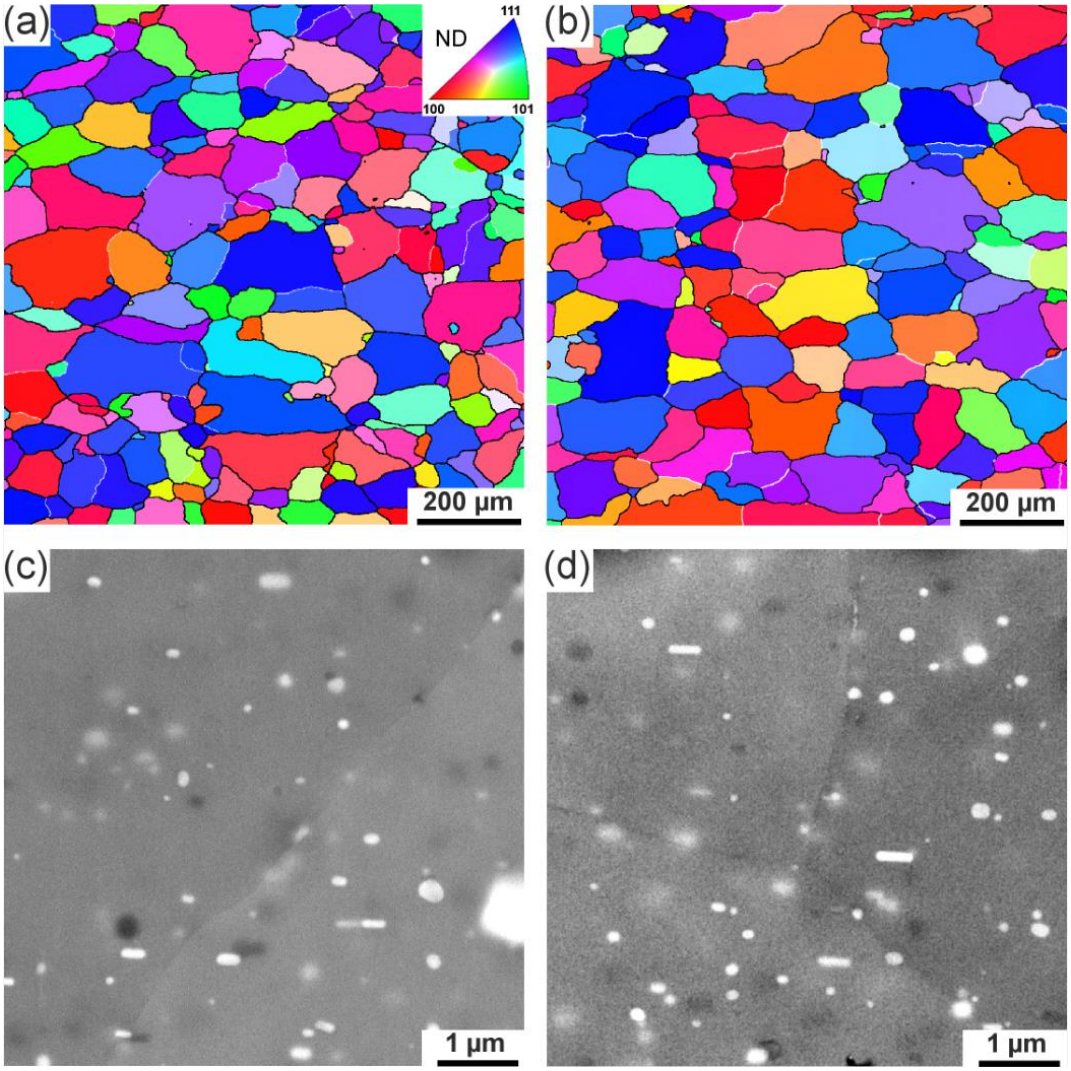

Fig. 6.2. The microstructure of sample 1 (a, c) and sample 4 (b, d) at ~40 µm below the surface observed in the ED-TD plane using SEM-based techniques: (a, b) orientation maps obtained using EBSD. The color code for orientations is shown in the inset in (a). White and black lines indicate LABs and HABs, respectively; (c, d) BSE images showing coarse intermetallic particles (bright features). The ED is parallel to the scale bar.

BSE images in Fig. 6.2(c, d) show the presence of coarse intermetallic particles within grains. In sample 1, these grain interior particles contain Al, Fe, Mn and Si, as determined using EDS. However, in sample 4 some coarse particles contain small amounts of Cu in addition to Al, Fe, Mn and Si. For example, the coarse particle in Fig. 6.3 contains ~80 % Al, 8 % Fe, 5 % Si, 7 % Mn and 0.2 % Cu (all in wt%). Note that these measurements were made in the central region of the particle and that the composition gradually changed towards its edges as a result of the limited spatial resolution of the SEM-based EDS analysis (see Fig. 6.3b). Since fine β'', β' and β particles are not seen in the obtained BSE images,

TEM-based techniques were used to characterize the size and the spatial distribution of these types of precipitates.

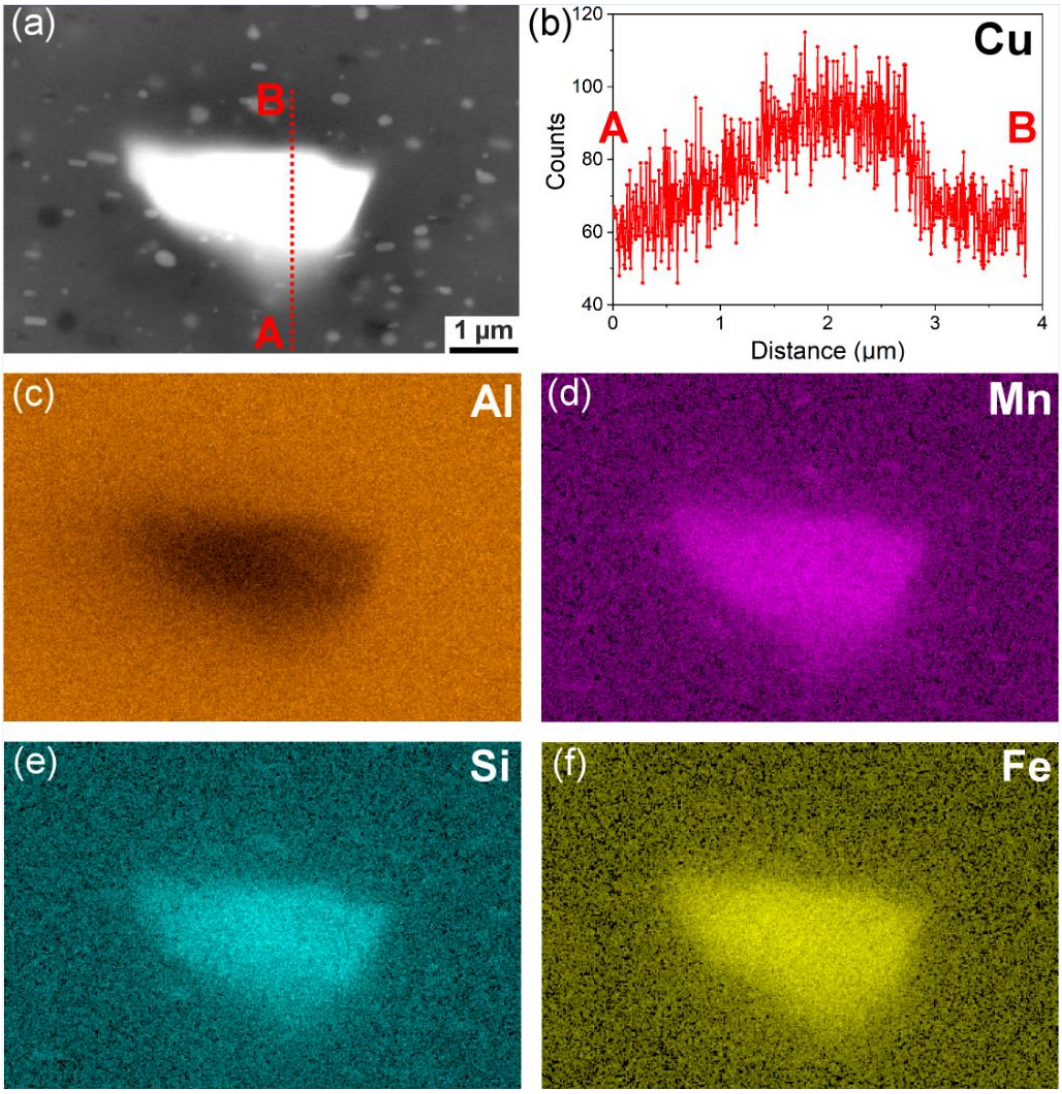

Fig. 6.3. SEM-based analysis of coarse particles in sample 4: (a) BSE image of a region, where both EDS line scanning along the A-B line and elemental mapping were performed; (b) line scan data showing an increased concentration of Cu in the coarse particle; (c-f) elemental maps for Al, Mn, Si and Fe.

6.3.1.3 TEM analysis

Bright field TEM images and HAADF images showing both GBs and grain interior regions are presented in Fig. 6.4 and Fig. 6.5, respectively. Comparing the different alloys, sample 1 with the smallest concentration of Cu contains the lowest number density of needle-shaped β'' and rod-shaped β' precipitates (Fig. 6.4a). The average length of the β' precipitates is also different in the different samples, being largest (210 nm) in sample 1 and smallest (75 nm) in sample 4. Note that some rod- and needle-shaped precipitates are

aligned parallel to the electron beam and therefore are seen as small circles/dots in the TEM images. Such precipitates were not taken into account when measuring the average lengths. Regions adjacent to the GBs in Fig. 6.4 either demonstrate a reduced frequency of β'' and β' precipitates or are totally free of precipitates. These regions are collectively termed precipitate free zones (PFZs) in this work. The width of the observed PFZs is 0.2–0.5 μm in sample 1, but only ~0.1 μm in sample 4.

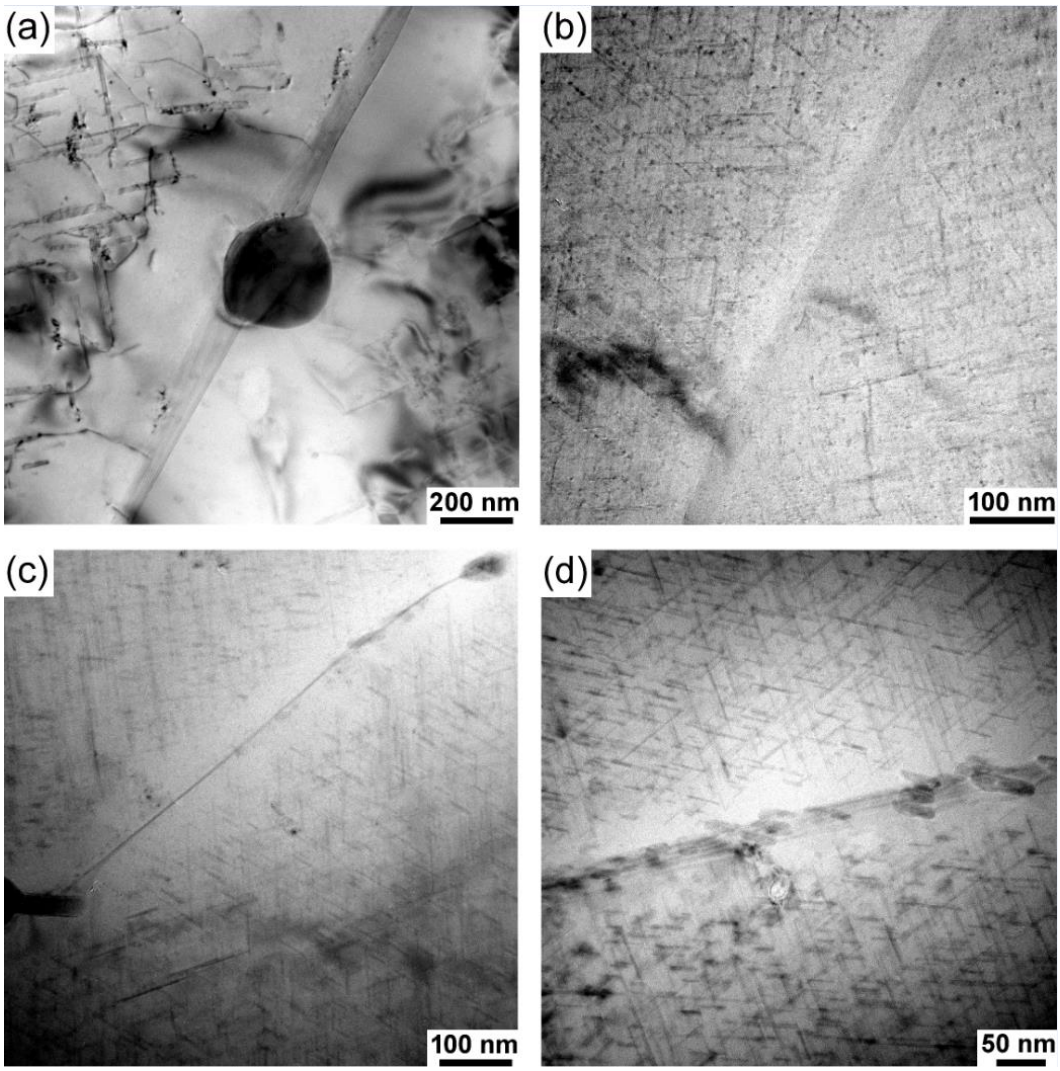

Fig. 6.4. Bright field TEM images showing precipitates and PFZs in the vicinity of GBs: (a) sample 1; (b) sample 2; (c) sample 3; (d) sample 4.

Particles of different types are present along GBs. As an example, several GB particles analyzed by EDS in sample 4 are shown in Fig. 6.5. These particles are identified either as β-phase (Mg_2Si) or as particles composed of Mg, Si, Cu and Al, see Fig. 6.5(a, b). In the following, the latter particles are described as Q/Q' since the analysis of coherency with the Al matrix needed to distinguish between stable Q and metastable Q' particles [22]

was not conducted in our work. In the region shown in Fig. 6.5(c, d), elemental maps demonstrate both β particles and a Cu-rich film along a high angle GB. Similar films were observed along six other boundaries out of sixteen HABs analyzed by EDS in sample 4.

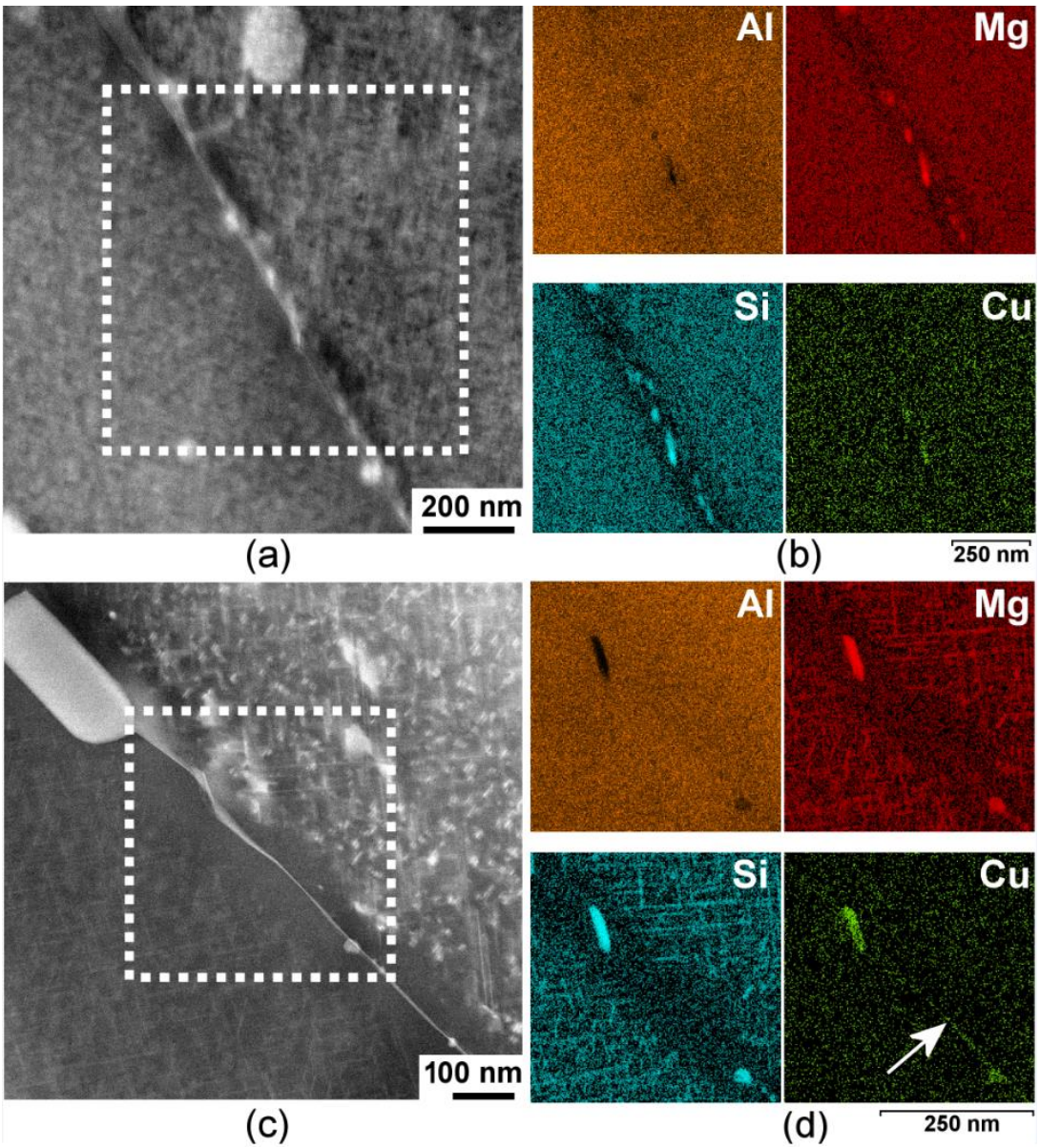

Fig. 6.5. HAADF-STEM images (a, c) and elemental maps (b, d) in GB regions in sample 4. The maps correspond to the framed regions in (a, c). In (c, d) the misorientation across the boundary determined using TKD is 55° ⟨243⟩. Note the presence of a Cu-rich film along the GB indicated by the arrow in (d).

Boundaries containing segregations of Cu are less frequent in sample 1; out of ten GBs inspected using EDS, only two boundaries with a clearly increased concentration of Cu were found. One of these boundaries is shown in Fig. 6.6a. Since the concentration of Cu along this boundary is too low to observe the film in the elemental map, only line-scan

data are presented in Fig. 6.6b. This figure indicates that there is an increased concentration of Cu at the boundary compared to that in the adjacent regions. Inspection of several GBs in sample 1 reveals the presence of the β phase, but no Q/Q' particles.

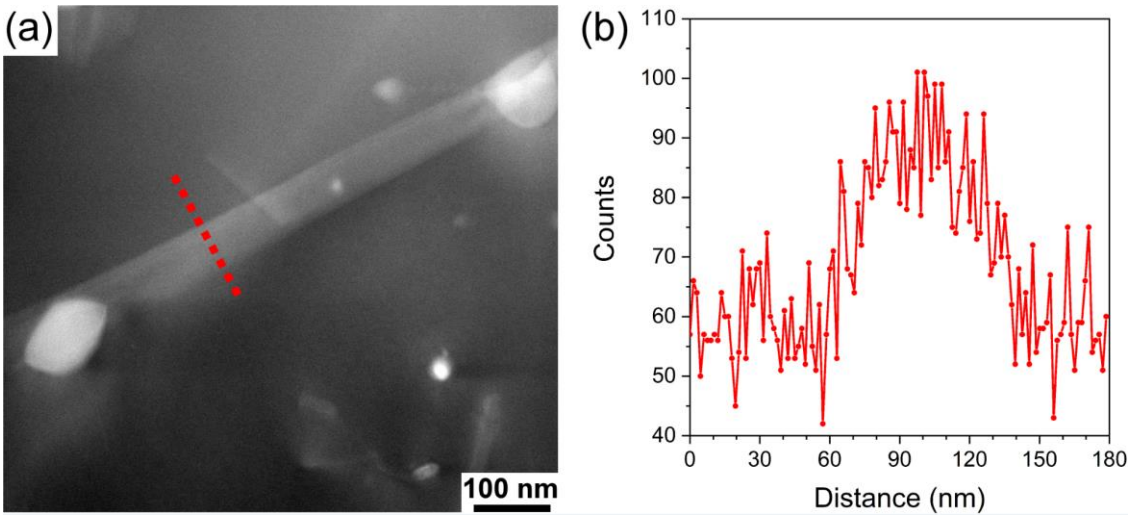

Fig. 6.6. GB with segregations of Cu in sample 1: (a) HAADF-STEM image; (b) variation of Cu content identified by EDS along the red line in (a).

6.3.2 Samples after the IGC tests

6.3.2.1 SEM observations

SEM images from the ED-TD plane exposed to the corrosive solution for 24 h demonstrate that IGC in samples 1, 2 and 3 is localized, with few regions containing clusters of corroded boundaries, see Fig. 6.7(a, b). Corrosion affects many more boundaries in sample 4 with 0.05 wt% Cu though IGC is still not truly uniform (Fig. 6.7d, h). Corroded regions framed in Fig. 6.7a-d are shown in more detail in Fig. 6.7(e-h), where a clear difference in the extent of corrosion is seen for the different samples. A small number of boundaries affected by IGC is observed in sample 1, while greater numbers of corroded boundaries are seen in the samples with the higher concentrations of Cu. The width of observable corroded boundaries in each sample varies from ~0.3 μm to several micrometers. Furthermore, it is seen that in each region there are cavities on the surface, which correspond to grains fallen out during the IGC tests (Fig. 6.7e-h). SEM images taken from the ED-ND section indicate that the IGC depth is also sensitive to the Cu content (Fig. 6.8). Whereas IGC is shallow in samples 1 and 2 (see Fig. 6.8a, b), the IGC affects much deeper regions in samples 3 and 4 (see Fig. 6.8c, d).

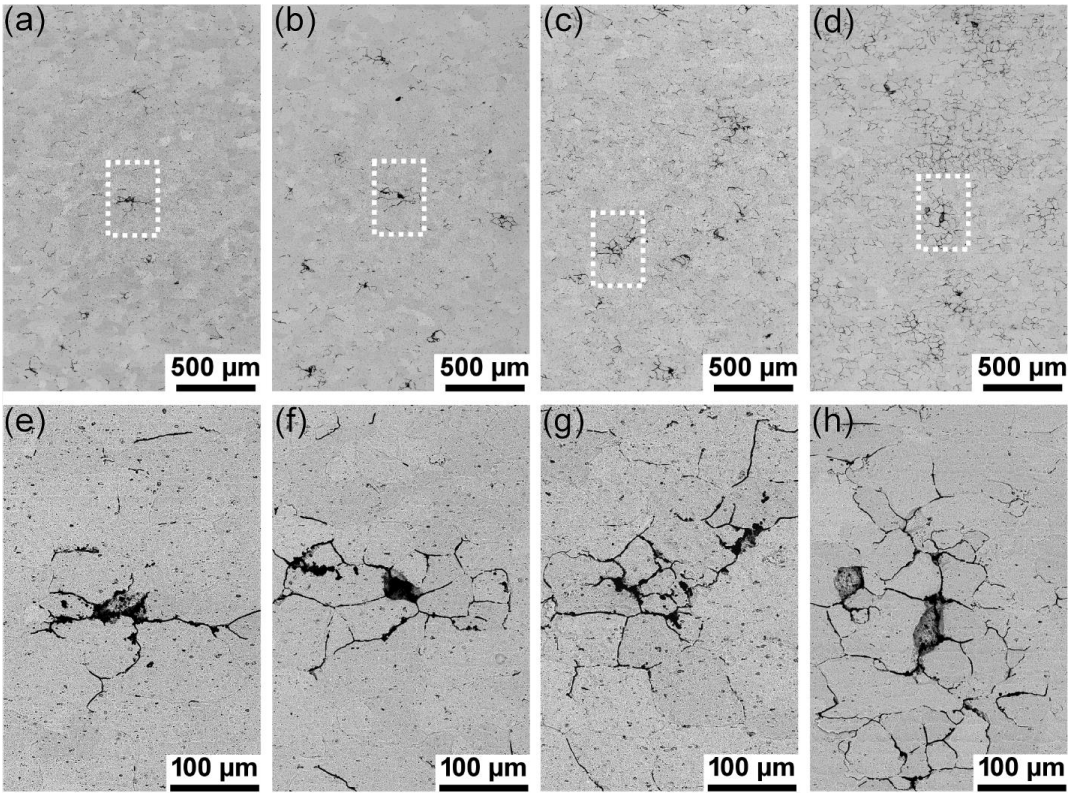

Fig. 6.7. BSE images showing the surface inspected in the ED-TD plane after the 24-h corrosion test: (a, e) sample 1; (b, f) sample 2; (c, g) sample 3; (d, h) sample 4. The framed regions in (a-d) are shown at a higher magnification in (e-h). The cavities seen on the surface are locations where grains fell out during the test. The ED is parallel to the scale bar.

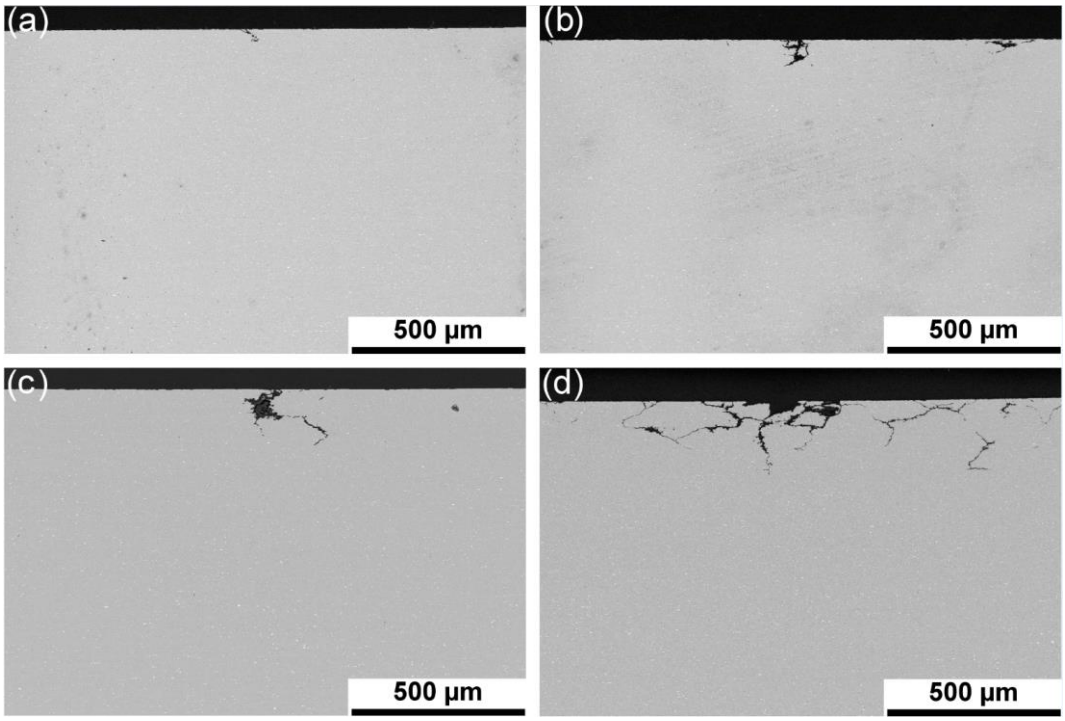

Fig. 6.8. BSE images showing the depth of the IGC attack in the ED-ND plane observed after the 24-h corrosion test: (a) sample 1, (b) sample 2, (c) sample 3, (d) sample 4. The ED is parallel to the scale bar.

Quantitative analysis of the SEM images in each section is presented in Fig. 6.9 both for 24-h tests and for 72-h tests. The number of corroded boundaries per unit area (N_C) observed in the SEM images taken after the 24-h test is 25 mm^{-2} in sample 1 and it steadily increases to 77 mm^{-2} with increasing copper content to ~0.03 wt% (sample 3). A further increase in the Cu content to 0.05 wt% (sample 4) leads to a drastic increase in N_C to 258 mm^{-2}. As expected, the 72-h exposure to the corrosive solution results in greater N_C for each sample. Interestingly, N_C values obtained from the SEM images for samples 1, 2 and 3 after the 72-h exposure are still smaller than that for sample 4 after the 24-h exposure (see Fig. 6.9a). The greatest N_C=367 mm^{-2} is recorded in this work for sample 4 exposed for 72 h.

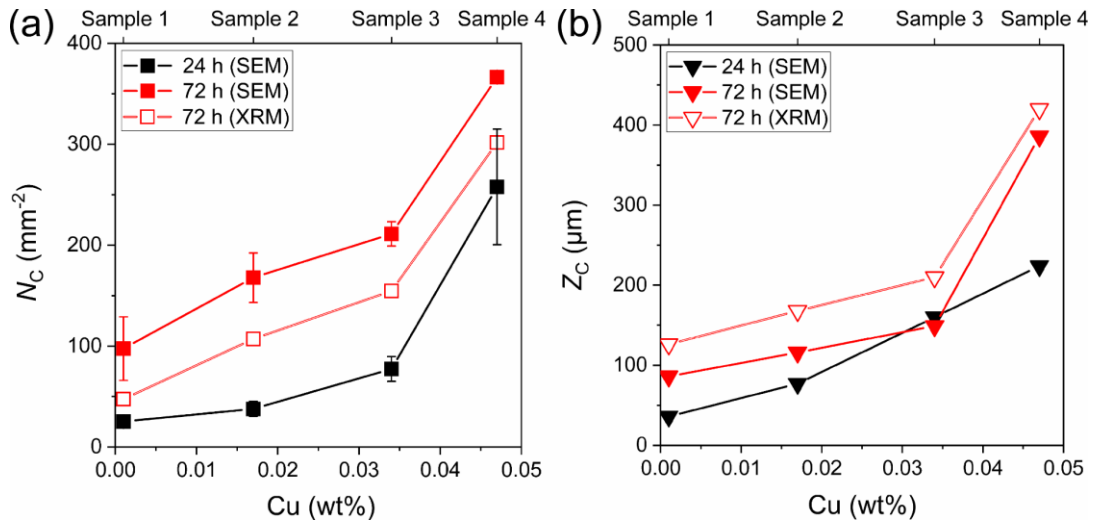

Fig. 6.9. Parameters of IGC in the samples with different concentrations of Cu after the 24-h and 72-h corrosion tests: (a) number of corroded boundaries per unit area N_C calculated based on SEM examinations of the ED-TD plane; (b) maximum depth of the IGC attack Z_C measured either from SEM images taken from the ED-ND plane after the 24-h corrosion test or from XRM data collected after the 72-h corrosion test.

Fig. 6.9b shows that the maximum depth of the IGC attack (Z_C) in samples 1 and 2 after the 24-h IGC test is limited to ~40 µm and ~80 µm, respectively. In samples 3 and 4 subjected to the 24-h test, Z_C is 160 µm and ~220 µm, respectively. Larger Z_C values are measured after the 72-h exposure for samples 1, 2 and 4 inspected using SEM. The slightly smaller SEM-based Z_C value found in sample 3 after the 72 h-test than that after the 24-h test suggests that the polished 2D sections might not represent the actual maximum IGC depth in the given samples. Similar to N_C, the measured Z_C values in samples 1, 2 and 3 after the 72-h test are all smaller than that in sample 4 after the 24-h test, see Fig. 6.9b. For each sample and test duration, IGC is confined to the recrystallized layer, with no

penetration into the non-recrystallized interior layer. Note that in our previous IGC experiments on sample 4, where specimens with a somewhat thinner recrystallized layer were tested, corrosion during the 72-h exposure propagated beyond the recrystallized layer [15].

6.3.2.2 XRM observations

Although 3D XRD images were obtained for each cylindrical specimen corroded during the 72-h test, only one image for the topmost surface layer of sample 4 with the most extensive IGC is presented in Fig. 6.10. This image covers a thickness of 21 μm and shows identified corroded GB regions in red. It is seen that some corroded boundaries in this image are not continuous, but broken into fragments. This discontinuity can partly be caused by the limited spatial resolution of the reconstructed XRM image, where undetected corroded boundary regions can be narrower than the pixel size (2.1 μm, see Section 2.4).

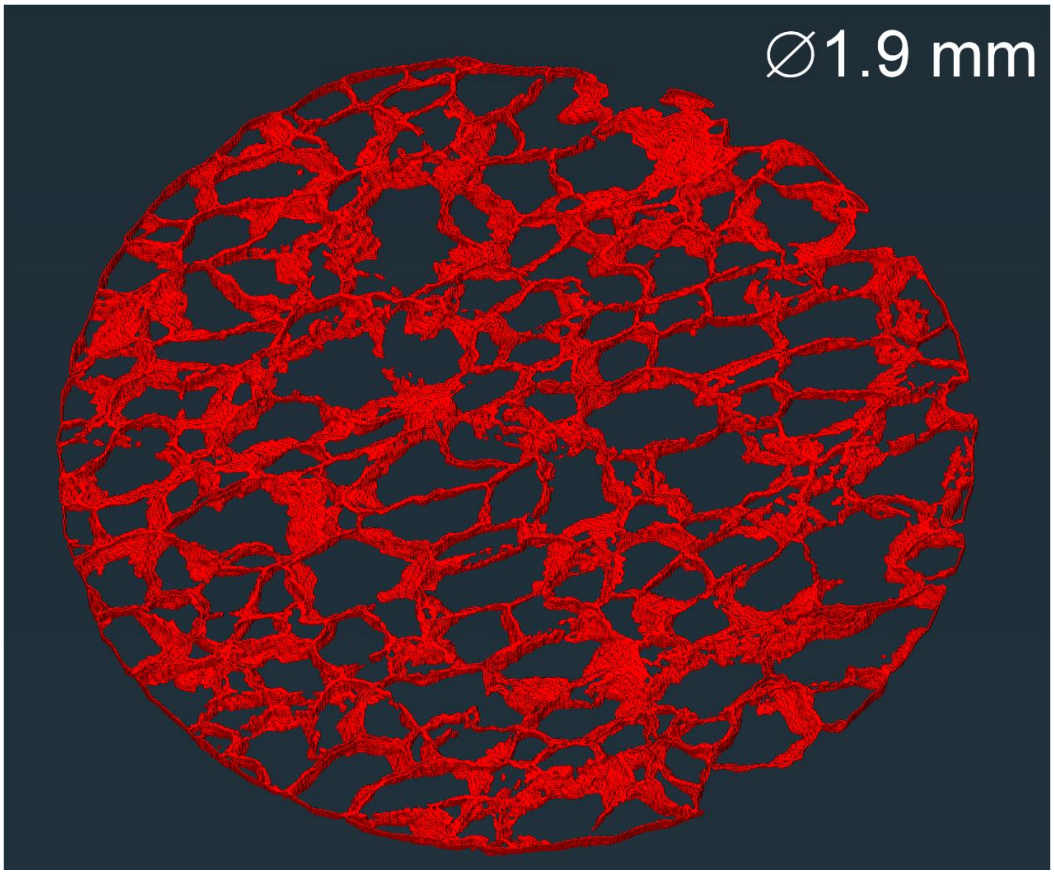

Fig. 6.10. 3D XRM image of the topmost surface layer of sample 4 subjected to the 72-h test showing identified corroded boundaries in red.

The frequency of narrow corroded boundaries missed because of the limited spatial resolution in the XRM experiment can be evaluated by comparing N_C values measured for the topmost surface in the XRM and SEM images. Analysis of the XRM- and SEM-based N_C data in Fig. 6.9a indicates that for each sample surface XRM detects smaller numbers of corroded boundaries than SEM. In contrast, when Z_C values are compared, the XRM reveals corroded boundaries at larger depths than those seen in the polished ED-ND sections of the SEM specimens (see Fig. 6.9b).

To give a better overview of the XRM data at different depths in each sample IGC-tested for 72 h, Fig. 6.11 and Fig. 6.12 present several 2D sections of the reconstructed 3D volumes, where dark lines correspond to corroded boundaries. It is seen that while a considerable number of boundaries are corroded on the topmost surface of sample 1, the frequency of the corroded boundaries decreases rapidly with increasing distance from the surface (see Fig. 6.11a). No corroded boundaries in this sample are observed at depths below 130 μm. N_C for the other samples demonstrates a similar decreasing trend as the distance from the surface increases, but with greater frequencies of corroded boundaries than in sample 1 (see Fig. 6.11b-d and Fig. 6.13).

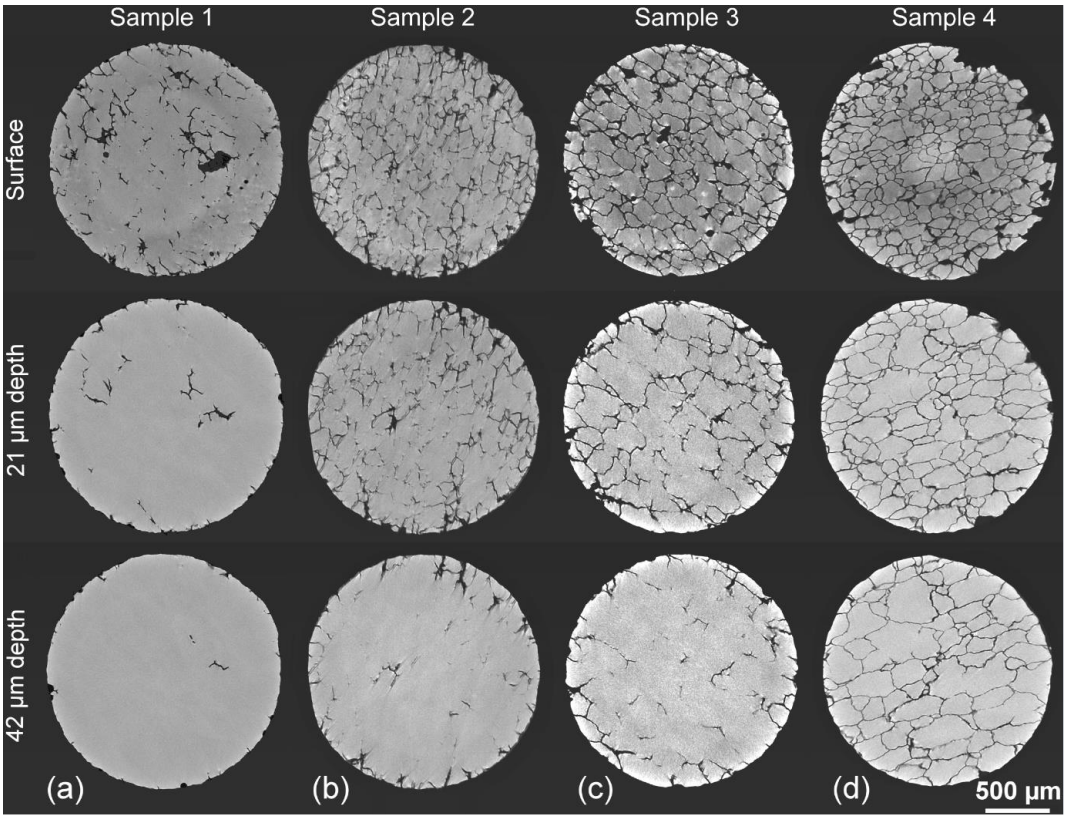

Fig. 6.11. XRM images showing the ED-TD plane at the surface and two depths below the surface of the samples after the 72-h corrosion test: (a) sample 1; (b) sample 2; (c) sample 3; (d) sample 4.

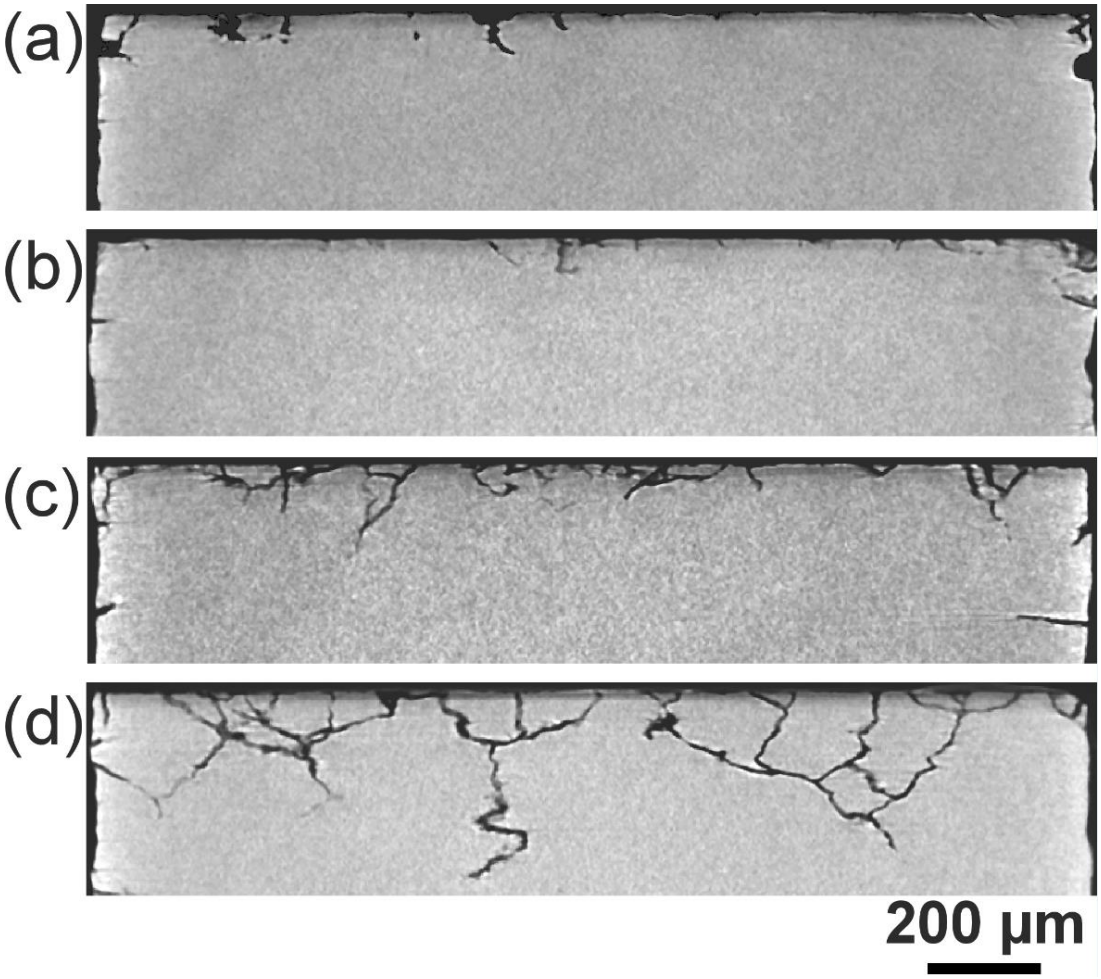

Fig. 6.12. XRM images showing the ED-ND plane of the samples after the 72-h corrosion test: (a) sample 1; (b) sample 2; (c) sample 3; (d) sample 4.

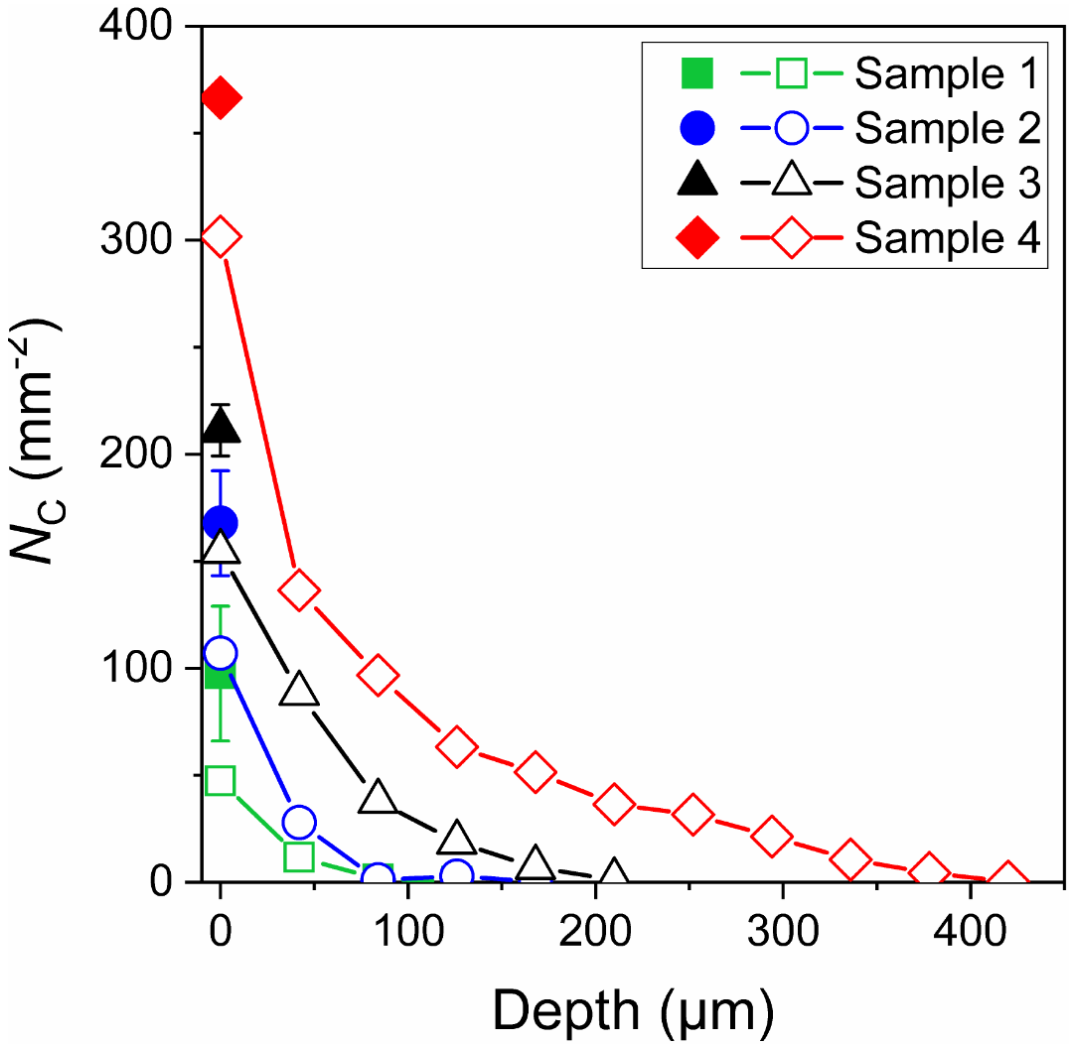

Fig. 6.13. N_C as a function of depth measured after the 72-h corrosion test. Open and solid symbols are XRM-based data and SEM-based data, respectively.

6.4 Discussion

The most significant result obtained in this work is the observation of IGC directly related to the presence of tiny (0.001 to 0.05 wt%) concentrations of Cu in aged AA6082-T6 alloys. It is important to emphasize that although IGC was previously observed in 6xxx-series alloys with 0.001 wt% Cu, IGC was not attributed to the presence of Cu in their composition [17]. In Ref.[17], samples with 0.001 wt% Cu were termed Cu-free and IGC in these samples was considered to be due to the presence of Mg_2Si precipitates along GBs and adjacent PFZs. Therefore, our findings extend the Cu range that can potentially result in IGC in 6xxx-series alloys. It should be noted that since very little IGC is found in the sample with 0.001 wt% Cu subjected to the accelerated corrosion test, alloys with such a low concentration of copper are not expected to demonstrate significant corrosion under

normal service conditions. Thus, the extent of IGC in alloys with this Cu content can be characterized as negligibly small. In contrast, pronounced IGC occurs as the copper content increases to 0.05 wt%. In addition to the effect of the Cu content, the present work demonstrates that measured parameters of IGC are also sensitive to the choice of characterization technique.

6.4.1 Effect of Cu content on the microstructure and IGC

Our observations indicate that an increase in the Cu content from 0.001 to 0.05 wt% affects several microstructural characteristics such as the size and number density of precipitates in grain interiors as well as the width of PFZs and the extent of Cu segregation along GBs. As the microstructures in samples 2 and 3 are intermediate between those in samples 1 and 4, only the differences between the microstructures of sample 1 with the lowest Cu content and sample 4 with the highest Cu content will be analyzed in the following.

Based on the TEM/STEM observations, the key microstructural differences between these two samples are schematically shown in Fig. 6.14. This figure illustrates that compared to sample 4, sample 1 is characterized by a smaller number density and coarser β'' and β' precipitates, wider PFZs and very few boundaries with segregated Cu. Considering the extremely low concentration of Cu in sample 1, it is remarkable that Cu segregations at some boundaries are found in this sample. To our knowledge, the observation of Cu-segregations was not previously observed in 6xxx-series alloys with such a low Cu concentration. Whereas boundaries inspected in sample 1 do not contain Q/Q' particles, such particles are present in sample 4. These microstructural differences are directly related to the small, but significant differences in the Cu content.

The increased number density of rod- and needle-shaped precipitates within the grain interiors in sample 4 can be caused by inclusion of Cu atoms in clusters, which act as precursors of the precipitates formed during aging. According to Zandbergen et al. [23], the change in the cluster composition facilitates transformation of Cu-bearing clusters into more stable precipitates. Therefore, a high frequency of small precipitates is produced in sample 4 with the highest Cu content. Since the concentration of Cu in sample 1 is too low to form Mg-Si-Cu clusters [23], it is suggested that only Mg-Si clusters can form in sample 1, which results in fewer, but coarser precipitates (cf. Fig. 6.4a and Fig. 6.4d). Similar effects of varying Cu content on the size and number density of precipitates in aged

AlMgSi(Cu) alloys with varying concentrations of Cu were reported by Esmaeili and Lloyd [24], Murayama et al. [25] and Xiao et al. [26].

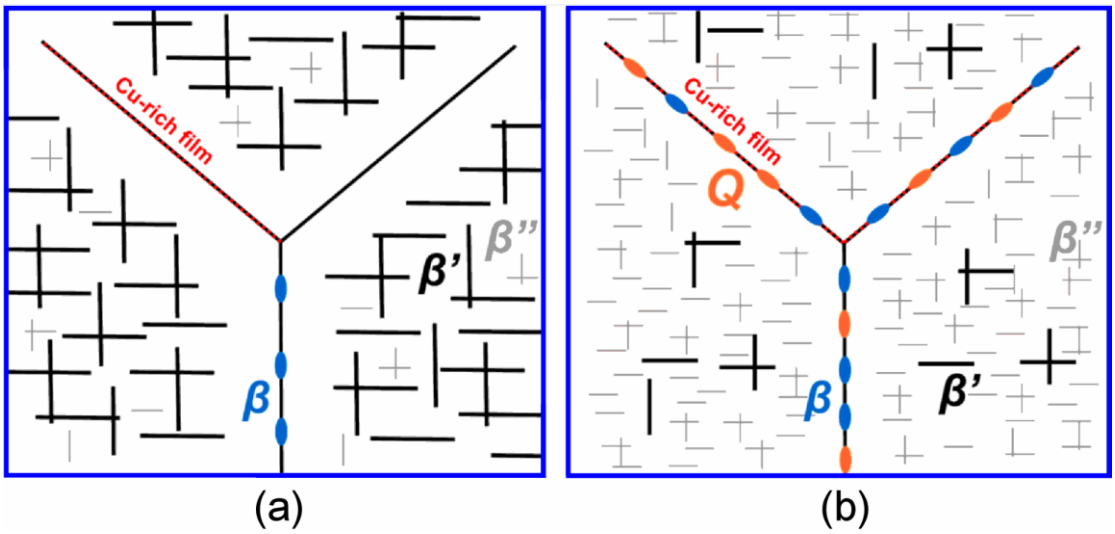

Fig. 6.14. Schematic illustration of GBs and grain interiors in the samples either with the lowest Cu content or with the highest Cu content: (a) sample 1; (b) sample 4 (b). Three long black lines joining in the center represent grain boundaries. Letter Q represents Q/Q' particles shown in orange. β phase particles are shown in blue, while β'' and β' precipitates are shown as short black and gray lines, respectively. Cu-rich films along the GBs are represented by dashed red lines. Coarse intermetallic particles such as those seen in Fig. 6.2c,d and Fig. 6.3 are not included here.

As is evident from Fig. 6.3, Fig. 6.5 and Fig. 6.6, Cu atoms can also segregate at some coarse particles within grains and along GBs, though the extent of segregation is sensitive to the amount of Cu in the alloy composition. In sample 4 (and probably also in samples 2 and 3), GB segregations can at first create a Cu-rich film, followed by the formation of Q/Q' particles. Although a small number of boundaries with the Cu-rich film found in this work does not allow statistical analysis of correlations between the boundary type and the presence of the film, it is considered that HABs are generally more prone to segregate Cu than LABs. It is, however, pertinent to mention that in an alloy with 0.4 wt% Cu, segregation of copper was found to occur along boundaries even with very low (<1°) misorientations [27].

The Cu-rich film and particles are of critical importance for IGC because galvanic coupling is produced between these cathodic sites and PFZs [8–11]. Obviously, the more Cu is present in the chemical composition, the more Cu atoms can segregate along GBs, which causes anodic dissolution of PFZs and hence IGC. Taking into account that the width of corroded GB regions observed in the SEM images was typically wider (up to several

micrometers) than the PFZ width, it is clear that IGC is not restricted solely to PFZs and that corrosion can propagate also into regions close to PFZs.

The quantitative analysis of IGC in the four samples studied in this work reveals that the number of corroded boundaries N_C and the corrosion depth Z_C are sensitive to the tiny concentrations of Cu and that IGC becomes rather severe in the sample containing 0.05 wt% Cu (see Fig. 6.7, Fig. 6.8 and Fig. 6.9). Although the extent of IGC increases as the test duration increases from 24 h to 72 h, the N_C and Z_C values for samples 1, 2 and 3 exposed to the corrosive solution for 72 h are all smaller than those for sample 4 after the 24-h test (see Fig. 6.9). This indicates that although any Cu content above 0.001 wt% leads to increased IGC in the tested samples, the strongly detrimental effect is observed at Cu concentrations greater than ~0.03 wt%.

It was previously proposed that β-phase GB particles can undergo selective dissolution of Mg in the corrosive environment, resulting in Si-rich remnants [28,29], which behave similar to Si-rich cathodic particles [30] and thus also contribute to IGC. Since Mg can leach out also of fine β'' and β' precipitates, it can be assumed that the larger number density of precipitates in sample 4 could further enhance the anodic dissolution of PFZs in this alloy. On the other hand, Larsen et al. [11] suggested that Si-rich remnants of the β-phase and even elemental Si precipitates were not efficient cathodes in 6xxx-series alloys.

6.4.2 Effect of characterization technique on quantitative parameters of IGC

Both SEM and XRM data were used in the present experiment to characterize IGC in the sample corroded for 72 h. The obvious advantage of XRM for characterization of IGC is the ability to non-destructively obtain 3D images of corroded boundaries. This ability enables 3D visualization of the IGC attack with no need to conduct serial sectioning or to inspect specimens from different planes. It is not surprising that the lower spatial resolution of XRM leads to smaller N_C values for the topmost surface of each sample compared to those obtained using SEM (see Fig. 6.9a). Despite the lower resolution, the XRM analysis successfully captures the key differences in the extent of IGC at different depths of the samples, where N_C decreases with increasing depth (see Fig. 6.11 and Fig. 6.13). It is considered that this decrease does not only indicate that certain time is required for IGC to propagate along individual GBs, but also reflects the through-thickness variation

in the recrystallized grain size of the extruded samples (Fig. 6.1), where N_C is significantly smaller at depths with coarser recrystallized grains.

The fact that XRM gives greater Z_C values than SEM (Fig. 6.9b) highlights the benefit of XRM in detecting corroded boundaries in 3D. While polished sections studied using SEM do not necessarily contain boundaries corroded to the maximum IGC depth, XRM collects information from the entire specimen volume and is thus better suited for identifying Z_C values in individual specimens, provided that the width of the corroded boundaries is greater than the resolution limit. It is believed that the spatial resolution of XRM will continue to improve, thus allowing more detailed 3D studies of IGC in Al-alloys and other metallic materials. It should also be noted that XRM combined with diffraction contrast tomography can provide useful 3D information on IGC as a function of misorientation angle and other crystallographic parameters [31].

6.5 Conclusions

The microstructure and intergranular corrosion in an acidified salt solution have been investigated in four extruded AA6082-T6 alloys with tiny concentrations of Cu (0.001, 0.02, 0.03 and 0.05 wt%). The following conclusions are obtained:

1. The concentration of Cu in the range 0.001–0.05 wt% has significant influence on the number density of β'' and β' precipitates in grain interiors. Such precipitates in the sample containing 0.001 wt% Cu are less frequent than those in the samples with higher Cu-content. Furthermore, β'' and β' precipitates are more extended and precipitate free zones are broader in the sample with the lowest concentration of Cu compared to those in the other samples.
2. Evidence of Cu segregation is observed along few boundaries in the sample with 0.001 wt% Cu. No other particles other than β-phase particles are seen along grain boundaries in this sample. A larger number of boundaries containing the Cu-rich film are found in the sample with 0.05 wt% Cu. In this sample, both β-phase and Q/Q' particles are observed along grain boundaries.
3. The tiny concentrations of Cu affect the susceptibility to intergranular corrosion in the AA6082-T6 extrusions. After the 24-h IGC test, the extent of IGC is negligibly small in the sample with 0.001 wt% Cu, but becomes significant in the sample with 0.05 wt% Cu. The maximum depth of the IGC attack measured in SEM images

increases from ~40 µm in the sample with 0.001 wt% Cu to 220 µm in the sample with 0.05 wt% Cu.

4. The extent of intergranular corrosion increases as the test duration increases from 24 h to 72 h. Nevertheless, the samples with copper concentrations < 0.04 wt% are found to be less corroded after the 72-h test than the sample containing 0.05 wt% Cu after the 24-h test.
5. Quantitative parameters of IGC are sensitive to the choice of characterization technique. Due to a higher spatial resolution of SEM, more corroded boundaries per unit area are revealed on the specimen surface using SEM than by XRM. However, since XRM collects information from the entire specimen volume, the maximum corrosion depths identified by XRM are found to be greater than those measured based on SEM observations of 2D sections.

Data availability

The raw/processed data required to reproduce these findings cannot be shared at this time as the data also forms part of an ongoing study

Acknowledgments

The authors would like to thank Hydro Aluminium for providing material. The authors also thank the staff at the DTU Nanolab for their technical assistance during STEM experiments. EHB and RA acknowledge funding from the Independent Research Fund Denmark (grant number 9041-00240A). The authors acknowledge Dr. C. Gundlach for the useful discussions of the XRM data.

Conflict of Interest

The authors declare that they have no known competing financial interests or personal relationships that could have appeared to influence the work reported in this paper.

CRediT authorship contribution statement

Emad H. Bartawi: Conceptualization, Methodology, Investigation, Formal analysis, Writing - Original Draft. **Oleg V. Mishin:** Investigation (EBSD), Formal analysis (EBSD), Writing - Review & Editing. **Ghada Shaban:** Formal analysis, Writing - Review & Editing. **F. Grumsen:** Formal analysis. **Jan H. Nordlien:** Writing - Review & Editing. **Rajan Ambat:** Conceptualization, Supervision, Writing - Review & Editing, Project administration, Funding acquisition.

References

[1] Wrought aluminium alloys, in: Light alloys (fifth edition), Eds: I. Polmear, D. StJohn, J.-F. Nie, M. Qian, Butterworth-Heinemann (2017) 157–263, doi: 10.1016/B978-0-08-099431-4.00004-X.

[2] S.J. Murtha, New 6XXX aluminum alloy for automotive body sheet applications. SAE International (1995) 950718, doi: 10.4271/950718 UI.

[3] G. Svenningsen, M. Hurlen, Effect of high temperature heat treatment on intergranular corrosion of AlMgSi (Cu) model alloy, Corros. Sci. 48 (2006) 258–272, doi: 10.1016/j.corsci.2004.12.003.

[4] Y. Zou, Q. Liu, Z. Jia, Y. Xing, L. Ding, X. Wang, The intergranular corrosion behavior of 6000-series alloys with different Mg/Si and Cu content, Appl. Surf. Sci. 405 (2017) 489–496, doi: 10.1016/j.apsusc.2017.02.045.

[5] T. Saito, S. Muraishi, C.D. Marioara, S.J. Andersen, J. Røyset, R. Holmestad, The effects of low Cu additions and predeformation on the precipitation in a 6060 Al-Mg-Si alloy, Metall. Mater. Trans. A 44 (2013) 4124–4135, doi: 10.1007/s11661-013-1754-3.

[6] J. Man, L. Jing, S.G. Jie, The effects of Cu addition on the microstructure and thermal stability of an Al–Mg–Si alloy, J. Alloys Compd., 437 (2007) 146–150, doi: 10.1016/J.JALLCOM.2006.07.113.

[7] M.H. Larsen, J.C. Walmsley, O. Lunder, R.H. Mathiesen, K. Nisancioglu, Intergranular corrosion of copper-containing AA6xxx AlMgSi aluminum alloys, J. Electrochem. Soc., 155 (2008) C550, doi: 10.1149/1.2976774.

[8] G. Svenningsen, J. Erik, A. Bjørgum, J. Halvor, Y. Yu, K. Nisancioglu, Effect of low copper content and heat treatment on intergranular corrosion of model AlMgSi alloys, Corros. Sci. 48 (2006) 226–242, doi: 10.1016/j.corsci.2004.11.025.

[9] G. Svenningsen, M.H. Larsen, J.H. Nordlien, K. Nisancioglu, Effect of thermomechanical history on intergranular corrosion of extruded AlMgSi(Cu) model alloy, Corros. Sci. 48 (2006) 3969–3987, doi: 10.1016/j.corsci.2006.03.018.

[10] G. Svenningsen, M.H. Larsen, J.C. Walmsley, J.H. Nordlien, K. Nisancioglu, Effect of artificial aging on intergranular corrosion of extruded AlMgSi alloy with small Cu content, Corros. Sci. 48 (2006) 1528–1543, https://doi.org/10.1016/j.corsci.2005.05.045.

[11] M.H. Larsen, J.C. Walmsley, O. Lunder, K. Nisancioglu, Effect of excess silicon

and small copper content on intergranular corrosion of 6000-series aluminum alloys, J. Electrochem. Soc. 157 (2010) C61-C68, doi: 10.1149/1.3261804.

[12] BS EN ISO 11846:2008, Corrosion of metals and alloys. Determination of resistance to intergranular corrosion of solution heat-treatable aluminium alloys, Br. Stand. Inst. (2005).

[13] X. Zhang, X. Zhou, J.O. Nilsson, Corrosion behaviour of AA6082 Al-Mg-Si alloy extrusion: The influence of quench cooling rate, Corros. Sci. 150 (2019) 100–109, doi: 10.1016/j.corsci.2019.01.030.

[14] C.D. Marioara, A. Lervik, J. Grønvold, O. Lunder, S. Wenner, T. Furu, R. Holmestad, The correlation between intergranular corrosion resistance and copper content in the precipitate microstructure in an AA6005A alloy. Metall Mater Trans A 49 (2018) 5146–5156, doi: 10.1007/s11661-018-4789-7.

[15] E.H. Bartawi, O.V. Mishin, G. Shaban, J.H. Nordlien, R. Ambat, Electron microscopy analysis of grain boundaries and intergranular corrosion in aged Al-Mg-Si alloy doped with 0.05wt% Cu, Corr. Sci. 209 (2022) 110758, doi: 10.1016/j.corsci.2022.110758.

[16] X. Zhang, Y. Lv, T. Hashimoto, J.-O. Nilsson, X. Zhou, Intergranular corrosion of AA6082 Al–Mg–Si alloy extrusion: the influence of trace Cu and grain boundary misorientation, J. Alloy. Compd. 853 (2021), 157228, https://doi.org/10.1016/j.jallcom.2020.157228.

[17] S.K. Kairy, P.A. Rometsch, C.H.J. Davies, N. Birbilis, On the intergranular corrosion and hardness evolution of 6xxx series Al alloys as a function of Si: Mg ratio, Cu content, and aging condition, Corrosion 73 (2017) 1280-1295, https://doi.org/10.5006/2506.

[18] Standard practice for evaluating intergranular corrosion resistance of heat treatable aluminum alloys by immersion in sodium chloride + hydrogen peroxide solution, ASTM G110-92(2015).

[19] H. Zhan, J.M.C. Mol, F. Hannour, L. Zhuang, H. Terryn, J.H.W. de Wit, The influence of copper content on intergranular corrosion of model AlMgSi (Cu) alloys, Mater. Corros. 59 (2008) 670–675, doi: /10.1002/maco.200804110.

[20] Z. Jin, C. Cai, T. Hashimoto, Y. Yuan, D. Kang, J. Hunter, X. Zhou. Alkaline etching and desmutting of aluminium alloy: The behaviour of Mg2Si particles. J. Alloys Compd. 842 (2020) 155834.

[21] L.A. Feldkamp, L.C. Davis, J.W. Kress, Practical cone beam algorithm, J. Opt. Soc. Am. A 1 (1984) 612–619.

[22] D.J Chakrabarti, D.E Laughlin, Phase relations and precipitation in Al–Mg–Si alloys with Cu additions, Progr. Mater. Sci. 49 (2004) 389-410, doi: 10.1016/S0079-6425(03)00031-8.

[23] M.W. Zandbergen, A. Cerezo, G.D.W. Smith, Study of precipitation in Al–Mg–Si Alloys by atom probe tomography II. Influence of Cu additions, Acta Mater. 101 (2015) 149–158, doi: 10.1016/J.ACTAMAT.2015.08.018.

[24] S. Esmaeili, D.J. Lloyd, Effect of composition on clustering reactions in AlMgSi(Cu) alloys, Scr. Mater., 50 (2004) 155–158, doi: 10.1016/j.scriptamat.2003.08.030.

[25] Murayama, M., Hono, K., Miao, W. F., & Laughlin, D. E. (2001). The effect of Cu additions on the precipitation kinetics in an Al-Mg-Si alloy with excess Si. Metallurgical and materials transactions A, 32, 239-246.

[26] Q. Xiao, H. Liu, D. Yi, D. Yin, Y. Chen, Y. Zhang, B. Wang, Effect of Cu content on precipitation and age-hardening behavior in Al-Mg-Si-xCu alloys. J. Alloys Compd. 695 (2017): 1005-1013. doi: 10.1016/j.jallcom.2016.10.221.

[27] A. Lervik, S. Wenner, O. Lunder, C.D. Marioara, R. Holmestad, Grain boundary structures and their correlation with intergranular corrosion in an extruded Al-Mg-Si-Cu alloy, Mater. Charact. 170 (2020), 110695, doi: 10.1016/j.matchar.2020.110695.

[28] F. Zeng, Z. Wei, J. Li, C. Li, X. Tan, Z. Zhang, Z. Zheng, Corrosion mechanism associated with Mg2Si and Si particles in Al–Mg–Si alloys, Trans. Nonferrous Met. Soc. China 21 (2011) 2559–2567, doi: 10.1016/S1003-6326(11)61092-3.

[29] F. Eckermann, T. Suter, P.J. Uggowitzer, A. Afseth, P. Schmutz, The influence of MgSi particle reactivity and dissolution processes on corrosion in Al–Mg–Si alloys, Electrochim. Acta 54 (2008), 844–855, doi: 10.1016/J.ELECTACTA.2008.05.078.

[30] A.K. Bhattamishra, K. Lal, Microstructural studies on the effect of Si and Cr on the intergranular corrosion in Al-Mg-Si alloys, Materials & Design 18 (1997) 25–28. doi: 10.1016/S0261-3069(97)00027-7.

[31] Y. Zhao, S. Niverty, X. Ma, N. Chawla, Correlation between corrosion behavior and grain boundary characteristics of a 6061 Al alloy by lab-scale X-ray diffraction contrast tomography (DCT), Mater. Charact., 193 (2022) 112325, doi:

10.1016/j.matchar.2022.112325.

7. Paper III

Toward high intergranular corrosion resistance in Al-Mg-Si alloys: influence of minor additions of Cu and Zn

Emad H. Bartawi[1,*], Calin D. Marioara[2], Ghada Shaban[1], Ehsan Rahimi[3], Oleg V. Mishin[1], Jonas K. Sunde[4], Yaiza Gonzalez-Garcia[3], Randi Holmestad[5], Rajan Ambat[1]

[1] Department of Civil and Mechanical Engineering, Technical University of Denmark, Kgs. Lyngby 2800, Denmark

[2] Materials and Nanotechnology, SINTEF Industry, Trondheim N-7465, Norway

[3]Department of Materials Science and Engineering, Delft University of Technology, Mekelweg 2, 2628 CD Delft, The Netherlands

[4] Hydro Extrusions, Innovation & Technology Precision Tubing, Drammensveien 264, 0283, Oslo, Norway

[5]Department of Physics, NTNU, Norwegian University of Science and Technology, 7491 Trondheim, Norway

[*]Corresponding author: ehaba@mek.dtu.dk

Keywords: Al-Mg-Si alloys; Intergranular corrosion; Precipitations; TEM; HR-STEM

Abstract

Adding certain alloying elements such as copper and zinc into Al-Mg-Si alloys, even at a trace level, may increase the susceptibility to intergranular corrosion (IGC). This work has systematically examined how minor additions of Zn influence IGC in a 6082 Al-Mg-Si alloy containing low Cu concentration. The results also demonstrate how low Cu and/or Zn content may strongly impact the crystal structure of the primary Al-Mg-Si hardening precipitates found in the peakaged condition. The alloy containing 0.05 wt% Cu exhibited a low IGC resistance. However, the IGC resistance increased significantly with a minor addition of Zn (0.06 wt%). Transmission electron microscopy analysis indicated that Zn segregated into grain boundaries and was incorporated into Q/Q′ particles in many cases.

The results are thought to be of particularly relevant on the topic of recycling, where incorporation of minor trace element levels is practically unavoidable.

7.1 Introduction

Al-Mg-Si alloys are widely used in different industrial applications as extruded profiles, e.g., marine, architecture, aerospace, and automotive applications, owing to their good formability, high strength-to-weight ratio, excellent recycling potential, and good corrosion resistance [1,2]. Despite the good corrosion resistance of Al-Mg-Si alloys, various issues linked to localized corrosion attacks are still noticed especially following inadequate heat treatment process or adding certain types of alloying elements such as Zn and/or Cu [3–5]. The demand for Al-Mg-Si alloys in the automotive sector is rising, driven by an increased need for light-weight requirement of battery electrical vehicles (BEVs). Therefore, intensive studies on the processing technology, mechanical and electrical properties, and alloy composition design for the 6xxx series have been performed [6–9]. The intergranular corrosion (IGC) susceptibility in Al-Mg-Si alloys is associated with a micro galvanic coupling between high (anodic) and low (cathodic) electrochemically active sites at grain boundaries in the alloy microstructure.

In Cu-added Al-Mg-Si alloys, it is believed that the IGC occurs as a result of differences in the corrosion potential between the anodic sites (precipitate free zones (PFZ) and the Al matrix) and the cathodic sites (Cu-rich films and Cu-containing particles such as Q/Q′) [10–13]. The susceptibility to IGC corrosion is not only related to the chemical composition, but also to aging conditions, which play a considerable role in determining the IGC resistance in the Al-Mg-Si alloys [12,14–16]. For instance, Svenningsen et al. [12] have studied the IGC resistance in Al-0.57Mg-0.93Si and Al-0.52Mg-0.6Si alloys with 0.005 wt% and 0.12 wt% Cu, respectively. The results showed that alloy with 0.12 wt% Cu content had increased susceptibility to IGC. However, the IGC is closely related to the thermal history at such amount of Cu. The IGC susceptibility of Al-Mg-Si-Cu alloys has been mainly ascribed to the presence of the Cu-containing Q/Q′ phases and/or Cu film formed along grain boundaries. It is claimed that IGC can be limited by keeping the Cu level below 0.1 wt% [12,17,18]. However, our recent work showed that the IGC is highly influenced by even smaller additions of Cu (≤ 0.048 wt%) [19,20]. The results showed the presence of Q/Q′ particles and Cu-rich films along some investigated high-angle grain boundaries with distinguished PFZs. Closely distributed Q/Q′ and β particles were

documented along coincidence site lattice (CSL) grain boundaries with distinguished PFZs [19]. Moreover, closely distributed Q/Q′ and β particles were recorded along low-angle grain boundaries without a well-developed PFZ [19].

The Mg/Si ratio, Zn addition, Cu concentration, and heat treatment conditions noticeably influence the precipitate types, densities, and sizes in Al-Mg-Si alloys [10,21–23]. It is generally proved that the precipitation sequence in Cu-free Al-Mg-Si alloys is given as:

SSSS → clusters→ GP-zones→ β″→ β′, U1, U2, B′→ β+Si.

Here, SSSS denotes the supersaturated solid solution.

A more complex precipitation sequence is reported in the Cu-containing Al-Mg-Si alloys. The interest in adding copper is connected to improving age hardening response as Cu promotes a higher number density of precipitates that display enhanced thermal stability [24–29]. Further, Cu addition gives rise to significant changes in clusters and precipitate compositions [10,30–32]. The precipitation sequence in the presence of relatively high copper concentration is given as [24,27,28]:

SSSS → clusters→ GP-zones→ β″→ L → β'_{Cu}, S, Q′, C → Q + Si.

Lately, the effect of Zn addition on the precipitation and mechanical properties of Al-Mg-Si alloys has been given greater attention as a result of the hardening improvement that can be achieved by adding Zn in a relatively high concentration [33–37]. For example, Ding, et al. investigated the impact of relatively high Zn content (≥ 0.5 wt%) on the age hardening response in Al-Mg-Si alloys [35]. The results showed a considerable improvement in age hardening after adding 3 wt% of Zn compared to 0.5 wt% of Zn. The observed improvement was linked to the coexistence of different types of precipitates, e.g., β-Mg_2Si and η-$MgZn_2$, in an Al-Mg-Si matrix subjected to 200 °C for 24 h. The same observation was made by Guo et al. [36], who reported that the addition of 1 wt% of Zn will enhance the hardening response in Al-0.82Mg-0.91Si alloys. Work concerning the influence of Zn addition on the precipitate crystal structures was conducted by Saito et al. [3,38]. The results exhibited that Zn has a weak preference for occupancy of specific atomic sites in Al-Mg-Si precipitates. Moreover, no measurable effect on the precipitate structures was detected in the alloys containing up to 0.1 wt% Zn.

Concerning the intergranular corrosion of Al-0.5Mg-0.4Si alloys in T6 temper with Zn, Saito et al. studied the IGC in an Al-Mg-Si alloy with a low level of Zn content (0.01, 0.11 and 1 wt%) [3]. Based on the results, a minor addition of Zn (≤ 0.1 wt%) has a negligible influence on the IGC resistance. However, strong evidence of IGC attacks was observed in the alloy containing a higher amount of Zn (1 wt%). The influence of 0.2 wt% Zn addition was investigated by Chi et al. [39], which demonstrated a higher penetration depth than for alloys with 0.05 wt% Zn content. Zn additions were found to result in a higher number density of grain boundary particles and wider PFZs, resulting in more susceptibility to IGC. Moreover, Al-Mg-Si-0.2Cu with relatively high Zn content (0.1-1.78wt%) was investigated by Yamaguchi et al. [40]. Particularly high IGC resistance in the alloy containing 0.1 wt% Zn after 20 min of baking heat treatment was documented, while alloys with higher than 0.1wt% Zn showed low IGC resistance.

Summarizing previous observations, it should be noted that the effect of low Zn content (≤ 0.06 wt%) in conjunction with low Cu concentration (0.05 wt%) on microstructure and IGC susceptibility in Al-Mg-Si alloys has not been studied. Cu and Zn are common alloying elements in several Al alloys. Presently, these elements are practically unavoidable in recycled Al-Mg-Si alloys and therefore expected to be found at low concentrations in future alloys containing increasingly higher levels of recycled metal content. Therefore, it is essential to understand to which degree low concentrations of Cu and/or Zn (scrap-related impurity) will influence Al-Mg-Si alloys' microstructure and IGC resistance. Such information will determine the highest scrap fractions that can be added to the virgin aluminium without sacrificing its corrosion resistance. In addition, how and at which concentrations Zn and/or Cu affect the crystal structure of hardening precipitates in Al-Mg-Si alloys in T6 temper remains unclear. Hence, the present work intends to provide detailed information regarding the influence of Zn and Cu on precipitation and investigate possible ways of enhancing the IGC properties of Al-Mg-Si alloys containing a small Cu concentration. To characterize the microstructure, precipitate crystal structure, and the IGC in Al-Mg-Si alloy, a variety of electron microscopy techniques has been adopted in this work. High-angle annular dark-field scanning transmission electron microscopy (HAADF-STEM) was employed to characterize the precipitate structures formed in the Al-Mg-Si alloys in peakaged (PA) condition. In addition, electron backscatter diffraction (EBSD) and scanning electron microscopy (SEM) were used to investigate the microstructure and the

intergranular corrosion. Likewise, utilizing atomic force microscopy (AFM) coupled with scanning Kelvin probe force microscopy (SKPFM), we elucidate the surface potential difference at the grain boundary containing Cu/Zn thin film and its matrix vicinity.

7.2 Experimental methods

7.2.1 Material for investigation

The chemical compositions of the 6082-Al-Mg-Si samples used in the present work are given in Table 7.1. The ingots were homogenized at 575 °C for 135 min. Thereafter, the materials were extruded at a ram speed of 5.6 mm/s and an average billet temperature of 530 °C into flat profiles with a thickness of 4 mm. The extruded profiles were water-quenched, stretched 0.5 %, and afterward subjected to a two-step aging hardening process to achieve the peakaged condition. Hydro Aluminium designates this condition as the T6 condition, which is used in the current work as the designation for the as-received material.

Table 7.1. Chemical composition (wt%) of Al 6082-T6 samples used in the present study.

Alloy	Cu	Mg	Si	Fe	Zn	Mn	Al
A1	0.048	0.64	0.96	0.22	0.003	0.54	Balance
A2	0.050	0.63	0.94	0.21	0.022	0.55	Balance
A3	0.050	0.64	0.94	0.22	0.041	0.56	Balance
A4	0.050	0.63	0.95	0.21	0.059	0.580	Balance

7.2.2 Microstructure characterizations

Four alloys with 0.05 wt% Cu and different Zn contents (0.003, 0.02, 0.04, and 0.06 wt%) were labeled as A1, A2, A3, and A4, respectively (shown in Table 7.1). The initial microstructure characterization was performed using Light Optical Microscopy (LOM) to observe the microstructure of the surface, longitudinal direction, and transverse direction. The 25 × 10 × 4 mm^3 specimens were first mechanically ground and polished to 1 μm to get a mirror surface. Thereafter, tetrafluoroboric acid was utilized for electrochemical etching. The optical micrographs were obtained using a Zeiss Axio Vert.A1 microscope. The corrosion morphology of the surface and cross-section was investigated after a 24 h immersion test using an AFEG 250 Analytical ESEM under a high-vacuum atmosphere.

The EBSD analysis of the as-received microstructure was conducted in the ED-TD plane. Prior to EBSD, the top surface of the extruded material was mechanically polished and then electropolished to obtain good-quality EBSD patterns. The thickness of the surface layer removed by polishing was estimated to be ~40 µm. EBSD data were collected in several regions, covering a total area of 2 mm^2 with a step size of 1 µm.

Specimens for Transmission Electron Microscope (TEM) were first polished to approximately 100 µm thickness and punched into 3 mm discs. After that, the specimens were electropolished in a solution of 800 ml ethanol, 100 ml 2-butoxyethanol, and 100 ml perchloric acid (65 %) at a temperature between -25 and -20 °C. Grain boundary (GB) investigations were conducted with a Titan Analytical 80-300ST TEM equipped with an Oxford energy-dispersive X-ray spectroscopy (EDS) detector X-Max 80TLE operated at 300 kV. A double-corrected JEOL ARM200CF microscope operated at 200 kV was employed to obtain Z-contrast, atomic resolution HAADF-STEM images of hardening precipitates. The probe size was 0.10 nm, with 27.42 mrad convergence semi-angle. The inner and outer collection angles of the HAADF detector were 51 and 203 mrad, respectively. To reduce scanning noise, fast Fourier transform (FFT) filtering was applied on all images using a circular band pass mask to remove all periods shorter than approximately 0.15 nm, which is close to the shortest separation of projected atomic columns in precipitates in Al-Mg-Si(-Cu) alloys as viewed in cross-section.

7.2.3 AFM/SKPFM surface characterization

To reveal the impact of the minor addition of Cu/Zn as impurities on the surface potential difference in Al-Mg-Si 6082 alloy's grain boundaries, AFM/SKPFM surface-sensitive analysis was performed on the marked samples. The samples were mechanically polished up to 0.25 µm, 30 s OP-S polishing, and then marked by FIB-SEM using Xe source. AFM/SKPFM surface analyses were performed by Bruker Dimension Edge™ instrument with an n-type doped silicon pyramid single crystal tip coated with PtIr5 (SCM-Pit probe, with a height and tip radius of 10–15 µm and 20 nm, respectively). The local surface potential was recorded in the dual-scan mode. The topography map was recorded in the first scan in tapping mode. The tip was lifted to 100 nm in the second scan, and the surface potential was obtained by following the topography contour registered in the first scan. The topography and surface potential images were captured under ex-situ conditions in an air atmosphere at 22 °C and an approximate relative humidity of 32 %. Moreover, the

following parameters were fixed for all AFM/SKPFM measurements, including a pixel resolution of 512 × 512, zero-bias voltage, tip-biased, and scan frequency rate of 0.3 Hz.

7.2.4 Intergranular corrosion test (IGC)

The influence of trace level Zn content on microstructure and intergranular corrosion of Al-Mg-Si samples was investigated in the present study. Specimens of 25 × 20 × 4 mm^3 were first alkaline etched at 56 °C in a solution containing 8 % NaOH for 5 min. The specimens were subsequently immersed in nitric acid for 2 minutes, rinsed in distilled water, and dried in a cool air stream. The intergranular corrosion test was performed by exposing the prepared specimens to an acidified salt solution containing 10 ml/l of concentrated HCl and 30 g/l NaCl at room temperature for 24 h. The IGC test was performed according to standard BS ISO 11846 method B [41]. The studied materials have a duplex microstructure with a deformed center layer and a recrystallized surface layer. In the present work, the attention was given to investigating the recrystallized surface layer exposed to external conditions. Lacomit varnish was used to isolate the specimen's side edges from being exposed to the acidified solution during the IGC test as it is more active than the surface layer. After the 24 h immersion test, the specimens were rinsed in distilled water, then dried in a cool air stream. IGC investigation was performed considering both surface morphology and cross-section observation. The IGC investigation was conducted using SEM.

7.3 Results

7.3.1 Microstructure characterization

The microstructure of the four studied Al 6082-T6 samples along the transverse direction, longitudinal direction, and the surface is shown in Fig. 7.1. The dual microstructure was revealed, comprising a recrystallized layer on the top and bottom surface and a deformed centered layer. The thickness of the recrystallized layer varied from approximately 400 to 500 μm, as seen in Fig. 7. 1(a, b, c, and d). It is worth mentioning that the recrystallized layer consists of different grain sizes based on the depth. The average size of the grains close to the top surface is approximately 30 μm, while several hundred μm grain size can be observed close to the deformed layer.

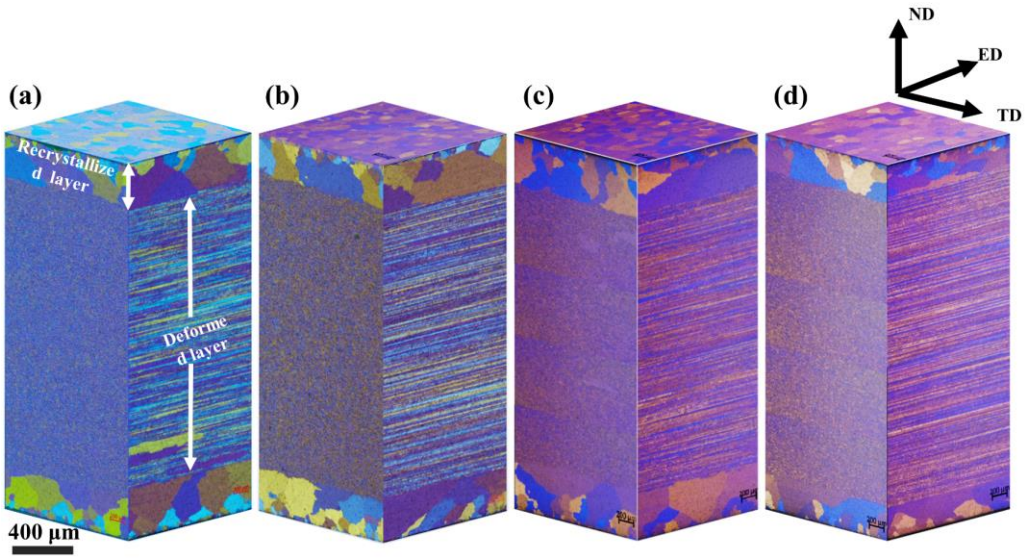

Fig. 7.1. 3D-Optical observation of microstructure of extruded Al 6082-T6 samples A1, A2, A3 and A4 after mechanical polishing and electrochemical etching in Tetrafluoroboric acid: (a) sample A1, (b) sample A2, (c) sample A3, and (d) sample A4.

Orientation maps obtained using EBSD from samples A1 and A4 at a depth of ~40 µm indicate that the grain size in both samples is similar, ~40–60 µm (see Fig. 7.2). Also, fractions of low angles boundaries, f_{LAB}, are similar (9–10 %) in these samples (see Table 7.2). Crystallographic textures are weak, with slightly increased fractions of the Goss {110}⟨001⟩ and shear {001}⟨110⟩ components. Note that fractions of texture components shown for sample A1 in Table 7.2 are slightly different from those reported in our previous paper [19]. This difference reflects the fact that in the present work, the texture info was collected at ~40 µm, while in [19] the entire recrystallized layer was covered by EBSD.

Table 7.2. Characteristics of the microstructure and texture in the AA6082-T6 samples analyzed using EBSD.

Sample	Average grain size (µm)	f_{LAB} (%)	Fractions of texture components (%)				
			G {110}⟨001⟩	Bs {110}⟨112⟩	S {123}⟨634⟩	Cu {112}⟨111⟩	Shear {001}⟨110⟩
A1	63	9	6	1	5	2	7
A4	41	10	9	1	3	4	10

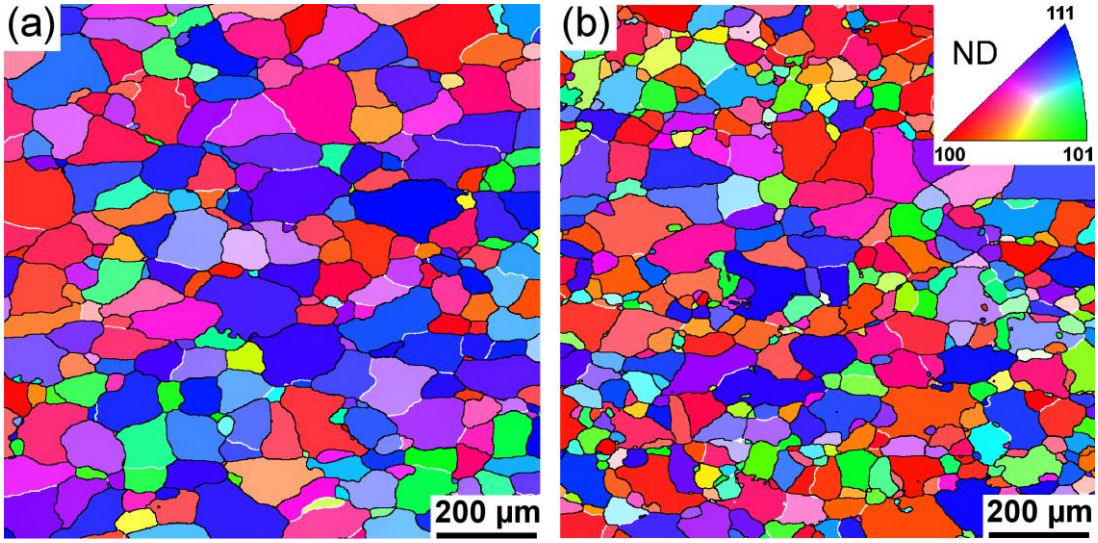

Fig. 7.2. Orientation maps for samples A1 and A4. White and black lines correspond to LABs and HABs, respectively.

7.3.2 Intergranular corrosion behavior of the studied alloys

To investigate the effect of Zn on IGC resistance in the presence of 0.05 wt% Cu, the accelerated corrosion test was performed. The obtained SEM micrographs of the surface morphology of corroded A1, A2, A3, and A4 samples are shown in Fig. 7.3 (a, b, c, d), respectively. At low Zn (0.003 wt%) and 0.05 wt% Cu contents, the IGC has invaded the surface. At the same time, higher IGC resistance was obtained by adding 0.06 wt% Zn (A4) as the number of corroded GBs was considerably decreased compared to samples A1, A2, and A3. As a result of the GBs of some grains being completely corroded, some cavities on the corroded surface of all studied alloys within the IGC network were observed. Moreover, the number of fallen grains in sample A1 was higher than in sample A4 (Zn-added), as shown in Fig. 7.3 (a) and (d), respectively. It is worth mentioning that the extension of the IGC observed in sample A4 is much less than the one observed in sample A1, seen in Fig. 7.3(e-h).

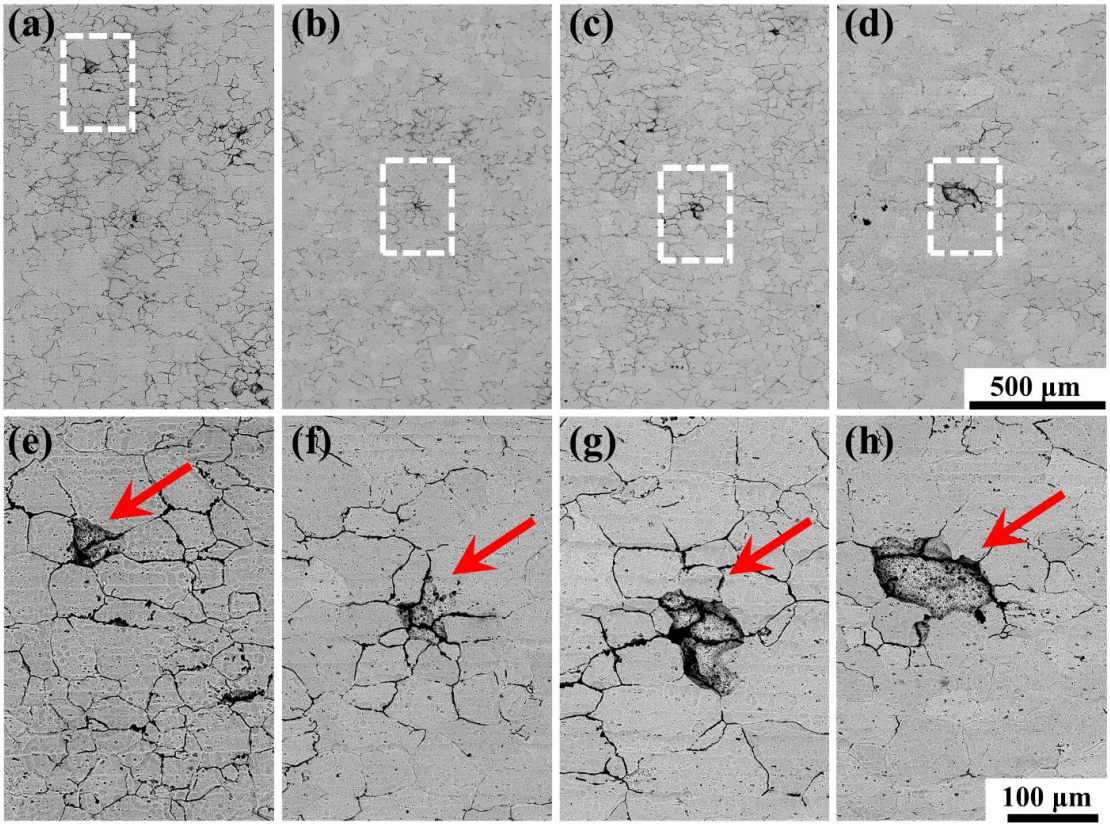

Fig. 7.3. SEM (BSE) micrographs of alloys with different zinc content after 24 h exposure in acidified solution: (a) Alloy A1, (b) Alloy A2, (c) Alloy A3, and (d) Alloy A4; (e, f, g and h) magnified BSE images of framed area in (a, b, c, and d) showing typical IGC morphology of alloys A1, A2, A3, and A4 respectively.

The maximum penetration depth of the IGC of the four investigated alloys after 24 h immersion test was measured and shown in Fig. 7.4. The observed variation in IGC penetration depth is thought to be impacted by differences in the addition of Zn, which influences the IGC resistance of the Al-Mg-Si-0.05Cu alloys in the PA condition. The maximum penetration depth was observed in sample A1 with 0.05 wt% of Cu and the lowest amount of Zn (0.003 wt%), while the depth considerably decreased by adding 0.06 wt% Zn, as shown in Fig. 7.4d. This observation indicates that Zn addition plays a significant role in defining IGC resistance in Al-Mg-Si alloys with low levels of Cu. This agrees with the observations in Fig. 7.3, which indicated that sample A4 has significantly less corroded GBs than samples A1-3.

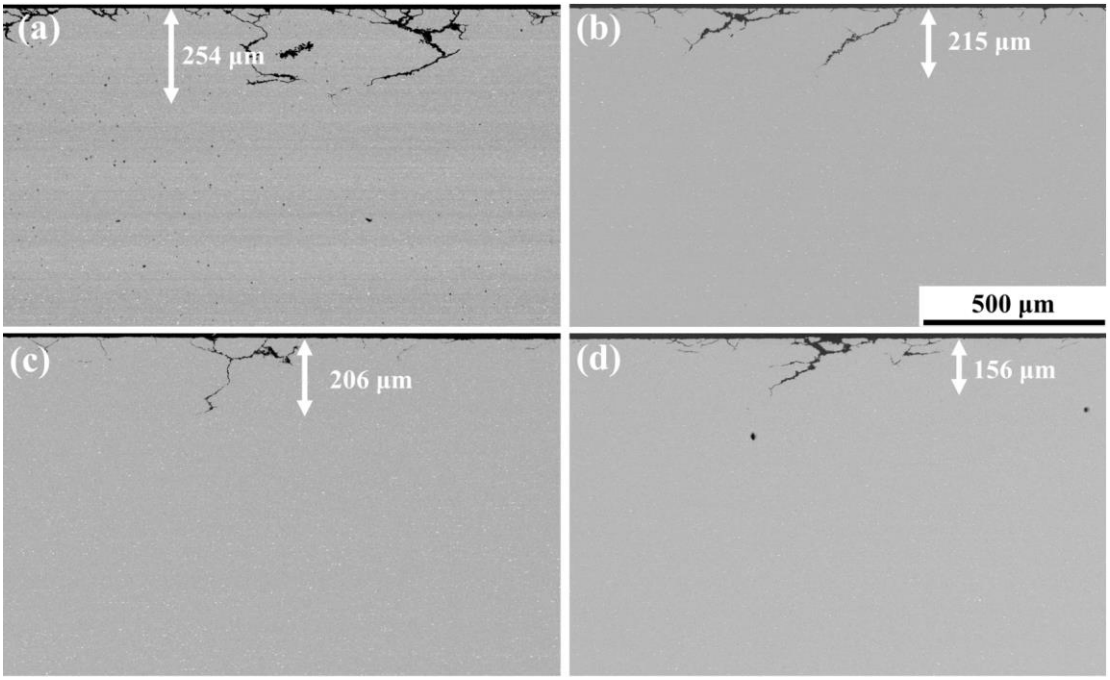

Fig. 7.4. Typical corrosion-sectional morphologies and corrosion penetration depth of the corroded samples under different minor addition of Zn (a) alloy A1, (b) alloy A2, (c) alloy A3, (d) alloy A4.

7.3.3 TEM/STEM Analysis of grain boundaries and precipitates

To reveal the nature of grain boundaries and PFZs, which directly contribute to IGC, all the studied alloys were investigated by TEM. Bright-field images acquired from the grain boundaries are shown in Fig. 7.5. The TEM micrographs show clear precipitate free zones with a width of approximately 100 nm for all investigated alloys, which is reasonable considering the material has been water-quenched after extrusion and aged to T6 temper. No clear difference in the width of PFZs is observed in samples A1-4. All samples showed the presence of fine needle-shaped and rod-shaped precipitates in the matrix adjacent to the PFZs. Moreover, all samples also showed discrete grain boundary particles. It is worth mentioning that no apparent differences in the precipitates' number density and size were observed between the alloys in both matrix and GBs.

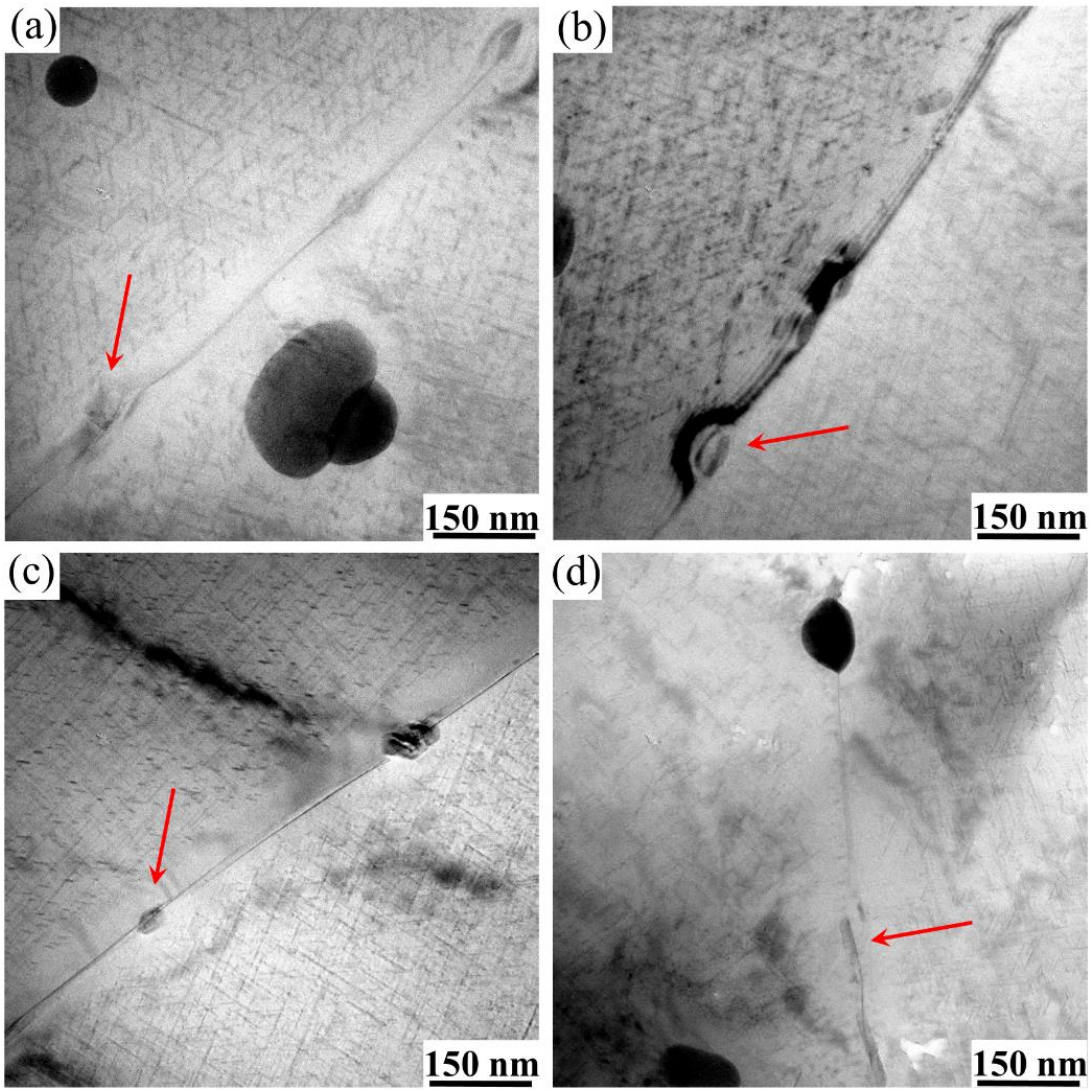

Fig. 7.5. Typical BF –TEM images of Al-Mg-Si-T6 alloy under different minor additions of Zn (a) sample A1, (b) sample A2, (c) sample A3, and (d) sample A4.

To understand the influence of minor amounts of Zn on the grain boundary chemistry and GB particles, samples A1 and A4 with the lowest and highest levels of Zn, respectively, were studied by STEM. The possible variations in the elemental composition and chemistry of grain boundaries were analyzed using EDS mapping carried out in STEM mode. Fig. 7.6 (a, c) shows a HAADF-STEM image of GBs in sample A1, which are aligned parallel to the electron beam. The local chemistry and the elemental composition of the grain boundaries and the grain boundary particle in sample A1 are shown in the EDS maps in Fig. 7.6 (b and d). A continuous PFZ with a width of approximately 100 nm to 110 nm can be readily observed on either side of the grain boundary. The EDS maps showed a continuous Cu film along the grain boundaries even in the presence of Cu-rich particle, see Fig. 7.6b. However, not all investigated GBs in alloy A1 demonstrated a Cu-enriched thin

layer; instead, some examined GB showed only discrete Q/Q′ particles along with β particles (see supplementary chapter Fig. S.1).

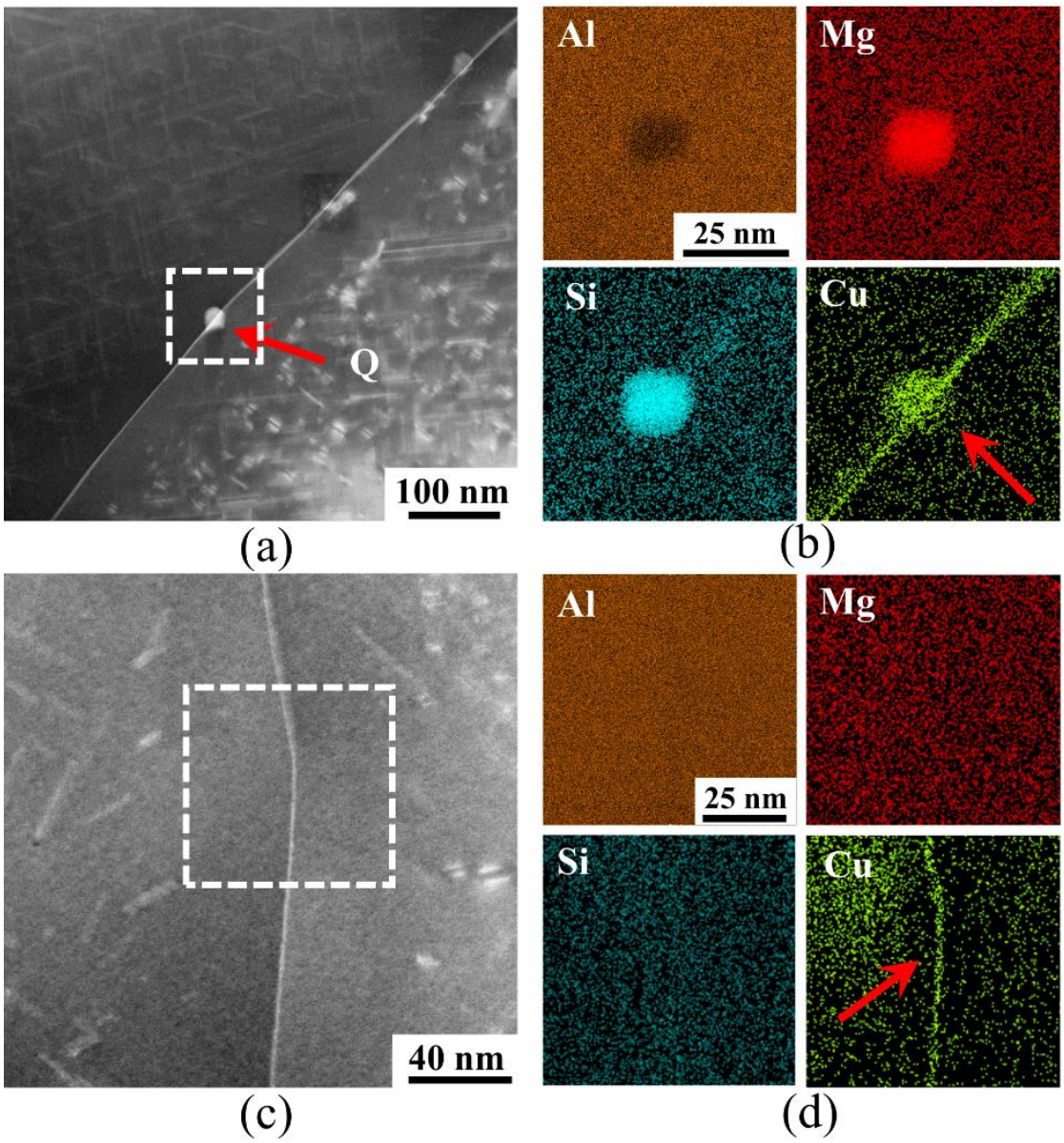

Fig. 7.6. (a, c) HAADF-STEM images showing the grain boundaries are parallel to the electron beam for A1. (b, d) Elemental maps of GB regions in sample A1, where the maps correspond to the framed regions in (a, c).

The grain boundary of sample A4 with 0.06 wt% Zn and the corresponding EDS maps are shown in Figs. 7.7 and 7.8. Similar to sample A1, a readily distinguishable PFZ was detected along the aligned grain boundary. A continuous Cu-rich film and a Zn- rich film are detected along some investigated grain boundaries of sample A4, as presented in Figs. 7.7 and 7.8.

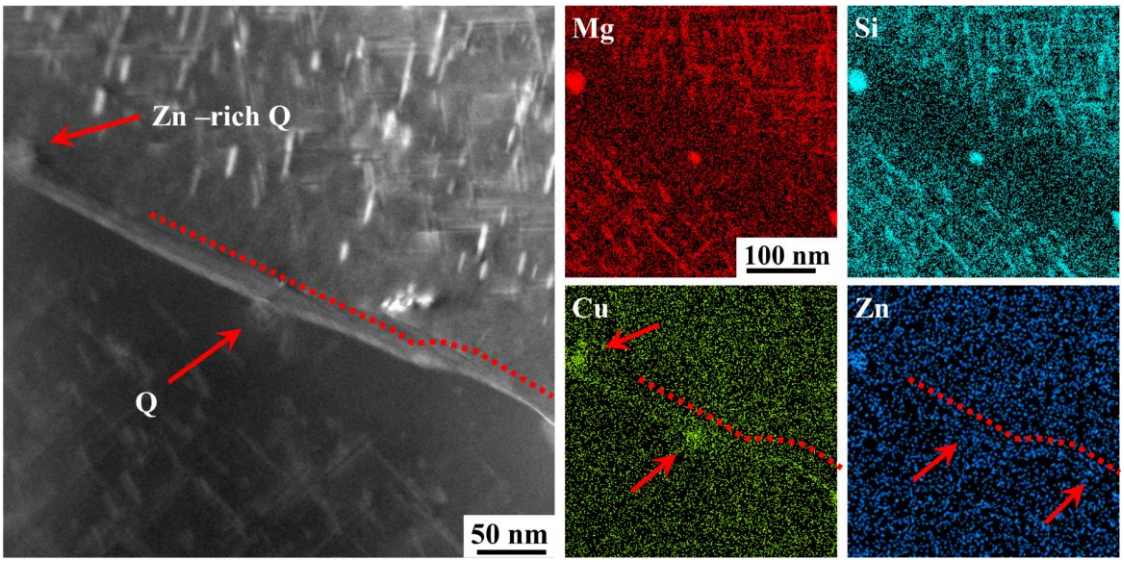

Fig. 7.7. HAADF-STEM image showing the grain boundary in sample A4, containing 0.05 wt% Cu and 0.06 wt% Zn. Corresponding Mg, Si, Cu, and Zn maps are displayed. The red arrow in the Zn map points to the Zn-film following the Cu and the grain boundary morphology.

Moreover, the Zn-EDS line scan in Fig. 7.8 shows a sharp Zn signal that closely matches the Cu signal at the grain boundary and a Zn-depleted zone of approximately 20 nm on either side. Based on several observations, the Zn concentration along the grain boundary, due to segregation, is less than that for Cu. Therefore, a higher Cu signal was observed along all investigated grain boundaries. Moreover, not all investigated grain boundaries showed Cu and Zn-rich films; in some cases, only a Cu film or clean grain boundaries were observed. Further, the TEM results indicate that Zn has a high affinity to incorporate into grain precipitates. The EDS maps and line scan in Figs. 7.7, and 7.8 show that the grain boundaries contain two types of distantly separated precipitates identified as Q/Q′ and Zn-containing Q/Q′ particles.

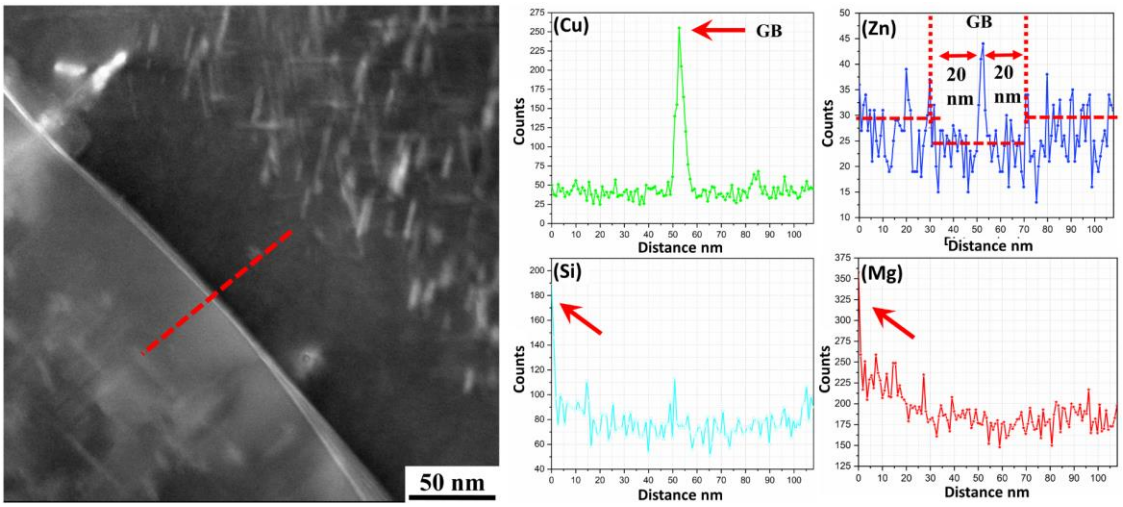

Fig. 7.8. HAADF-STEM image for sample A4 showing the GB is parallel to the electron and the EDS line scan corresponding to the dashed line over GB showing the presence of Zn and Cu rich films. The horizontal dashed-red lines in the Zn map indicate the average Zn concentration in the near grain boundary region (~20 nm) and in the precipitate free zone (~50 nm).

All the atomic resolution HAADF-STEM images shown in this work were taken from alloy A1 (with 0.05 wt% Cu) and alloy A4 (with 0.05 wt% Cu and 0.06 wt% Zn. Since the precipitates in the studied alloys grow along 〈0 0 1〉 Al directions, the Al matrix was aligned in a 〈0 0 1〉 Al zone axis, which enables imaging of precipitates cross-sections. The images were FFT-filtered as described in the experimental methods section, and atomic columns were overlaid, thus solving the precipitate atomic structures. The overlay was based on the solved crystal structures of the different metastable phases in the Al-Mg-Si(-Cu) system [23,28,42–44], the construction rules of such precipitates from [45] combined with Z-contrast information. According to the construction rules, every Al atom in the overlay is surrounded by 4 atoms found in different plane, every Mg by 5 and every Si by 3 (making it a triangular site). Cu in the Q' and C-phase unit cells is also a triangular site, while Cu atoms located at the precipitate/matrix incoherent interface could be surrounded by 4 atoms, as Al. In alloy A4 the bright columns that do not relate to known Cu configurations are assumed to be partly occupied by Zn.

Examples of the most common precipitate crystal structures in samples A1 and A4 are shown in Figs. 7.9 and 7.10, respectively. The precipitates presented can be considered representative for each alloy as they were chosen from a series of images. Starting with Fig. 7.9(a, c, and d) acquired from alloy A1, β″ and fragmented β″ (containing at least one unit configuration different from β″ structural unit) are the primary precipitates observed in the alloy.

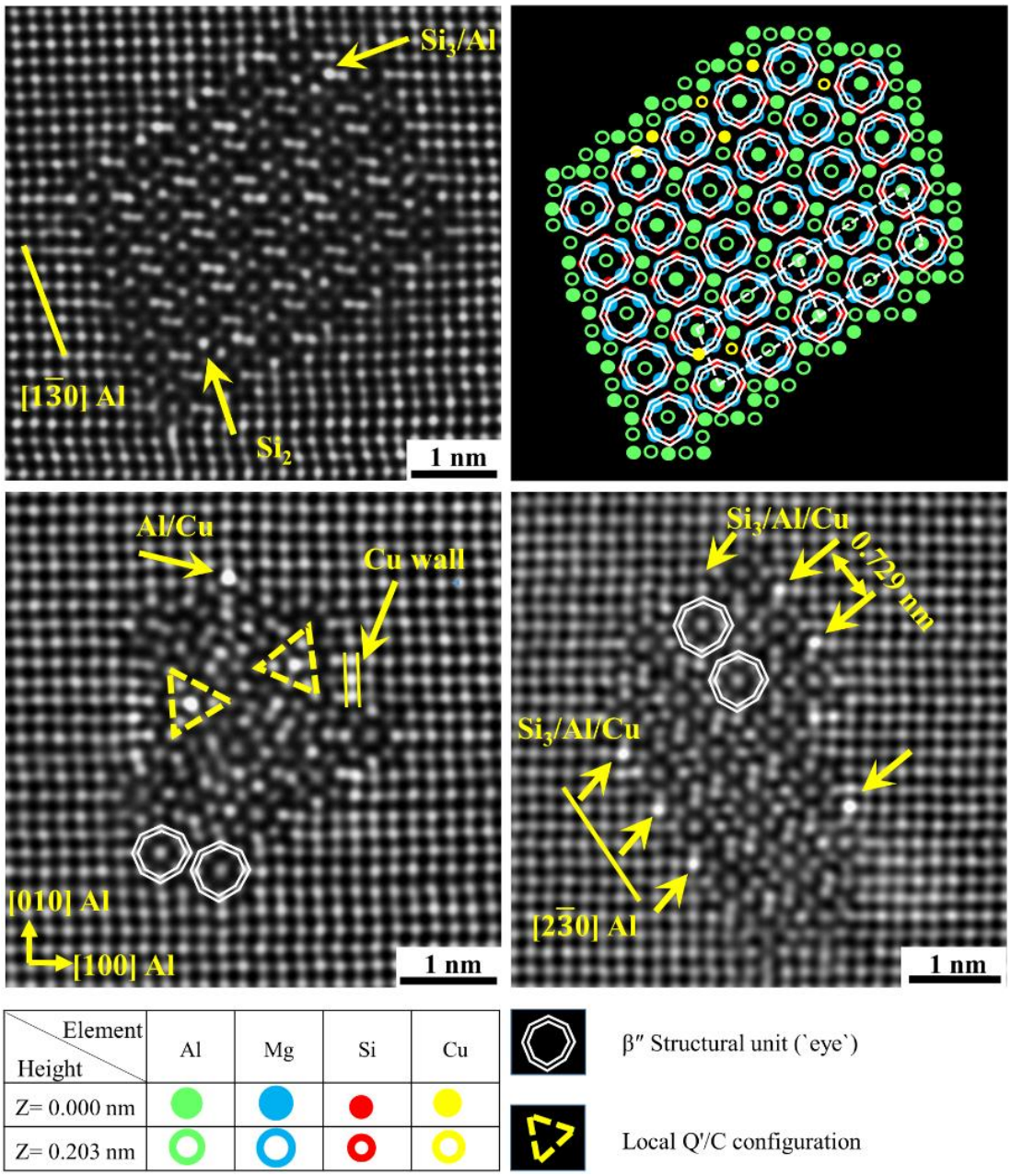

Fig. 7.9. HAADF-STEM lattice images (a, c, and d) of precipitates cross-section for Al-Mg-Si alloy with 0.05 wt% Cu (A1) T6, and (b) shows the suggested atomic overlay of (a).

Almost all precipitates in sample A1 showed some columns with a higher intensity than other equivalent columns due to partial occupancy of Cu. Interestingly, 0.05 wt% of Cu affected the precipitates noticeably and unexpectedly, according to the literature considering both the concentration and aging condition. Q′/C configurations were observed in the β″ precipitate crystal structures, leading to an alteration of its crystal structure, as seen in Fig. 7.9(c). Precipitates in sample A4 exhibited noticeable differences concerning their crystal structures as more disordered structure was noticed compared to sample A1,

see Fig. 7.10(a, d). Moreover, brighter columns inside β″ structure, namely Si_3/Al, Si_1, and Si_2 sites are observed, see Fig. 7.10.c.

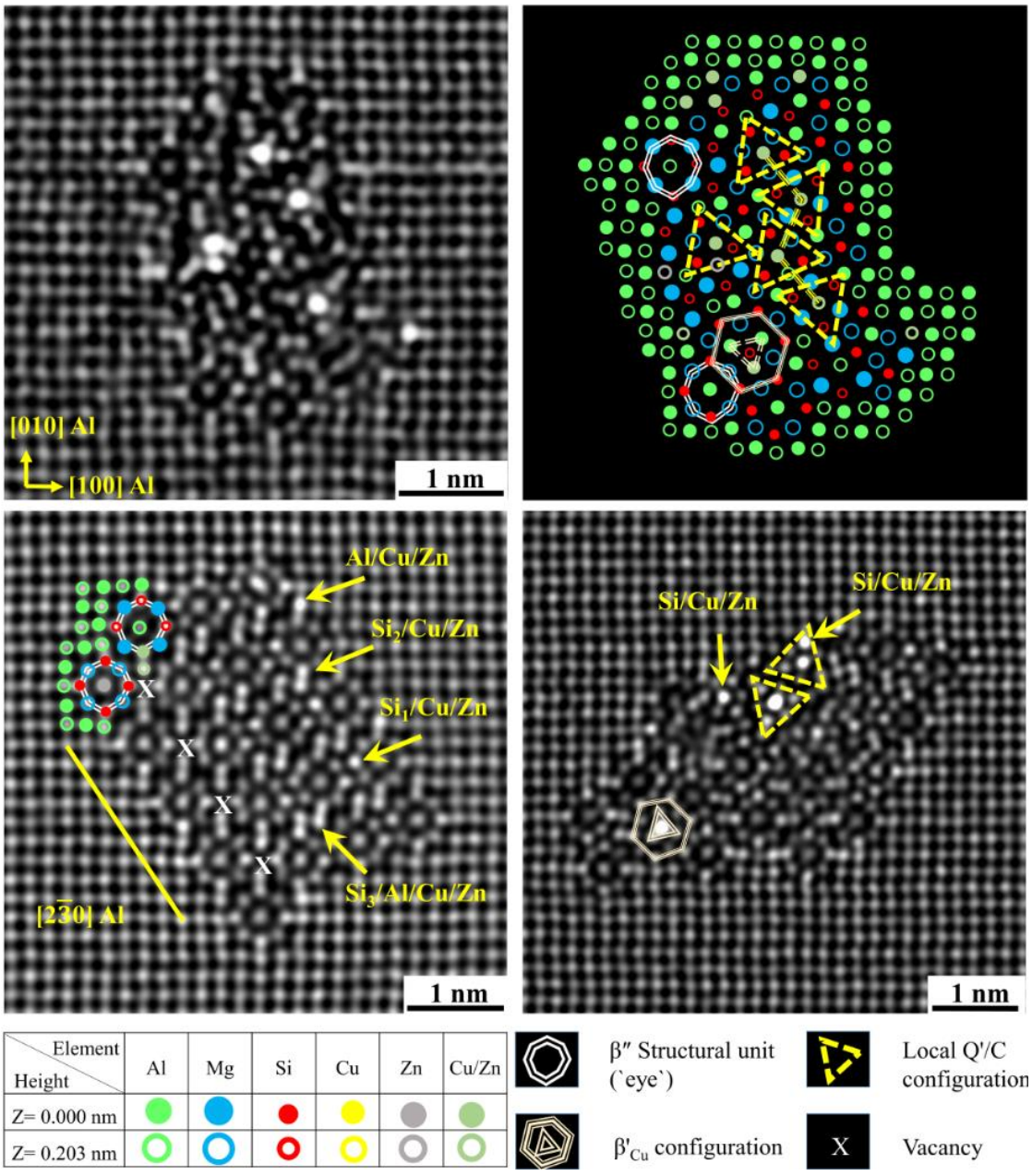

Fig. 7.10. HAADF-STEM lattice images (a, c, and d) of precipitates cross-section for Al-Mg-Si alloy with 0.05 wt% Cu and 0.06 wt% Zn (A4 T6), (b) the corresponding suggested atomic overlay of (a).

7.3.4 AFM/SKPFM analysis of grain boundaries

The segregation of Cu and Zn toward the grain boundaries and forming the Cu/Zn-rich films with different work function energy (WFE) and surface potential than the matrix, can act as a potential site for the initiation of micro galvanic coupling. Thus, accelerating/slowing down the occurrence of the intergranular corrosion depending on the

concentration of each element along the grain boundaries (as confirmed in STEM images in Figs. 7.7 and 7.8). Therefore, the AFM/SKPFM maps of grain boundary in A4 containing the Cu/Zn nanometric-enriched film were performed to evaluate the surface potential and/or surface charge difference at the grain boundary.

Fig. 7.11(a, b) displays the low magnification topography and surface potential images of grain boundary alongside various large separated intermetallic (IM) and dispersoid particles. It is discernible that all distributed large IMPs represent the lowest surface potential with various values than the matrix (~30-80 mV) due to the slight variation in the local distribution of chemical composition and/or oxide film. To better ascertain the local surface potential and/or surface charge at the GB, a high-magnified AFM/SKPFM of the GB region was conducted as presented in Fig. 7.11 (c, d). The SEM image in Fig. 7.11(e) obviously proves the two different grains and the grain boundary corresponding to AFM/SKPFM images, see Fig. 7.11(c, d). Moreover, all selected sites crossing the grain boundary in Fig. 7.11(f, g) exhibit approximately the same surface potential difference value of ~5 mV that is higher than the grain boundary region and Al matrix.

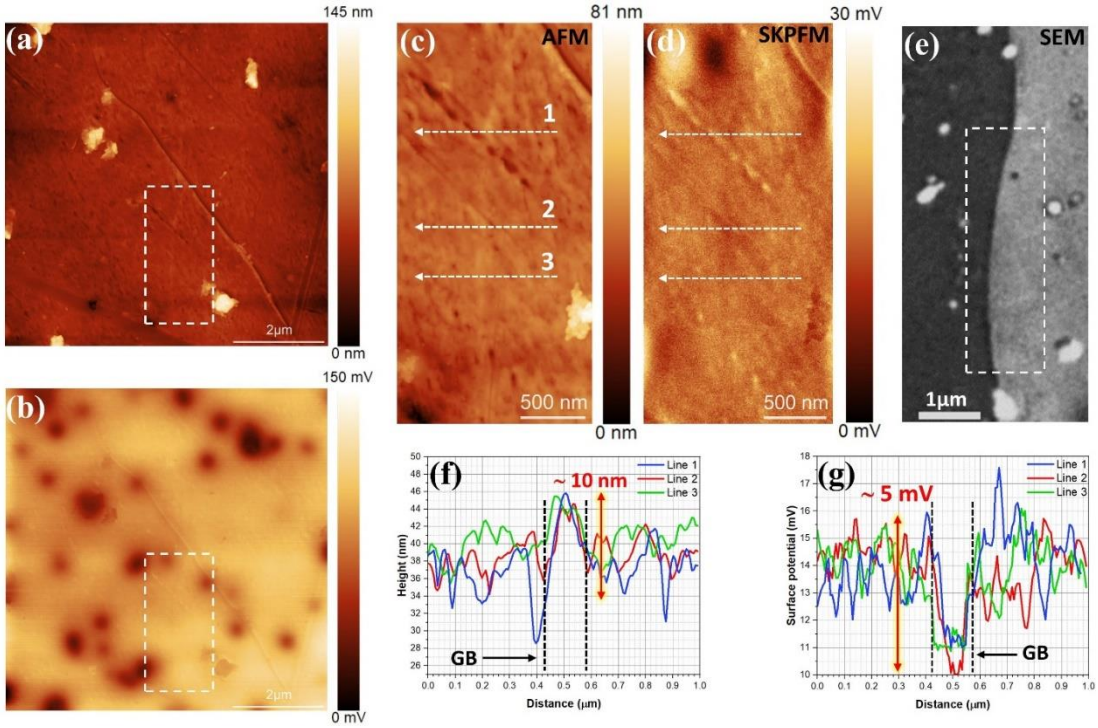

Fig. 7.11. Low magnification of (a) topography and (b) surface potential maps of grain boundary in A4. High magnification of (c) topography and (d) surface potential maps of grain boundary in the marked region in (a) and (b), (e) SEM image of analyzed grain boundary by AFM/SKPFM, (f, g) topography and surface potential line profiles obtained from (c) and (d).

7.4 Discussion

The corrosion behavior of the surface layer directly exposed to the surrounding environment is crucial in this study. As shown in Fig. 7.1, the material surface comprises a recrystallized layer with a thickness of ca. 0.4 mm. A key finding from this study is the observation that improved corrosion properties can be obtained by controlling the Zn-additions in the presence of a low Cu concentration (0.05 wt%). Further, minor additions of Zn and Cu can significantly affect the crystal structure of the hardening precipitates. Critical insights into the different behavior of Cu and Zn concerning segregation toward the grain boundaries and the affinity to enter and alter the precipitate crystal structures are obtained. To the best of the authors' knowledge, this work constitutes the first detailed investigation into the effect of combined Cu and Zn additions in low concentrations for the industrially important AA6082-T6. Our findings provide evidence of the possibility of improving the intergranular corrosion resistance of recycled 6xxx Al alloys by balancing the Zn/Cu addition levels without compromising the mechanical properties by aging.

7.4.1 Microstructure

As shown in Fig. 7.5, no apparent differences could be observed in the microstructure for different additions of Zn. All studied alloys showed the presence of needle-shaped β″ and rod-shaped β′ precipitates. Moreover, no clear difference in the size and number density of the precipitates was recorded. This result is in agreement with Saito et al. [3], who studied the effect of Zn up to 1 wt% addition on the precipitation in Al-Mg-Si alloys. Moreover, based on HAADF-STEM images shown in Fig. 7.10, the Cu/Zn addition did not alter the precipitation sequence nor introduce different types of precipitates usually found in Al-Zn-Mg alloys, such as η-$MgZn_2$ or its precursor.

In sample A1, Cu atoms incorporate into the crystal structure of the β″ precipitates and preferentially replace or partially occupy the Si_3/Al atomic columns [46,47], see Fig. 7.9(a, d). For the disordered precipitates, at least two of the following precipitate phase substructures coexisted within one single precipitate: β″, $β'_{Cu}$, or Q'/C, see Fig. 7.9(c). These findings demonstrate how 0.05 wt% Cu can influence the precipitate structures in Al-Mg-Si alloys in PA conditions. Sunde et al. [48,49] investigated the influence of low Cu additions on the crystal structure of Al-Mg-Si precipitates under different aging conditions. It was reported that the majority of the precipitates in 6082-type alloys with 0.03 and 0.09

wt% Cu at PA condition were pure β″. In the 0.03 wt% Cu alloy, Cu atoms did not affect the crystal structure of β″, showing only slight enrichment of specific atomic columns in the β″ structure, or residing at the β″/Al interface, which is also seen in Fig. 7.9(d). This is similar to previous observations for a leaner Al-Mg-Si-0.09 wt% Cu alloy studied by Saito et al. [50], where the presence of Cu at the β″/Al interface was demonstrated to suppress the misfit dislocations recorded in the absence of Cu. In agreement with the findings of the present study, β'_{Cu} sub-units were only found in β″ precipitates in the presence of 0.09 wt% Cu alloy for 6082-T6 [40]. Therefore, our finding extends the Cu critical range that can introduce different types of sub-unit structures of well-known phases in Al-Mg-Si in the PA condition from 0.09 to 0.05 wt%. β'_{Cu} is structurally identical to the β'_{Ag} precipitate phase studied by Marioara et al. [51].

In alloy A4 (0.06 wt% Zn), changes in the precipitate structure and an increase of the fraction of disordered precipitates were observed; see Fig. 7.10(a, d). The β″ precipitate is still the primary hardening precipitate, but in particular the amount of fragmented structures is increased significantly when compared to alloy A1. As expected, no Al-Mg-Zn system precipitate phases (e.g. η-$MgZn_2$ or its precursors) were found in the alloy A4 microstructure, which requires much higher Zn concentrations. Saito et al. [3] reported that only Al-Mg-Si system precipitate types were observed in an Al-Mg-Si alloy containing up to 1 wt% Zn, with no evidence of the formation of Al-Mg-Zn system precipitates. Ding et al. [35] reported that the fast age hardening response observed in Al-Mg-Si with 3 wt% Zn was directly related to the formation of η-$MgZn_2$.

7.4.2 Susceptibility to IGC

Grain boundaries in the studied alloys showed a clear difference in the chemical composition of grain boundary particles as well as the solid-state film formed by adding small Zn concentrations. The presence of a Cu film along the grain boundaries as well as the Q/Q′ precipitates in sample A1 is thought to be the driving force for the IGC to take place, resulting in a low IGC resistance. Moreover, the additional presence of β (Mg_2Si) precipitates will promote IGC as they will act as an anode when exposed to the acidified solution [1,5,52]. The selective dissolution of Mg from β (Mg_2Si) precipitates [53,54] leaves Si-rich remnants, which will further act as active cathodes supporting the cathodic sites until the oxidation of Si occurs [12,53,55,56]. This observation explained the relatively high IGC susceptibility of alloy A1 as the Cu film in addition to the Q/Q′ phases

will act as a cathode and the adjacent area, together with β particles, will act as an anode resulting in the dissolution of PFZs and GBs [14,57–59].

On the other hand, as the Zn concentration is increased, the extension of the IGC and the penetration depth decreased notably, see Figs. 7.3 and 7.4, respectively. In the absence of Zn, Q/Q′ precipitates, β particles, and Cu films were observed along the GBs. With the addition of 0.06 wt% Zn, Q/Q′ precipitates, Q/Q′ precipitates with Zn, as well as Cu and Zn films were observed along the GBs, as seen in Figs. 7.6, 7.7 and 7.8. The Zn segregation to a Q/Q′ grain boundary particles can be clearly seen in Fig. 7.7. Based on STEM observations and previous literature findings, Zn is likely located both at or near the precipitate/matrix interface, as well as inside the precipitate crystal structure, and thus may affect its electrochemical potential. Furthermore, indications of Zn films at the grain boundaries at such very low Zn concentrations are observed (see Figs. 7.7 and 7.8). Any Zn presence at or near GBs may act to reduce the detrimental effect of Cu by balancing the potential difference between GBs, GB particles, and PFZ. The results indicate that this could be the case when Zn is added in approximately similar levels as for Cu at low concentrations, thus minimizing the potential differences between PFZ and the Al matrix, and therefore resulting in better IGC performance.

The influence of 0.2 wt% of Zn on the IGC of Al-0.91Mg-0.97Si alloys was studied by Chi et al. [39] using GB/T 7998—2005 standard [60]. According to their results, 0.2 wt% Zn addition negatively influenced the IGC resistance in Al-Mg-Si alloy in PA condition. Guo et al. [61] investigated the effect of 1, 2, 3, and 4 wt% of Zn on the IGC resistance in Al-0.9Mg-0.6Si with 0.2 wt% Cu. It is claimed that the susceptibility to IGC increased with increasing Zn content up to 1 wt%, then decreased after Zn concentration exceeded 1 wt%. The highest IGC resistance in the PA Al-Mg-Si with 0.2 wt% Cu was obtained with 3 wt% Zn addition. Adding only Zn or Cu to Al-Mg-Si alloys will generally influence the IGC resistance negatively, and the effect is often proportional to the element concentration [1,59,62–64]. In this study, Figs. 7.3 and 7.4 show strong evidence that Zn additions can offset the negative effect of Cu additions on IGC resistance. The effect is evident when Zn additions are added at almost similar levels as for Cu, 0.06 wt% versus 0.05 wt% for the two elements, respectively.

However, in some cases, a higher Cu concentration at the grain boundaries can negatively influence the IGC resistance due to the unbalanced electrochemical potential.

The lower surface potential observed in the lower part of Fig. 7.11d can be considered a clear example of the compositional heterogeneity at the grain boundary due to unbalanced Cu/Zn concentrations. The low magnitude of the surface potential and/or surface charge difference between the GB and it is adjacent area originated due to the formation of a native oxide film, particularly in the aluminum alloy (γ-Al_2O_3 with a considerable band gap energy) [65]. Consequently, this native oxide film considerably affects the total surface potential and/or surface charge signal that causes less tendency to establish an intensive electrostatic force between metal/oxide and tip-apex in SKPFM surface-sensitive technique [66].

A schematic illustration of the fundamental principle of Kelvin probe analysis alongside energy diagrams between the GB region and AFM tip apex is demonstrated in Fig. 7.12. Since the AFM tip-apex is larger than the real GB [67], the surface potential map of the grain boundary detected by the Kelvin probe is an electrical grain boundary with a space charge region (mixing of surface potential/surface charge) instead of crystallographic grain boundaries. Therefore, due to the localized charges at grain boundaries as defect states, a band bending in energy levels appears, resulting in establishing the "contact potential difference" (ΔCPD) [68,69]. Likewise, this band bending is slightly downward, which confirms the depletion of the electrons in GB surrounding (positive charges) due to different surface potential or WFE between GB and G or PFZ regions.

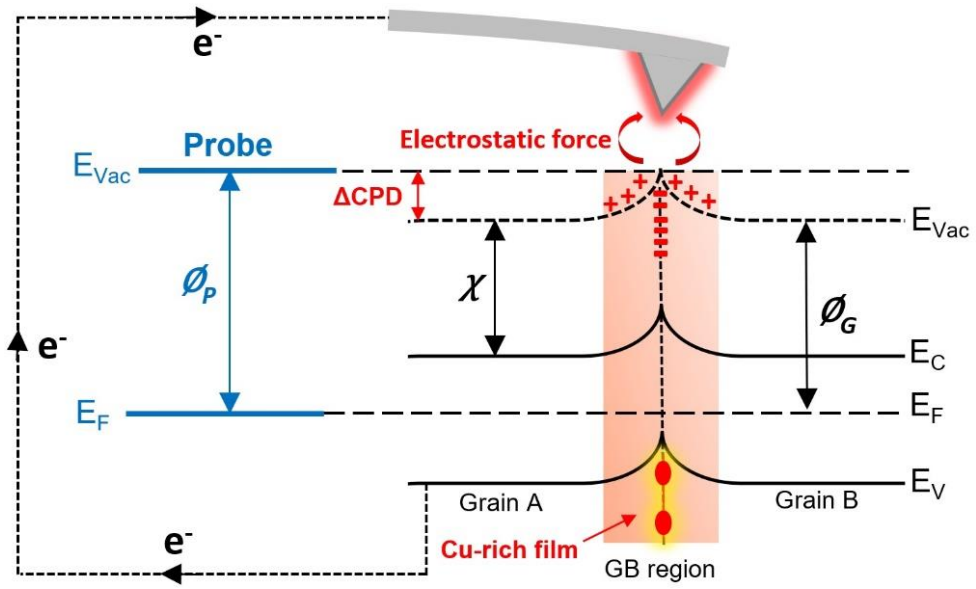

Fig. 7.12. Schematic demonstration of the SKPFM principle along with the energy level diagram during the electrostatic interaction between a conductive AFM tip-apex and GB/grain interface composed by Cu enriched-trace at the grain boundary, The abbreviations defined as valence and

conduction bands (E_V and E_C), Fermi level (E_F), electron affinity (χ), and vacuum level (E_{Vac}), work function energy of probe and grain ($\emptyset_p$ and $\emptyset_G$).

7.5 Conclusions

This study reveals an important strategy for improving the intergranular corrosion resistance of a 6082 Al-Mg-Si alloy with 0.05 wt% Cu in the PA condition by introducing approximately similar Zn addition (0.06 wt%). The results indicate that the underlying mechanism involves minimizing the potential differences between grain boundary regions, grain boundary particles, precipitate free zones, and the Al matrix. Furthermore, this work demonstrates how minor additions of Zn and/or Cu can influence the crystal structure of Al-Mg-Si precipitates in PA condition. The following conclusions were drawn:

- The 0.05 wt% Cu-containing Al-Mg-Si alloy in the PA condition is found to be highly susceptible to IGC. The driving force for the IGC is the formation of Cu-rich films in addition to the presence of Q/Q′ and β particles along the grain boundaries.
- The intergranular corrosion resistance in Al-Mg-Si with the minor addition of Cu can be controlled by adding an appropriate amount of Zn. In this work, 0.06 wt% Zn addition noticeably suppressed the intergranular corrosion in Al-Mg-Si with 0.05 wt% Cu. The presence of Zn in Q/Q′ precipitates and at a relatively higher concentration at the grain boundary, along with the Cu-rich film, reduced the driving force for the IGC by reducing the potential difference between the cathodic and the anodic sites.
- Introducing 0.05 wt% Cu and 0.06 wt% Zn to Al-Mg-Si can significantly influence the precipitate crystal structures as a high number of the precipitates was found to be disordered. Two different Cu-containing sub-units were detected in the crystal structure of β″ precipitates; the Q′/C sub-unit and β'_{Cu} sub-unit.
- Once Cu is entering the precipitates, it enters them within its established unit structures, e.g., Q/Q′ and/or β'_{Cu} unit structures. However, Zn did not show a tendency to occupy specific columns in the precipitate structure.

CRediT authorship contribution statement

Emad H. Bartawi: Conceptualization, Methodology, Investigation, Formal analysis, Writing - Original Draft, **Calin D. Marioara:** Writing - Review & Editing, Formal analysis, **Ghada Shaban:** Formal analysis, **Ehsan Rahimi:** Writing - Review & Editing, Formal analysis, **Oleg Mishin:** Writing - Review & Editing, Formal analysis, Jonas K. Sunde: Writing - Review & Editing, **Yaiza Gonzalez-Garcia**: Writing - Review & Editing, **Randi Holmestad:** Writing - Review & Editing**, Rajan Ambat:** Conceptualization, Supervision, Writing - Review & Editing, Project administration, Funding acquisition.

Acknowledgements

The authors would like to thank Hydro Aluminium, Norway, for supplying the material. The authors also would like to thank Dr. J. Kling from DTU Nanolab and Dr. Ruben Bjørge from SINTEF Industry for their assistance during STEM experiments. EHB and RA acknowledge funding from the Independent Research Fund Denmark (grant number 9041-00240A). Also, this project has received funding from the European Union's Horizon 2020 research and innovation programme under grant agreement No 823717 – ESTEEM3. The HR-STEM work was conducted on the NORTEM (Norwegian Research Council project number: 197405) infrastructure at the TEM Gemini Centre, Trondheim, Norway.

Data Availability

The raw/processed data required to reproduce these findings cannot be shared at this time as the data also forms part of an ongoing study.

References

[1] J.R. Davis, Corrosion of aluminum and aluminum alloys, ASM international, 1999.

[2] J. Hirsch, Recent development in aluminium for automotive applications, Trans. Nonferrous Met. Soc. China. 24 (2014) 1995–2002.

[3] T. Saito, S. Wenner, E. Osmundsen, C.D. Marioara, S.J. Andersen, J. Røyset, W. Lefebvre, R. Holmestad, The effect of Zn on precipitation in Al-Mg-Si alloys, Philos. Mag. 94 (2014) 2410–2425.

[4] C.D. Marioara, A. Lervik, J. Grønvold, O. Lunder, S. Wenner, T. Furu, R. Holmestad, The correlation between intergranular corrosion resistance and copper content in the precipitate microstructure in an AA6005A alloy, Metall. Mater. Trans. A. 49 (2018) 5146–5156.

[5] X. Zhang, X. Zhou, J.O. Nilsson, Corrosion behaviour of AA6082 Al-Mg-Si alloy extrusion: The influence of quench cooling rate, Corros. Sci. 150 (2019) 100–109.

[6] C. Poletti, M. Rodriguez-Hortalá, M. Hauser, C. Sommitsch, Microstructure development in hot deformed AA6082, Mater. Sci. Eng. A. 528 (2011) 2423–2430.

[7] J. Hu, W. Zhang, D. Fu, J. Teng, H. Zhang, Improvement of the mechanical properties of Al-Mg-Si alloys with nano-scale precipitates after repetitive continuous extrusion forming and T8 tempering, J. Mater. Res. Technol. 8 (2019) 5950–5960.

[8] A. Serizawa, T. Sato, M.K. Miller, Effect of cold rolling on the formation and distribution of nanoclusters during pre-aging in an Al–Mg–Si alloy, Mater. Sci. Eng. A. 561 (2013) 492–497.

[9] F. Serradj, R. Guemini, H. Farh, K. Djemmal, Study of mechanical and electrical properties of AlMgSi alloys, in: Ann. Chim. (Paris. 1914), 2010: pp. 59–69.

[10] D.J. Chakrabarti, D.E. Laughlin, Phase relations and precipitation in Al–Mg–Si alloys with Cu additions, Prog. Mater. Sci. 49 (2004) 389–410.

[11] W. Yang, S. Ji, Z. Li, M. Wang, Grain boundary precipitation induced by grain crystallographic misorientations in an extruded Al-Mg-Si-Cu alloy, J. Alloys Compd. 624 (2015) 27–30.

[12] G. Svenningsen, J.E. Lein, A. Bjørgum, J.H. Nordlien, Y. Yu, K. Nisancioglu, Effect of low copper content and heat treatment on intergranular corrosion of model AlMgSi alloys, Corros. Sci. 48 (2006) 226–242.

[13] C. Schnatterer, D. Zander, Influence of the grain boundary chemistry on the intergranular corrosion mechanisms of a high-strength Al-Mg-Si alloy, Surf. Interface Anal. 48 (2016) 750–754.

[14] G. Svenningsen, M.H. Larsen, J.C. Walmsley, J.H. Nordlien, K. Nisancioglu, Effect of artificial aging on intergranular corrosion of extruded AlMgSi alloy with small Cu content, Corros. Sci. 48 (2006) 1528–1543.

[15] G. Svenningsen, M.H. Larsen, J.H. Nordlien, K. Nisancioglu, Effect of thermomechanical history on intergranular corrosion of extruded AlMgSi(Cu) model alloy, Corros. Sci. 48 (2006) 3969–3987.

[16] Z. Wang, H. Li, F. Miao, W. Sun, B. Fang, R. Song, Z. Zheng, Improving the intergranular corrosion resistance of Al–Mg–Si–Cu alloys without strength loss by a two-step aging treatment, Mater. Sci. Eng. A. 590 (2014) 267–273.

[17] H. Hug, Ueber den einflußgeringer schwermetallgehalte auf die korrosionsbeständigkeit von Al-Mg-Si Legierungen, Aluminium. 23 (1941) 33.

[18] K. Nisancioglu, Ø. Strandmyr, Corrosion of AlMgSi alloys with Cu additions: the effect of Cu content up to 0.9 weight percent, Report no, STF34 A78052, SINTEF, Trondheim, Norw. (1978).

[19] E.H. Bartawi, O. V. Mishin, G. Shaban, J.H. Nordlien, R. Ambat, Electron microscopy analysis of grain boundaries and intergranular corrosion in aged Al-Mg-Si alloy doped with 0.05 wt% Cu, Corros. Sci. 209 (2022) 110758.

[20] E.H. Bartawi, O.V. Mishin, G. Shaban, F. Grumsen, J.H. Nordlien, R. Ambat, The effect of trace level copper content on intergranular corrosion of extruded AA6082-T6 alloys, Mater. Chem. Phys. (2023) 128303.

[21] J.F. Nie, Physical metallurgy of light alloys, Fifth Edit, Elsevier, 2014.

[22] S.K. Kairy, P.A. Rometsch, K. Diao, J.F. Nie, C.H.J. Davies, N. Birbilis, Exploring the electrochemistry of 6xxx series aluminium alloys as a function of Si to Mg ratio, Cu content, ageing conditions and microstructure, Electrochim. Acta. 190 (2016) 92–103.

[23] T. Saito, E.A. Mørtsell, S. Wenner, C.D. Marioara, S.J. Andersen, J. Friis, K. Matsuda, R. Holmestad, Atomic structures of precipitates in Al–Mg–Si alloys with small additions of other elements, Adv. Eng. Mater. 20 (2018) 1800125.

[24] W.F. Miao, D.E. Laughlin, Effects of Cu content and preaging on precipitation characteristics in aluminum alloy 6022, Metall. Mater. Trans. A. 31 (2000) 361–371.

[25] M. Murayama, K. Hono, W. Miao, D.E. Laughlin, The effect of Cu additions on the precipitation kinetics in an Al-Mg-Si alloy with excess Si, Metall. Mater. Trans. A. 32 (2001) 239–246.

[26] Z. Jia, L. Ding, L. Cao, R. Sanders, S. Li, Q. Liu, The influence of composition on the clustering and precipitation behavior of Al-Mg-Si-Cu alloys, Metall. Mater. Trans. A. 48 (2017) 459–473.

[27] C. Cayron, L. Sagalowicz, L. Sagalowicz, P.A. Buffat, Structural phase transition in Al-Cu-Mg-Si alloys by transmission electron microscopy study on an Al-4 wt% Cu-1 wt% Mg-Ag alloy reinforced by SiC particles, Philos. Mag. A. 79 (1999) 2833–2851.

[28] C.D. Marioara, S.J. Andersen, T.N. Stene, H. Hasting, J. Walmsley, A.T.J. Van Helvoort, R. Holmestad, The effect of Cu on precipitation in Al-Mg-Si alloys, Philos. Mag. 87 (2007) 3385–3413.

[29] C.D. Marioara, S.J. Andersen, J. Røyset, O. Reiso, S. Gulbrandsen-Dahl, T.E. Nicolaisen, I.E. Opheim, J.F. Helgaker, R. Holmestad, Improving thermal stability in Cu-containing Al-Mg-Si alloys by precipitate optimization, Metall. Mater. Trans. A. 45 (2014) 2938–2949.

[30] T. Saito, C.D. Marioara, S.J. Andersen, W. Lefebvre, R. Holmestad, Aberration-corrected HAADF-STEM investigations of precipitate structures in Al-Mg-Si alloys with low Cu additions, Philos. Mag. 94 (2014) 520–531.

[31] K. Matsuda, S. Ikeno, Y. Uetani, T. Sato, Metastable phases in an Al-Mg-Si alloy containing copper, Metall. Mater. Trans. A. 32 (2001) 1293–1299.

[32] L. Arnberg, B. Aurivillius, E. Wahlström, G. Malmros, J. Sjöblom, T.G. Strand, V.F. Sukhoverkhov, The Crystal Structure of Al(x)Cu2Mg(12-x)Si7, (h-AlCuMgSi)., Acta Chem. Scand. 34 (1980) 1–5.

[33] X. Xu, W. Zhu, M. Yuan, C. Liang, Y. Deng, The effect of Zn content on the microstructure and mechanical properties of the Al-mg-Si alloy, Mater. Charact. 198 (2023) 112714.

[34] S. Zhu, Z. Li, L. Yan, X. Li, S. Huang, H. Yan, Y. Zhang, B. Xiong, Natural aging behavior in pre-aged Al–Mg–Si–Cu alloys with and without Zn addition, J. Alloys Compd. 773 (2019) 496–502.

[35] X.P. Ding, H. Cui, J.X. Zhang, H.X. Li, M.X. Guo, Z. Lin, L.Z. Zhuang, J.S. Zhang, The effect of Zn on the age hardening response in an Al-Mg-Si alloy, Mater. Des. 65 (2015) 1229–1235.

[36] M.X. Guo, Y.D. Zhang, G.J. Li, S.B. Jin, G. Sha, J.S. Zhang, L.Z. Zhuang, E.J. Lavernia,

Solute clustering in Al-Mg-Si-Cu-(Zn) alloys during aging, J. Alloys Compd. 774 (2019) 347–363.

[37] W. Yang, W. Shen, R. Zhang, K. Cao, J. Zhang, L. Liu, Enhanced age-hardening by synergistic strengthening from MgSi and MgZn precipitates in Al-Mg-Si alloy with Zn addition, Mater. Charact. 169 (2020) 110579.

[38] T. Saito, F.J.H. Ehlers, W. Lefebvre, D. Hernandez-Maldonado, R. Bjørge, C.D. Marioara, S.J. Andersen, R. Holmestad, HAADF-STEM and DFT investigations of the Zn-containing β'' phase in Al-Mg-Si alloys, Acta Mater. 78 (2014) 245–253.

[39] S. Chi, Y. Deng, X. Xu, X. Guo, Influence of minor Zn addition on precipitation behavior and intergranular corrosion properties of Al-Mg-Si alloy, Materials (Basel). 13 (2020) 650.

[40] N.N.M. K., N.M. S., Effect of Zn addition on bulk microstructure of lead-free solder SN100C, AIP Conf. Proc. 1901 (2017) 60005.

[41] E.N. ISO, Corrosion of metals and alloys. Determination of resistance to intergranular corrosion of solution heat-treatable aluminium alloys, Br. Stand. Inst. (2005).

[42] S.J. Andersen, H.W. Zandbergen, J. Jansen, C. Træholt, U. Tundal, O. Reiso, The crystal structure of the β″ phase in Al-Mg-Si Alloys, Acta Mater. 46 (1998) 3283–3298.

[43] S.J. Andersen, C.D. Marioara, R. Vissers, A. Frøseth, H.W. Zandbergen, The structural relation between precipitates in Al–Mg–Si alloys, the Al-matrix and diamond silicon, with emphasis on the trigonal phase U1-MgAl2Si2, Mater. Sci. Eng. A. 444 (2007) 157–169.

[44] S.J. Andersen, C.D. Marioara, A. Frøseth, R. Vissers, H.W. Zandbergen, Crystal structure of the orthorhombic U2-Al4Mg4 Si4 precipitate in the Al-Mg-Si alloy system and its relation to the β′ and β″ phases, Mater. Sci. Eng. A. 390 (2005) 127–138.

[45] S.J. Andersen, C.D. Marioara, J. Friis, R. Bjørge, Q. Du, I.G. Ringdalen, S. Wenner, E.A. Mørtsell, R. Holmestad, T. Saito, J. Røyset, O. Reiso, Directionality and column arrangement principles of precipitates in Al-Mg-Si-(Cu) and Al-Mg-Cu linked to line defect in Al, Mater. Sci. Forum. 877 (2017) 461–470.

[46] R. Vissers, M.A. van Huis, J. Jansen, H.W. Zandbergen, C.D. Marioara, S.J. Andersen, The crystal structure of the β′ phase in Al–Mg–Si alloys, Acta Mater. 55 (2007) 3815–3823.

[47] H.S. Hasting, A.G. Frøseth, S.J. Andersen, R. Vissers, J.C. Walmsley, C.D. Marioara, F. Danoix, W. Lefebvre, R. Holmestad, Composition of B″ precipitates in Al-Mg-Si alloys by atom probe tomography and first principles calculations, J. Appl. Phys. 106 (2009) 106.12.

[48] J.K. Sunde, C.D. Marioara, R. Holmestad, The effect of low Cu additions on precipitate crystal structures in overaged Al-Mg-Si(-Cu) alloys, Mater. Charact. 160 (2020) 110087.

[49] J.K. Sunde, C.D. Marioara, A.T.J. van Helvoort, R. Holmestad, The evolution of precipitate crystal structures in an Al-Mg-Si(-Cu) alloy studied by a combined HAADF-STEM and SPED approach, Mater. Charact. 142 (2018) 458–469.

[50] T. Saito, F.J.H. Ehlers, W. Lefebvre, D. Hernandez-Maldonado, R. Bjørge, C.D. Marioara, S.J. Andersen, E.A. Mørtsell, R. Holmestad, Cu atoms suppress misfit dislocations at the β″/Al interface in Al-Mg-Si alloys, Scr. Mater. 110 (2016) 6–9.

[51] C.D. Marioara, J. Nakamura, K. Matsuda, S.J. Andersen, R. Holmestad, T. Sato, T. Kawabata, S. Ikeno, HAADF-STEM study of β-type precipitates in an over-aged Al-Mg-Si-Ag alloy, Philos. Mag. 92 (2012) 1149–1158.

[52] R.K. Gupta, N.L. Sukiman, K.M. Fleming, M.A. Gibson, N. Birbilis, Electrochemical behavior and localized corrosion associated with Mg2Si particles in Al and Mg alloys, ECS Electrochem. Lett. 1 (2012) 1–4.

[53] F. Eckermann, T. Suter, P.J. Uggowitzer, A. Afseth, P. Schmutz, The influence of MgSi particle reactivity and dissolution processes on corrosion in Al–Mg–Si alloys, Electrochim. Acta. 54 (2008) 844–855.

[54] K.M. Fleming, A. Zhu, J.R. Scully, Corrosion of AA6061 brazed with an Al-Si alloy: Effects of Si on metallurgical and corrosion behavior, Corrosion. 68 (2012) 1126–1145.

[55] F.L. Zeng, Z.L. Wei, J.F. Li, C.X. Li, X. Tan, Z. Zhang, Z.Q. Zheng, Corrosion mechanism associated with Mg2Si and Si particles in Al–Mg–Si alloys, Trans. Nonferrous Met. Soc. China. 21 (2011) 2559–2567.

[56] L.I. Chaoxing, L.I. Jinfeng, B. Nick, J.I.A. Zhiqiang, Z. Ziqiao, Synergetic effect of Mg2Si and Si particles on intergranular corrosion of Al-Mg-Si alloys through multi-electrode coupling system, J. Chinese Soc. Corros. Prot. 30 (2010) 107–113.

[57] S.K. Kairy, T. Alam, P.A. Rometsch, C.H.J. Davies, R. Banerjee, N. Birbilis, Understanding the origins of intergranular corrosion in copper-containing Al-Mg-Si alloys, Metall. Mater. Trans. A Phys. Metall. Mater. Sci. 47 (2016) 985–989.

[58] M.H. Larsen, J.C. Walmsley, O. Lunder, R.H. Mathiesen, K. Nisancioglu, Intergranular corrosion of copper-containing AA6xxx AlMgSi aluminum alloys, J. Electrochem. Soc. 155 (2008) C550.

[59] Y. Zou, Q. Liu, Z. Jia, Y. Xing, L. Ding, X. Wang, The intergranular corrosion behavior of

6000-series alloys with different Mg/Si and Cu content, Appl. Surf. Sci. 405 (2017) 489–496.

[60] G. 7998-2005, Test method for intergranular corrosion of aluminium alloy, China Int. Stand. (2005).

[61] M.X. Guo, J.Q. Du, C.H. Zheng, J.S. Zhang, L.Z. Zhuang, Influence of Zn contents on precipitation and corrosion of Al-Mg-Si-Cu-Zn alloys for automotive applications, J. Alloys Compd. 778 (2019) 256–270.

[62] X. Xu, Y. Deng, Q. Pan, X. Guo, Enhancing the intergranular corrosion resistance of the Al–Mg–Si alloy with low Zn content by the interrupted aging treatment, Metall. Mater. Trans. A. 52 (2021) 4907–4921.

[63] M.H. Larsen, J.C. Walmsley, O. Lunder, K. Nisancioglu, Significance of low copper content on grain boundary nanostructure and intergranular corrosion of AlMgSi(Cu) model alloys, in: Mater. Sci. Forum, Trans Tech Publications Ltd, 2006: pp. 667–672.

[64] H. Zhan, J.M.C. Mol, F. Hannour, L. Zhuang, H. Terryn, J.H.W. De Wit, The influence of copper content on intergranular corrosion of model AlMgSi(Cu) alloys, Mater. Corros. 59 (2008) 670–675.

[65] L. Nguyen, T. Hashimoto, D.N. Zakharov, E.A. Stach, A.P. Rooney, B. Berkels, G.E. Thompson, S.J. Haigh, T.L. Burnett, Atomic-scale insights into the oxidation of aluminum, ACS Appl. Mater. Interfaces. 10 (2018) 2230–2235.

[66] E. Rahimi, A. Imani, M. Lekka, F. Andreatta, Y. Gonzalez-Garcia, J.M.C. Mol, E. Asselin, L. Fedrizzi, Morphological and surface potential characterization of protein nanobiofilm formation on magnesium alloy oxide: their role in biodegradation, Langmuir. 38 (2022) 10854–10866.

[67] J. Gonzalez-Julian, K. Neuhaus, M. Bernemann, J. Pereira da Silva, A. Laptev, M. Bram, O. Guillon, Unveiling the mechanisms of cold sintering of ZnO at 250 °C by varying applied stress and characterizing grain boundaries by Kelvin probe force microscopy, Acta Mater. 144 (2018) 116–128.

[68] C. Leendertz, F. Streicher, M.C. Lux-Steiner, S. Sadewasser, Evaluation of Kelvin probe force microscopy for imaging grain boundaries in chalcopyrite thin films, Appl. Phys. Lett. 89 (2006).

[69] J. Zhan, Z. Chen, Q. Jiao, Y. Feng, C. Li, Y. Chen, F. Jiao, X. Kang, S. Li, T. Yu, G. Zhang, B. Shen, Study on strain relaxation distribution in GaN-based μLEDs by Kelvin probe force microscopy, Phys. Status Solidi Curr. Top. Solid State Phys. 14 (2017) 2–5.

8. Paper IV

Effect of minor addition of Zn on precipitate crystal structures and intergranular corrosion in 6082 Al-Mg-Si alloys

Emad H. Bartawi[1,*], Calin D. Marioara[2], Ehsan Rahimi[3], Ghada Shaban[1], Jonas K. Sunde[4], Yaiza Gonzalez-Garcia[3], Randi Holmestad[5], Rajan Ambat[1]

[1] Department of Civil and Mechanical Engineering, Technical University of Denmark, Kgs. Lyngby 2800, Denmark

[2] Materials and Nanotechnology, SINTEF Industry, Trondheim N-7465, Norway

[3]Department of Materials Science and Engineering, Delft University of Technology, Mekelweg 2, 2628 CD Delft, The Netherlands

[4] Hydro, Innovation & Technology, Drammensveien 264, 0283, Oslo, Norway

[5]Department of Physics, NTNU, Norwegian University of Science and Technology, 7491 Trondheim, Norway

Abstract

This work focuses on understanding the impact of low Zn additions in Al-Mg-Si alloys, e.g. as a result of recycling, particularly on the microstructure and intergranular corrosion resistance. We systematically investigated the IGC susceptibility associated with 6082 Al-Mg-Si alloy in the peakaged condition with 0.003, 0.02, 0.04, and 0.06 wt% Zn additions. The IGC was evaluated using the accelerated immersion corrosion test ISO 11856 method B. The results show that the minor addition of Zn negatively influences the IGC resistance of 6082 Al alloy. Zn was found to segregate along the grain boundaries, and the STEM-EDS results indicate that the Zn incorporates into the structure of β (Mg_2Si) precipitates. No Mg-Zn precipitates are found in Al-Mg-Si alloy with 0.06 wt% Zn in the peakaged condition. The results of this work concern how trace levels of Zn related to recycling can influence the IGC resistance and precipitate structures in 6082 Al-Mg-Si alloy in the peakaged condition.

Keywords: 6082 Al-Mg-Si alloy; Intergranular corrosion; precipitate crystal structure; HAADF-STEM; SKPFM.

8.1 Introduction

Weight reduction in automotive applications is an effective strategy to reduce energy consumption and, thus, CO_2 emissions [1]. Consequently, it comes as no surprise that heat treatable Al-Mg-Si alloys showed considerable potential in future automotive applications owing to their many attractive properties, such as low density, good formability, recyclability, high strength-to-weight ratio, and outstanding corrosion resistance [2–5]. However, other challenges remain to be considered, such as improving paint baking response, formability, and localized corrosion resistance [6–9]. Although Al-Mg-Si alloys generally demonstrate acceptable corrosion resistance, intergranular corrosion (IGC) can sometimes be notable due to the presence of certain alloying elements (e.g., Cu and Zn additions) or lack of control in thermal processing (e.g. slow quenching after extrusion). It is believed that intergranular corrosion in Al-Mg-Si alloys takes place as a result of microgalvanic coupling between grain boundary particles acting as anodes and the solute depleted precipitate free zone (PFZ) acting as cathode [10–12]. Shi et al. [12] studied the localized corrosion resistance of a Cu-free Al-0.61Mg-0.76Si (wt%) alloy. It was claimed that IGC in such alloys occurs due to Si segregation to the grain boundaries (GBs) acting as an effective cathode promoting IGC. The same observation was made by Bhattamishra and Lal [13], who explored Al-0.4Mg-1.0Si alloy.

It is also claimed that the Mg/Si ratio considerably affects the IGC resistance of Al-Mg-Si and Al-Mg-Si-Cu alloys [10,11]. Kairy et al. [10] argued that Cu-free Al-Mg-Si alloys with a lower Mg/Si ratio (0.336) were more susceptible to IGC than alloys with a higher Mg/Si ratio (2.192) in the peakaged (PA) condition. It is generally accepted that Cu additions at notable concentrations (approx. $\geq$ 0.1 wt%) can negatively influence the IGC resistance of Al-Mg-Si alloys in the underaged (UA) and PA conditions. The IGC in Al-Mg-Si-Cu alloys is attributed to microgalvanic coupling between grain boundary particles, Cu-rich films located along GBs, and precipitate free zones [14–20]. According to Zou et al. [11], Cu-containing alloys with a lower Mg/Si ratio (0.55) exhibited a severe IGC, while alloys with a higher Mg/Si ratio (2.13) showed improved corrosion resistance as the pitting corrosion was the primarily observed corrosion mechanism.

To date, the literature lacks studies investigating the influence of minor Zn concentrations (≤ 0.06 wt%), anticipated to be found in recycled Al-Mg-Si alloys, focusing on the effect on alloy microstructure and IGC resistance. It was reported that relatively high Zn (≥ 0.5 wt%) additions can significantly influence the precipitation and improve age hardening response in Al-Mg-Si alloys due to an increased volume fraction of clusters compared to Zn-free alloys [21–26]. The results of Saito et al. [27] showed that Zn-added Al-0.5Mg-0.4Si alloys (≤ 1 wt%) achieved a modest increase in hardness as a function of Zn content, which is related to the rise in the number density of needle-shaped precipitates. Moreover, no precipitates of the Al-Mg-Zn (Mg-Zn η-type) alloy system were detected in their studied alloys. Zhu et al. [28] also found that 0.6 wt% Zn addition did not alter the precipitation sequence of an artificially aged Al-0.9Mg-0.8Si alloy. At the same time, the improvement in the age hardening response and thus the mechanical properties observed in a Zn-added alloy (≥ 2.37 wt%) is attributed to the formation of η-$MgZn_2$ phase precipitates and its precursor normally found in the Al-Mg-Zn system [26,29].

On the topic of IGC, Saito et al. [27] investigated the influence of Zn (≤ 1 wt%) on the IGC resistance of Al-Mg-Si in T6 temper. The results showed that alloys with Zn addition ≤ 0.11 wt% exhibited negligible IGC susceptibility. However, severe IGC was recorded in the alloy containing 1 wt% Zn, indicating that there is a critical level of Zn additions affecting the IGC resistance of Al-Mg-Si alloy is set between 0.11 and 1 wt%. It is also reported that Zn diffuses into precipitates when Zn content is 1 wt%, while the distribution of Zn is not described when Zn concentration is ≤ 0.11 wt% [27]. Therefore, understanding the influence of low Zn additions on Al-Mg-Si alloys, as a result of recycling, on the microstructure and IGC is the key focus of this work.

It appears that Zn concentrations between 0.003 and 0.06 wt% are critical to defining the IGC resistance of recycled Al-Mg-Si alloys. Moreover, the influence of small concentrations of Zn on Al-Mg-Si precipitate crystal structures is still not understood. Therefore, the present study aims to elucidate how trace levels of Zn affect the microstructure and IGC resistance of Al-Mg-Si alloys, focusing on the industrially important 6082 Al-Mg-Si alloy. The microstructure and grain boundary misorientation were investigated using optical microscopy and electron backscatter diffraction (EBSD), respectively. Scanning electron microscopy (BSE-SEM) analysis was conducted on the surface and cross-section of the corroded samples to examine the extent and the penetration

depth, respectively. Scanning transmission electron microscopy (STEM) was used to study the microstructure and grain boundary chemistry. Atomic resolution STEM was utilized to analyze the influence of 0.06 wt% Zn on the precipitate structures. Furthermore, atomic force microscopy (AFM) coupled with scanning Kelvin probe force microscope (SKPFM) was employed to measure the surface potential difference along the grain boundary to elucidate the role of Zn.

8.2 Experimental methods

8.2.1 Material used

The extruded Al-Mg-Si alloys with different minor additions of Zn were manufactured to imitate the expected Zn level in recycled Al-Mg-Si alloys. The cast ingots were homogenized at 575 °C for 135 min according to industrial practice. Thereafter, the material was hot extruded and water-quenched. Subsequently, the material profiles were stretched 0.5 %, underwent two-step aging to reach the peakaged condition. Hydro Aluminium identified the achieved temper as T6.

Four alloy specimens with different Zn content (0.003, 0.02, 0.04, and 0.06 wt%) were manufactured and labeled R1, R2, R3, and R4, respectively (see Table 8.1).

Table 8.1. Chemical composition (wt%) of the artificially aged 6082 Al-Mg-Si alloy used in the present study.

Alloy	Al	Mg	Si	Zn	Cu	Fe	Mn
R1	Balance	0.65	0.97	0.003	0.001	0.22	0.54
R2	Balance	0.64	0.96	0.022	0.001	0.21	0.55
R3	Balance	0.64	0.94	0.041	0.001	0.21	0.54
R4	Balance	0.63	0.94	0.059	0.001	0.21	0.56

8.2.2 Microstructure characterization

Microstructure was first characterized using a Zeiss Axio Vert.A1 light optical microscope. Three main directions of observation are used in the following, referred to as longitudinal direction (L), transverse direction (TD), and normal direction (ND), which can be seen in Fig. 8.1. The 3D microstructure imaging of the samples is obtained from samples of 25 x 10 x 4 mm^3 size. The samples were ground, mechanically polished to 1 μm, and then electrochemical etched in tetrafluoroboric acid for 60 s before the analyses. After a 24

h immersion test, the corrosion morphology of the cross-section and surface was studied using an AFEG 250 Analytical ESEM operated under a high-vacuum atmosphere.

Transmission electron microscope (TEM) specimens were prepared from the top surface of the recrystallized layer of the extruded material profiles, see Fig. 8.1. The samples were firstly mechanically thinned by polishing to a thickness of approximately 100 µm and then punched into 3 mm diameter thin foils. The foil disks were then electropolished at – 25°C in a Struers A2 solution using a TenuPol-5 twin-jet system. Two TEM instruments were used in this work. (i) A spherical aberration (Cs) probe-corrected Titan Analytical 80-300ST microscope was employed to investigate the microstructure and grain boundary chemistry. The microscope was operated at 300 kV along with a windowless X-Max 80TLE detector. (ii) A spherical aberration (Cs) probe-corrected JEOL ARM200F was used to acquire atomically resolved high-angle annular dark-field (HAADF) STEM images operated at 200 kV using a detector collection angle of 42-178 mrad.

8.2.3 AFM and SKPFM surface characterization

To investigate the impact of Zn on the surface potential near alloy grain boundaries, atomic force microscopy (AFM) coupled with scanning Kelvin probe force microscopy (SKPFM) analysis was conducted. The samples were prepared by polishing to 0.25 µm followed by 30 s of OP-S and then the GB of interest were marked by a combined focused ion beam and scanning electron microscope (FIB-SEM). AFM/SKPFM measurements were performed by a Bruker Dimension Edge™ instrument with an n-type doped silicon pyramid single crystal tip coated with PtIr5 (SCM-Pit probe), with a height and tip radius of 10–15 µm and 20 nm, respectively. The local electronic surface potential was recorded in dual-scan mode. In the first scan, the topography map was recorded in tapping mode. The tip was lifted to 100 nm in the second scan, and the surface potential was obtained by following the topography registered in the first scan. Both the topography and surface potential images were captured under ex-situ conditions in an approximate relative humidity of 32 % and at 22 °C. Moreover, the following parameters were fixed for all AFM/SKPFM tests: pixel resolution of 512 × 512, tip-biased, zero-bias voltage, and scan frequency rate of 0.3 Hz.

8.2.4 IGC test

Corrosion tests were conducted on samples with a size of 25 x 20 x4 mm^3 by immersion in an acidified salt solution for 24 h according to BS-ISO 11846 method B. The samples were degreased in action, etched in 8 wt% sodium hydroxide solution for 5 min at 55 °C, rinsed in distilled water, and then desmutted in concentrated nitric acid. Before the IGC tests, the narrow sides of all tested specimens were lacquered by Lacomit varnish to avoid possible interference between the deformed and the recrystallized layers, as the former is more active than the latter. The IGC test was conducted by immersing the samples in acidified salt solution containing 10 ml/l HCl and 30 g/l NaCl. After 24 h immersion, the samples were thoroughly washed in distilled water, ethanol and then air-dried. Thereafter, the surface and cross-section morphologies were investigated using SEM.

8.3 Results

8.3.1 Microstructure characterization

All extruded and water-quenched samples revealed a dual microstructure comprising a recrystallized surface layer of approximately 400 μm thickness and a deformed center layer, as illustrated in Fig. 8.1 for sample R1. Although not shown, all other alloys showed similar microstructural features as for sample R1 shown in Fig. 8.1. It is worth noting that the grain sizes of the recrystallized surface layer vary with depth. The average size of the grains on the top surface is around 30 μm, while the grain size near the deformed layer can be several hundred μm. In the present research work, attention was given to exploring the recrystallized layer.

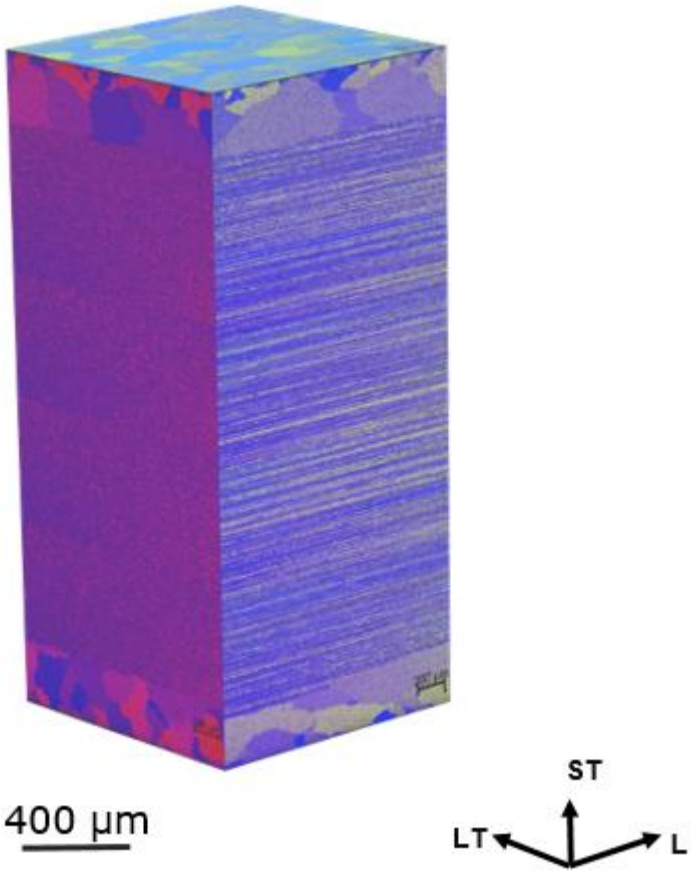

Fig. 8.1. 3D-optical observation illustrating the grain structure of the extruded 6082 (R1) in the peakaged condition after electrochemical etching in tetrafluoroboric acid.

8.3.2 Intergranular corrosion susceptibility of the studied samples

Fig. 8.2 (a, d) shows the alloy surfaces after 24 h immersion in an acidified salt solution, revealing a noticeable difference in the IGC attack for different alloys. A typical localized IGC corrosion is observed in samples R1 and R2, whereas a transition toward a more uniform IGC is observed in sample R3, and a heavy uniform IGC is recorded in sample R4. A noticeably higher number of attacked grain boundaries is observed in sample R2 compared to sample R1, indicating that sample R1 has a higher IGC resistance than sample R2.

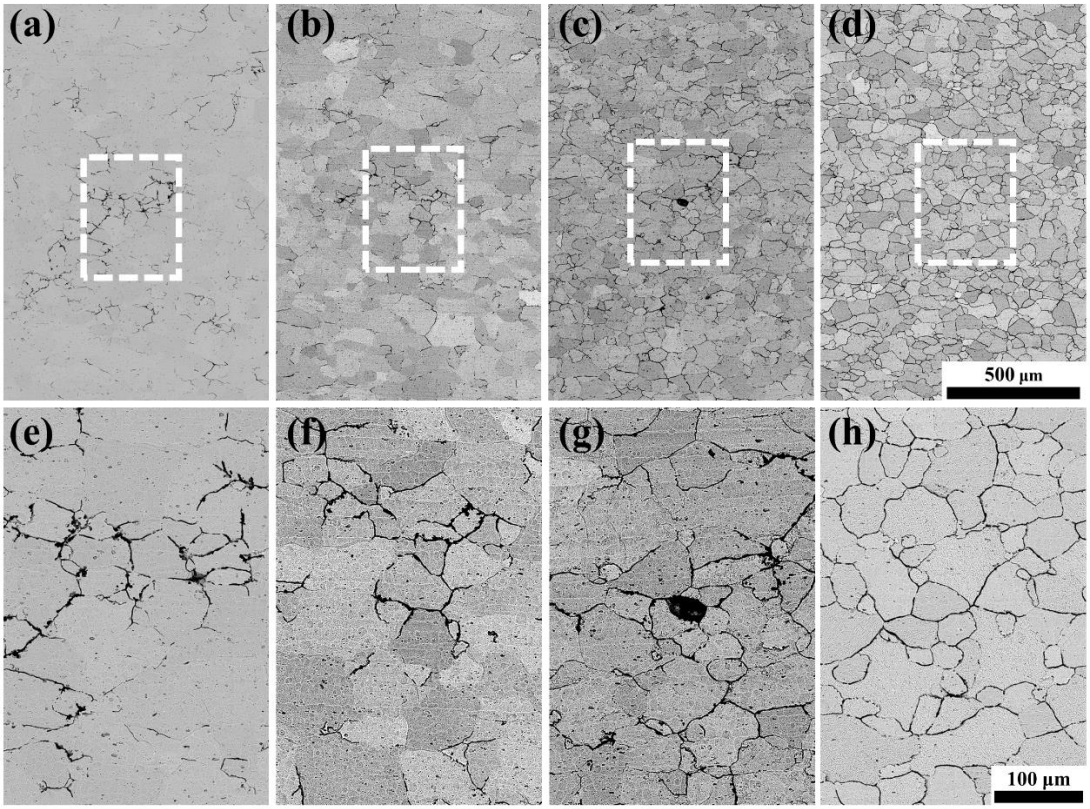

Fig. 8.2. SEM-BSE micrographs of the surface morphology after 24 h immersion in acidified salt solution of: (a) alloy R1, (b) alloy R2, (c) alloy R3, and (d) alloy R4.

Fig. 8.3(a, d) shows the cross-sectional IGC morphology of the studied alloys in PA condition after 24 h immersion in an acidified salt solution. The maximum penetration depth of ~138 µm is observed in sample R4 with the highest Zn addition. Observation of IGC extension and penetration with respect to the Zn additions indicates that minor Zn additions has higher negative influence on the IGC attack laterally than the penetration depth, as the latter only slightly increased as a function of Zn concentrations, see Fig. 8.3.

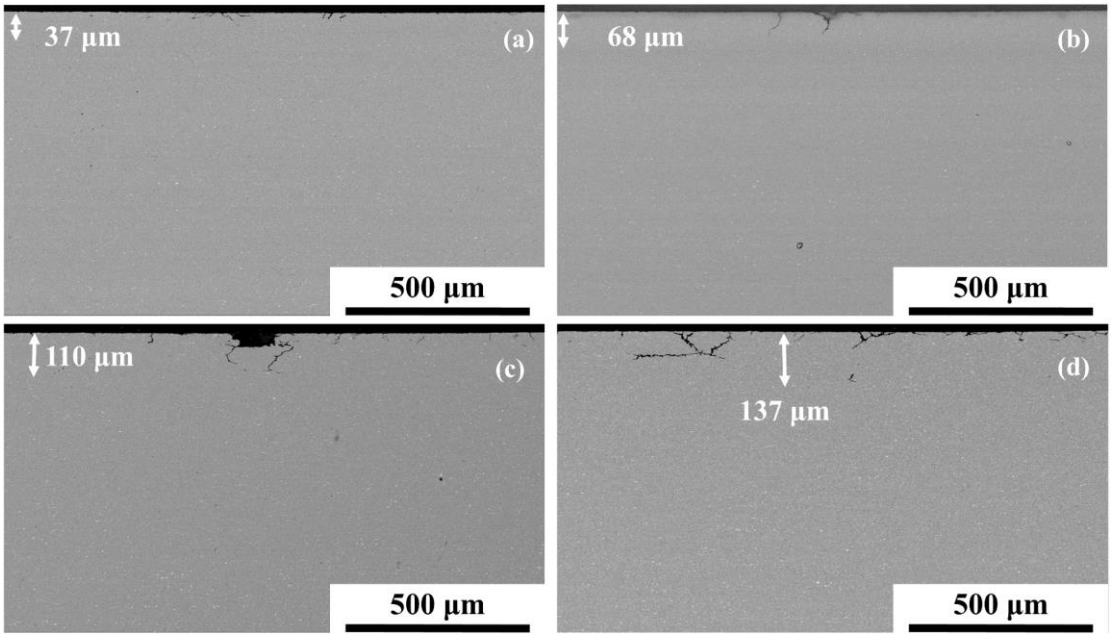

Fig. 8.3. SEM-BSE micrographs of the cross-section morphology after 24 h immersion in acidified salt solution of: (a) alloy R1, (b) alloy R2, (c) alloy R3, and (d) alloy R4.

8.3.3 (S)TEM analysis of grain boundaries and precipitates

The bright field-TEM images of the four examined alloys with the grain boundaries orientated parallel to the incident electron beam are shown in Fig. 8.4. Precipitate free zones (PFZ) of approximately 100 nm width can be readily observed along the grain boundaries of all investigated alloys. Moreover, observation of several grain boundaries for all studied alloys confirmed the presence of particles located along the grain boundaries. The density of such precipitates varied from grain boundary to grain boundary. However, some investigated grain boundaries of sample R1 are free from particles (not shown). Dispersoids and intermetallic particles are detected in the microstructure of the studied alloys. Such particles showed dark contrast as they contain heavy elements (Mn and Fe), which scatter electrons more intensely than the adjacent aluminium matrix. The precipitates in the grain interior are moderately different in samples R1 and R4, see Fig. 8.4(c, f), as slightly denser and finer precipitates are observed in sample R4 compared to sample R1.

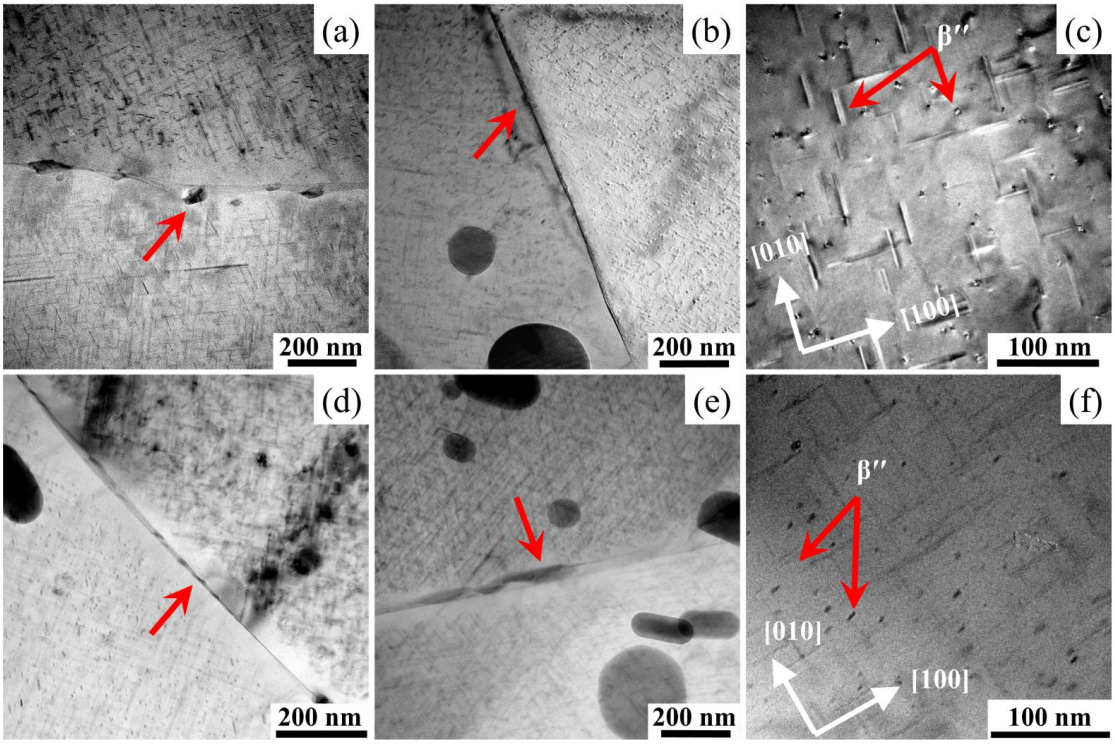

Fig. 8.4. Typical TEM images of Al-Mg-Si alloy in the peakaged condition; (a) alloy R1, (b) alloy R2, (c) alloy R1 microstructure observed in <100> Al zone axis, (d) alloy R3, (e) alloy R4, and (f) alloy R4 microstructure observed in <100> Al zone axis. Red arrows in (a), (b), (d) and (e) indicate grain boundary precipitates.

To analyze the influence of minor additions of Zn on the grain boundary chemistry, EDS-STEM (HAADF) analysis was performed on samples R1 and R4. The results obtained from sample R1 showed GB particles enriched in Si and Mg identified as Mg-Si precipitates, see Fig. 8.5(b, d). The EDS maps also reveal the presence of Mg and Si depleted zone of approximately 100 nm in the vicinity of the grain boundary, see Fig. 8.5d. Moreover, no clear Zn-containing particle or Zn-rich film are detected at such low Zn concentration, see Fig. 8.5(b, d).

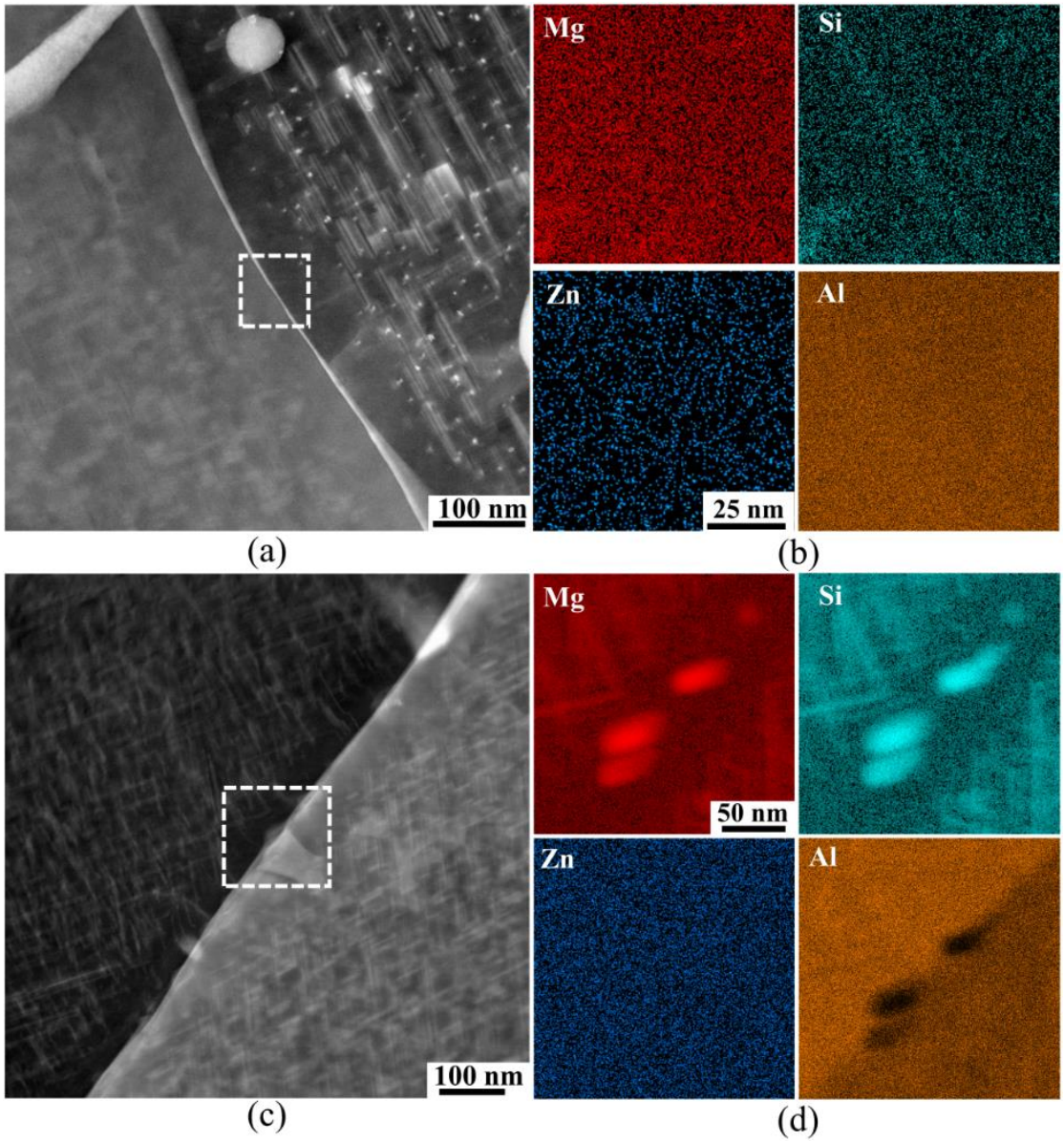

Fig. 8.5. HAADF-STEM images showing the grain boundaries for alloy R1 in the peakaged condition, containing 0.003 wt% Zn and their corresponding Al, Mg, Si, and Zn EDS elemental maps at the grain boundaries regions.

Fig. 8.6 displays two typical grain boundaries of the sample R4, revealing the presence of grain boundary particles. Fig. 8.6b shows relatively distantly separated GB particles, while in Fig. 8.6d, the GB particles are closely spaced, forming a Zn path. The corresponding EDS elemental maps in Fig. 8.6(b, d) reveal that such precipitates are rich in Mg, Si, and with clear presence of Zn. Interestingly, noticeable Mg and Si depletion along the grain boundary can be noticed, but not for Zn. Moreover, no distinct continuous film rich in Zn is detected along the grain boundary. This indicates that Zn is more uniformly distributed in the PFZ and grain interior.

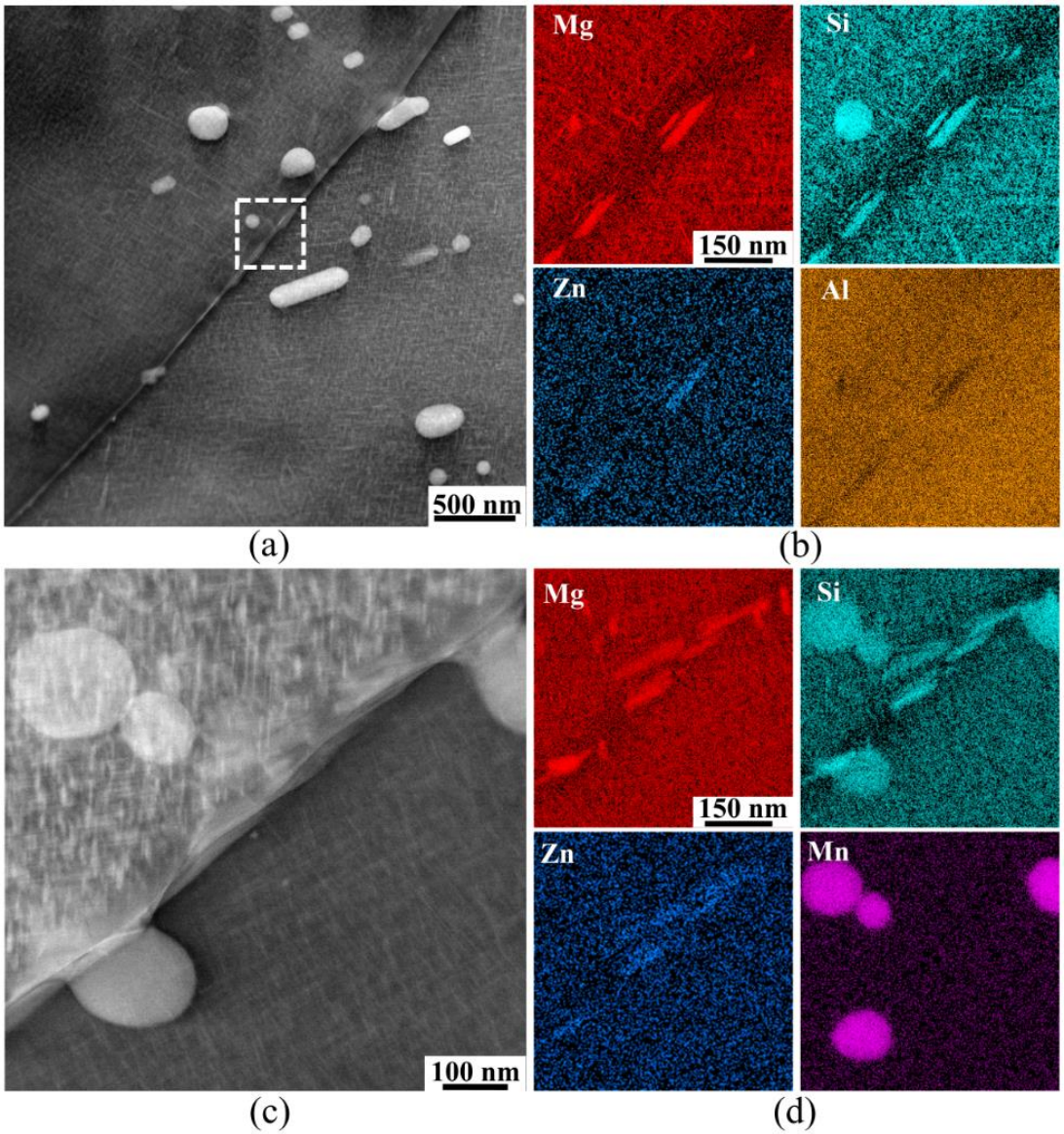

Fig. 8.6. HAADF-STEM images showing the grain boundaries for sample R4 alloy in the peak aged condition, containing 0.06 wt% Zn and their corresponding Al, Mg, Si, and Zn EDS elemental maps of the grain boundary regions.

Atomic resolution Z-contrast HAADF-STEM imaging was conducted on sample R4 to explore whether 0.06 wt% Zn will influence the crystal structure of hardening precipitates observed in its microstructure and demonstrated in Fig. 8.7. The hardening precipitates of Al-Mg-Si alloys grow in 〈0 0 1〉 Al directions. Therefore, all images were taken at 〈0 0 1〉 Al zone axis orientation. To minimize the noise, fast Fourier transform (FFT) filtering is applied through a circular band pass mask to remove all distances shorter than 1.5 Å. Atomic overlay was conducted on representative β″ precipitates based on the construction rules of precipitates in the Al-Mg-Si(-Cu) alloy system from [30] and on similarity to well-known precipitate crystal structures in Al-Mg-Si alloys [31,32]. Fig. 8.7a

shows FFT-filtered images of β″ precipitate found in the microstructure of sample R4. The atomic overlay shows that the precipitate consists of eye structural configurations. Interestingly, Zn is observed to occupy Si_1, Si_2, and Si_3/Al in the β″ structural unit. Furthermore, Zn is noticed to partially occupy Si_2 columns in β″ precipitates/Al interface, see Fig. 8.7c. Also, a Q′/C local configuration is observed in the β″ structure, see Fig. 8.7d.

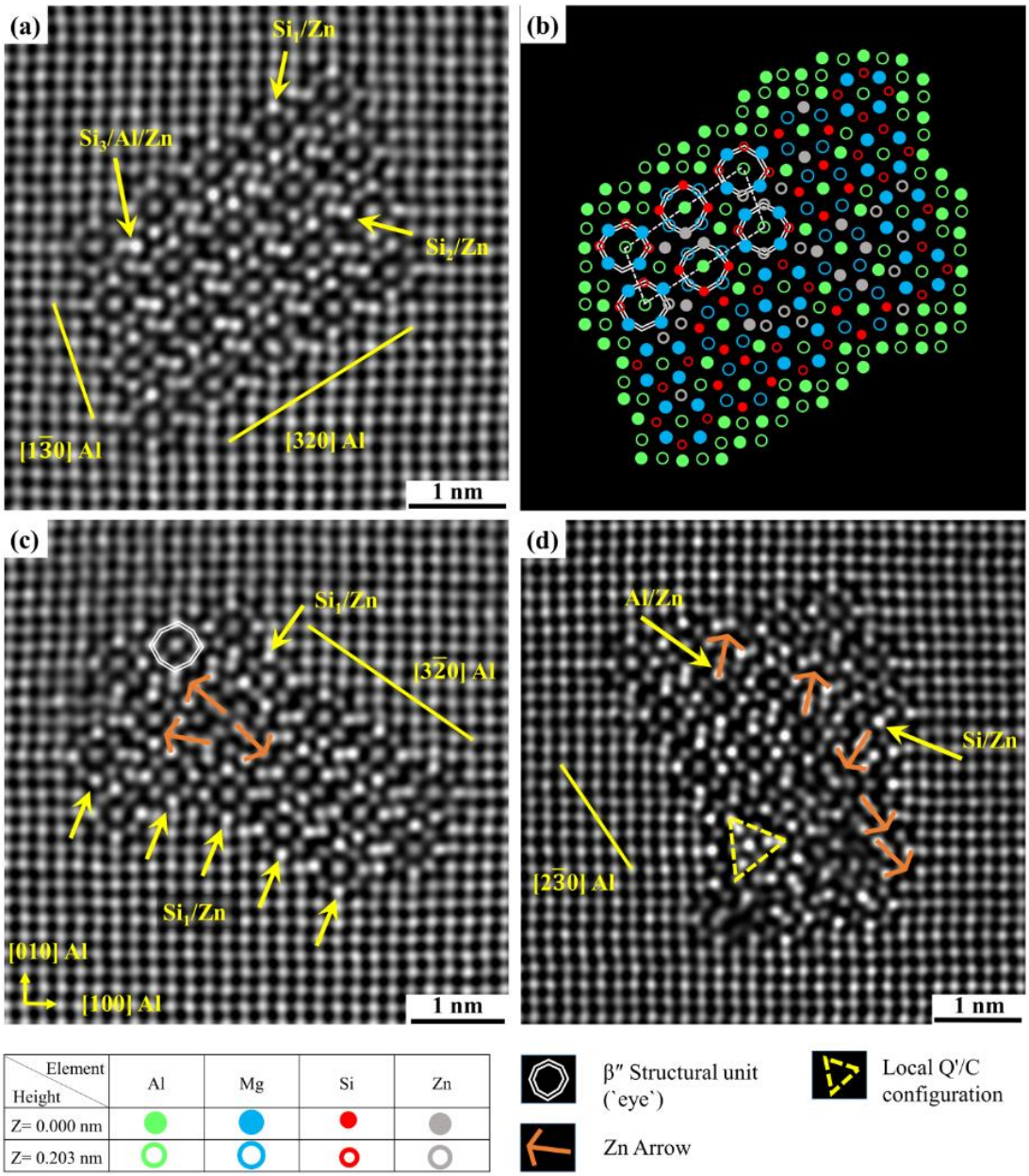

Fig. 8.7. (a, c, and d) HAADF-STEM image of Zn containing β" precipitates cross-section taken from alloy R4 with 0.06 Zn wt%. (a) FFT Filtered image, (b) suggested overlay of (a) based on the roles (Al, Mg, Si, and Zn are considered.

8.3.4 AFM/SKPFM analysis of grain boundaries

The presence of Zn-enriched precipitates located along the grain boundaries of sample R4 which was not evident in sample R1 (lowest amount of Zn) leads to a difference in the chemical behavior and especially electronic properties at grain boundary/grain (GB/G) interfaces. The electronic properties probed here include surface charge, electrical surface potential, and work function energy (WFE, ∅). Therefore, revealing some information related to these electronic properties' evolutions at the GB/G interface with and without Zn-enriched precipitates can give better knowledge to predict the different driving forces for galvanic coupling at GB/G interface (e.g. intergranular corrosion attacks) [33]. On this account, AFM coupled with SKPFM maps of grain boundaries in two different alloys namely R4 with Zn-enriched precipitates and R1 without were conducted to evaluate the electrical surface potential and/or surface charge difference at the GB/G interface. Fig. 8.8(a, b) present topography and surface potential maps of grain boundaries at a triple junction in sample R1. Three intermetallic particles (IMPs) are also located in the scanned region, one of which is located on or close to a GB. From the surface potential map and its corresponding histogram analysis (Fig. 8.8c), it is observed that the IMPs have the lowest and different surface potential compared to the Al matrix (~40 mV, ~50 mV, and ~70 mV).

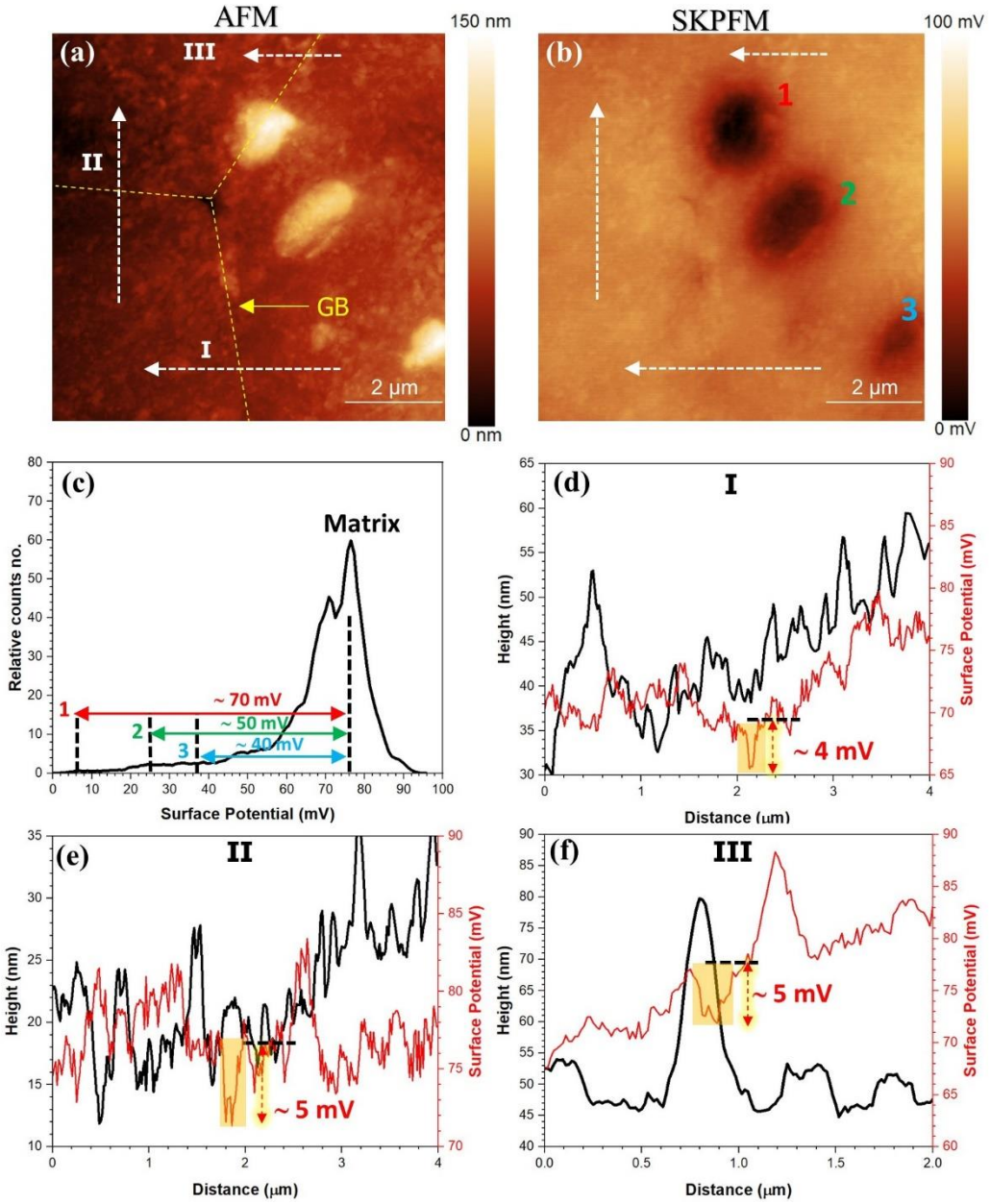

Fig. 8.8. (a) Topography and (b) surface potential maps of alloy R1 near triple grain boundary point. (c) Surface potential histogram of SKPFM map in (b) that visualizes the surface potential difference between three distributed intermetallic particles and the Al matrix. (d,e, and f) Topography and surface potential line profiles in (a) and (b).

Utilizing the line profile of topography and its corresponding surface potential across three different grain boundaries, Fig. 8.8(d, e, f), it was noticed that all grain boundaries approximately exhibit the same surface potential difference value (~4 or 5 mV) compared to the grain boundary adjacent (~200 nm). However, in the case of sample R4, AFM and SKPFM maps exhibit a better recognizable grain boundary with a higher surface potential distribution (brighter color) than the Al matrix, as presented in Fig. 8.9(a, b). In addition, the two-line profiles of topography and corresponding surface potential in Fig.

8.9(c, d) indicate that the grain boundary region in sample R4 has a higher surface potential difference (~10 mV) than sample R1 (~4 mV). It is important to specify that since the tip is biased the low potential (dark region) indicates the cathode and the higher potential (bright region) indicates the anode [34].

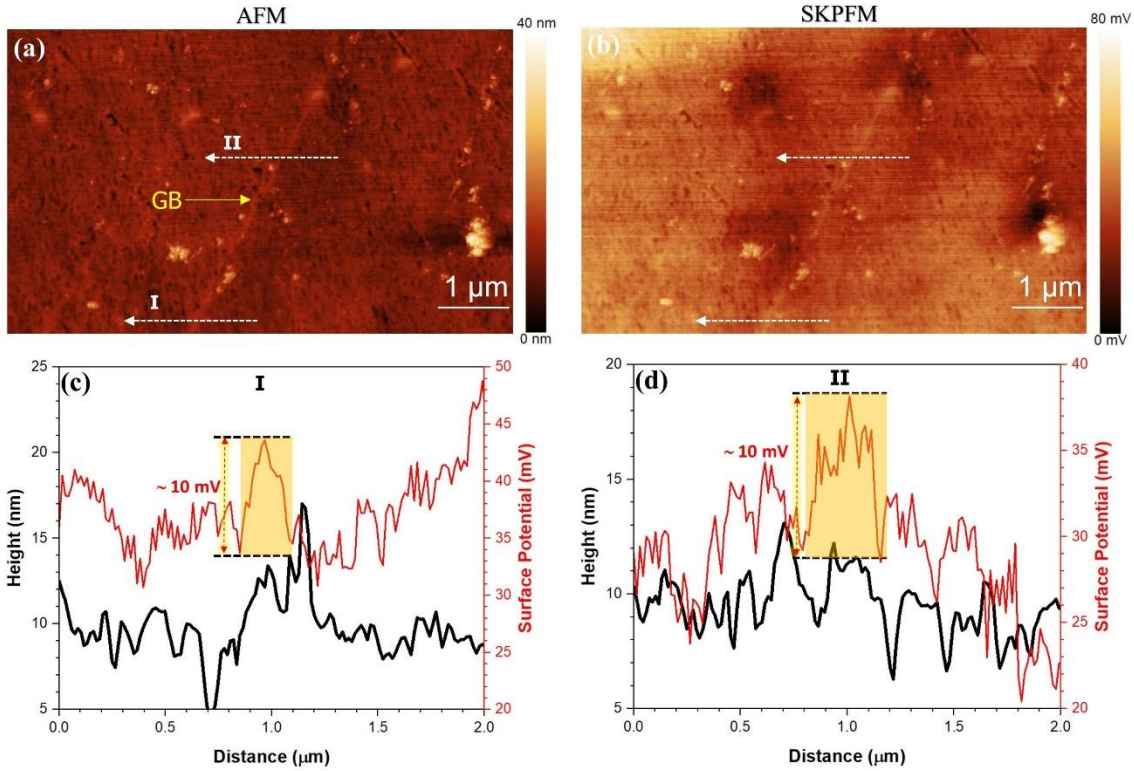

Fig. 8.9. (a) Topography and (b) surface potential maps of GB/G interface in alloy R4 (Zn-enriched trace in grain boundary). (c and d) Topography and surface potential line profiles in (a) and (b).

8.4 Discussion

The focus of the present study was to investigate the effect of very low levels of Zinc on IGC of recrystallized surface layer of the extruded material, characterized by peripheral coarse grains (PCG). Such coarse-grained surface recrystallized layers can be found in medium to high-strength 6082 Al-Mg-Si alloys used in many industrial applications, including the automotive sector. It is reported that the formation and extension of the PCG layer are closely linked to alloy composition, homogenization temperature, extrusion parameters, and die design [35–37]. The primary motivation of this work is to examine the influence of minor addition of Zn $\leq$ 0.06 wt% expected to be found in recycled Al-Mg-Si alloys on the IGC resistance of the recrystallized surface layer, and how Zn affects the age hardening precipitates formed.

8.4.1 Microstructure investigations

The morphology of the bulk precipitates in samples R1 and R4 shown in Fig. 8.4(c, f) indicates that the vast majority of these precipitates are β″ (needle-shaped) with a minor fraction of β′ (rod-shaped) precipitates. Slightly finer and denser precipitates can be observed in sample R4 compared with sample R1. Ding et al. [26] have investigated the influence of 0.5 and 3 wt% Zn on the age hardening response of Al-0.98Mg-0.44Si and Al-0.99Mg-0.54Si alloys at different aging conditions. The results showed that the meta-stable precursor phases of β-Mg_2Si precipitates (β″) are the main phase when the Zn concentration is 0.5 wt%. However, the meta-stable precipitates of η-$MgZn_2$ can be formed in the microstructure of 3 wt% Zn-containing Al-Mg-Si in the PA condition. In the current work, no Mg-Zn precipitates were observed in the microstructure of the sample R4 as such minor addition of Zn did not change the precipitation sequence of studied 6082 Al-Mg-Si alloys. This observation is also in agreement with Chi et al. [38], who investigated the influence of 0.2 wt% Zn on the precipitation behavior and IGC in Al-0.9Mg-1.1Si. However, 0.06 wt% Zn noticeably affects the crystal structure of primary hardening precipitates (β″) observed in the current study, as seen from Fig. 8.7(c, d).

Saito et al. [27] studied the influence of different levels of Zn on mechanical and corrosion properties, as well as on precipitate structures in an Al-0.5Mg-0.4Si alloy. The results showed that the alloy with 1.02 wt% Zn addition showed disordered precipitates as a low amount of Zn entered the precipitate crystal structure. At the same time, it is concluded that alloys with Zn ≤ 0.1 wt% did not show a measurable influence on the precipitate structure, mechanical properties and IGC susceptibility. Interestingly, the majority of the investigated precipitates in sample R4 in the current study showed that Zn is incorporated into their crystal structure, partially occupying certain atomic columns, see Fig. 8.7(a, c, d).

8.4.2 Effect of Zn on intergranular corrosion

The findings from the current research reveal that low levels of Zn can clearly affect the IGC resistance and precipitate structures of the peakaged 6082 Al-Mg-Si alloys. As shown in Fig. 8.2, considerable differences between the four studied alloys in the susceptibility to IGC can be observed. In the sample R4, IGC nearly invaded the surface as a uniform IGC, while less severity was recorded in samples R3, R2, and R1, respectively.

The observed IGC in sample R1 occurred due to the selective anodic dissolution of β (Mg_2Si) precipitates located along the GBs as a result of microgalvanic coupling with the PFZ acting as a cathode [10,12,39]. In addition, the presence of a trace level of Cu in this alloy might also play a role as a discontinued Cu-rich film was reported by Bartawi et al [40]. The susceptibility to IGC increased by increasing the Zn addition indicating that the deterioration observed in the IGC resistance is directly attributed to the minor addition of Zn.

It has been found that the intergranular corrosion resistance of 2-4 wt% Zn containing Al-0.9Mg-0.6Si-0.2Cu is higher than that of Zn free or 1 wt% Zn alloys in the PA condition, while the alloys were more susceptible to IGC in the overaged (OA) condition [41]. The improvement observed in the PA condition was attributed to the transformation from Zn-rich film to discontinuous grain boundary particles that can easily occur at high Zn concentration (2-4 wt%). However, the decrease in the IGC resistance when Zn increased from 0 to 1 wt% was related to the coarsening of grain boundary particles. Moreover, the deterioration in the IGC resistance recorded in the OA condition was related to the formation Mg-Zn and Mg-Si-Zn precipitates and narrower PFZ. Saito et al. [27] showed that alloys with 0.002, 0.012, and 0.11 wt% Zn (Al-0.5Mg-0.4Si) had negligible IGC susceptibility. Therefore, the authors concluded that Zn content below 0.1 wt% has limited impact on the IGC resistance in Al-Mg-Si alloys. At the same time, the results obtained by Xu et al. [42] on Al-0.86Mg-1.12Si alloys revealed that an alloy with 0.25 wt% Zn was more susceptible to IGC than the one with 0.04 wt%. It is claimed that the Zn-added alloy showed approximately 10 nm wider PFZ and assumed a lower Zn solute content in the PFZ, causing higher susceptibility to IGC. The EDS -STEM investigations of several grain boundaries for sample R4 did not show a distinguished Zn-depleted zone, see Fig. 8.6. This observation is supported by the experimental work conducted by Saito et al. [27] to explore the influence of high Zn concentration (1.02 wt%) on precipitation in Al-0.47Mg-0.39Si, as no distinguished Zn-depleted zone was recorded. Therefore, it can be concluded that the global solute concentration of Zn in the depleted zone is slightly different from their concentrations in the matrix as the HR-STEM conducted on the precipitates in the grain interior confirmed that these precipitates consume the Zn. This implies that the corrosion potential of the depleted Zone will be slightly different than the corrosion potential of the matrix. Consequently, the driving force for IGC recorded in sample R4 was due to the microgalvanic coupling between the PFZ as a cathode, and the

Zn-rich precipitates decorating the GBs serving as an anode and at the same time, the adjacent Al matrix will act as a cathode leading to the dissolution of the PFZ. This observation is supported by the SKPFM results, as a lower potential was measured at the GB region at the width of approximately 200 nm to reach its peak value at the width of approximately 100 nm, see Fig. 8.9. Therefore, it can be stated that the average potential of the near grain boundary (Al matrix) is slightly higher (acting as a cathode) than the grain boundary region (acting as an anode). It is essential to mention that the formation of a native oxide film, specifically in the aluminum alloy (γ-Al_2O_3 with a large band gap energy) [43], significantly affects the total surface potential and/or surface charge distribution. This will lead to less tendency to establish an intensive electrostatic force between metal/oxide and tip-apex in SKPFM surface-sensitive technique [44]. Interestingly, a more discernible signal was recorded in sample R4 compared to sample R1, which is thought to be a result of the presence of Zn in the grain boundary particles, see Figs, 8.8 and 8.9. Moreover, The IMPS observed in TEM images (e.g., Fig. 8.6) show different surface potential with respect to the adjacent region. The various observed values with respect to the Al matrix (~40 mV, ~50 mV, and ~70 mV) are due to the variation in the chemical composition and different oxide films on top of them compared to the Al matrix.

A schematic representation of the fundamental principle of SKPFM analysis alongside energy diagrams between the GB/G and AFM tip apex is provided (Fig. 8.10) to better visualize the impact of Zn-enriched precipitates located along the grain boundary (Fig. 8.6) on enhancing the total surface potential and/or surface charge difference. It should be emphasized that the surface potential map of grain boundaries detected by SKPFM in this study are electrical grain boundaries with a space charge region (surface potential/surface charge) instead of crystallographic grain boundaries since the AFM tip-apex is bigger than the real GB [45]. Hence, because of the localized charges at grain boundaries as defect states, a band bending occurs, resulting in changing the WFE value. In the case of sample R1, the band bending is slightly downward (the rectangle-colored region in Fig. 8.10) with a lower "contact potential difference" (ΔCPD) which confirms less driving force for galvanic coupling at the GB/G interface and lowers the depletion of the electrons in grain boundary surrounding [46,47]. Although, the nanometric Zn-enriched trace at grain boundaries of sample R4 triggers a more downward band bending or higher ΔCPD which confirms both higher driving force for galvanic coupling or intergranular corrosion attacks at GB/G interface and the depletion of the electrons in GB surrounding.

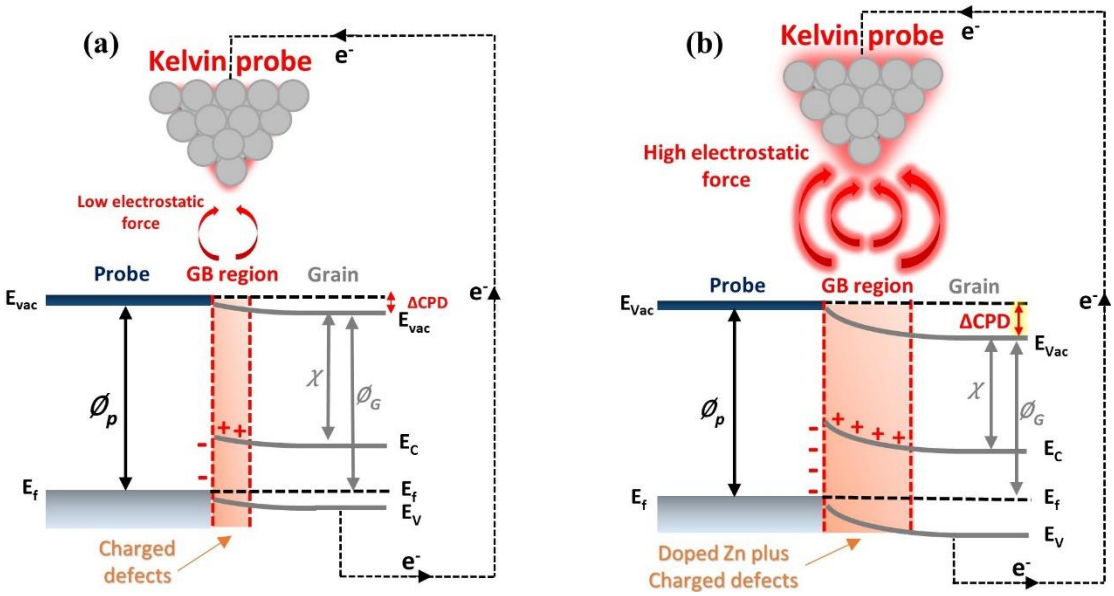

Fig. 8.10. Schematic demonstration of the SKPFM principle along with the energy level diagram during the electrostatic interaction between a conductive AFM tip-apex and GB/G interface without (a) and with (b) Zn enriched-trace at the grain boundary, The abbreviations defined as valence and conduction bands ($E_V$and E_C), Fermi level (E_f), electron affinity (χ), and vacuum level (E_{Vac}), work function energy of probe and grain ($\emptyset_p$ *and* $\emptyset_G$).

8.5 Conclusions

In the current work, the influence of minor additions of Zn on the precipitate crystal structure and IGC in extruded 6082 Al-Mg-Si alloys has been investigated. The following conclusions are drawn from the current work:

1. Minor addition of Zn (0.06 wt%) significantly affects the IGC resistance of 6082 Al-Mg-Si alloys in the peakaged condition as the IGC extension dramatically influenced compared to the penetration depth.
2. The grain boundary particles of sample R4 are morphologically different from those observed in sample R1 as more elongated and bigger grain boundary particles are observed in sample R4. However, no apparent difference in the width of PFZs is recorded for different Zn additions.
3. More negative potential was measured along the grain boundary of sample R4 (0.06 wt% Zn-added) compared to its adjacent matrix, indicating that the adjacent matrix will act as a cathode with respect to the PFZ and GB precipitates.

4. The primary hardening precipitates observed in the current work in the peakaged condition are pure β″, as the formation of Mg-Zn η-type precipitates requires a higher Zn solution in the Al matrix
5. TEM observations clearly show that low concentrations of Zn can promote precipitate phase sub-structures of Q'/C, which is normally found in Al-Mg-Si(-Cu) alloys. This indicates that Zn can have a similar role as Cu inside these crystal structures.
6. Zn partially occupies Si_1, Si_2, and Si_3/Al columns in pure β″, but not Mg_1/Al, Mg_2, and Mg_3 sites.

CRediT authorship contribution statement

Emad H. Bartawi: Conceptualization, Methodology, Investigation, Formal analysis, Writing - Original Draft, **Calin D. Marioara:** Writing - Review & Editing, Formal analysis, **Ehsan Rahimi:** Writing - Review & Editing, Formal analysis, **Ghada Shaban:** Formal analysis, Writing - Review & Editing, **Jonas K. Sunde:** Writing - Review & Editing, **Yaiza Gonzalez-Garcia**: Writing - Review & Editing, **Randi Holmestad:** Writing - Review & Editing**, Rajan Ambat:** Conceptualization, Supervision, Writing - Review & Editing, Project administration, Funding acquisition.

Acknowledgements

The authors would like to acknowledge Hydro Aluminium, Norway, for providing material. The authors also thank Dr. Ruben Bjørge from SINTEF Industry and Dr. J. Kling from DTU Nanolab for his technical assistance during STEM experiments. Emad H. Bartawi and Rajan Ambat acknowledge funding from the Independent Research Fund Denmark (grant number 9041- 00240A). Also, this project has received funding from the European Union's Horizon 2020 research and innovation programme under grant agreement No 823717 – ESTEEM3.

Data Availability

The raw/processed data required to reproduce these findings cannot be shared at this time as the data also forms part of an ongoing study.

References

[1] A.C. Serrenho, J.B. Norman, J.M. Allwood, The impact of reducing car weight on global emissions: the future fleet in Great Britain, Philos. Trans. R. Soc. A Math. Phys. Eng. Sci. 375 (2017) 20160364.

[2] D.J. Chakrabarti, D.E. Laughlin, Phase relations and precipitation in Al–Mg–Si alloys with Cu additions, Prog. Mater. Sci. 49 (2004) 389–410.

[3] J. Hirsch, Recent development in aluminium for automotive applications, Trans. Nonferrous Met. Soc. China. 24 (2014) 1995–2002.

[4] W.S. Miller, L. Zhuang, J. Bottema, A.J. Wittebrood, P. De Smet, A. Haszler, A. Vieregge, Recent development in aluminium alloys for the automotive industry, Mater. Sci. Eng. A. 280 (2000) 37–49.

[5] J.R. Davis, Corrosion of aluminum and aluminum alloys, ASM international, 1999.

[6] D. V. Wilson, Aluminium versus steel in the family car — the formability factor, J. Mech. Work. Technol. 16 (1988) 257–277.

[7] V.M. Simões, M.C. Oliveira, H. Laurent, L.F. Menezes, The punch speed influence on warm forming and springback of two Al-Mg-Si alloys, J. Manuf. Process. 38 (2019) 266–278.

[8] R. Abi-Akl, D. Mohr, Paint-bake effect on the plasticity and fracture of pre-strained aluminum 6451 sheets, Int. J. Mech. Sci. 124–125 (2017) 68–82.

[9] H. Zhong, P.A. Rometsch, L. Cao, Y. Estrin, The influence of Mg/Si ratio and Cu content on the stretch formability of 6xxx aluminium alloys, Mater. Sci. Eng. A. 651 (2016) 688–697.

[10] S.K. Kairy, P.A. Rometsch, C.H.J. Davies, N. Birbilis, On the intergranular corrosion and hardness evolution of 6xxx series Al alloys as a function of Si:Mg ratio, Cu Content, and aging condition, Corrosion. 73 (2017) 1280–1295.

[11] Y. Zou, Q. Liu, Z. Jia, Y. Xing, L. Ding, X. Wang, The intergranular corrosion behavior of 6000-series alloys with different Mg/Si and Cu content, Appl. Surf. Sci.

405 (2017) 489–496.

[12] A. Shi, B.A. Shaw, E. Sikora, The role of grain boundary regions in the localized corrosion of a copper-free 6111-like aluminum alloy, Corrosion. 61 (2005) 534–547.

[13] A.K. Bhattamishra, K. Lal, Microstructural studies on the effect of Si and Cr on the intergranular corrosion in Al-Mg-Si alloys, Mater. Des. 18 (1997) 25–28.

[14] M.H. Larsen, J.C. Walmsley, O. Lunder, R.H. Mathiesen, K. Nisancioglu, Intergranular corrosion of copper-containing AA6xxx AlMgSi aluminum alloys, J. Electrochem. Soc. 155 (2008) C550.

[15] F. Eckermann, T. Suter, P.J. Uggowitzer, A. Afseth, P. Schmutz, The influence of MgSi particle reactivity and dissolution processes on corrosion in Al–Mg–Si alloys, Electrochim. Acta. 54 (2008) 844–855.

[16] W. Yang, S. Ji, Z. Li, M. Wang, Grain boundary precipitation induced by grain crystallographic misorientations in an extruded Al-Mg-Si-Cu alloy, J. Alloys Compd. 624 (2015) 27–30.

[17] T. Minoda, H. Yoshida, Effect of grain boundary characteristics on intergranular corrosion resistance of 6061 aluminum alloy extrusion, Metall. Mater. Trans. A. 33 (2002) 2891–2898.

[18] S.K. Kairy, T. Alam, P.A. Rometsch, C.H.J. Davies, R. Banerjee, N. Birbilis, Understanding the origins of intergranular corrosion in copper-containing Al-Mg-Si alloys, Metall. Mater. Trans. A Phys. Metall. Mater. Sci. 47 (2016) 985–989.

[19] M. de Haas, S.M. van Scherpenzeel, J.T.M. de Hosson, Grain boundary segregation and precipitation in aluminium alloy AA6061, Mater. Sci. Forum. 519–521 (2006) 467–472.

[20] F.L. Zeng, Z.L. Wei, J.F. Li, C.X. Li, X. Tan, Z. Zhang, Z.Q. Zheng, Corrosion mechanism associated with Mg2Si and Si particles in Al–Mg–Si alloys, Trans. Nonferrous Met. Soc. China. 21 (2011) 2559–2567.

[21] M.X. Guo, G. Sha, L.Y. Cao, W.Q. Liu, J.S. Zhang, L.Z. Zhuang, Enhanced bake-

hardening response of an Al–Mg–Si–Cu alloy with Zn addition, Mater. Chem. Phys. 162 (2015) 15–19.

[22] Y.H. Cai, C. Wang, J.S. Zhang, Microstructural characteristics and aging response of Zn-containing Al-Mg-Si-Cu alloy, Int. J. Miner. Metall. Mater. 20 (2013) 659–664.

[23] M.X. Guo, Y. Zhang, X.K. Zhang, J.S. Zhang, L.Z. Zhuang, Non-isothermal precipitation behaviors of Al-Mg-Si-Cu alloys with different Zn contents, Mater. Sci. Eng. A. 669 (2016) 20–32.

[24] S. Zhu, Z. Li, L. Yan, X. Li, S. Huang, H. Yan, Y. Zhang, B. Xiong, Natural aging behavior in pre-aged Al–Mg–Si–Cu alloys with and without Zn addition, J. Alloys Compd. 773 (2019) 496–502.

[25] M.X. Guo, Y.D. Zhang, G.J. Li, S.B. Jin, G. Sha, J.S. Zhang, L.Z. Zhuang, E.J. Lavernia, Solute clustering in Al-Mg-Si-Cu-(Zn) alloys during aging, J. Alloys Compd. 774 (2019) 347–363.

[26] X.P. Ding, H. Cui, J.X. Zhang, H.X. Li, M.X. Guo, Z. Lin, L.Z. Zhuang, J.S. Zhang, The effect of Zn on the age hardening response in an Al-Mg-Si alloy, Mater. Des. 65 (2015) 1229–1235.

[27] T. Saito, S. Wenner, E. Osmundsen, C.D. Marioara, S.J. Andersen, J. Røyset, W. Lefebvre, R. Holmestad, The effect of Zn on precipitation in Al-Mg-Si alloys, Philos. Mag. 94 (2014) 2410–2425.

[28] S. Zhu, Z. Li, L. Yan, X. Li, S. Huang, H. Yan, Y. Zhang, B. Xiong, Effects of Zn addition on the age hardening behavior and precipitation evolution of an Al-Mg-Si-Cu alloy, Mater. Charact. 145 (2018) 258–267.

[29] L. Li, S. Ji, Q. Zhu, Y. Wang, X. Dong, W. Yang, S. Midson, Y. Kang, Effect of Zn concentration on the microstructure and mechanical properties of Al-Mg-Si-Zn alloys processed by gravity die casting, Metall. Mater. Trans. A. 49 (2018) 3247–3256.

[30] S.J. Andersen, C.D. Marioara, J. Friis, R. Bjørge, Q. Du, I.G. Ringdalen, S. Wenner,

E.A. Mørtsell, R. Holmestad, T. Saito, J. Røyset, O. Reiso, Directionality and column arrangement principles of precipitates in Al-Mg-Si-(Cu) and Al-Mg-Cu linked to line defect in Al, Mater. Sci. Forum. 877 (2017) 461–470.

[31] T. Saito, E.A. Mørtsell, S. Wenner, C.D. Marioara, S.J. Andersen, J. Friis, K. Matsuda, R. Holmestad, Atomic structures of precipitates in Al–Mg–Si alloys with small additions of other elements, Adv. Eng. Mater. 20 (2018) 1800125.

[32] S.J. Andersen, H.W. Zandbergen, J. Jansen, C. Træholt, U. Tundal, O. Reiso, The crystal structure of the β″ phase in Al-Mg-Si Alloys, Acta Mater. 46 (1998) 3283–3298.

[33] Z. Esfahani, E. Rahimi, M. Sarvghad, A. Rafsanjani-Abbasi, A. Davoodi, Correlation between the histogram and power spectral density analysis of AFM and SKPFM images in an AA7023/AA5083 FSW joint, J. Alloys Compd. 744 (2018) 174–181.

[34] C. Örnek, C. Leygraf, J. Pan, On the Volta potential measured by SKPFM–fundamental and practical aspects with relevance to corrosion science, Corros. Eng. Sci. Technol. 54 (2019) 185–198.

[35] Y. Birol, Effect of Cr and Zr on the grain structure of extruded en AW 6082 alloy, Met. Mater. Int. 20 (2014) 727–732.

[36] Y. Mahmoodkhani, J. Chen, M.A. Wells, W.J. Poole, N.C. Parson, The effect of die bearing geometry on surface recrystallization during extrusion of an Al-Mg-Si-Mn alloy, Metall. Mater. Trans. A Phys. Metall. Mater. Sci. 50 (2019) 5324–5335.

[37] P.K. Saha, Aluminum Extrusion Technology, ASM International, 2000.

[38] S. Chi, Y. Deng, X. Xu, X. Guo, Influence of minor Zn addition on precipitation behavior and intergranular corrosion properties of Al-Mg-Si alloy, Materials (Basel). 13 (2020) 650.

[39] K.M. Fleming, A. Zhu, J.R. Scully, Corrosion of AA6061 brazed with an Al-Si alloy: Effects of Si on metallurgical and corrosion behavior, Corrosion. 68 (2012) 1126–1145.

[40] E.H. Bartawi, O. V. Mishin, G. Shaban, J.H. Nordlien, R. Ambat, Electron microscopy analysis of grain boundaries and intergranular corrosion in aged Al-Mg-Si alloy doped with 0.05 wt% Cu, Corros. Sci. 209 (2022) 110758.

[41] M.X. Guo, J.Q. Du, C.H. Zheng, J.S. Zhang, L.Z. Zhuang, Influence of Zn contents on precipitation and corrosion of Al-Mg-Si-Cu-Zn alloys for automotive applications, J. Alloys Compd. 778 (2019) 256–270.

[42] X. Xu, Y. Deng, Q. Pan, X. Guo, Enhancing the intergranular corrosion resistance of the Al–Mg–Si alloy with low Zn content by the interrupted aging treatment, Metall. Mater. Trans. A. 52 (2021) 4907–4921.

[43] L. Nguyen, T. Hashimoto, D.N. Zakharov, E.A. Stach, A.P. Rooney, B. Berkels, G.E. Thompson, S.J. Haigh, T.L. Burnett, Atomic-scale insights into the oxidation of aluminum, ACS Appl. Mater. Interfaces. 10 (2018) 2230–2235.

[44] E. Rahimi, A. Imani, M. Lekka, F. Andreatta, Y. Gonzalez-Garcia, J.M.C. Mol, E. Asselin, L. Fedrizzi, Morphological and surface potential characterization of protein nanobiofilm formation on magnesium alloy oxide: their role in biodegradation, Langmuir. 38 (2022) 10854–10866.

[45] J. Gonzalez-Julian, K. Neuhaus, M. Bernemann, J. Pereira da Silva, A. Laptev, M. Bram, O. Guillon, Unveiling the mechanisms of cold sintering of ZnO at 250 °C by varying applied stress and characterizing grain boundaries by Kelvin probe force microscopy, Acta Mater. 144 (2018) 116–128.

[46] T. Glatzel, S. Sadewasser, R. Shikler, Y. Rosenwaks, M.C. Lux-Steiner, Kelvin probe force microscopy on III–V semiconductors: the effect of surface defects on the local work function, Mater. Sci. Eng. B. 102 (2003) 138–142.

[47] C. Leendertz, F. Streicher, M.C. Lux-Steiner, S. Sadewasser, Evaluation of Kelvin probe force microscopy for imaging grain boundaries in chalcopyrite thin films, Appl. Phys. Lett. 89 (2006).

9. Paper V

Effect of aging temperature on microstructure and intergranular corrosion of Al-Mg-Si alloys with low concentrations of Cu and Zn

Emad H. Bartawi[1,*], Ghada Shaban[1], Calin D. Marioara[2], Ruben Bjørge[2], Oleg V. Mishin[1], Randi Holmestad[3], Rajan Ambat[1]

[1] Section of Materials and Surface Engineering, Department of Civil and Mechanical Engineering, Technical University of Denmark, Kgs. Lyngby 2800, Denmark

[2] Materials and Nanotechnology, SINTEF Industry, Trondheim N-7465, Norway

[3] Department of Physics, NTNU, Norwegian University of Science and Technology, 7491 Trondheim, Norway

Keywords: 6082 Al-Mg-Si alloy; Aging temperature, Intergranular corrosion; Precipitate crystal structure; TEM.

Abstract

The influence of aging temperature on the intergranular corrosion resistance of Al-Mg-Si alloys with tiny concentrations of Cu and Zn concerning recycled alloys has been investigated. The results revealed that minor additions of Cu and Zn negatively affect the intergranular corrosion resistance in the peakaged condition. A Cu-rich film and Cu/Zn containing β particles are detected in the underaged condition in the alloy containing 0.05 wt% Cu and 0.06 wt% Zn. High-angle annular dark-field scanning transmission electron microscopy shows that the fine precipitates in the overaged condition in the alloy with 0.05 wt% Cu and 0.06 wt% Zn comprise one or more of the following sub-unit structures: β″, β′, U1, U2, or Q′/C. Consuming Cu and Zn by grain boundary particles and hardening precipitates can influence the electrochemical potential of the Al matrix and precipitate free zone, hence, the intergranular corrosion resistance.

9.1 Introduction

Due to the increase in global demand for energy and pressure to reduce CO_2 emission, several sectors, including transportation and electrical industries, constantly seek

to develop and increase the use of aluminium to reduce the weight and increase the efficiency of final products. This will lead to increased use of recycled materials as they have economic and environmental benefits due to reduced need of primary materials, conserves energy, and most importantly, lower CO_2 emissions [1]. One of the major challenges of recycling is the detrimental effect of impurities expected to be found in the final recycled products. Al-Mg-Si alloys are sensitive to the alloying elements as small concentrations of certain elements such as Fe, Mn, Cu, or Zn might influence their mechanical and corrosion properties [2–5]. Therefore, increasing the recycling process efficiency (using more scrap) requires a deep understanding of how different alloying elements (as impurities) can affect the mechanical properties and corrosion resistance of recycled Al alloys.

Unbalanced alloying elements and/or unfavorable heat treatment (e.g., quenching rate, aging time, and temperature) will adversely influence the intergranular corrosion (IGC) resistance of Al-Mg-Si alloys [6–11]. IGC occurs due to the microgalvanic coupling between grain boundaries (GBs) and precipitate free zones (PFZs) leading to the dissolution of the anodic part. Cu addition at relatively high concentrations ($\geq$ 0.13 wt%) greatly reduces IGC resistance of Al-Mg-Si alloys, especially in the peakaged (PA) conditions [10,12–18]. Due to the claim that Cu addition $\leq$ 0.1 wt% will not significantly influence the IGC resistance of Al-Mg-Si alloys [19,20], limited work concerning low Cu content was conducted confirming the hypothesis mentioned above [9,14,16,21]. For instance, Svenningsen et al. [14,21] studied the effect of 0.02 wt% Cu addition on the IGC of Al-Mg-Si alloy. The results showed that the alloys with such concentration were resistant to IGC. The same observation was made by Larsen et al. [16]. Moreover, several studies on Al-Mg-Si alloys with Cu content $\leq$ 0.02 wt%, using the term Cu-free, were conducted to investigate the influence of the Mg/Si ratio on the IGC of Al-Mg-Si alloys [10,16,22,23]. In such studies, IGC was directly linked to the presence of β particles and the role of such low Cu content on IGC was completely ignored. However, in the most recent work, Bartawi et al. [2] studied the influence of low Cu addition (0.05 wt%) on the IGC in Al-Mg-Si-T6 alloy. The results showed Cu-rich film and Q/Q′ particles along some high-angle grain boundaries, indicating that Cu as low as 0.05 wt% greatly influences IGC resistance of Al-Mg-Si alloys.

In particular, cooling rate and aging parameters (time and temperatures) can significantly affect the non-equilibrium and equilibrium segregations along grain boundaries. Such segregations will lead to the movement of the impurities toward the grain boundaries and thus reduce the concentration of solute atoms of Mg, Si, Zn, and Cu in the GB vicinities during quenching and aging processes, hence PFZs are formed [24–26]. The influence of cooling rate has been the focus of interest in many studies [14,21,27,28]. It was reported that the quenching rate affected GB particles and the width of the PFZs and, thus IGC resistance of Al-Mg-Si alloys. For instance, Zhang et al. [28] claimed that air-cooling improved the IGC resistance of Al-Mg-Si-Cu alloy as wide PFZs and distantly separated coarse β/Q particles along grain boundaries (GBs) were observed. However, the water-quenched alloy showed narrow PFZs and dense β particles with a higher Q fraction than air-cooled alloy subjected to the same aging conditions. The aging time and temperature are the other important factors affecting IGC resistance [29,30]. The water-quenched Al-Mg-Si-Cu alloys are highly susceptible to IGC in the underaged (UA) and PA conditions due to the presence of Q particles and Cu-enriched film along GBs [7,10–14,16,17]. Further, aging can increase the IGC resistance of Al-Mg-Si-Cu alloys as no Cu-rich film was observed, and Q/Q′ particles were distributed discontinuously along the GB [12,14].

As mentioned above, Cu has a detrimental effect on the IGC resistance of Al-Mg-Si alloy in the UA and PA conditions. Overaging such alloys can improve their resistance, but it is usually accompanied by sacrificing the hardness and strength [6,13,31,32]. However, improving the IGC resistance in Al-Mg-Si alloys by equalizing the potential difference between GB particles, grain interiors, and PFZs via Zn addition has not been previously systematically studied in detail. The influence of Zn on the final appearance of Al-Mg-Si alloys after caustic etching was the focus of attention due to its negative impact on the anodizing response [33–37]. Zn concentration was set to a maximum of 0.03 wt% in Al-Mg-Si to avoid the spangle defect during the anodizing process [33,34]. However, the influence of Zn on the IGC of Al-Mg-Si alloys has only more recently come to attention after reporting a potential improvement in the mechanical properties of Al-Mg-Si alloys that can be achieved by adding Zn at a relatively high concentration (≥ 1 wt%). Such improvement is attributed to the increase in the volume fraction of the clusters and the formation of η $MgZn_2$ and η’ precipitates [5,38–43]. Saito et al. [5] investigated the influence of Zn addition on the mechanical properties and IGC resistance of a Cu-free Al-

Mg-Si alloy. The results showed no measurable impact on the mechanical properties and IGC resistance of Al-Mg-Si alloys with up to 0.11 wt% Zn. Chi et al. [44] studied the effect of Zn (0.05 and 0.2 wt%) and aging on the IGC resistance of Cu-free Al-Mg-Si alloys according to GB/T 7998—2005 standard used to investigate the IGC of 2xxx, 5xxx, and 7xxx series [45]. The results showed that alloy with 0.2 wt% was more susceptible to IGC than the alloy with 0.05 wt%.

It appears that there has been no dedicated work concerning the influence of aging temperature on the microstructure and IGC in Al-Mg-Si alloys in the presence of tiny concentrations of Cu and Zn, expected in the recycled alloys. Moreover, the precipitate GB compositions are not documented in a 6082 alloy with very low Cu and Zn concentrations. Therefore, the present work aims to investigate the influence of minor addition of Cu and Zn on the microstructure, GB chemistry, and IGC resistance of Al-Mg-Si alloys in different aging conditions. The surface and cross-section morphologies of the corroded samples were investigated through a scanning electron microscopy (SEM). GB chemistry, microstructure, and precipitates crystal structures were studied using scanning/transmission electron microscopy (STEM) combined with energy dispersive spectroscopy (EDS).

9.2 Experimental methods

9.2.1 Material used

In this work, three extruded Al-Mg-Si alloys (AA6082) with different trace levels of Zn and Cu were used. The alloys were subjected to the same heat treatment at 540 °C for 30 min followed by water-quenching to room temperature. Thereafter, the samples were artificially aged for 5 h at different temperatures 130, 140, 150, 165, 175, 185, 200, 220, and 240 °C to obtain underaged, peakaged and overaged (OA) conditions. The chemical compositions of the studied alloys are given in Table 9.1.

Table 9.1. As received chemical composition (wt%) of Al 6082 alloys used for investigation

Alloy	Al	Mg	Si	Zn	Cu	Fe	Mn
L1	Balance	0.64	0.97	0.003	0.034	0.22	0.54
L2	Balance	0.63	0.94	0.022	0.034	0.21	0.56
L3	Balance	0.63	0.95	0.059	0.050	0.21	0.58

9.2.2 IGC test

Specimens of 25 x 20 x 4 mm^3 have been sectioned from flat profiles and subjected to different aging temperatures for the IGC test. The IGC resistance was tested and determined according to the standard BS-ISO 11846 method B. The corrosion test involves degreasing in acetone, alkaline etching in 8 wt% sodium hydroxide (NaOH) at 55 °C for 5 min, followed by 2 min desmutting in concentrated nitric acid (HNO_3). Prior to the IGC test, Lacomit varnish was utilized on the cut edges to avoid any possible interaction between the center layer, which comprises big elongated grains and recrystallized surface layer. Subsequently, the samples were immersed for 24 h in an acidified salt solution consisting of 30 g/l sodium chloride and 10 ml/l hydrochloric acid (HCl). After the immersion test, the samples were rinsed in distilled water and ethanol, followed by air drying. The cross-section and surface morphologies were examined by scanning electron microscopy using an AFEG 250 Analytical ESEM microscope.

9.2.3 Microstructure characterization and hardness test

Three alloys with different trace levels of Cu and Zn are labeled as L1, L2, and L3, as shown in Table 9.1. To reveal the microstructure of the studied alloys, specimens of 25 x 10 x 4 mm^3 were ground, mechanically polished to 1 μm, followed by electrochemical etching in tetrafluoroboric acid for 60 sec. The microstructure was acquired afterward using Zeiss Axio Vert.A1 optical microscope.

The EBSD analysis of the heat treated alloy L3 was conducted in the plane containing the extrusion direction (ED) and the transverse direction (TD). Prior to EBSD, the top surface of the extruded material was mechanically polished and then electropolished to obtain good-quality EBSD patterns. The thickness of the surface layer removed by polishing was estimated to be ~40 μm. EBSD data were collected in several regions, covering a total area of 2 mm^2 with a step size of 1 μm.

To investigate the recrystallized surface layer in the transmission electron microscope (TEM), specimens from selected alloys were prepared. The specimens were mechanically thinned to about 100 μm thickness and then electropolished in a solution containing 10 % perchloric acid, 65 %, and 90 % ethanol at about -25 °C using a TenuPol-5 twin-jet system. Two TEM instruments were used to investigate the GBs and precipitate crystal structures in the OA condition. GB chemistries were studied using Titan Analytical 80-300ST microscope operated at 300 kV occupied with Oxford energy dispersive

spectroscopy (EDS) X-Max 80TLE detector. High-resolution high-angle annular dark-field images were recorded using a Cs-corrected JEOL ARM200F microscope.

Vickers hardness testing was performed to characterize the influence of aging temperature and trace levels of Zn and Cu on the alloy hardness and correlate that to IGC resistance. The hardness test was conducted at room temperature under a load of 500 g for an indentation time of 15 s using the microhardness tester (DuraScan 70 G5).

9.3 Results

9.3.1 Grain structures

Since the investigated alloys show similar grain structures, only images for alloy L3 are shown in Fig. 9.1. Optical micrographs taken from three orthogonal planes are shown in Fig. 9.1a. It is seen that the microstructure is fully recrystallized, with fine grains (~20 μm) at the immediate surface. Moreover, grains extended over several millimeters along the extrusion direction (ED) at depth greater than 500 μm can be noticed. Microstructural region focused in this work is the surface layer.

Fig. 9.1b shows an orientation map obtained using the EBSD technique at a depth of ~40 μm of sample L3 aged at 240 °C for 5 h. The grain size at this depth is measured to be 80 μm and the fraction of low angle boundaries is 12 %. Similar to observations in the sample containing 0.05 wt% Cu and 0.003 wt% Zn studied in our previous work [2], the recrystallized layer contains a weak texture with an increased fraction of the shear $\{001\}\langle 110\rangle$ component.

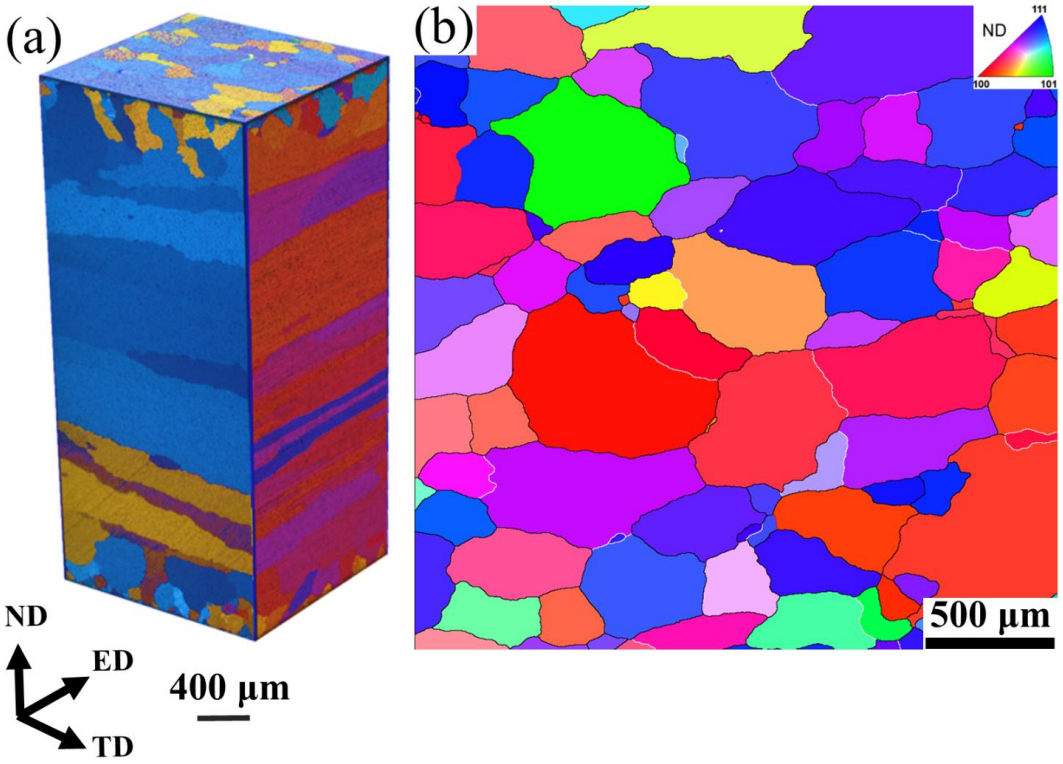

Fig. 9.1. Grain structures of alloy L3: (a) optical micrographs taken from in three orthogonal planes; (b) orientation map showing the microstructure in the ED-TD section at a depth of ~40 µm. White and black lines indicate LABs and HABs, respectively. The ED is parallel to the scale bar.

9.3.2 Age hardening response

The effects of the aging temperature on hardness for the three studied alloys are shown in Fig. 9.2a. Hardness curves show three stages namely: (i) underaging, (ii) peakaging, and (iii) overaging. It is seen that the alloys remain in the UA (lower HV) conditions as long as the temperature is ≤ 165 °C. After aging at 165 °C hardness values are 121 ± 2.4 HV, 105 ± 2.4 HV, and 106 ± 1.5 HV for alloys L1, L2, and L3, respectively. Subsequently, the hardness of the alloys increases with increasing aging temperature, reaching the PA conditions at 175 °C for alloys L1 and L2 and at 185 °C for alloy L3. The peak hardness values for alloys L1, L2, and L3 are 126 ± 1, 113 ± 1.8, and 127 ± 1.9 HV, respectively. The hardness decreases in the OA conditions attained at higher temperatures, see Fig. 9.2a. The maximum IGC penetration depth as a function of aging temperature can be seen in Fig. 9.2b. The lowest IGC penetration depth is observed in the UA conditions, however, increasing the aging time increases the penetration depth until reaching the maximum penetration depth at 185 °C. Further increasing the temperature resulted in lower

penetration depth until all investigated alloys reached the lowest value at 240 °C compared to all other aging temperatures.

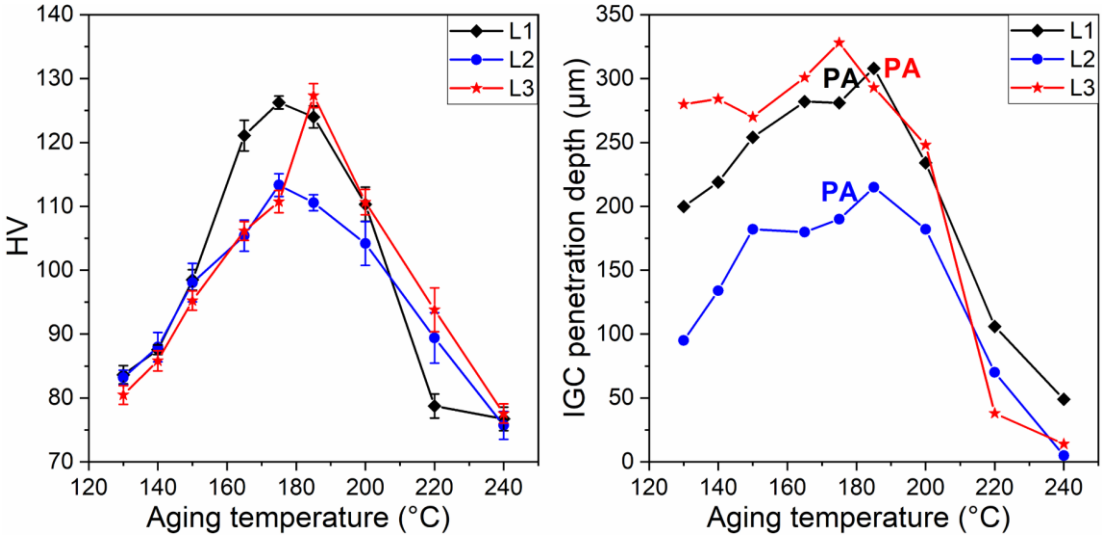

Fig. 9.2. Vickers hardness (a) and maximum IGC penetration depth (b) for the different alloys as a function of aging temperature. "PA" in (b) indicates peakaged condition.

9.3.3 Evaluation of IGC

The accelerated IGC tests indicate that alloys L1 and L3 are highly susceptible to IGC in the UA condition (130-165 °C), as uniform IGC is observed in Fig. 9.3. As the aging temperature increases to 185 °C, the susceptibility to IGC of alloy L1 decreases, and morphology of attack is shifting towards localized IGC, see Fig. 9.3. Compared to other alloys, alloy L2 shows higher IGC resistance after aging in the range of 130 - 200 °C, though the susceptibility to IGC increases also in this alloy after increasing the aging temperature up to 175 °C.

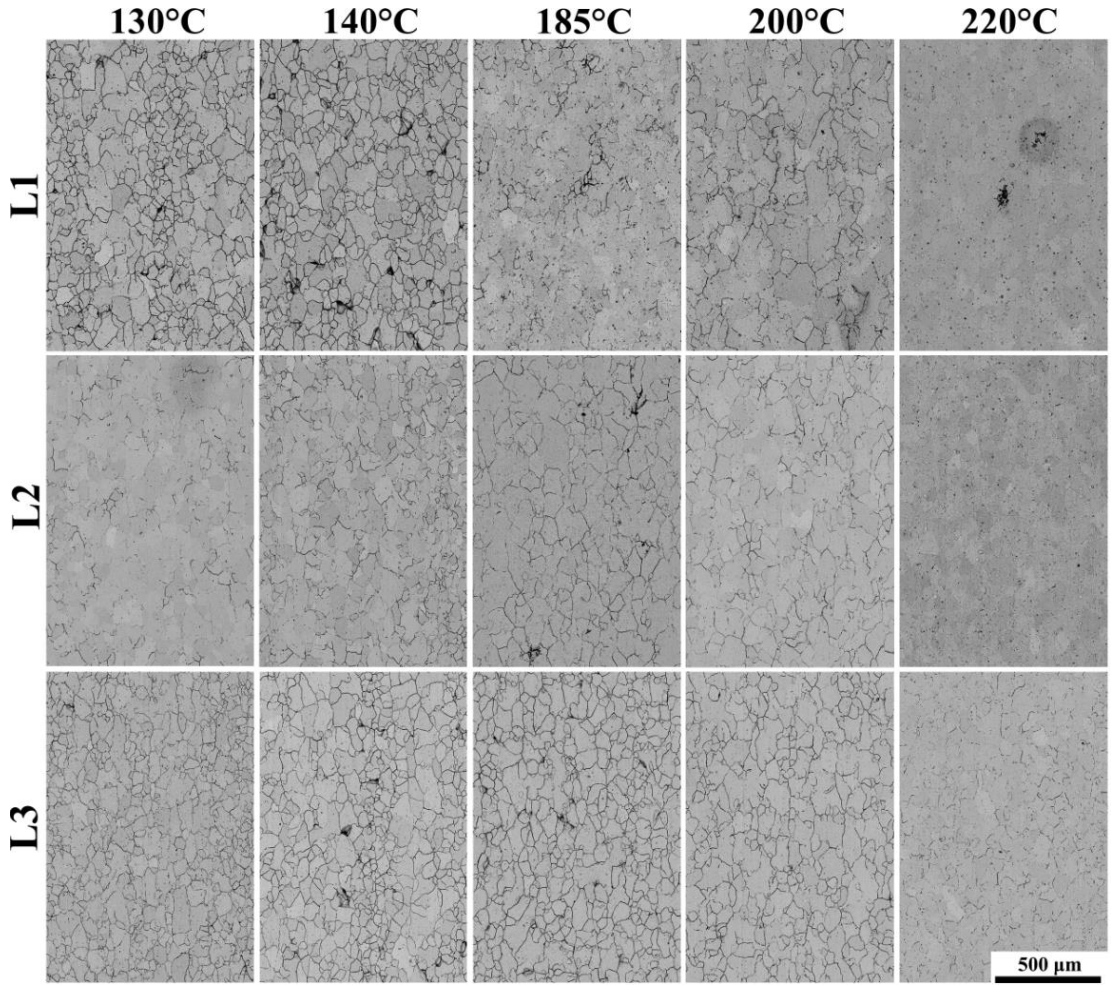

Fig. 9.3. BSE-SEM images showing the surface of the different alloys after the IGC tests. The numbers on the top correspond to the temperatures of aging.

The IGC resistance seems notably improved in the PA and OA conditions as shown in Figs. 9.3 and 9.4. However, Fig. 9.2b provides clear evidence that the PA and slightly OA conditions are characterized by the highest IGC penetration depth and that corrosion depths are small in the strongly UA alloy L1 and in the strongly OA conditions of each alloy. For example, IGC is almost eliminated by aging each alloy at 220 and 240 °C, see Figs. 9.3, 9.4, and supplementary chapter Fig. S.2. As shown in Figs. 9.3 and 9.4, alloy L3 shows low IGC resistance in the UA and PA conditions. However, the susceptibility to IGC decreases in the OA condition showing a noticeable improvement at aging temperatures of 220 and 240 °C. It is interesting to note that, unlike alloy L1 (0.003 wt% Zn), the IGC extension (lateral attack) in alloy L3 does not show notable improvement in the PA condition (Fig. 9.3).

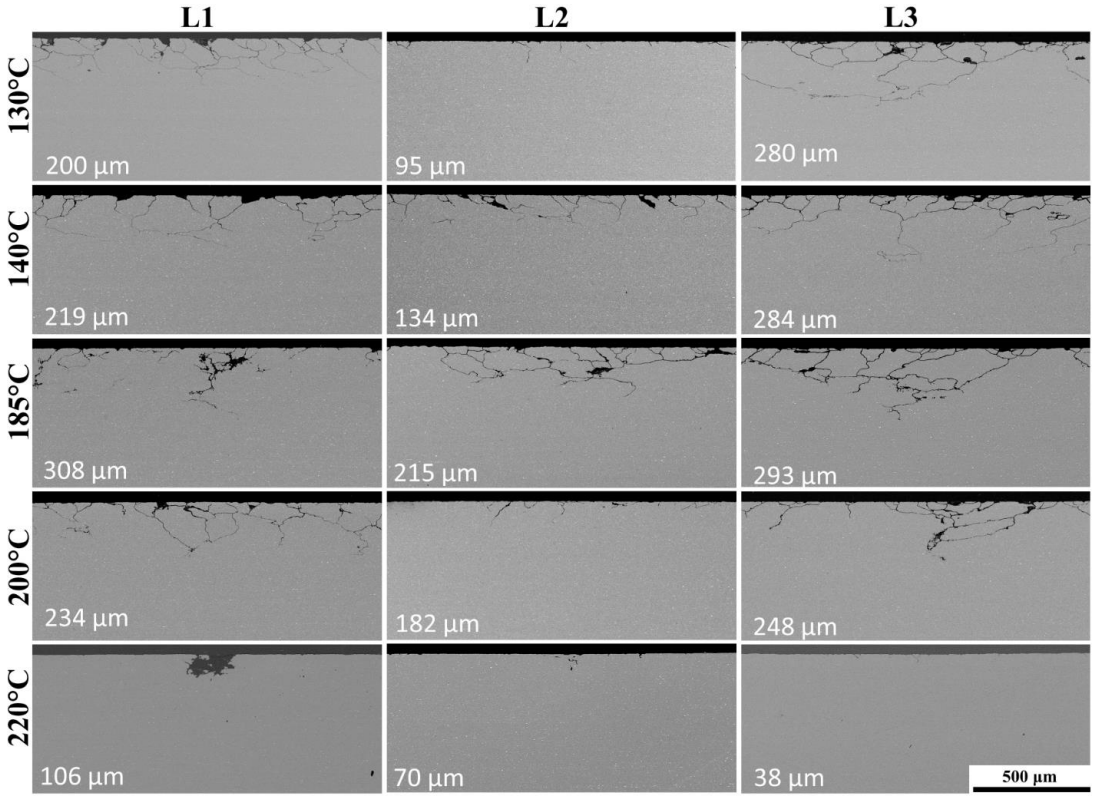

Fig. 9.4. BSE-SEM images from the cross-sections of the different alloys after the IGC test. The numbers on the left side correspond to temperatures of aging.

9.3.4 TEM/STEM analysis of GB particles and bulk precipitates

According to the hardness results demonstrated in Fig. 9.2, the alloys aged for 5 h at temperatures up to 165, 175-185, and above 185 °C are in the UA, PA, and OA conditions, respectively. Moreover, based on the accelerated corrosion test, the IGC was significantly influenced by the aging temperature and minor additions of Cu and Zn. Therefore, the microstructure and GB chemistry associated with one of the representative aging conditions are shown for alloys L2 and L3. Furthermore, alloy L3 with the addition of 0.05 wt% Cu and 0.06 wt% Zn (Cu/Zn ratio of 0.816) has been selected to reveal the effect of trace level of Cu and Zn on the precipitate structures in the OA condition (at 240 °C for 5 h).

In order to reveal characteristics of the GB particles and grain interior precipitates of the studied alloy L2 (at 130 °C) and alloy L3 (at 140 and 240 °C), Fig. 9.5 demonstrates typical HAADF-STEM images of alloys L2 in UA (130 °C), and L3 in UA (140 °C) and OA (240 °C) conditions. From Fig. 9.5a, it can be observed that the GB of alloy L2, aligned almost parallel to the electron beam, contains no visible GB particles or distinguished PFZ. However, the GB of alloy L3 at 140 °C contains fine particles distributed along the GB,

see Fig. 9.5c. Also, a depleted zone of approximately 45 nm is observed at a high magnification as shown as inset in Fig. 9.5c. The matrix of alloys L2, and L3 at the UA condition shows roughly spherical bright spots deriving from very fine phases as shown in Fig. 9.5(b, d). The high-resolution STEM, inset in Fig. 9.5d, shows that most of these particles, which exhibited close to a spherical morphology, have a diameter > 2nm. However, increasing the aging temperature to 240 °C led to significant changes in the alloy microstructure and GB particles. Fig. 9.5e shows coarse GB particles and intragranular precipitates in alloy L3 aged at 240 °C for 5 h (see the solid red arrows). A readily distinguished PFZ along the GB can be noticed. The matrix of alloy L3 in the OA condition shows the presence of rod shape precipitates (β′) as a primary phase, while needle-shaped precipitates (β″) are still observed, see Fig. 9.5f.

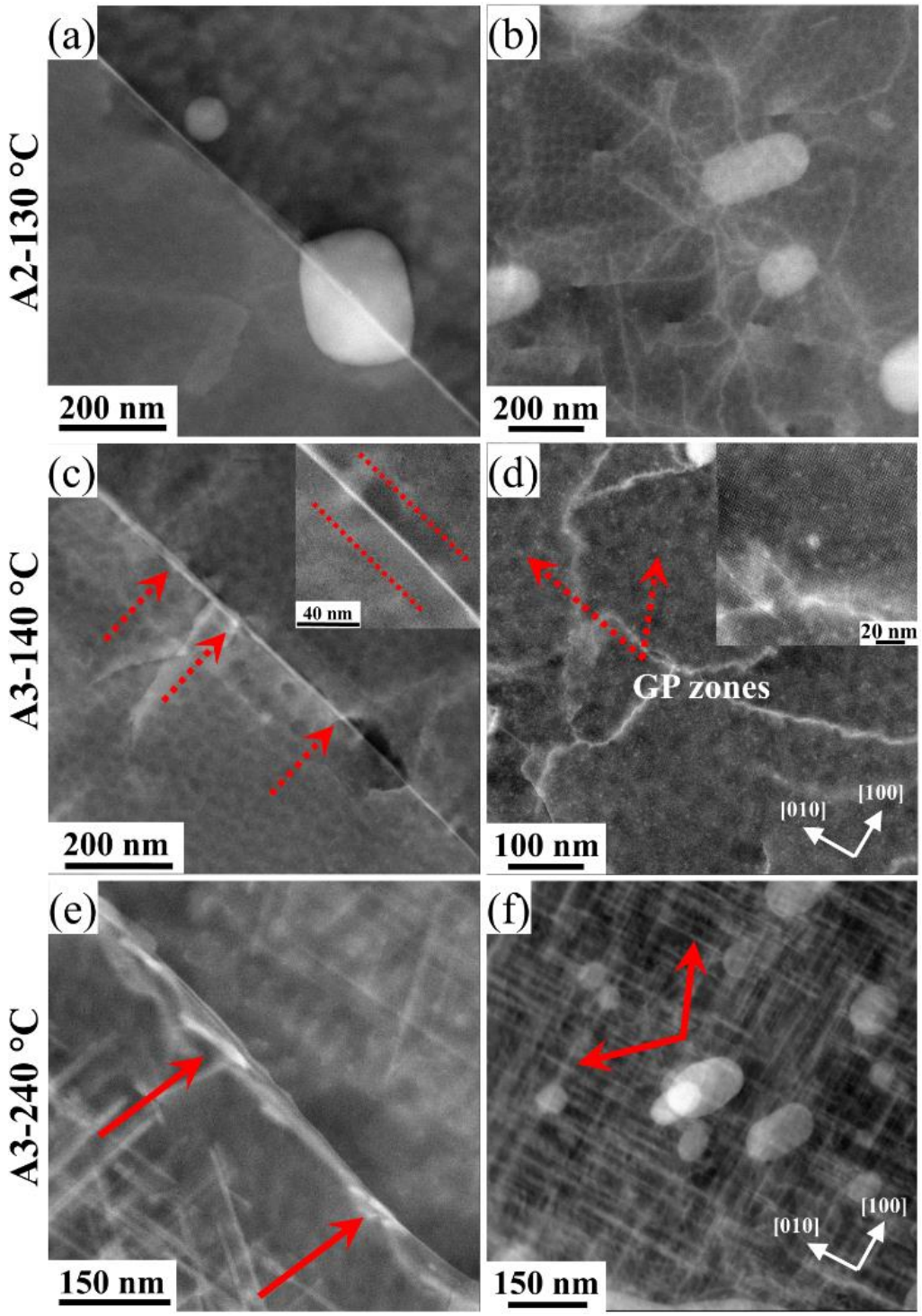

Fig. 9.5. HAADF-STEM micrographs of alloy L2 aged at 130 °C (a), alloy L3 at aged 140 °C (c), and alloy L3 aged at 240 °C (e); (a, c, e) HAADF images showing GB regions, (b, d, f) HAADF images of the grain interior microstructure of alloy L2 aged at 130 °C, alloy L3 at aged 140 °C, and alloy L3 aged 240 °C, respectively. Red arrows in (c and e) indicate the GB particles, while in (d and f) indicate the GP zones and bulk precipitates.

To investigate the GB chemistry, alloys L2 at UA and L3 in UA and OA conditions were subjected to EDS analysis. Fig. 9.6 shows HAAD-STEM images of alloy L2 in UA

condition with their corresponding EDS elemental maps displayed in Fig. 9.6(b, d). The GBs in such aging conditions and low Cu/Zn are either clean GBs or boundaries with distantly separated particles. Fig. 9.6(a, b) shows a clean GB, with no particles or Cu/Zn film detected. However, the EDS maps in Fig. 9.6d reveal the presence of Si particles with a low amount of Mg, which could evolve to β particles at higher aging temperatures. More investigation conducted on such GBs showed particles containing Mg and Si, suggesting that such particles belong to the β phase (Mg-Si particles). Furthermore, it is important to note that no Cu/Zn-rich films are detected along investigated GBs of the alloy L2.

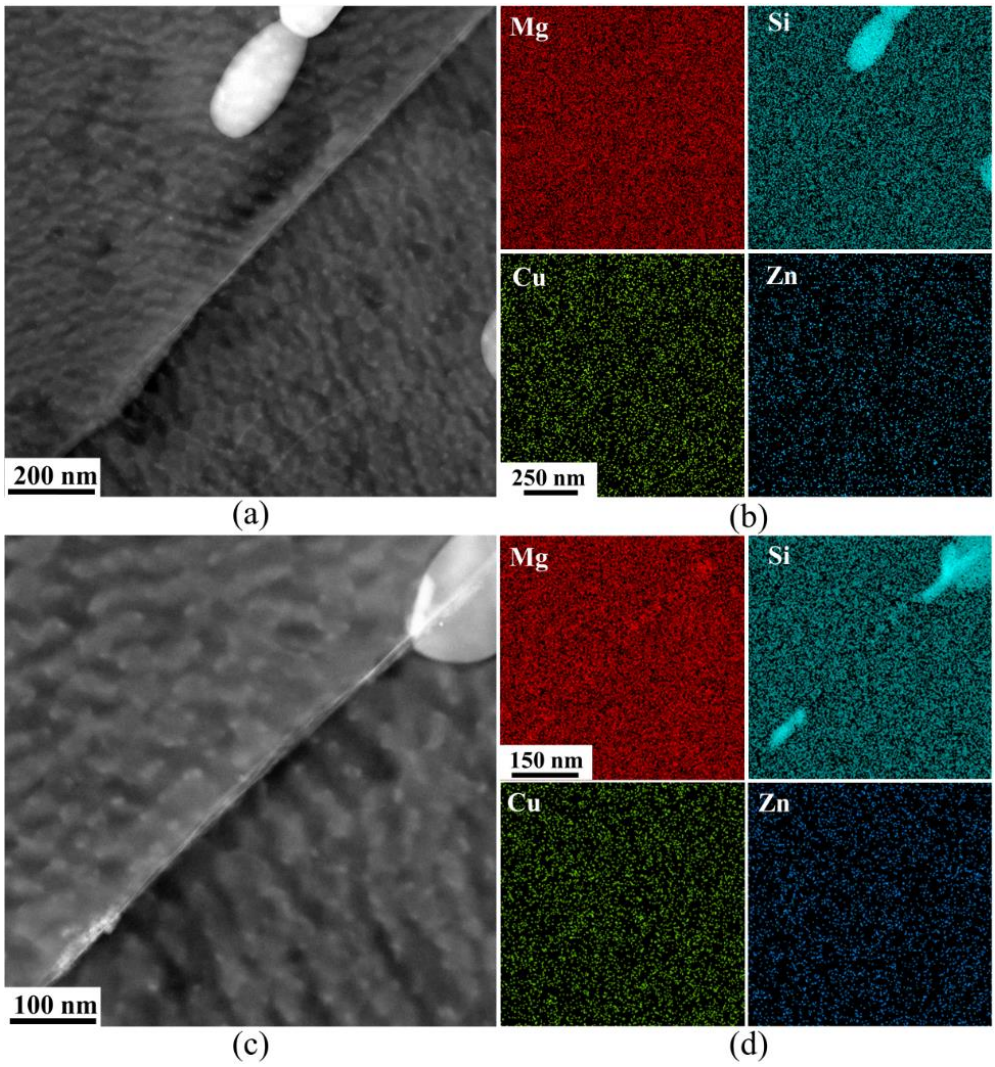

Fig. 9.6. STEM images of alloy L2 aged at 130 °C: (a, b) HAADF images showing GBs parallel to the electron beam. No PFZ is seen in the grain boundary regions; (b, d) elemental maps.

Fig. 9.7 shows HAAD-STEM images of alloy L3 in UA condition and their corresponding GB region elemental maps. Based on several observations, the GB region can be divided into two groups. Firstly, GBs decorated with fine particles containing Mg,

Si, and, interestingly, Cu and Zn are also observed, see Fig. 9.7(a, b). Furthermore, a depleted Mg and Si zone can be clearly noticed, and no Cu-rich film is detected in this type as shown in Fig. 9.7b. Secondly, GBs with distantly separated particles are noticed in Fig. 9.7(c, d). The compositions of the observed particles of this group are similar to the ones in the first group. However, the important finding for the second group is that a Cu-rich film is detected along this GBs, despite a very low Cu concentration (0.05 wt%) and aging temperature (140 °C) in alloy L3, see Fig. 9.7d.

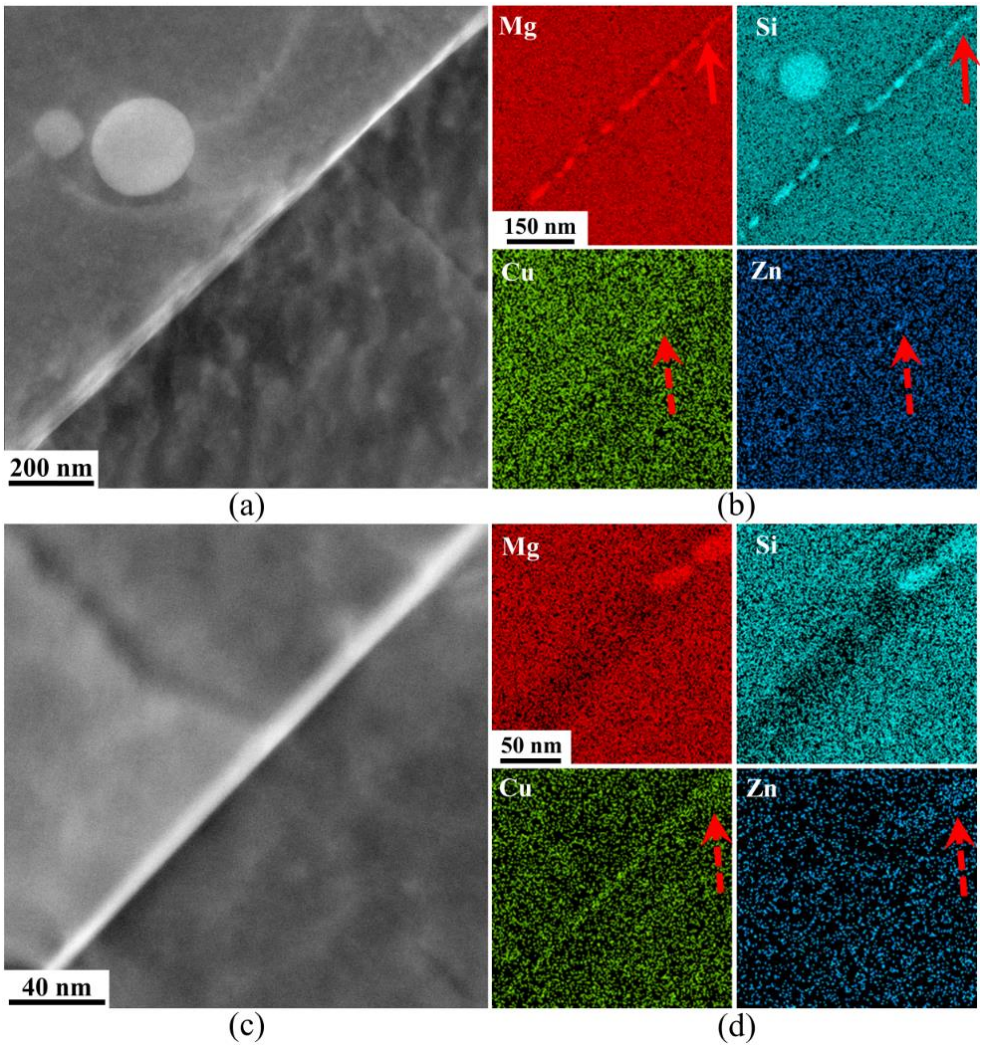

Fig. 9.7. STEM images of alloy L3 aged at 140 °C for 5 h; (a) HAADF showing a grain boundary decorated with very fine grain boundary particles; (b) corresponding EDS element maps of the same area; (c) HAADF image of grain boundary; (d) corresponding element maps. Arrows show GB particles containing Mg, Si, Cu and Zn.

Interestingly some of GB particles found in alloy L3 in the UA condition contain Zn, but not Cu as shown in Fig. 9.8a. Based on several observation of alloy L3 in the UA, fine GB particle of approximately 15 nm are observed. The results indicate that these

particles are Mg-Si, Mg-Si with Cu and Zn, and Mg-Si with Zn particles, see Figs. 9.7 and 9.8a.

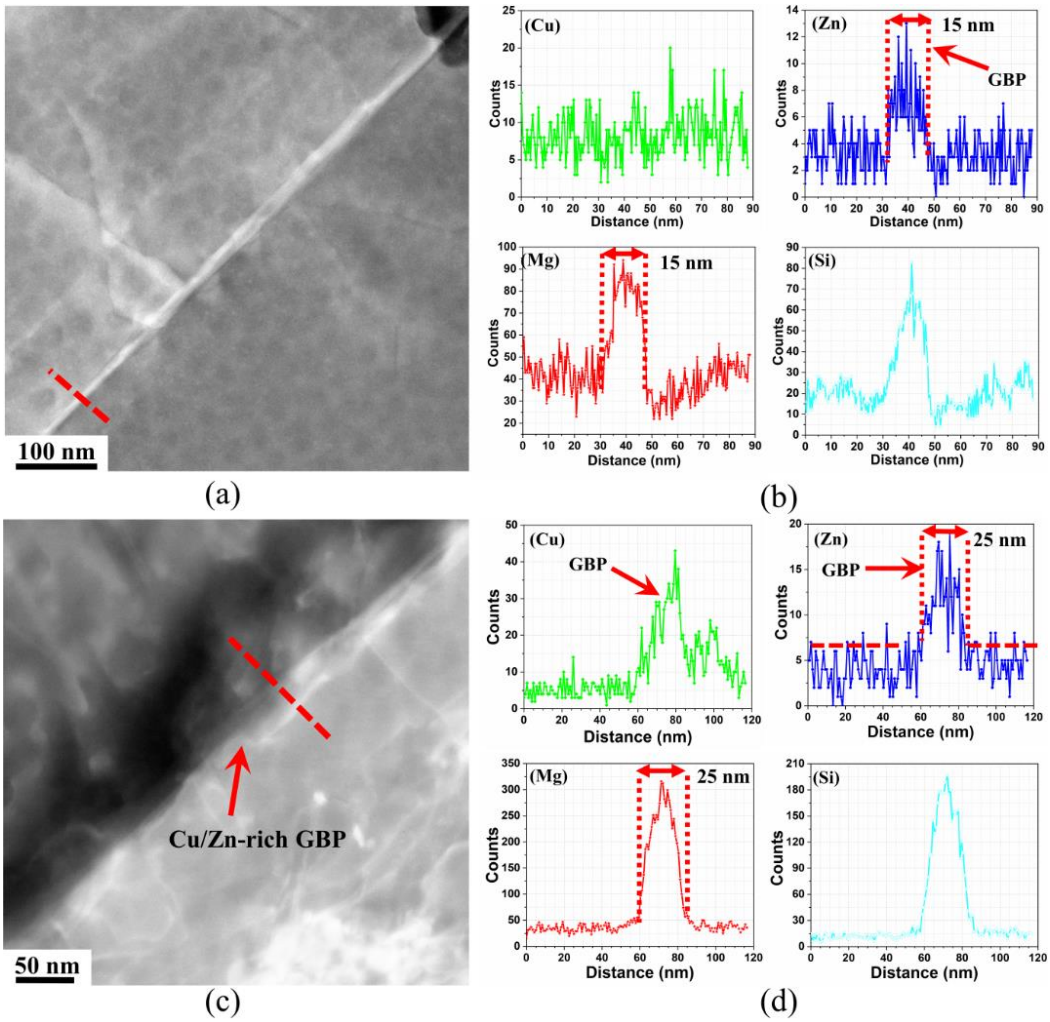

Fig. 9.8. (a) HAADF-STEM image showing a grain boundary of alloy L3 aged at 140 °C, and (b) EDS line scan corresponding to the red dashed line in (a); (c) HAADF-image showing a grain boundary of alloy L3 aged at 240 °C, and (d) EDS line scan corresponding to the red dashed line over the GB in (c). Arrows show the GB particles.

As the aging temperature increases to 240 °C and OA conditions is reached, Figs. 9.8b and 9.9 shows coarse particles containing Mg, Si, Cu, and Zn along the GBs. In this condition, no Cu-rich film is detected along the GBs. Furthermore, coarse intragranular precipitates are observed in this condition, see Figs. 9.5f and 9.9 (a, b).

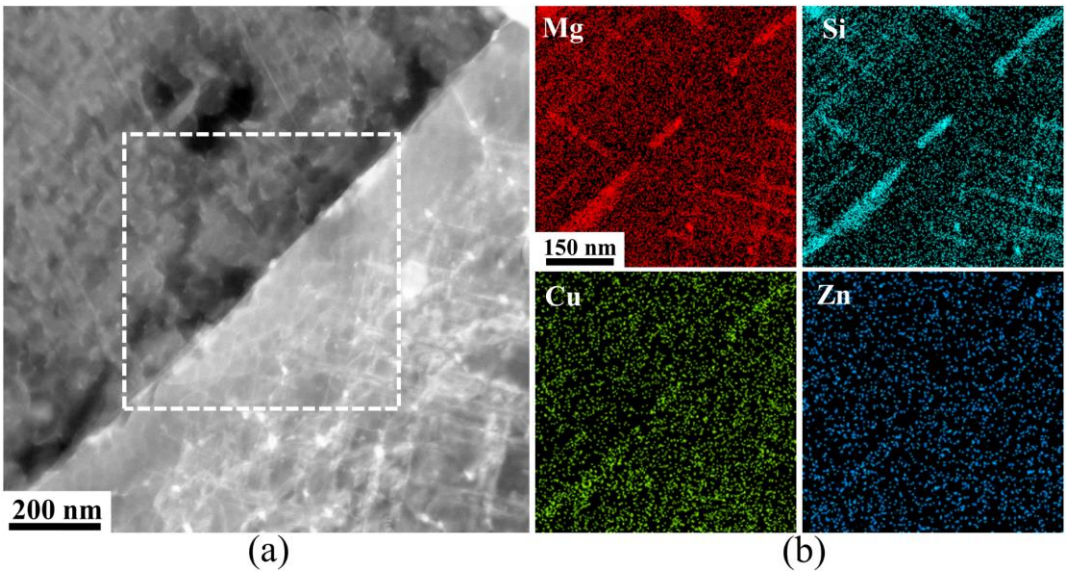

Fig. 9.9. (a) HAADF-STEM images of alloy L3 aged at 240 °C, and (b) EDS elemental maps corresponding to the framed area in (a).

The atomic resolution STEM images shown in the current work were taken from alloy L3 aged at 240 °C, which is known to achieve the OA condition. The precipitates in Al-Mg-Si alloy are grown along <100> Al directions. Therefore, the cross-section of the precipitates shown in Fig. 9.10 was taken from <100> Al zone axis. To reduce the noise by removing all distances shorter than 1.5 Å, fast Fourier transform (FFT) filtering is conducted using a band pass mask. The atomic overlay shown in Fig. 9.10e was achieved considering the construction rules of the precipitates found in the Al-Mg-Si-Cu alloy [46] and the similarity to the well know precipitates in the Al-Mg-Si-Cu system [47]. Fig. 9.10(a-c) demonstrates a typical example of the precipitates found in the Al-Mg-Si alloy with 0.05 wt% Cu and 0.06 wt% Zn in the OA condition. Interestingly, the sub-unit structure of β″ in addition to Q′/C and B′ precipitates can be observed in Fig. 9.10. Also, some atomic columns that do not belong to well-known precipitates structures exhibit a noticeably higher contrast than other neighboring columns due to the partial occupancy of Cu/Zn atoms, see dashed red arrow in Fig. 9.10a.

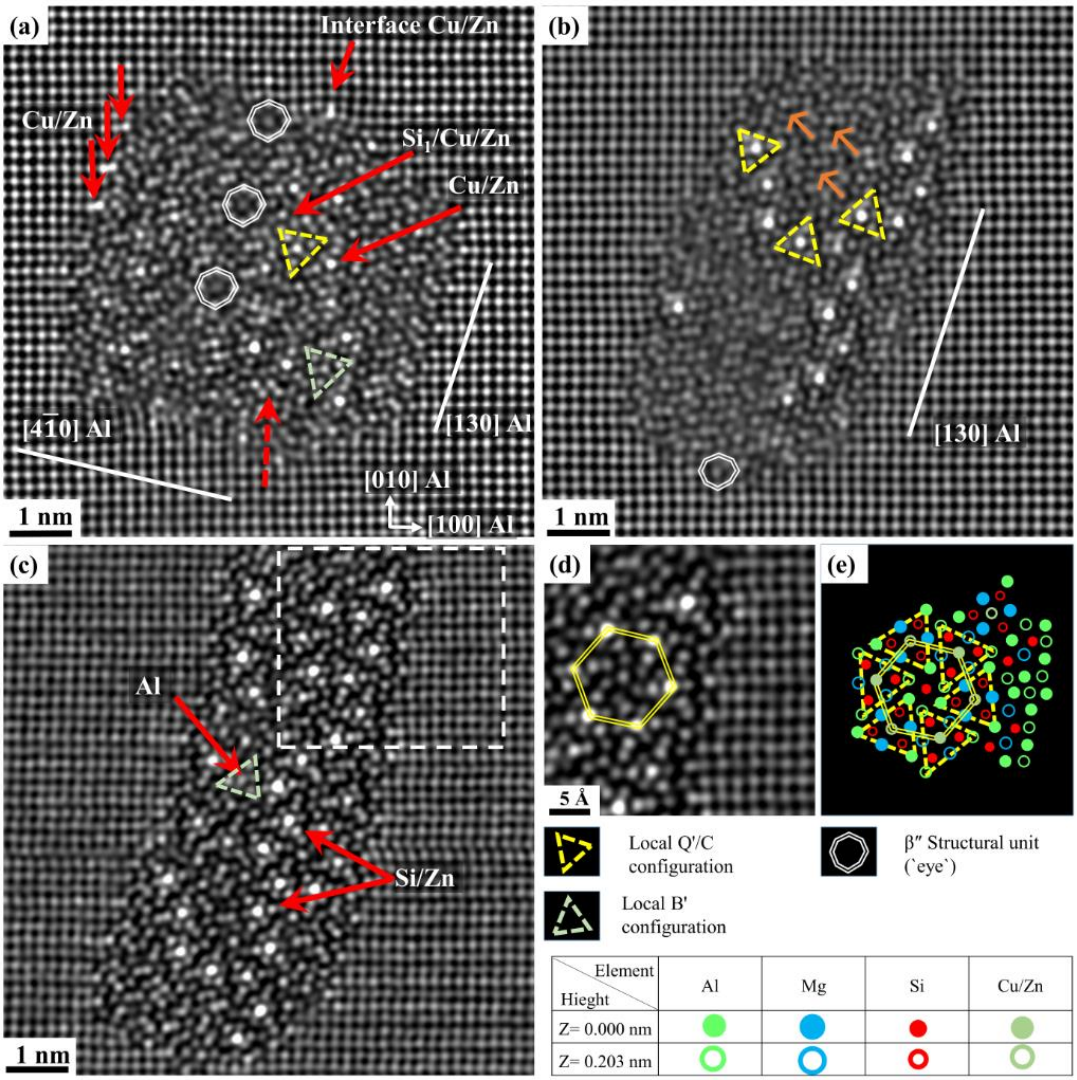

Fig. 9.10. HAADF STEM images of the cross-section of precipitates in the microstructure of alloy L3 aged at 240 °C. (a, b, and c) FFT filtered images, (d) magnified image of the selected area in (c), (e) suggested atomic overlay based on the roles considering the following atoms Al, Si, Mg, Cu and Zn.

9.4 Discussion

The IGC resistance of Al-Mg-Si alloys is determined by GB chemistry which is greatly influenced by different types of segregated solute elements and formed phases located along the GBs. The type, density, and size of the GB particles as well as the impurity-rich films (e.g., Cu or Zn film concentration and continuity) formed along the GB can be greatly influenced by the heat treatment condition and alloy compositions. The segregation causes solute depletion in the GB vicinities during quenching from high temperature and subsequent nucleation and growth of GB particles during aging [26,48]. The present results show the influence of tiny concentrations of Cu/Zn, and aging

temperature on microstructure, precipitate crystal structure (alloy L3 in OA condition) and IGC resistance, which is relevant to the recycling of aluminum alloys. The biggest challenge in recycling is the scrap quality, i.e., the maximum amount of Al scrap that can be added to virgin aluminum without poisoning the final products with impurity elements such as Fe, Mn, Cu and Zn as a result of the deviation from the standard alloy composition [49].

9.4.1 Effect of aging temperature on microstructure

Since all samples were water-quenched after solution heat treatment, any microstructure and GB chemistry variation within the same alloy will be ascribed to different aging temperatures. It is reported that the precipitate growth and coarsening are closely controlled by Mg atoms [26,50] in 6xxx series alloys. The diffusion coefficient of Mg in Al will increase as the temperature increases. This explains the fine GB particles formed at low temperatures (130 and 140 °C) and clusters/GP zones in the grain interior, see Fig. 9.5(a, b, c, d). The STEM results indicate that the matrix of alloys L2 and L3 in the UA condition consists primarily of roughly disc-shaped very fine phases, identified as Guinier–Preston (GP) zones [51].

Furthermore, alloy L2 shows two types of GBs, namely clean GBs with no sign of particles, Fig. 9.6a, and GBs with distantly separated very fine particles. The particles along such GBs are identified as Si-rich particles and Mg + Si-rich particles. At the same time, the STEM results indicate the presence of three types of fine GB particles in alloy L3 based on their composition. Namely, Mg-Si particles, indicated by solid red arrow in Fig. 9.7(b), Cu and Zn-containing Mg-Si particles, shown by dashed red arrow in Fig. 9.7(b, d), and Zn-containing Mg-Si particles, indicated by red arrow in Fig. 9.8b. Furthermore, a high number density of fine GB particles are observed in alloy L3 in the UA condition, which can be attributed to higher Cu and Zn concentrations [52–54]. STEM results obtained from the further aged sample L3 (240 °C) show a significant transformation in the precipitate morphology as coarse precipitates in the grain interior, see Fig. 9.5(e, f). The heavily fragmented phases observed in alloy L3 show several sub-unit structures such as β″, β′, and/or Q′/C in their structures see Fig. 9.10. Sunde et al. [55] investigated Al-Mg-Si alloy with 0.03 (S) and 0.09 (C) wt% in different aging conditions and reported that β″, β′, U2, and/or Q′/C were noticed in the fragmented precipitate structures of alloys S and C aged at

180 °C for 12 h and 24 h. The difference between the alloys S and C at both aging conditions was the portion of Cu containing unit structures as a complete Q′ unit cell was observed in C after 12 h and 24 h aging. In the present work, a complete Q′/C unit structure is observed in many precipitates in alloy L3 with 0.05 wt% Cu, see Fig. 9.10(c, e). Moreover, abnormally brighter columns are observed in the precipitate structures that do not belong to the solved structure in Al-Mg-Si alloys. Such columns are believed to be due to the presence of Zn, see Fig. 9.10a.

9.4.2 Effect of aging temperature and concentration of Cu and Zn on IGC resistance

It is generally accepted that IGC of Al-Mg-Si alloy with relatively high Cu content (≥ 0.1 wt%) is caused by microgalvanic coupling between anodic part (e.g., PFZ) and cathodic path (Cu-rich film supported by Q/Q′ particles) [9,14,18,27,56,57]. However, limited work has been conducted to investigate the influence of a minor amount of Cu (≤ 0.06 wt%) on the IGC of Al-Mg-Si alloy [2,14,27,28]. Zhang et al. [28] investigated the impact of the quenching rate on the IGC of Al-0.68Mg-1.1Si-0.04Zn-0.06Cu. The results showed that the quenching rate dramatically influences the IGC resistance of Al-Mg-Si-T6 alloys. However, no Cu-rich film was detected, in addition to that, only 5-10 % of the GB particles were Q phase, while the rest were Mg-Si particles. Therefore, the authors concluded that the root cause of the IGC at different quenching rates cannot be conclusively identified based on their results. Hence, the current work would be a cornerstone for subsequent studies concerning recycled (dirty) alloys and the potential ways to reduce the detrimental effect of the impurities such as Cu, Zn, and Fe.

As revealed in Figs. 9.2 and 9.3, alloy L2 significantly differs in its IGC resistance at different aging temperatures. The distinct IGC resistance after aging at 130 °C (UA condition) is attributed to the absence of Cu- and/or Zn-rich films, distantly separated fine particles, and non-distinguished Mg and Si depleted zones, see Fig. 9.6. Moreover, in this condition, some GBs show that these fine GB particles contain Mg, Si and low amount of Cu and Zn (not shown). Consequently, the absence of continues cathodic path (Cu film and closely spaced GB particles, e.g., Q phase) and anodic path (PFZs and closely spaced β and Zn-containing β particles) result in high IGC resistance in alloy L2. However, further aging noticeably reduces the IGC resistance of alloy L2 as more lateral IGC attack and a deeper penetration depth are observed in the samples aged at 140, 150, and 165 °C as shown in

Figs. 9.2, 9.3, and supplementary chapter Fig. S.2. The lower IGC resistance in these cases is attributed to the GB particles coarsening leading to the formation of distinguished PFZ as well as the formation of the solute-rich film, namely Cu-rich film. Comparing the IGC results of alloys L1 and L2, it is evident that the Zn addition improves the IGC resistance at all aged conditions, Figs. 9.2 and 9.3, indicating that the Cu/Zn ratio of 1.58 effectively suppresses the IGC caused by Cu and Zn in alloy L1. The STEM investigations conducted on alloy L3 indicate that the Zn incorporated into the GB particles even in the very early stage of aging, see Figs. 9.7 and 9.8b. However, an unbalanced Cu/Zn ratio could provide an opposite effect leading to high IGC susceptibility.

Furthermore, alloy L3 (0.05Cu and 0.06Zn wt%) is found to be highly susceptible to IGC at the UA and PA conditions. The EDS-STEM results showed the presence of Cu-rich film, depleted zone and closely spaced particles containing Mg, Si and a noticeable amount of Cu and/or Zn, see Figs. 9.7, 9.8a, and 9.9. Since the electrochemical behavior of the GB particles is highly reliant on the compositions, the detected particles containing Cu and Zn are believed to significantly contribute to the IGC in alloy L3 at the UA and PA conditions. Moreover, the detected PFZs are believed to have a considerable contribution to IGC as the high number density of GB particles will consume considerable amount of Mg and Si atoms, while only clusters/GP zones are formed in the grain interior, see Fig. 9.5d. Accordingly, the solute concentrations of Mg, Si, Zn, and Cu in the matrix should be high compared to PFZs; thus, a different electrochemical potential is expected between PFZs and the matrix. As a result, the Cu-rich film, the GB particles, Al matrix adjacent to the PFZ, and the presence of narrow PFZ will provide the driving force for the IGC to initiate and propagate on alloy L3. Interestingly, the IGC in alloy L3 is noticeably improved in the OA condition (aged at 220 and 240 °C). The absence of GB Cu-rich film appears to increase the IGC resistance, see Fig. 9.9. Moreover, the EDS-STEM maps show that the GB particles are rich in Mg, Si, Cu and Zn. Additionally, Cu-rich precipitates in the grain interior are observed. Therefore, the solute concentration of Mg, Si, Cu and Zn in the matrix should be relatively low, which leads to almost the same solute concentrations in the PFZs. Consequently, the improvement in the IGC resistance at high aging temperatures is attributed to the decrease in the electrochemical potential difference between the GB particles, PFZ and adjacent Al matrix due to consuming the Mg, Si, Cu and Zn by GB

particles and grain interior precipitates resulting in the noticeably lower driving force for IGC to take place on the surface and propagate in alloy L3 aged at 240 °C.

9.5 Conclusions

The alloy composition (i.e., Cu and Zn) and aging temperature are found to have a significant influence on the hardness, microstructure, IGC resistance and precipitate structures.

1. Tiny concentrations of Cu and Zn are shown to have a significant impact on the IGC resistance in different aging conditions. The results show that 0.03 wt% Cu has a detrimental effect on the IGC resistance of Al-Mg-Si in UA and PA conditions. The IGC resistance can be improved by further aging to reach high performance in the OA (at 220-240 °C) conditions, but at the expense of hardness.
2. The Cu/Zn ratio of 1.58 in alloy L2 containing minor amounts of Cu and Zn is found to be an excellent proportion to significantly reduce the negative impact of Cu and Zn on the IGC resistance with no noticeable reduction in hardness.
3. Aging temperature dramatically influences the composition of grain boundary particles in the presence of trace levels of Cu and Zn. The size, density and composition of grain boundary particles are also considerably affected by the aging temperature, dense and fine particles in alloy L3 are observed in UA condition. In contrast, coarser particles are observed in the PA condition.
4. Minor additions of Cu and Zn have noticeable influence on the bulk precipitate structures in the OA condition. A Q′/C, β″ and B′ local configurations are observed in alloy L3 aged at 240 °C.

CRediT authorship contribution statement

Emad H. Bartawi: Conceptualization, Methodology, Investigation, Formal analysis, Writing - Original Draft, **Ghada Shaban:** Writing - Review & Editing, Formal analysis, **Calin D. Marioara:** Writing - Review & Editing, Formal analysis, Investigation, **Ruben Bjørge:** Writing - Review & Editing, Investigation. **Oleg Mishin:** Writing - Review & Editing, Investigation (EBSD), Formal analysis (EBSD), **Randi Holmestad:** Writing - Review & Editing**, Rajan Ambat:** Conceptualization, Supervision, Writing - Review & Editing, Project administration, Funding acquisition.

Acknowledgements

The authors express their thanks to Hydro Aluminium, Norway, for supplying the materials. The authors extend their gratitude to Dr. J. Kling from DTU Nanolab for his technical assistance in the STEM experiments. EHB and RA acknowledge funding from the Independent Research Fund Denmark (grant number 9041- 00240A). Also, this project has also received funding from the European Union's Horizon 2020 research and innovation programme under grant agreement No 823717 – ESTEEM3. The Research Council of Norway (RCN) is acknowledged for funding the NTNU atom probe facility through the Norwegian Laboratory for Mineral and Materials Characterization (MiMaC) project number: 269842.

Data Availability

The raw/processed data required to reproduce these findings cannot be shared at this time as the data also forms part of an ongoing study

References

[1] N. Arab, The Challenges of Aluminum Recycling From End-of-Life Vehicles, J. Environ. Friendly Mater. 1 (2017) 19–25.

[2] E.H. Bartawi, O. V. Mishin, G. Shaban, J.H. Nordlien, R. Ambat, Electron microscopy analysis of grain boundaries and intergranular corrosion in aged Al-Mg-Si alloy doped with 0.05 wt% Cu, Corros. Sci. 209 (2022) 110758.

[3] O. Access, The Effect of chemical composition on EN AW 6XXX series aluminum alloys, IntechOpen, 2023.

[4] W. Samuel R., The impact of recycling on the mechanical properties of 6XXX series aluminum alloys, J. Sib. Fed. Univ. 11 (2018) 409–418.

[5] T. Saito, S. Wenner, E. Osmundsen, C.D. Marioara, S.J. Andersen, J. Røyset, W. Lefebvre, R. Holmestad, The effect of Zn on precipitation in Al-Mg-Si alloys, Philos. Mag. 94 (2014) 2410–2425.

[6] A.P. Sekhar, A. Samaddar, A.B. Mandal, D. Das, Influence of ageing on the intergranular corrosion of an Al–Mg–Si alloy, Met. Mater. Int. 27 (2021) 5059–5073.

[7] Y. Zheng, B. Luo, C. He, Y. Su, Effect of aging time on microstructure evolution and corrosion behavior of an Al-Mg-Si alloy, Mater. Res. Express. 6 (2019) 116582.

[8] W.J. Liang, P.A. Rometsch, L.F. Cao, N. Birbilis, General aspects related to the corrosion of 6xxx series aluminium alloys: Exploring the influence of Mg/Si ratio and Cu, Corros. Sci. 76 (2013) 119–128.

[9] M.H. Larsen, J.C. Walmsley, O. Lunder, K. Nisancioglu, Significance of low copper content on grain boundary nanostructure and intergranular corrosion of AIMgSi(Cu) model alloys, in: Mater. Sci. Forum, Trans Tech Publications Ltd, 2006: pp. 667–672.

[10] M.H. Larsen, J.C. Walmsley, O. Lunder, K. Nisancioglu, Effect of excess silicon and small copper content on intergranular corrosion of 6000-series aluminum alloys,

J. Electrochem. Soc. 157 (2010) C61.

[11] V. Guillaumin, Influence of overaging treatment on localized corrosion of Al 6056, Corrosion. 56 (2000) 12–23.

[12] H. Li, P. Zhao, Z. Wang, Q. Mao, B. Fang, R. Song, Z. Zheng, The intergranular corrosion susceptibility of a heavily overaged Al-Mg-Si-Cu alloy, Corros. Sci. 107 (2016) 113–122.

[13] G. Svenningsen, M.H. Larsen, J.C. Walmsley, J.H. Nordlien, K. Nisancioglu, Effect of artificial aging on intergranular corrosion of extruded AlMgSi alloy with small Cu content, Corros. Sci. 48 (2006) 1528–1543.

[14] G. Svenningsen, M.H. Larsen, J.H. Nordlien, K. Nisancioglu, Effect of thermomechanical history on intergranular corrosion of extruded AlMgSi(Cu) model alloy, Corros. Sci. 48 (2006) 3969–3987.

[15] C. Schnatterer, D. Zander, Influence of the grain boundary chemistry on the intergranular corrosion mechanisms of a high-strength Al-Mg-Si alloy, Surf. Interface Anal. 48 (2016) 750–754.

[16] M.H. Larsen, J.C. Walmsley, O. Lunder, R.H. Mathiesen, K. Nisancioglu, Intergranular corrosion of copper-containing AA6xxx AlMgSi aluminum alloys, J. Electrochem. Soc. 155 (2008) C550.

[17] S.K. Kairy, T. Alam, P.A. Rometsch, C.H.J. Davies, R. Banerjee, N. Birbilis, Understanding the origins of intergranular corrosion in copper-containing Al-Mg-Si alloys, Metall. Mater. Trans. A Phys. Metall. Mater. Sci. 47 (2016) 985–989.

[18] S. Kumari, S. Wenner, J.C. Walmsley, O. Lunder, K. Nisancioglu, Progress in understanding initiation of intergranular corrosion on AA6005 aluminum alloy with low copper content, J. Electrochem. Soc. 166 (2019) C3114–C3123.

[19] H. Hug, Ueber den einflußgeringer schwermetallgehalte auf die korrosionsbeständigkeit von Al-Mg-Si Legierungen, Aluminium. 23 (1941) 33.

[20] K. Nisancioglu, Ø. Strandmyr, Corrosion of AlMgSi alloys with Cu additions: the

effect of Cu content up to 0.9 weight percent, Report no, STF34 A78052, SINTEF, Trondheim, Norw. (1978).

[21] G. Svenningsen, M.H. Larsen, J. Lein, J. Nordlien, K. Nisancioglu, Intergranular corrosion of extruded AA6000-series model alloys, Proc. 9th Int. Conf. Alum. Alloy. (2004) 818–824.

[22] S.K. Kairy, P.A. Rometsch, K. Diao, J.F. Nie, C.H.J. Davies, N. Birbilis, Exploring the electrochemistry of 6xxx series aluminium alloys as a function of Si to Mg ratio, Cu content, ageing conditions and microstructure, Electrochim. Acta. 190 (2016) 92–103.

[23] S.K. Kairy, P.A. Rometsch, C.H.J. Davies, N. Birbilis, On the intergranular corrosion and hardness evolution of 6xxx series Al alloys as a function of Si:Mg ratio, Cu Content, and aging condition, Corrosion. 73 (2017) 1280–1295.

[24] P. Lejček, Grain boundary segregation in metals, Springer Series in Materials Science, 2010.

[25] H. Jiang, R.G. Faulkner, Modelling of grain boundary segregation, precipitation and precipitate-free zones of high strength aluminium alloys - II. Application of the models, Acta Mater. 44 (1996) 1865–1871.

[26] M. de Haas, S.M. van Scherpenzeel, J.T.M. de Hosson, Grain boundary segregation and precipitation in aluminium alloy AA6061, Mater. Sci. Forum. 519–521 (2006) 467–472.

[27] G. Svenningsen, J.E. Lein, A. Bjørgum, J.H. Nordlien, Y. Yu, K. Nisancioglu, Effect of low copper content and heat treatment on intergranular corrosion of model AlMgSi alloys, Corros. Sci. 48 (2006) 226–242.

[28] X. Zhang, X. Zhou, J.O. Nilsson, Corrosion behaviour of AA6082 Al-Mg-Si alloy extrusion: The influence of quench cooling rate, Corros. Sci. 150 (2019) 100–109.

[29] K. El-Menshawy, A.W.A. El-Sayed, M.E. El-Bedawy, H.A. Ahmed, S.M. El-Raghy, Effect of aging time at low aging temperatures on the corrosion of aluminum alloy 6061, Corros. Sci. 54 (2012) 167–173.

[30] Z. Wang, H. Li, F. Miao, W. Sun, B. Fang, R. Song, Z. Zheng, Improving the intergranular corrosion resistance of Al-Mg-Si-Cu alloys without strength loss by a two-step aging treatment, Mater. Sci. Eng. A. 590 (2014) 267–273.

[31] ASM International, Handbook Committee, and American Society for Metals. Heat Treating Division. Heat treating. Vol. 4. ASM international, (1991).

[32] A.P. Sekhar, A.B. Mandal, D. Das, Mechanical properties and corrosion behavior of artificially aged Al-Mg-Si alloy, J. Mater. Res. Technol. 9 (2020) 1005–1024.

[33] M. Lableu, F. Savard, R.T. Alcan, Metallurgical Assessment of Acid Etch as Anodizing Pretreatment, in: Anodizing Conf. Montr., 2010: p. 12.

[34] A. Lutz, L. Malet, J. Dille, L.H. de Almeida, L. Lapeire, K. Verbeken, S. Godet, H. Terryn, I. De Graeve, Effect of Zn on the grain boundary precipitates and resulting alkaline etching of recycled Al-Mg-Si-Cu alloys, J. Alloys Compd. 794 (2019) 435–442.

[35] Ø. Bauger, O. Reiso, H. Bjerkaas, T. Hauge, S.K. Fjeldbo, Aluminium extrusion alloy suitable for etched and anodized components, U.S. Patent No. 11,542,576. 3 Jan, 2023.

[36] M.U.F. Chandia, Ø. Bauger, T. Furu, Effect of composition, grain size and texture on the etching response of 6xxx alloys, in: Proc. 12th Int. Conf. Alum. Alloy., 2010: pp. 781–786.

[37] Ø. Bauger, H. Bjerkaas, Aspects of preferential grain etching during alkaline pre-etching step before anodizing of aluminum profiles, in: Proc. Tenth Int. Alum. Extrus. Technol. Semin., 2012: pp. 421–430.

[38] L. Li, S. Ji, Q. Zhu, Y. Wang, X. Dong, W. Yang, S. Midson, Y. Kang, Effect of Zn concentration on the microstructure and mechanical properties of Al-Mg-Si-Zn alloys processed by gravity die casting, Metall. Mater. Trans. A. 49 (2018) 3247–3256.

[39] X.P. Ding, H. Cui, J.X. Zhang, H.X. Li, M.X. Guo, Z. Lin, L.Z. Zhuang, J.S. Zhang, The effect of Zn on the age hardening response in an Al-Mg-Si alloy, Mater. Des.

65 (2015) 1229–1235.

[40] S. Zhu, Z. Li, L. Yan, X. Li, S. Huang, H. Yan, Y. Zhang, B. Xiong, Natural aging behavior in pre-aged Al–Mg–Si–Cu alloys with and without Zn addition, J. Alloys Compd. 773 (2019) 496–502.

[41] M.X. Guo, J.Q. Du, C.H. Zheng, J.S. Zhang, L.Z. Zhuang, Influence of Zn contents on precipitation and corrosion of Al-Mg-Si-Cu-Zn alloys for automotive applications, J. Alloys Compd. 778 (2019) 256–270.

[42] M.X. Guo, X.K. Zhang, J.S. Zhang, L.Z. Zhuang, Effect of Zn addition on the precipitation behaviors of Al–Mg–Si–Cu alloys for automotive applications, J. Mater. Sci. 52 (2017) 1390–1404.

[43] M.X. Guo, G. Sha, L.Y. Cao, W.Q. Liu, J.S. Zhang, L.Z. Zhuang, Enhanced bake-hardening response of an Al–Mg–Si–Cu alloy with Zn addition, Mater. Chem. Phys. 162 (2015) 15–19.

[44] S. Chi, Y. Deng, X. Xu, X. Guo, Influence of minor Zn addition on precipitation behavior and intergranular corrosion properties of Al-Mg-Si alloy, Materials (Basel). 13 (2020) 650.

[45] G. 7998-2005, Test method for intergranular corrosion of aluminium alloy, China Int. Stand. (2005).

[46] S.J. Andersen, C.D. Marioara, J. Friis, R. Bjørge, Q. Du, I.G. Ringdalen, S. Wenner, E.A. Mørtsell, R. Holmestad, T. Saito, J. Røyset, O. Reiso, Directionality and column arrangement principles of precipitates in Al-Mg-Si-(Cu) and Al-Mg-Cu linked to line defect in Al, Mater. Sci. Forum. 877 (2017) 461–470.

[47] T. Saito, E.A. Mørtsell, S. Wenner, C.D. Marioara, S.J. Andersen, J. Friis, K. Matsuda, R. Holmestad, Atomic structures of precipitates in Al–Mg–Si alloys with small additions of other elements, Adv. Eng. Mater. 20 (2018) 1800125.

[48] H. Jiang, R.G. Faulkner, Modelling of grain boundary segregation, precipitation and precipitate-free zones of high strength aluminium alloys - I. The model, Acta Mater. 44 (1996) 1857–1864.

[49] D. Raabe, D. Ponge, P.J. Uggowitzer, M. Roscher, M. Paolantonio, C. Liu, H. Antrekowitsch, E. Kozeschnik, D. Seidmann, B. Gault, F. De Geuser, A. Deschamps, C. Hutchinson, C. Liu, Z. Li, P. Prangnell, J. Robson, P. Shanthraj, S. Vakili, C. Sinclair, L. Bourgeois, S. Pogatscher, Making sustainable aluminum by recycling scrap: The science of "dirty" alloys, Prog. Mater. Sci. 128 (2022) 100947.

[50] Z. Wang, H. Li, F. Miao, W. Sun, B. Fang, R. Song, Z. Zheng, Improving the intergranular corrosion resistance of Al–Mg–Si–Cu alloys without strength loss by a two-step aging treatment, Mater. Sci. Eng. A. 590 (2014) 267–273.

[51] J. Buha, R.N. Lumley, A.G. Crosky, K. Hono, Secondary precipitation in an Al–Mg–Si–Cu alloy, Acta Mater. 55 (2007) 3015–3024.

[52] C.D. Marioara, S.J. Andersen, T.N. Stene, H. Hasting, J. Walmsley, A.T.J. Van Helvoort, R. Holmestad, The effect of Cu on precipitation in Al-Mg-Si alloys, Philos. Mag. 87 (2007) 3385–3413.

[53] Z. Jia, L. Ding, L. Cao, R. Sanders, S. Li, Q. Liu, The influence of composition on the clustering and precipitation behavior of Al-Mg-Si-Cu alloys, Metall. Mater. Trans. A. 48 (2017) 459–473.

[54] S. Zhu, Z. Li, L. Yan, X. Li, S. Huang, H. Yan, Y. Zhang, B. Xiong, Effects of Zn addition on the age hardening behavior and precipitation evolution of an Al-Mg-Si-Cu alloy, Mater. Charact. 145 (2018) 258–267.

[55] J.K. Sunde, C.D. Marioara, R. Holmestad, The effect of low Cu additions on precipitate crystal structures in overaged Al-Mg-Si(-Cu) alloys, Mater. Charact. 160 (2020) 110087.

[56] Y. Zou, Q. Liu, Z. Jia, Y. Xing, L. Ding, X. Wang, The intergranular corrosion behavior of 6000-series alloys with different Mg/Si and Cu content, Appl. Surf. Sci. 405 (2017) 489–496.

[57] C.D. Marioara, A. Lervik, J. Grønvold, O. Lunder, S. Wenner, T. Furu, R. Holmestad, The correlation between intergranular corrosion resistance and copper content in the precipitate microstructure in an AA6005A alloy, Metall. Mater. Trans.

A. 49 (2018) 5146–5156.

10. Paper VI

Effect of aging time on microstructure and intergranular corrosion of 6082 Al-Mg-Si alloy with minor additions Cu and Zn

Emad H. Bartawi[1,*], Ghada Shaban[1], Rajan Ambat[1]

[1] Department of Civil and Mechanical Engineering, Technical University of Denmark, Kgs. Lyngby 2800, Denmark

Keywords: 6082 Al-Mg-Si alloy; Aging time, Intergranular corrosion; STEM.

Abstract

The influence of aging time (1, 2, 4, and 24 h) and minor addition of Cu (≤ 0.05 wt%), Zn (≤ 0.06 wt%), and Cu+Zn on the microstructure and intergranular corrosion resistance of Al-Mg-Si alloy is investigated. It is revealed that even minor addition of Cu and/or Zn can negatively affect the IGC resistance of Al-Mg-Si alloys. However, the results indicate that the Cu/Zn ratio of approximately 1.54 is appropriate for achieving good corrosion resistance in all aging conditions, which can be further improved by applying proper heat treatments. The results clearly indicate that Zn has a lower affinity than Cu to incorporate into GB and intragranular precipitates in the same aging conditions.

10.1 Introduction

The pursuit of reducing energy consumption for aluminium production and, thus, CO_2 emissions finds increased attention as the latter has become an inevitable requirement to reduce the environmental impact and air pollution. Several benefits can be obtained by recycling aluminium scrap, such as fuel savings, reducing the demand for bauxite ore, making material more sustainable, and reducing the cost required to produce the same amount of primary aluminium alloys. Moreover, considering the fast growth of aluminium in automotive applications as the most favorable material, recycling gives a great opportunity to shift toward greater sustainability and less cost [1]. However, the biggest challenge facing aluminum recycling is the amount of scrap materials that can be used without significantly reducing the required mechanical properties and corrosion resistance of Al-Mg-Si alloys. The corrosion resistance of Al-Mg-Si alloys is highly influenced by certain alloying elements such as Cu, Zn, Mn, and Fe. It is claimed that the intergranular

granular corrosion (IGC) resistance of Al-Mg-Si alloys will not be negatively influenced if the Cu and Zn content is kept less than 0.1 wt% [2–4].

The IGC resistance of Al-Mg-Si alloys with relativity high Cu content (≥ 0.1 wt%) is extensively studied [5–9]; however, investigations on the susceptibility to IGC with low Cu content ((≤ 0.06 wt%) are limited. For instance, Svenningsen et al. [10] investigated the effect of aging and low Cu content, 0.0005 and 0.02 wt%, on the IGG resistance of Al-0.5Mg-0.6Si and Al-0.6Mg-0.9Si alloys, respectively. The results revealed that alloys with such copper content are resistant to IGC. In a separate study, Zhang et al. [11] studied the influence of quenching rate on the IGC behavior of Al-0.68Mg-1.1Si with 0.06 Cu and 0.04 wt% Zn. The results demonstrated the lack of Cu, Zn, or Cu+Zn-rich films along the grain boundaries (GBs) in such low Cu and Zn content. Moreover, less than 10% of the GB particles were identified as Q phase in the water-quenched and peakaged alloy, while the Q fraction was even less (approximately 5%) in the air-cooled and peakaged alloy. The remaining observed particles in such low Cu (0.06 wt%) and Zn (0.04 wt%) were identified as Mg_2Si phases. Consequently, the authors reported that the root cause of IGC observed in the air-cooled and water-quenched alloys in such low Cu and Zn content was not conclusively determined. However, Bartawi et al. [12] investigated the influence of GB orientation on the IGC resistance of 6082-Al-Mg-Si alloy with 0.05 wt% Cu in the peakaged (PA) condition. The results evidently showed the presence of Cu-rich film, Cu-rich particles, and β particles along some grain boundaries.

Furthermore, limited work has been conducted to investigate the influence of Zn on the IGC resistance of Al-Mg-Si alloys [4,13–15]. For example, Guo et al. [15] explored the effect of Zn content on precipitation and IGC resistance of Al-0.9 Mg-0.6Si alloys with relatively high Cu content (0.2 wt%). The results showed that the IGC resistance was initially decreased by adding 1 wt% Zn and then exhibited a gradual increase after exceeding 1 wt% Zn addition. Additionally, the results indicated that the IGC resistance could be noticeably improved by overaging the alloys containing between 2.0 - 4.0 wt% Zn, which is claimed to be attributed to the formation of discontinued Mg-Zn, Mg-Si Zn-rich particles along the GBs, and narrower PFZ. At the same time, Saito et al. [4] investigated the influence of Zn (up to 1 wt%) on the IGC of Al-0.5Mg-0.4Si at different aging conditions. It was reported that Zn content up to 0.1 wt% did not have a measurable impact on the IGC resistance of Al-Mg-Si alloys, emphasizing that the critical level of Zn

that negatively can influence the IGC resistance lies between 0.1 and 1 wt%. The results also demonstrated that the high susceptibility to IGC in the alloy containing 1 wt% Zn was due to the presence of Zn-rich film along the GBs in the PA condition.

To date and to the best of the authors' knowledge, there is no detailed work concerning the influence of minor Zn and Cu additions (individually or in combination) close to the impurity levels ((≤ 0.06 wt%) on the microstructure and IGC resistance of Al-Mg-Si alloys. The critical reported levels of Cu and Zn additions, as individual elements, that can negatively influence the IGC resistance of Al-Mg-Si alloys is 0.05 wt% Cu and close to 0.1 wt% for the Zn. This dramatically limits the ambition of increasing the amount of the low-quality post-consumer scrap and thus reducing the CO_2 emission and the cost of the final Al products. Hence, understanding the critical level of these elements in combination or individually may help eliminate or mitigate their negative influence on the IGC resistance of Al-Mg-Si alloys, enabling more scrap to be used. Therefore, the purpose of the current study is to investigate the impact of scrap-related impurities (i.e., Cu ≤ 0.05 wt% and Zn ≤ 0.06 wt%) and aging time (1, 2, 5, and 24 h) on the microstructure and IGC of 6082-Al-Mg-Si alloys. In the current study, scanning transmission electron microscopy (STEM) was adopted to investigate the microstructure and the GB chemistry. Moreover, scanning electron microscopy is used to assess the IGC resistance as a function of aging time and Cu/Zn content in Al-Mg-Si alloy.

10.2 Experimental methods

10.2.1 Material used

In the present study, five extruded Al-Mg-Si alloys (AA6082) with different minor additions of Cu and Zn were manufactured to mimic the expected Cu and Zn amount in the recycled Al-Mg-Si alloys. To study the impact of aging time on the IGC and microstructure, the alloys were heat treated at 540 °C for 30 min, thereafter, the alloys were water-quenched to room temperature. Subsequently, the alloys were artificially aged at 185 °C for different aging times 1, 2, 5, and 24 h to obtain underaged (UA), peakaged, and overaged (OA) conditions. The chemical compositions of the five investigated alloys are shown in Table 10.1.

Table 10.1. Chemical composition (wt%) of Al 6082 alloys investigated in the this work

Alloy	Al	Mg	Si	Zn	Cu	Fe	Mn
S1	Balance	0.65	0.97	0.003	0.001	0.22	0.54
S2	Balance	0.64	0.96	0.003	0.048	0.22	0.54
S3	Balance	0.63	0.94	0.022	0.034	0.21	0.56
S4	Balance	0.63	0.94	0.059	0.001	0.21	0.56
S5	Balance	0.63	0.95	0.059	0.050	0.21	0.58

10.2.2 IGC test

Corrosion test were carried out on specimens of 25 x 20 x 4 mm^3 by immersing them in an acidified solution for 24 h according to the standard BS-ISO 11846 method B. Prior to the IGC test, the specimens were degreased in acetone, alkaline etched in 8 wt% sodium hydroxide (NaOH) for 5 min at 55 °C and finally desmutted for 2 min in concentrated nitric acid (HNO_3). Thereafter, Lacomit varnish was applied on the sectioned edges to avoid the possible interference between the surface and the center layer. Subsequently, the IGC test was performed by immersing the samples in a solution of 30 g/l sodium chloride and 10 ml/l hydrochloric acid (HCl). Following that, the specimens were rinsed in distilled water and air dried. The cross-section and surface morphologies were investigated using AFEG 250 Analytical ESEM microscope.

10.2.3 Microstructure characterizations and hardness test

The five alloys used in this work with different minor additions of Cu and Zn are labeled as S1, S2, S3, S4, and S5, see Table 10.1. Specimens of 25 x 10 x 4mm^3 were used to investigate the microstructure. Firstly, the samples were ground, mechanically polished to 1 μm, and etched for 60 sec in tetrafluoroboric acid. Finally, the microstructure was obtained using light optical microscope Zeiss Axio Vert.A1.

STEM investigation was carried out on relevant specimens, alloy S2 aged for 24 h and S4 aged for 1 and 24 h, along their GBs and in the grain interior to reveal the GB chemistry and grain interior microstructure. Specimens were prepared from the top recrystallized surface layer by mechanical polishing to ~100 μm thickness, followed by punching of 3 mm diameter discs. The punched discs were then electropolished using a

TenuPol-5 twin-jet system in a solution containing 90 % ethanol and 10 % perchloric acid 65 % at ~-25 °C. Titan Analytical 80-300ST microscope equipped with Oxford energy dispersive X-ray (EDX) detector X-Max 80TLE operated at 300 kV was used in this study.

Vickers Hardness measurements were carried out to explore the influence of aging time and minor additions of Zn and Cu on the hardness of Al-Mg-Si alloys and correlate that to susceptibility to IGC. The hardness test was performed with a load of 500 g for a loading time of 15 s at room temperature using the micro hardness machine DuraScan 70 G5.

10.3 Results

10.3.1 Microstructure characterization

The investigated alloys exhibit large elongated grains along extrusion direction surrounded by a recrystallized surface layer as shown in Fig. 10.1. Since all studied alloys exhibit similar grain structure, only microstructure for alloy S2 is shown. The recrystallized surface layer exhibits a discrepancy in the grain size as a function with the distance from the top surface. Approximately 20 μm grain size are observed at the immediate surface, while several hundreds of μm can be observed near the center layer. Investigating the surface layer was the focus of interest of the current work.

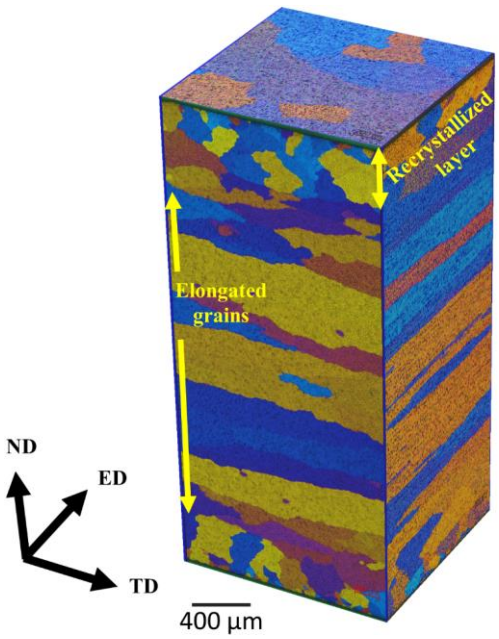

Fig. 10.1. 3D optical image of alloy S2 after mechanical polishing and etching in Tetrafluoroboric acid

10.3.2 Age hardening and intergranular corrosion behavior 2806

The relation between the hardness and IGC resistance of the aged alloys at 185 °C for different aging times (1, 2, 5, and 24 h) is demonstrated in Fig. 10.2. Based on the hardness values, three age hardening stages of UA, PA, and OA conditions can be observed. It can be noticed that the studied alloys are in the UA condition as long as the aging time is 1 h, while in the medium OA condition (small drop in HV) when the aging temperature is 24 h. Interestingly, when alloys S2 and S4 aged for 2 h, the specimens are in the PA condition, and the hardness values are 116 ± 1.5 and 112.5 ± 3, respectively. At the same time, the PA condition for alloys S1, S3, and S5 are obtained after 5 h aging, and the peak hardness values are 113.1 ± 2.3, 110.6 ± 1.3, and 127.3 ± 1.9 HV, respectively, see Fig. 10.2a. It is worth mentioning that the defined PA are based on the picked time intervals, which may not necessarily correspond to precise PA hardness as the current work aims to investigate the IGC behavior at different aging conditions considering UA, PA, and OA.

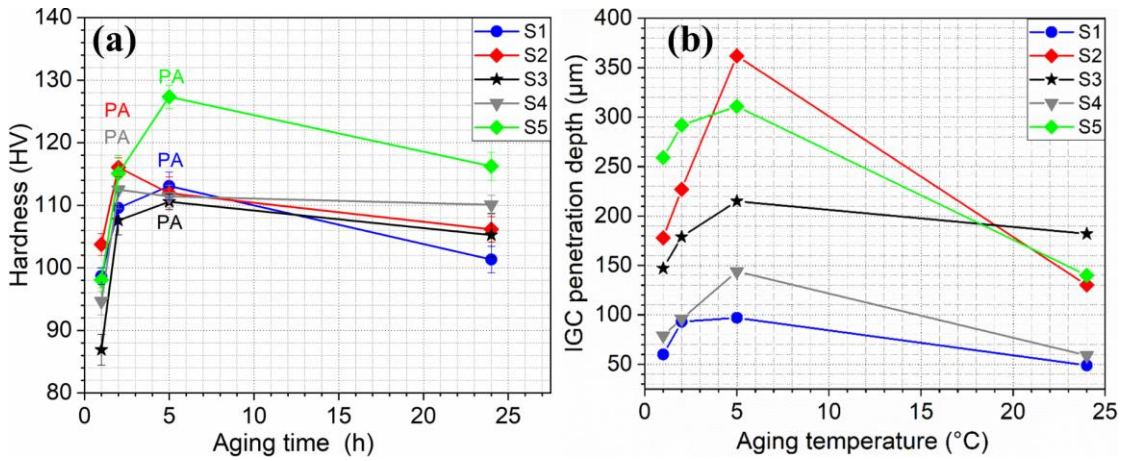

Fig. 10.2. Age hardening curve (a) and maximum IGC penetration depth (b) for alloys S1, S2, S3, S4, and S5 aged at 185 °C for 1, 2, 5, and 24 h, (PA) in (a) indicates PA condition.

Based on the accelerated corrosion test, alloy S1 exhibits the highest IGC resistance in all aging conditions as only localized IGC can be observed considering both the surface and cross-section morphologies, see Figs. 10.3 and 10.4. However, alloy S1 is more susceptible to IGC at the PA condition compared to UA and OA conditions as the penetration depth reached up to ~97 μm in the PA condition, see Figs. 10.2b and 10.4. Moreover, alloy S2 with 0.05 wt% Cu displays a uniform IGC, as the IGC spreads across the entire surface and high penetration depth of 362 μm after 5 h aging is recorded, see Figs. 10.2b, 10.3 and 10.4. Furthermore, alloy S3 shows a clear improvement in its IGC

resistance compared to alloy S2 containing 0.05 wt% Cu. In the UA condition, alloy S4 demonstrates high IGC resistance, while with further increasing aging time to 2, 5 and even 24 h, lower IGC resistance is observed. Interestingly, unlike all other studied alloys, no significant improvement in the IGC resistance (lateral attack) is obtained in alloy S4 after 24 aging, see Fig. 10.3. However, lower penetration depth (vertical attack) is observed in the OA condition compared to UA and PA conditions, see Fig. 10.2b and 10.4. In addition, unlike alloys S2, S3, and S5, alloy S4 exhibits lower penetration depth as the results indicate that the IGC mostly affecting the top ~145 μm after 5 h aging and only ~79, 96, and ~59 μm after 1, 2, and 24 h aging, respectively, see Fig. 10.2b. The surface morphology of the corroded alloy S5 is comparable to that of alloy S2, however, the penetration depth of alloy S5 in the PA condition is less severe.

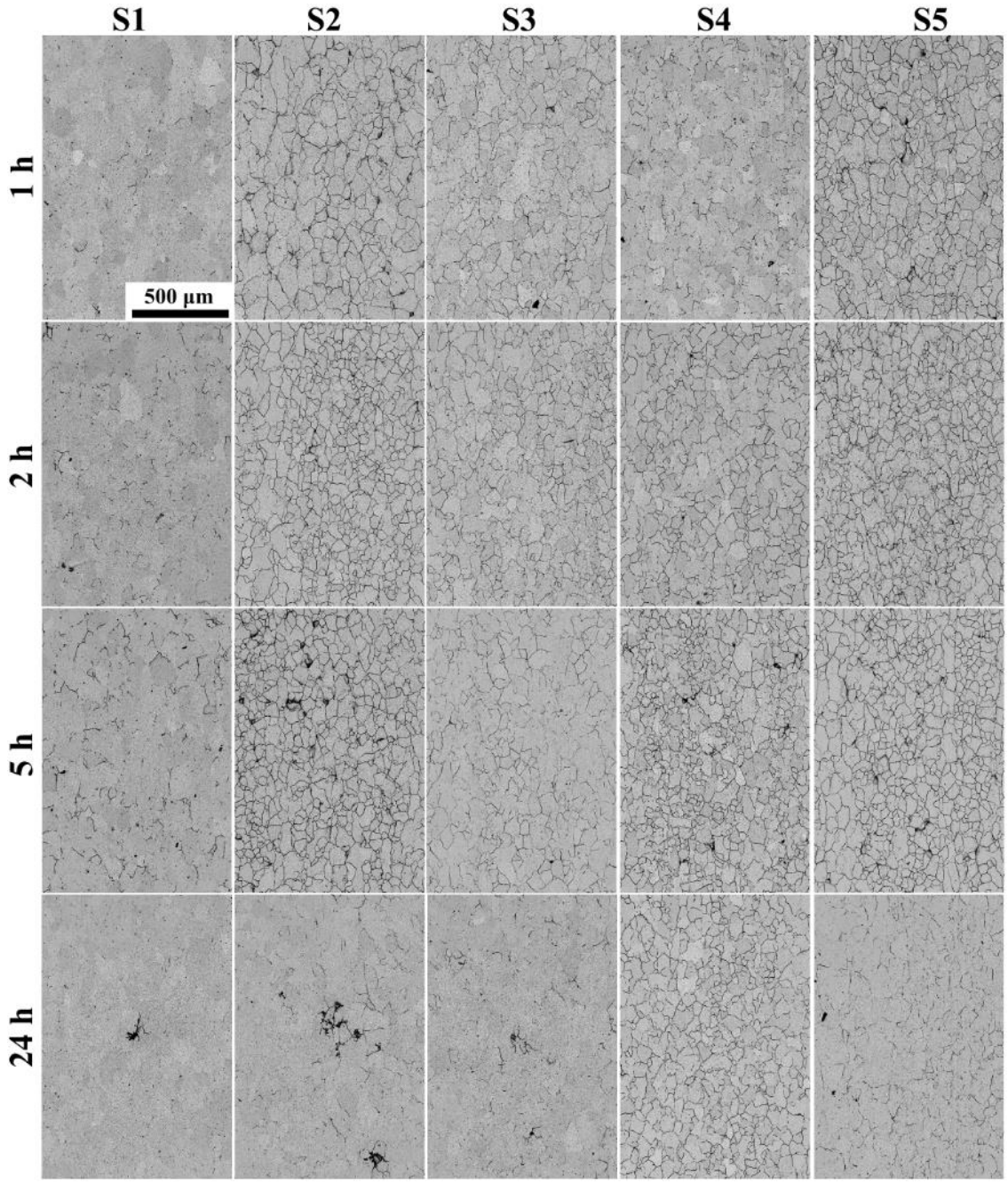

Fig. 10.3. BSE-SEM micrographs of the corroded surface for the investigated alloys after 24 h IGC test.

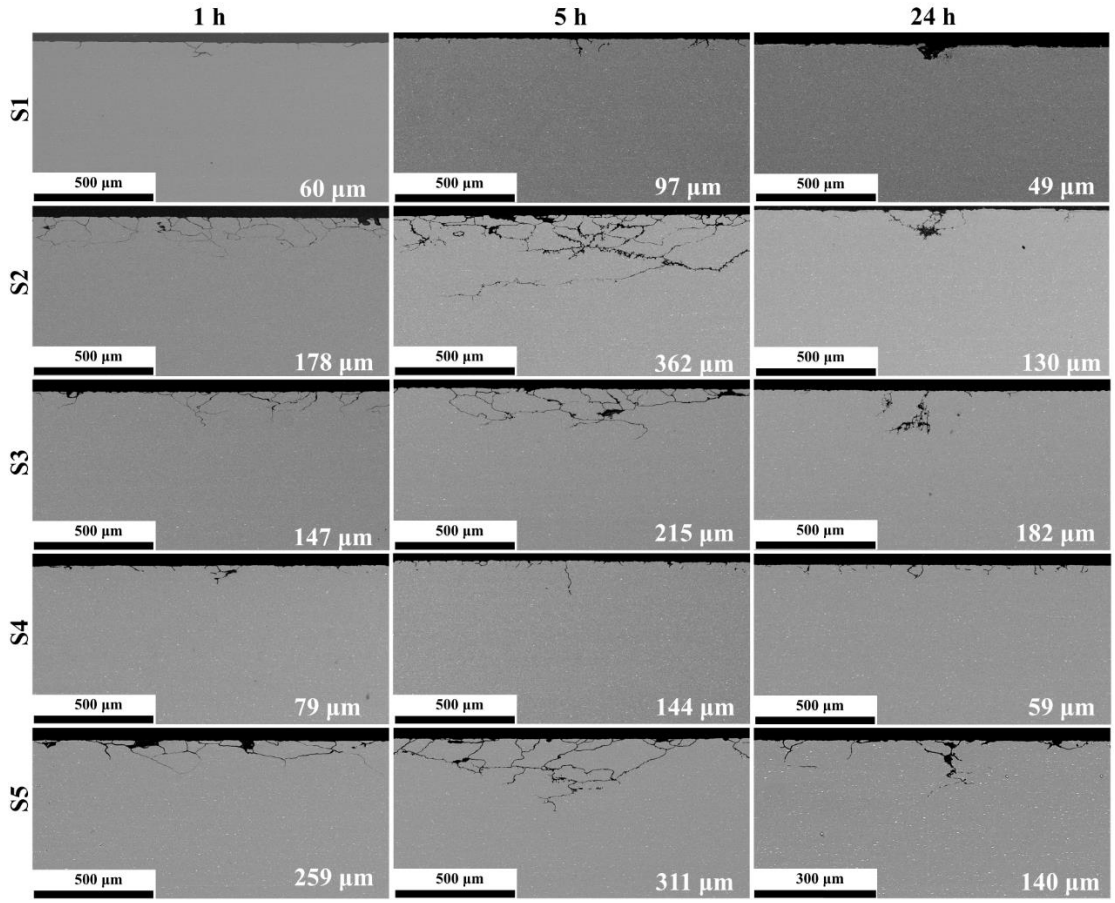

Fig. 10.4. BSE-SEM micrographs of cross-section of the IGC for the studied alloys after 24 h IGC immersion.

10.3.3 TEM/STEM analysis of grain boundaries and particles

Based on the IGC and hardness results demonstrated in Figs. 10.2, 10.3, and 10.4, alloy S2 aged for 24 h and alloy S4 aged for 1 and 24 h were selected for investigating their microstructure and the chemistry of their GBs and intragranular (bulk) precipitates using S/TEM. To reveal the GB structure and grain interior precipitates characteristics, Fig. 10.5 presents HAADF-STEM images for alloys S2 (aged for 24 h) and S4 (aged for 1 and 24 h). Observation of number of GBs of alloy S2, a PFZ width of ~110 nm and moderately closely spaced particles along the GB can be noticed, see Fig. 10.5a. Moreover, the majority of the bulk precipitates are needle-like phases with a size vary from several tens of nm to ~150 nm, see Fig. 10.5b. Furthermore, fine GB particles and intragranular needle-like precipitates are observed in alloy S4 after 1 h aging, see Fig. 10.5(c, d). With further increasing aging time to 24 h, coarser and moderately spaced GB particles and coarser intragranular precipitates can be observed, see Fig. 10.5(e-f).

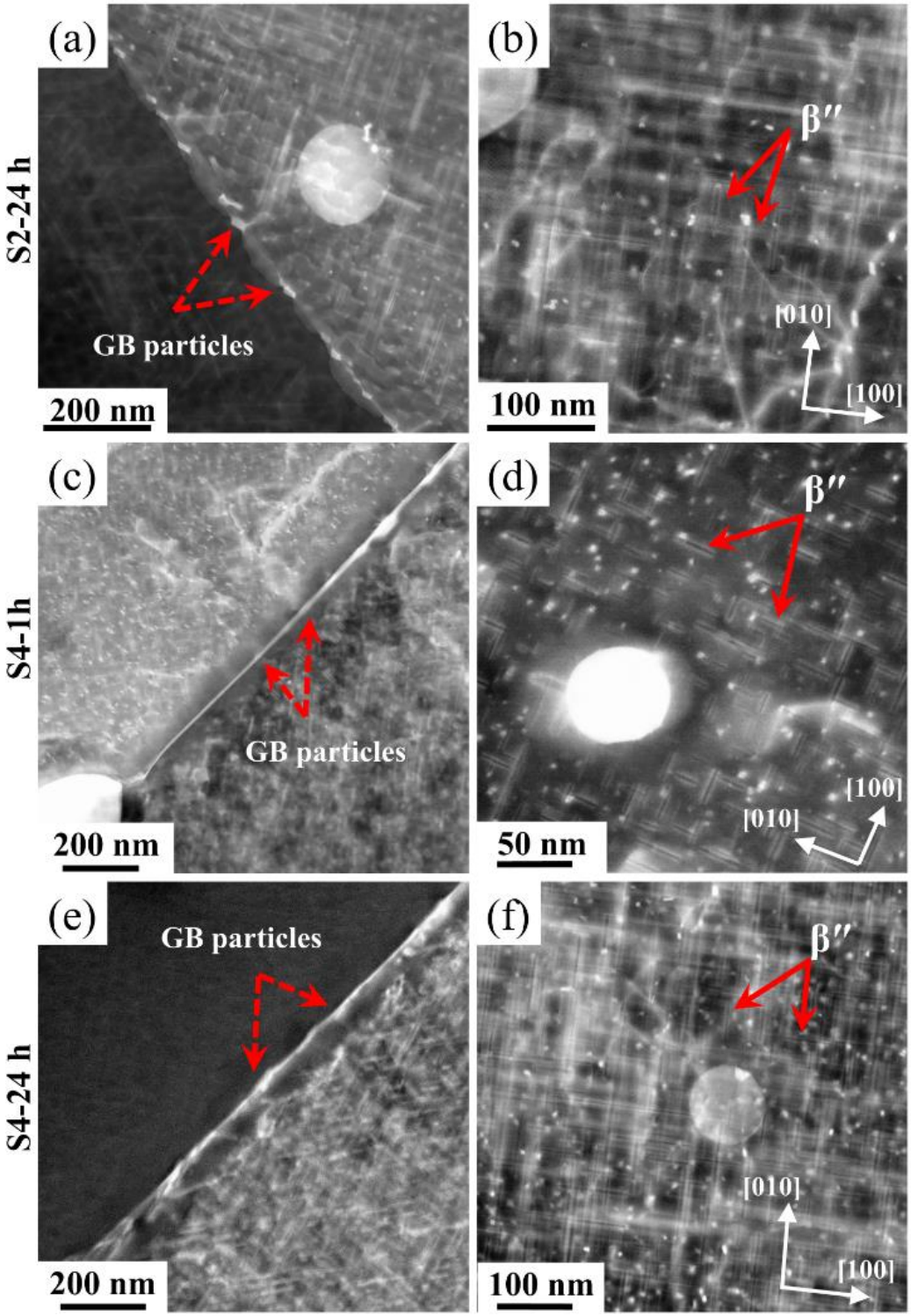

Fig. 10.5. HAADF-STEM images of grain boundaries (a, c, e) for alloy S2 after 24 h aging and alloy S4 after 1 h and 24 h aging, respectively. (b, d, f) HAADF-STEM images showing the microstructure of alloys S2 after 24 h aging and S4 after 1 and 24 h aging, respectively. The Solid red arrows indicate the bulk precipitates and the dashed red arrows indicate the GB particles.

Fig. 10.6(a, c) shows the intragranular precipitate of alloys S2 and S4 aged for 24 h. The HAADF-STEM images obtained from <001>Al zone axis, namely along the growing growth of the precipitation enabling investigating the cross-section of such phases. Observation of a number of cross-section indicates that ~90 % of these bulk precipitates showed a clear Cu signal, see Fig. 10.6b. Interestingly, the Zn-containing alloy (alloy S4) at the same aging condition, exhibited a distinctly different behavior as the Zn was detected only in ~30 of the investigated intragranular precipitates, see Fig. 10.6b. It is worth to mention that intragranular precipitates in alloy S4 aged at 1 h were also investigated, and found to be Mg-Si precipitates as no Zn was observed (not shown).

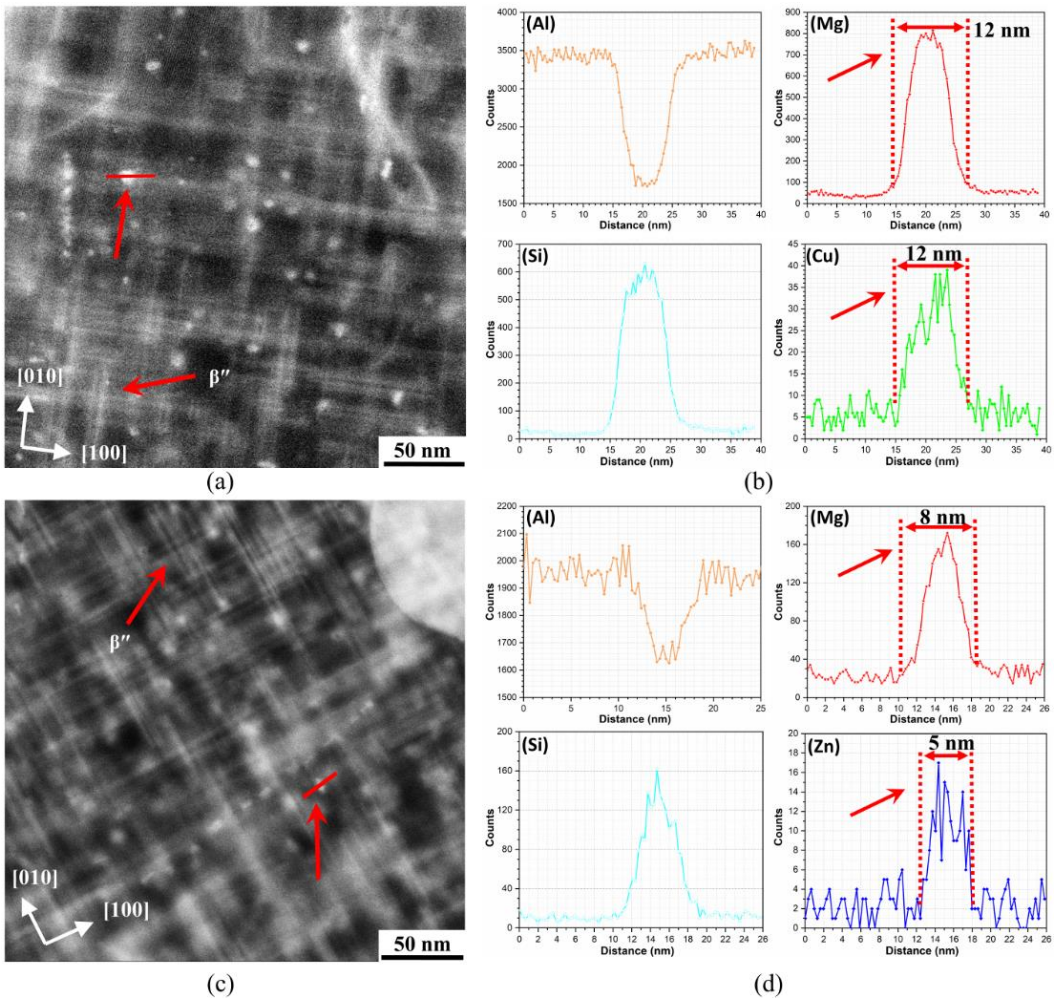

Fig. 10. 6. (a, c) HAADF-STEM microstructure of alloys S2 and S4 aged for 24 h, respectively, along with their EDS-line scan (b, d) conducted along the solid line crossing the cross-section of one of the intragranular precipitates in (a) and (c), respectively.

Concerning the GB chemistry, Fig. 10.7(a, c), shows a typical HAADF-STEM images of high angle and low angle boundaries, along with their corresponding EDS maps. Based on several observations, the GB particles of alloy S2 aged for 24 h are Cu-rich Mg-

Si particles, see Fig. 10.7 (b, d). The EDS maps also reveals the presence of continuous PFZ along the GBs in addition to Mg-Si intragranular precipitates in the matrix adjacent to GB, see Fig. 10.7(b, d).

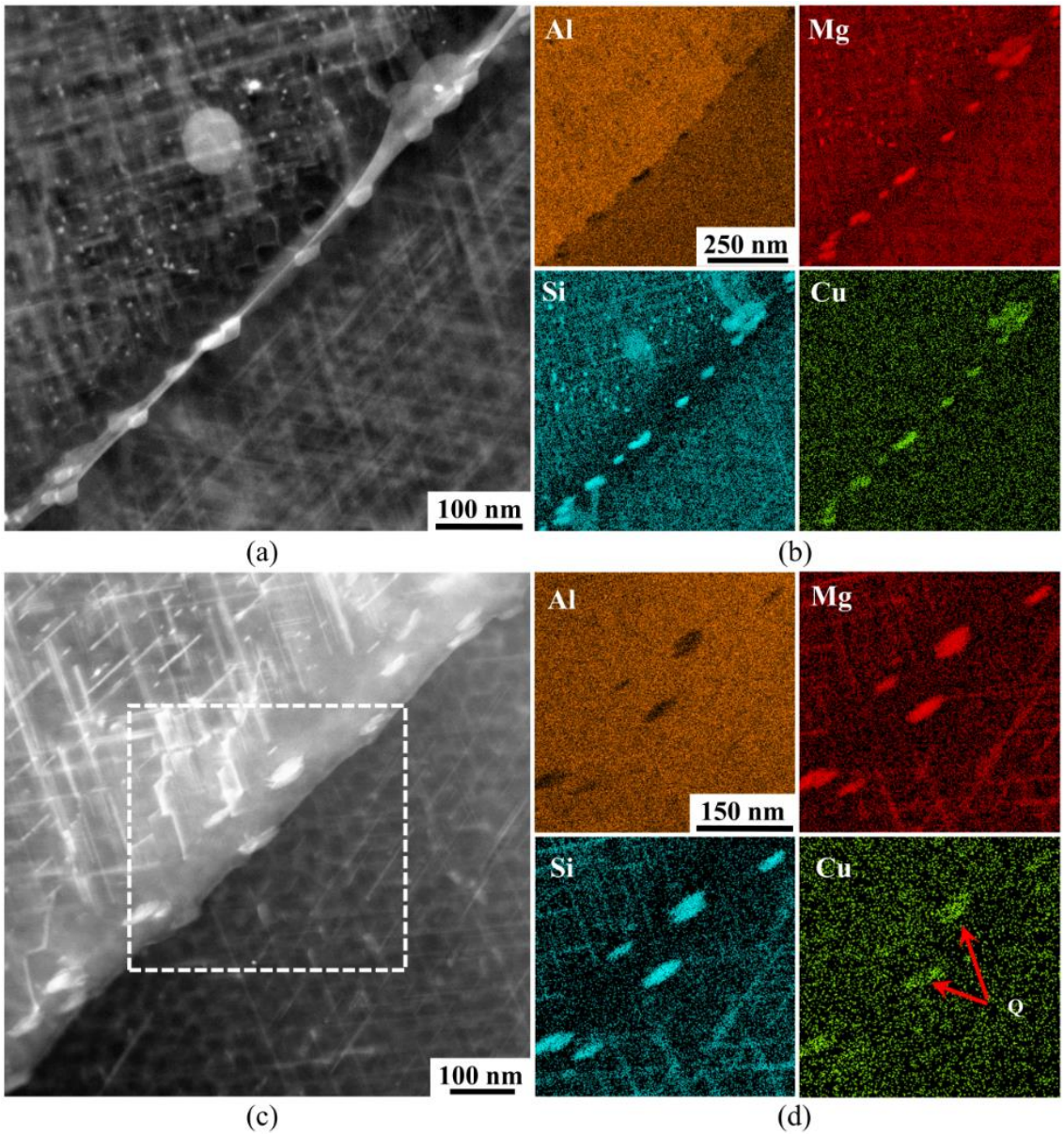

Fig. 10. 7. HAADF-STEM images of (a) high angle and (c) low angle grain boundaries of alloy S2 aged for 24 h, (b, d) corresponding Al, Mg, Si, and Cu EDS elemental maps.

To further investigate the effect of aging temperature on the GB particles, alloy S4 aged for 1 and 24 h was subjected to STEM analysis. Fine and moderately spaced particles are observed along the GBs of alloy S4 in the UA condition, see Fig. 10.8(a, c). The EDS-STEM analysis reveals the presence of two types of the GB particles in such aging condition, Mg-Si particles and Zn-rich Mg-Si particles, see Fig. 10.8(b, d).

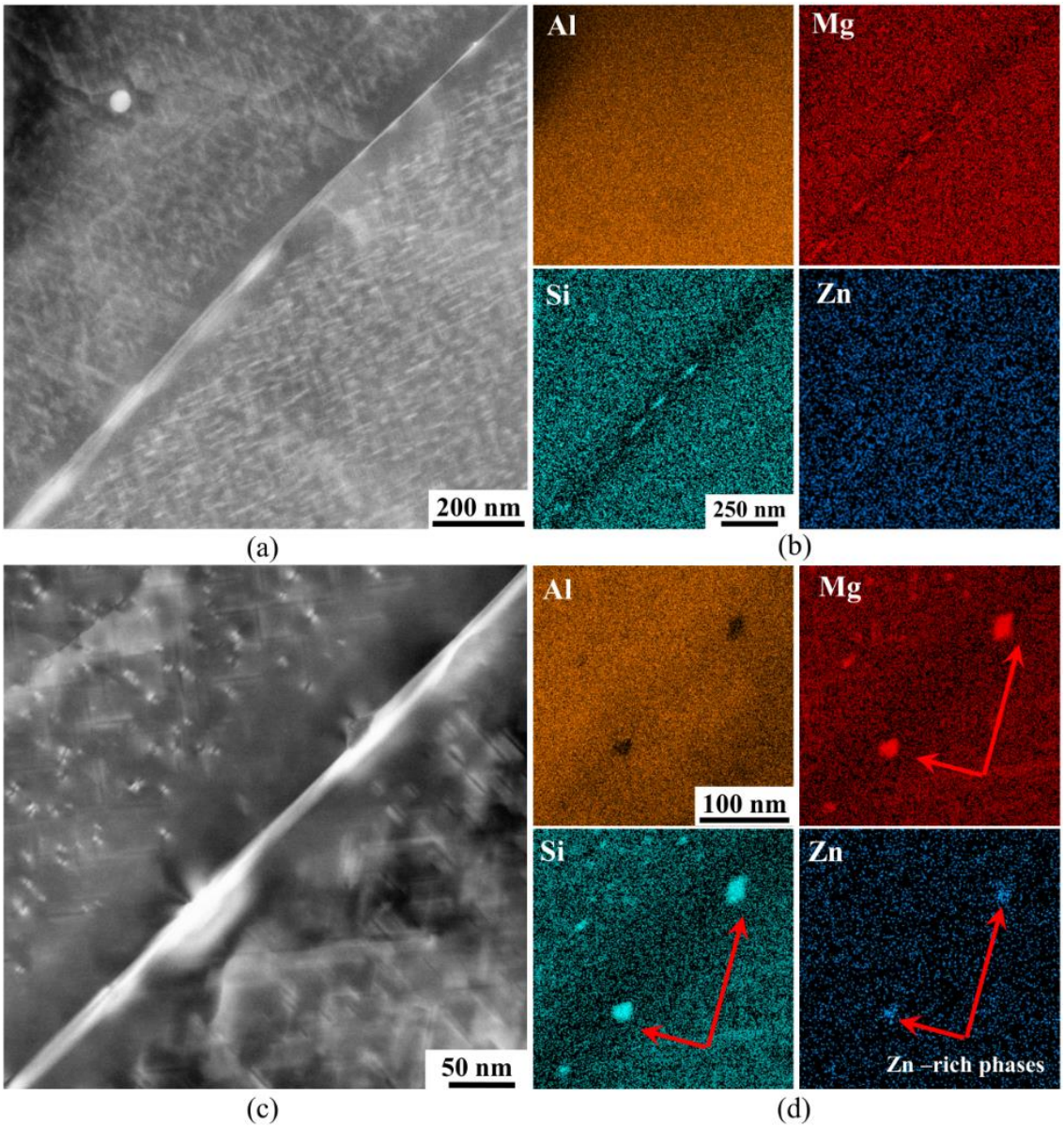

Fig. 10. 8. (a, c) HAADF-STEM images of alloy S4 aged for 1 h, (b, d) corresponding Al, Mg, Si, and Zn elemental maps. The red arrows indicate the Zn-rich Mg-Si particles.

With further increasing aging time to 24 h, coarser GB particles and readily discernible PFZ of ~110 nm can be observed. Interestingly, unlike alloy S2 aged for 24 h, the EDS maps of GBs of alloy S4 aged for 24 h indicate the presence of two types of particles Mg-Si and Zn-rich Mg-Si particles, see Fig. 10.9(b, d).

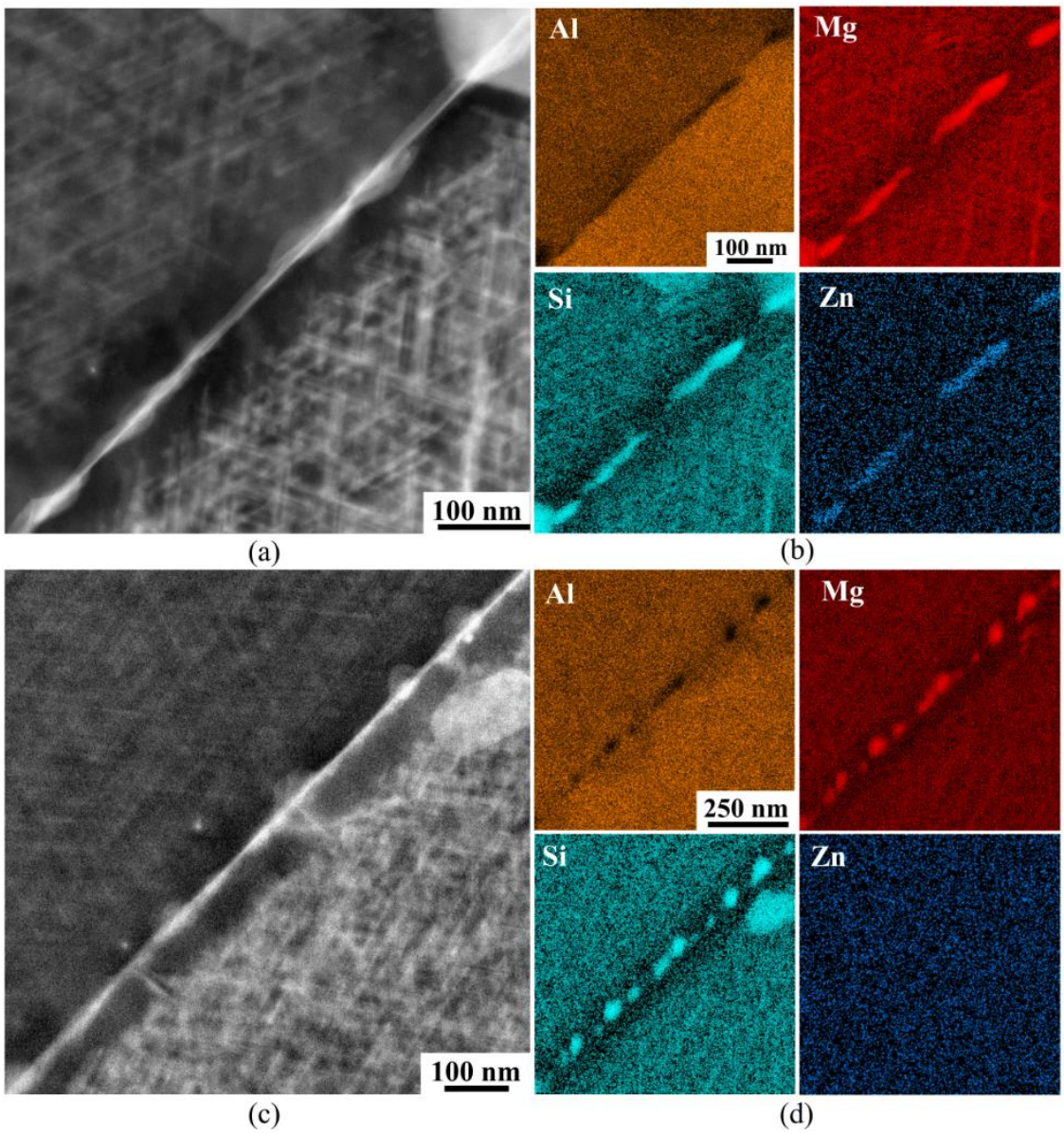

Fig. 10. 9. HAADF-STEM images (a, c) showing the grain boundaries of alloy S4 aged for 24 h.

10.4 Discussion

The findings from the current work reveals that aging time and even very low Cu (≤ 0.05 wt%) and Zn (≤ 0.06 wt%) content can greatly influence the microstructure and GB chemistry and thus the IGC resistance of Al-Mg-Si alloys. Concerning the influence of high Cu addition on the age hardening response, it is deemed that the peakaging hardness increases with Cu addition of (0.6 wt%) [16–19], while the time required to reach the peak hardness decreases [17]. However, conflicted results regarding reaching the peakaging time was reported by Xiao et al. [19]. Concerning the influence of Zn addition on the hardness, It was reported that Zn can improve the age hardening response and the peak hardness

[15,20–23]. In the current study, the combination of Cu and Zn with a very low amount clearly enhances the peak hardness of alloy S5, see Fig. 10.2, which can be attributed to the incorporation of Cu and Zn into the intragranular precipitate structures as indicated in Fig. 10.6. Precipitates that contain Cu, Zn, or Cu and Zn are noticed in the microstructure of the studied alloy and such precipitates are observed to have different structure than the precipitates usually observed in Cu/Zn-free Al-Mg-Si alloys [24–28].

It is widely accepted that the IGC susceptibility of Al-Mg-Si alloys is attributed to the GB compositions, namely GB particles and Cu/Zn-rich films [4,11,13,29–34]. In this particular scenario, the IGC occurs due to the microgalvanic coupling between the noble GBs particles and Cu/Zn-rich films and PFZ [10,35–37]. Kairy et al. [7] investigated the influence of aging condition on the IGC resistance of Al-Mg-Si alloys with high Cu content 0.3 and 0.89 wt%. It is claimed that the IGC penetration depth were decreased in the OA condition as a result of the growth of discrete GB particles by consuming the Cu located along the GBs. The same observation was made by Li et al. [6] who investigated the influence of aging condition on Al-1.0Mg-1.1Si-0.9Cu (wt%). Concerning the IGC in Al-Mg-Si alloys with Zn, Chi et al. [14] investigated the influence of 0.05 wt% Zn (termed without Zn) and 0.2 wt% addition on the IGC resistance of Al-0.9Mg-1Si in different aging conditions. It is reported that Zn addition resulted in a slightly wider PFZ, and coarser GB particles and thus less IGC resistance. Despite the relatively high Zn content (0.2 wt%), it is reported that the GB particles were identified as Mg-Si phases as no Zn was detected in such particles. Moreover, the results also indicated that the IGC resistance of the alloys was improved in the OA condition compared to UA and PA conditions. This behavior was attributed to wider PFZ and coarser GB particles observed in OA condition.

The presence of two types of GB particles (Mg-Si and Mg-Si-Zn particles) in alloy S4 after 24 h aging, along with approximately 30 % of the bulk precipitates being Zn-containing phases, clearly indicates that relatively high Zn concentration remains in the solid solution. Furthermore, the EDS-STEM results of alloy S2 aged for 24 h show the presence of Cu-rich GB particles along with approximately 90 % of the investigated bulk particles contain Cu, which indicate the high affinity of Cu to incorporate into the precipitate structure. The important finding in the current work is that the Zn did not show the same affinity as Cu to incorporate into particle structures of GB and intragranular precipitates, resulting in a higher Zn atoms remain in solid solution. Thus, different electrochemical potential of PFZ compared to the Mg-Si and Zn-rich GB particles can be

expected. Therefore, the presence of moderately spaced Mg-Si and Zn-rich GB particles will act as a driving force for the IGC to take place along the PFZ, which will act as a cathode in alloy S4, while both types of particles act as an anode. Incorporating the Zn into Mg-Si particles will not positively influence their electrochemical potential from the point view of corrosion as the corrosion potential of Zn [38] and β particles [39] measured in 0.1 M NaCl is -1.428 and -1.538 VSCE, respectively. Unlike alloy S4 (only Zn), alloy S2 (only Cu) show significant improvement in the IGC properties with further increasing the aging from 5 to 24 h. This behavior can be attributed to that Cu is incorporated into Mg-Si particles that decorating the GBs and also into Mg-Si particles in the grain interior, see Figs, 6b, and 10.7(b, d). By consuming the Cu by the Mg-Si GB particles, the electrochemical potential of such phases will be shifted to more positive values, which might at some point be very close to the PFZ potential (-0.823 VSCE [39]) leading to noticeably mitigating the IGC. Furthermore, by consuming the Cu presented in the PFZ and along the grain boundaries by GB particles, and the Cu presented in matrix by the Mg-Si bulk precipitates, it can be deduced that the PFZ and the matrix has close electrochemical potential, leading to mitigating the influence of the matrix. This hypothesis can explain the improvement in the IGC observed in alloy S2 after 24 h aging compared to 5 h aging, see Fig. 10.3. However, this hypothesis is not valid for Zn-containing alloys, as the Zn has lower corrosion potential compared to PFZ and a corrosion potential that is close to that for Mg-Si particles. In addition, the lower Zn affinity to incorporated into GB particles as well as into Mg-Si Al matrix precipitates compared to Cu can lead to different electrochemical potential between PFZ and Al matrix.

With further increasing the aging time from 5 to 24 h for alloys S3 and S5, the Cu and Zn atoms located in the GB region will be more consumed by the GB particles, which is believed to change their corrosion potential to be more close to Al matrix potential. The presence of Cu and Zn in the GB particles can mitigate the harmful effect that arises from the existence of only one of these two elements in the precipitate structures. Cu shifts the electrochemical potential of the GB precipitate toward more positive value, while Zn can shift it to the opposite direction. The Cu/Zn ratio in the GB particles as well as in the bulk precipitates, will determine their corrosion potential and thus the IGC resistance and the pitting corrosion in the OA condition. Therefore, an imbalance in this ratio due to unbalanced Cu/Zn additions as alloying elements and/or unfavorable heat treatment will negatively influence the electrochemical behavior of such precipitates. Based on the

accelerated corrosion test, it is believed that the Cu/Zn ratio in alloy S3 nearly reaches the appropriate ratio as a good corrosion resistance is observed in all aging conditions. The IGC resistance can be further improved by either slightly modifying the Cu/Zn addition (by increasing the Zn slightly in this particular alloy) or by optimizing the heat treatment processing (e.g., slower cooling rate, two-step aging).

As mentioned above, the Zn affinity to incorporate into GB particles and intragranular precipitates is observed to be lower than the Cu in the same aging condition, see Figs, 10.6, 10.7, 10.8, and 10.9. Therefore, it can be assumed that Cu in the PA condition in alloys S3 and S5 is presented in a higher concentration than required to shift the GB particle potential close to the PFZ. With further aging, the extension (lateral attack) and the penetration depth of the IGC are reduced, which can be considered as an indication that the Zn starts to balance the negative effect of Cu by bringing the corrosion potential of such GB particles close to PFZ potential. The low corrosion resistance of alloy S4 (only Zn), even after 24 h aging, strongly supports the hypothesis that introducing Cu and Zn into the alloy can mitigate the poisoning caused by the presence of one of these two elements. It is important to mention that the Cu/Zn ratio and aging parameters are absolutely crucial to obtain the desired IGC resistance of Al-Mg-Si alloys with such low Cu/Zn content. Based on our investigated alloys, it is evident that the Cu/Zn ratio of ~1.54 can be acceptable in alloys containing low Cu and Zn concentrations ($\leq$ 0.06 wt%).

10.5 Conclusion

In the current research study the IGC and microstructure of 6082 Al-Mg-Si alloy with different minor addition of Cu and Zn and different aging time were investigated. The grain boundary chemistry and the microstructure of the representative alloys and conditions were deeply analyzed using STEM. The following conclusions can be drawn:

- The peak hardness of Al-Mg-Si alloy is increased even with minor addition of Cu/Zn as the highest value obtained from alloy S5 after 5 h aging.
- The IGC resistance decreases by increasing the Cu and Zn content individually even in a very small concentration, while alloy S3 with 0.034 Cu and 0.022 Zn wt% shows improved IGC resistance compared to alloys S2 and S4. However, unbalanced Cu/Zn ratio will results in low corrosion resistance in the PA condition, which can be improved by aging without significant decrease in the hardness.

- Aging time has significant influence on the chemistry of the grain boundary and intragranular precipitates in the presence of minor addition of Cu and Zn in Al-Mg-Si alloy.
- The IGC resistance of Al-Mg-Si alloy with minor addition of Cu and Zn can be improved by keeping the Cu/Zn ratio near approximately 1.54.

CRediT authorship contribution statement

Emad H. Bartawi: Conceptualization, Methodology, Investigation, Formal analysis, Writing - Original Draft, **Ghada Shaban:** Writing - Review & Editing, Formal analysis, **Rajan Ambat:** Conceptualization, Supervision, Writing - Review & Editing, Project administration, Funding acquisition.

Acknowledgements

Emad H. Bartawi would like to thank Hydro Aluminium, Norway, for providing material. Emad H. Bartawi acknowledge the support from Dr. J. Kling from DTU Nanolab during STEM experiments. Emad H. Bartawi and Rajan Ambat acknowledge funding from the Independent Research Fund Denmark (grant number 9041- 00240A).

Data Availability

The raw/processed data required to reproduce these findings cannot be shared at this time as the data also forms part of an ongoing study.

References

[1] D. Raabe, D. Ponge, P.J. Uggowitzer, M. Roscher, M. Paolantonio, C. Liu, H. Antrekowitsch, E. Kozeschnik, D. Seidmann, B. Gault, F. De Geuser, A. Deschamps, C. Hutchinson, C. Liu, Z. Li, P. Prangnell, J. Robson, P. Shanthraj, S. Vakili, C. Sinclair, L. Bourgeois, S. Pogatscher, Making sustainable aluminum by recycling scrap: The science of “dirty” alloys, Prog. Mater. Sci. 128 (2022) 100947.

[2] K. Nisancioglu, Ø. Strandmyr, Corrosion of AlMgSi alloys with Cu additions: the effect of Cu content up to 0.9 weight percent, Report no, STF34 A78052, SINTEF, Trondheim, Norw. (1978).

[3] H. Hug, Ueber den einflußgeringer schwermetallgehalte auf die korrosionsbeständigkeit von Al-Mg-Si Legierungen, Aluminium. 23 (1941) 33.

[4] T. Saito, S. Wenner, E. Osmundsen, C.D. Marioara, S.J. Andersen, J. Røyset, W. Lefebvre, R. Holmestad, The effect of Zn on precipitation in Al-Mg-Si alloys, Philos. Mag. 94 (2014) 2410–2425.

[5] V. Guillaumin, Influence of overaging treatment on localized corrosion of Al 6056, Corrosion. 56 (2000) 12–23.

[6] H. Li, P. Zhao, Z. Wang, Q. Mao, B. Fang, R. Song, Z. Zheng, The intergranular corrosion susceptibility of a heavily overaged Al-Mg-Si-Cu alloy, Corros. Sci. 107 (2016) 113–122.

[7] S.K. Kairy, P.A. Rometsch, C.H.J. Davies, N. Birbilis, On the intergranular corrosion and hardness evolution of 6xxx series Al alloys as a function of Si:Mg ratio, Cu Content, and aging condition, Corrosion. 73 (2017) 1280–1295.

[8] A. Lervik, T. Danbolt, T. Furu, R. Holmestad, O. Lunder, Comparing intergranular corrosion in Al-Mg-Si-Cu alloys with and without α-Al(Fe,Mn,Cu)Si particles, Mater. Corros. 72 (2021) 575–584.

[9] S. Kumari, S. Wenner, J.C. Walmsley, O. Lunder, K. Nisancioglu, Progress in understanding initiation of intergranular corrosion on AA6005 aluminum alloy with low copper content, J. Electrochem. Soc. 166 (2019) C3114–C3123.

[10] G. Svenningsen, M.H. Larsen, J.H. Nordlien, K. Nisancioglu, Effect of thermomechanical history on intergranular corrosion of extruded AlMgSi(Cu) model alloy, Corros. Sci. 48 (2006) 3969–3987.

[11] X. Zhang, X. Zhou, J.O. Nilsson, Corrosion behaviour of AA6082 Al-Mg-Si alloy extrusion:

The influence of quench cooling rate, Corros. Sci. 150 (2019) 100–109.

[12] E.H. Bartawi, O. V. Mishin, G. Shaban, J.H. Nordlien, R. Ambat, Electron microscopy analysis of grain boundaries and intergranular corrosion in aged Al-Mg-Si alloy doped with 0.05 wt% Cu, Corros. Sci. 209 (2022) 110758.

[13] X. Xu, Y. Deng, Q. Pan, X. Guo, Enhancing the intergranular corrosion resistance of the Al–Mg–Si alloy with low Zn content by the interrupted aging treatment, Metall. Mater. Trans. A. 52 (2021) 4907–4921.

[14] S. Chi, Y. Deng, X. Xu, X. Guo, Influence of minor Zn addition on precipitation behavior and intergranular corrosion properties of Al-Mg-Si alloy, Materials (Basel). 13 (2020) 650.

[15] M.X. Guo, J.Q. Du, C.H. Zheng, J.S. Zhang, L.Z. Zhuang, Influence of Zn contents on precipitation and corrosion of Al-Mg-Si-Cu-Zn alloys for automotive applications, J. Alloys Compd. 778 (2019) 256–270.

[16] S. Zhu, Z. Li, L. Yan, X. Li, S. Huang, H. Yan, Y. Zhang, B. Xiong, Natural aging behavior in pre-aged Al–Mg–Si–Cu alloys with and without Zn addition, J. Alloys Compd. 773 (2019) 496–502.

[17] J. Man, L. Jing, S.G. Jie, The effects of Cu addition on the microstructure and thermal stability of an Al–Mg–Si alloy, J. Alloys Compd. 437 (2007) 146–150.

[18] T. Saito, S. Muraishi, C.D. Marioara, S.J. Andersen, J. Røyset, R. Holmestad, The effects of low Cu additions and predeformation on the precipitation in a 6060 Al-Mg-Si alloy, Metall. Mater. Trans. A Phys. Metall. Mater. Sci. 44 (2013) 4124–4135.

[19] X. Xuehong, Y. Deng, C. Shuiqing, G. Xiaobin, Effect of interrupted ageing treatment on the mechanical properties and intergranular corrosion behavior of Al-Mg-Si alloys, J. Mater. Res. Technol. 9 (2020) 230–241.

[20] X.P. Ding, H. Cui, J.X. Zhang, H.X. Li, M.X. Guo, Z. Lin, L.Z. Zhuang, J.S. Zhang, The effect of Zn on the age hardening response in an Al-Mg-Si alloy, Mater. Des. 65 (2015) 1229–1235.

[21] M.X. Guo, X.K. Zhang, J.S. Zhang, L.Z. Zhuang, Effect of Zn addition on the precipitation behaviors of Al–Mg–Si–Cu alloys for automotive applications, J. Mater. Sci. 52 (2017) 1390–1404.

[22] S. Zhu, Z. Li, L. Yan, X. Li, S. Huang, H. Yan, Y. Zhang, B. Xiong, Effects of Zn addition on the age hardening behavior and precipitation evolution of an Al-Mg-Si-Cu alloy, Mater. Charact. 145 (2018) 258–267.

[23] M.X. Guo, G.J. Li, Y.D. Zhang, G. Sha, J.S. Zhang, L.Z. Zhuang, E.J. Lavernia, Influence of Zn on the distribution and composition of heterogeneous solute-rich features in peak aged Al-Mg-Si-Cu alloys, Scr. Mater. 159 (2019) 5–8.

[24] C.D. Marioara, S.J. Andersen, T.N. Stene, H. Hasting, J. Walmsley, A.T.J. Van Helvoort, R. Holmestad, The effect of Cu on precipitation in Al-Mg-Si alloys, Philos. Mag. 87 (2007) 3385–3413.

[25] T. Saito, C.D. Marioara, S.J. Andersen, W. Lefebvre, R. Holmestad, Aberration-corrected HAADF-STEM investigations of precipitate structures in Al-Mg-Si alloys with low Cu additions, Philos. Mag. 94 (2014) 520–531.

[26] T. Saito, F.J.H. Ehlers, W. Lefebvre, D. Hernandez-Maldonado, R. Bjørge, C.D. Marioara, S.J. Andersen, R. Holmestad, HAADF-STEM and DFT investigations of the Zn-containing β'' phase in Al-Mg-Si alloys, Acta Mater. 78 (2014) 245–253.

[27] S.J. Andersen, C.D. Marioara, A. Frøseth, R. Vissers, H.W. Zandbergen, Crystal structure of the orthorhombic U2-Al4Mg4 Si4 precipitate in the Al-Mg-Si alloy system and its relation to the β′ and β″ phases, Mater. Sci. Eng. A. 390 (2005) 127–138.

[28] S.J. Andersen, H.W. Zandbergen, J. Jansen, C. Træholt, U. Tundal, O. Reiso, The crystal structure of the β″ phase in Al–Mg–Si alloys, Acta Mater. 46 (1998) 3283–3298.

[29] H. Zhan, J.M.C. Mol, F. Hannour, L. Zhuang, H. Terryn, J.H.W. De Wit, The influence of copper content on intergranular corrosion of model AlMgSi(Cu) alloys, Mater. Corros. 59 (2008) 670–675.

[30] M.H. Larsen, J.C. Walmsley, O. Lunder, K. Nisancioglu, Significance of low copper content on grain boundary nanostructure and intergranular corrosion of AlMgSi(Cu) model alloys, in: Mater. Sci. Forum, Trans Tech Publications Ltd, 2006: pp. 667–672.

[31] M.H. Larsen, J.C. Walmsley, O. Lunder, R.H. Mathiesen, K. Nisancioglu, Intergranular corrosion of copper-containing AA6xxx AlMgSi aluminum alloys, J. Electrochem. Soc. 155 (2008) C550.

[32] W. Yang, S. Ji, Z. Li, M. Wang, Grain boundary precipitation induced by grain crystallographic misorientations in an extruded Al-Mg-Si-Cu alloy, J. Alloys Compd. 624 (2015) 27–30.

[33] C. Schnatterer, D. Zander, Influence of the grain boundary chemistry on the intergranular corrosion mechanisms of a high-strength Al-Mg-Si alloy, Surf. Interface Anal. 48 (2016) 750–754.

[34] Y. Zou, Q. Liu, Z. Jia, Y. Xing, L. Ding, X. Wang, The intergranular corrosion behavior of 6000-series alloys with different Mg/Si and Cu content, Appl. Surf. Sci. 405 (2017) 489–496.

[35] M.H. Larsen, J.C. Walmsley, O. Lunder, K. Nisancioglu, Effect of excess silicon and small copper content on intergranular corrosion of 6000-series aluminum alloys, J. Electrochem. Soc. 157 (2010) C61.

[36] G. Svenningsen, M.H. Larsen, J.C. Walmsley, J.H. Nordlien, K. Nisancioglu, Effect of artificial aging on intergranular corrosion of extruded AlMgSi alloy with small Cu content, Corros. Sci. 48 (2006) 1528–1543.

[37] Z. Wang, H. Li, F. Miao, W. Sun, B. Fang, R. Song, Z. Zheng, Improving the intergranular corrosion resistance of Al–Mg–Si–Cu alloys without strength loss by a two-step aging treatment, Mater. Sci. Eng. A. 590 (2014) 267–273.

[38] H. Nady, Tricine [N-(Tri(hydroxymethyl)methyl)glycine] – A novel green inhibitor for the corrosion inhibition of zinc in neutral aerated sodium chloride solution, Egypt. J. Pet. 26 (2017) 905–913.

[39] N. Birbilis, R.G. Buchheit, Electrochemical characteristics of intermetallic phases in aluminum alloys: an experimental survey and discussion, J. Electrochem. Soc. 152 (2005) B140.

11. Paper VII

Atomic structure of hardening precipitates in Al-Mg-Si alloys: Influence of minor additions of Cu and Zn

Emad H. Bartawi[1,*], Calin D. Marioara[2], Ghada Shaban[1], Constantinos Hatzoglou[3], Randi Holmestad[4], Rajan Ambat[1]

[1] Department of Civil and Mechanical Engineering, Technical University of Denmark, Kgs. Lyngby 2800, Denmark

[2] Materials and Nanotechnology, SINTEF Industry, Trondheim N-7465, Norway

[3]Department of Materials Science and Engineering, NTNU, Norwegian University of Science and Technology, Trondheim 7491, Norway

[4]Department of Physics, NTNU, Norwegian University of Science and Technology, 7491 Trondheim, Norway

[*]Corresponding author: ehaba@dtu.dk

Keywords: 6082-Al-Mg-Si alloys; crystal structure; HAADF-STEM; APT

Abstract

The influence of 0.05 wt% Cu and 0.06 wt% Zn, individually and in combination, on the precipitate crystal structures has been investigated in Al-Mg-Si alloys in the peakaged and overaged conditions. Atomic resolution high-angle annular dark-field scanning transmission electron microscopy and atom probe tomography were adopted to assess whether such low concentrations can affect the hardening precipitate structures. The results indicate that low Cu and/or Zn can significantly influence the precipitate structures, as both elements showed a relatively high tendency to incorporate into precipitate structures. Moreover, it is found that Cu tends to enter the precipitate crystal structures based on its own configurations by occupying specific atomic columns in the precipitate structure. However, Zn exhibited a unique behavior through forming large areas with 2-fold

symmetry and mirror plane configurations not observed in precipitate structures nucleated in Al-Mg-Si alloys with Li, Ag, and Cu additions. The results obtained from this work are highly relevant to the topic of recycling, where the accumulation of certain alloying elements is almost unavoidable, thus, tight compositional control might be critical to avoid quality degradation.

11.1 Introduction

The heat treatable Al-Mg-Si alloys are intensively used in different applications such as automotive and construction sectors due to their attractive properties, e.g., recyclability, good corrosion resistance, high strength-to-weight ratio, and formability [1,2]. Using aluminium alloys in automotive applications is an effective strategy for weight reduction without losing performance and thus reducing CO_2 emissions [3]. Primary aluminium production requires high energy input due to the electrolysis process, however, recycling can save up to 95 % of the energy needed to produce the same amount of primary aluminium, significantly reducing CO_2 emission [4,5]. The type and the amount of certain alloying elements which can exist in the final recycled alloys as impurities (~0.02 at%) can significantly influence their IGC resistance, i.e., Cu and Zn. Several studies concerning Cu and Zn have reported that Cu (≥ 0.1 wt%) and Zn (≥ 0.1 wt%) can significantly influence the age hardening response [6–9], IGC resistance [10–12] and precipitation [7,13–15] in Al-Mg-Si alloys. However, the interest in investigating the influence of Cu and/or Zn as impurities (~0.02 at%) on the IGC resistance of the recycled Al-Mg-Si alloys has recently received particular attention [16,17] due to its importance in connection with recycled alloys.

It is commonly accepted that the sequence of precipitation in Al-Mg-Si system is given as [18,19]:

SSSS → clusters→ GP-zones→ β″→ β′, U1, U2, B′→ β+Si.

Here, SSSS stands for a supersaturated solid solution.

Several studies have proven that introducing Cu into Al-Mg-Si alloys can significantly enhance their mechanical properties through altering the clustering and precipitation behavior [9,13,20–25]. For example, Marioara et al. [13] investigated the influence of Cu addition on the precipitation in Al-Mg-Si alloys aged at 175 °C for different

aging times. The results indicated that the alloy with 0.3 wt% Cu exhibited finer microstructure and higher precipitate density and, thus, higher peak hardness compared to Cu-free alloys. It is also reported that in the peakaged (PA) condition, the Cu-containing precipitates comprise only between 20-30 % of β″ and pre-β″ precipitates, while the rest are Guinier-Preston (GP) zones and Q′ precursors, suggesting that β″ precipitates are not the primary hardening precipitates. Therefore, the Cu addition will lead to a more complex precipitation sequence in Al-Mg-Si alloys, which is given as [13,26–28]:

$$SSSS \rightarrow clusters \rightarrow GP\text{-}zones \rightarrow \beta'' \rightarrow L \rightarrow \beta'_{Cu}, S, Q', C \rightarrow Q + Si.$$

Recently, investigating the effect of Zn additions on the mechanical properties and precipitation in Al-Mg-Si alloys has become relevant due to the considerable potential of Zn in enhancing age hardening response during artificial aging [7,24,29–34]. Ding et al. [7] investigated the impact of Zn additions on the age hardening response in Al-0.99Mg-0.54Si (wt%) alloy. The results showed that at a relatively high concentration (3 wt%), Zn could enhance the age hardening response by forming GP (II)-zones of η-$MgZn_2$ and its precursor. Zhu et al. [24] reported that introducing Zn into Al-0.9Mg-0.8Si-0.2Cu (wt%) can increase the volume fraction and number density of GP zones and β″ precipitates, hence enhancing the age hardening response. It was also suggested that Zn additions can increase the portioning of Mg, Si, and Cu into clusters, enhancing the clustering formation and stimulating the transformation from clusters to precipitates (GP zones and β″). Xu et al. [31] reported that Zn addition up to 2.0 wt% did not change the precipitation sequences in Al-0.85Mg-1.1Si alloy, while the majority of the intragranular (bulk) precipitates in the alloy containing higher Zn content (4 wt%) consisted of β″ and a small amount of η′ precipitates.

One of the most relevant questions concerning recycling is related to the types and concentrations of scrap-related elements that Al-Mg-Si alloys can tolerate without negatively influencing their IGC resistance and mechanical properties. Also, since such impurities are undoubtedly unavoidable, it is important to know how to avoid negative influence of the impurities and retain properties similar to primary alloys. In this regard, a recent study on the impact of 0.05 wt% Cu content as a recycling impurity in 6082 Al-Mg-Si alloy has been reported by Bartawi et al. [16]. The results indicated that even such low Cu addition could cause a severe IGC in the PA condition, which is related to the presence of grain boundary (GB) particles and Cu-rich film along some GBs. Therefore, the current

work aims to provide a deep understanding of the influence of 0.05 wt% Cu and 0.06 wt% Zn, individually and in combination, on the precipitate crystal structure. Such information will directly assist in optimizing the IGC resistance of Al-Mg-Si alloys and thus moving toward more impurity-tolerant alloys by understanding the affinity of Cu and Zn to be incorporated into precipitate structures. The affinity and the degree of Cu and Zn incorporation into intragranular and GB particles will inevitably affect the corrosion potential of the Al matrix and the precipitates. Scanning transmission electron microscope (STEM) and atom probe tomography (APT) were employed in the current work to investigate the precipitate crystal structures and the chemical composition of bulk precipitates on the atomic scale.

11.2 Experimental methods

11.2.1 Material used

The chemical compositions of the Al-Mg-Si alloys used in the current research are displayed in Table 11.1. The homogenization process of the ingots was conducted at 575 °C for 135 min. A ram speed of 5.6 mm/s was adopted during the hot extrusion process. The average billet temperature during the extrusion was approximately 530 °C, and the final extruded flat profiles had a thickness of 4 mm. Thereafter, the material was water-quenched, stretched 0.5%, and finally underwent a two-step artificial aging process to reach the PA condition. Hydro Aluminium refers to this condition as the T6 condition, which is used in this paper as the designation for ‘as received material’. To investigate alloy O3 in the overaged (OA) condition, the alloy was heat treated for 30 min at 530 °C, water-quenched, and then artificially aged for 5 h at 240 °C. The OA alloy was denoted as alloy O4, see Table 11.1.

Table 11.1. Chemical composition (wt%) of 6082-Al-Mg-Si alloys studied in the present study.

Alloy No.	Al	Mg	Si	Mn	Fe	Cu	Zn
O1	Balance	0.64	0.96	0.54	0.22	0.048	0.003
O2	Balance	0.63	0.94	0.56	0.21	0.001	0.059
O3	Balance	0.63	0.95	0.58	0.21	0.050	0.059
O4	Balance	0.63	0.95	0.58	0.21	0.050	0.059

11.2.2 Microstructure characterization

For atomic resolution, high-angle annular dark-field scanning transmission electron microscopy (HAADF-STEM) specimens from each alloy were cut to ~400 μm thickness, then mechanically polished to ~100 μm, and eventually punched into 3 mm discs. The thin foils were then prepared using the TenuPol-5 twin-jet polishing system in a solution containing 900 ethanol and 100 ml perchloric acid 65 % at ~ -20 °C. A spherical aberration (Cs) probe-corrected JEOL ARM200F microscope operated at 200 kV was used to acquire the atomic resolution HAADF-STEM images of the bulk precipitates. The HAADF detector had a collection angle range of 51 to 203 mrad, and the probe size was 0.10 nm.

Three specimens of alloys O2 and O4 for atom probe tomography were prepared by electropolishing according to the methods and using solutions described in [35,36]. The APT analysis is done with a CAMECA LEAP 5000XS, operated in UV laser pulsing mode with a frequency of 200 kHz and a detection rate of 2 %. The base temperature is set at 40 K, and the laser energy is adjusted to obtain an equivalent pulse fraction of 25 % of the DC potential to avoid preferential evaporation [37] (i.e., around 100 pJ). Data reconstruction and processing were performed using the AP Suite 6.1 software tool and the Norwegian Atom Probe App (NAPA) software, developed in MATLAB® [38]. The APT results for each alloy are a synthesis of three separate evaporated volumes.

11.3 Results

Low magnification HAADF-STEM images in Fig. 11.1(a, b) show the microstructure of alloy O1 with 0.05 wt% Cu in the PA condition and alloy O4 with 0.05 wt% Cu and 0.06 wt% Zn alloy in the OA condition, respectively. Fine microstructure with needle-like β″ precipitates in alloy O1 in the PA condition can be observed, see Fig. 11.1a, while a coarser structure with long rod-like precipitates was noticed in alloy O4 in the OA condition. Although not shown, alloys O2 and O3 had similar microstructure as alloy O1. Based on Fig. 11.1, it's not clear whether Cu and/or Zn were incorporated into precipitate structures in such conditions and very low concentrations. Therefore, all alloys (O1, O2, O3, and O4) were investigated using atomic resolution HAADF-STEM.

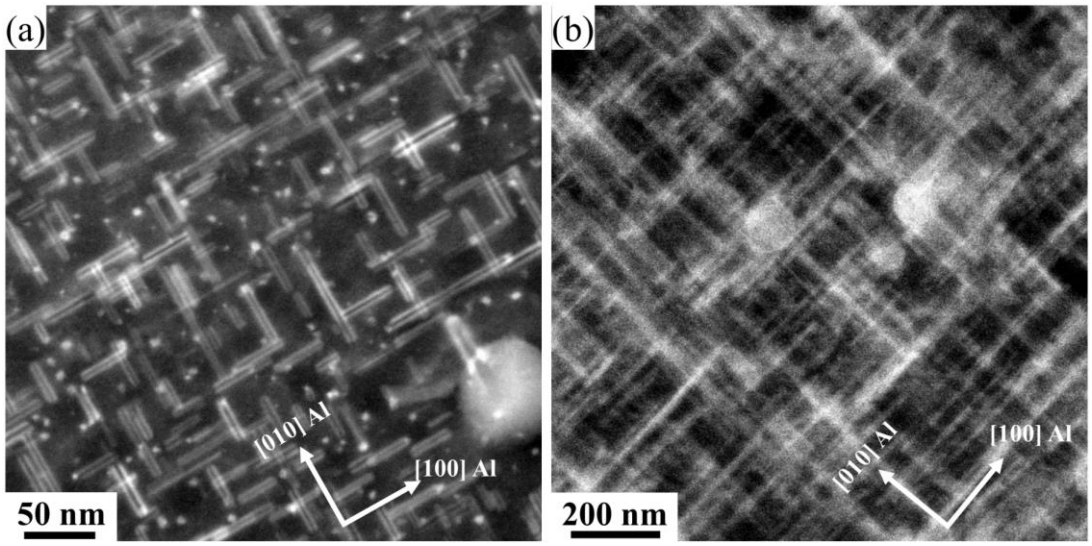

Fig. 11.1. HAADF-STEM images (a, b) of hardening precipitates in alloys O1 and O4, respectively.

The atomic resolution Z-contrast HAADF-STEM images were taken to determine the influence of minor addition of Cu (≤ 0.05 wt%) and Zn (≤ 0.06 wt%) individually and in combination on the hardening precipitate crystal structures in the base Al-Mg-Si alloy in the PA and OA conditions. Since the precipitates in the Al-Mg-Si system grow along 〈0 0 1〉 Al directions, all the acquired images were taken with the matrix oriented in a 〈0 0 1〉 Al zone axis, enabling the visualization of atomic columns in the precipitate cross-sections. All acquired images were filtered to reduce scanning noise by applying a fast Fourier transform (FFT) using the band pass mask, which removes all distances less than 1.5 Å. To solve the structure of the selected representative precipitates, the images were overlaid with atoms. The overlay was based on Z-contrast, the solved crystal structures of different types of hardening precipitates in the Al-Mg-Si-Cu system [13,39–42], and the construction rules of these precipitates from [43]. According to the rules, the precipitates follow the crystal structure of the face center cubic (FCC) Al matrix along their needle lengths, consisting in cross-section of two atomic planes (0 and ½) separated by 2.025Å, each with 4.05Å periodicity along the <001>Al. Therefore, the atomic overlays along the needle directions can be visualized as solute atomic columns on two atomic planes (or heights). The rules dictate that in the cross-section projection each Al atom in one plane is surrounded by four near neighbor atoms belonging to the other plane, Mg by five and Si, Cu by three. One consequence of the rules is that the Si atomic columns will have a near hexagonal configuration with approximately 4Å separation in the cross-section plane, also called the 'Si-network' [13,27,41,43].

Terms such as *pure*, *interface*, *fragmented*, and *mixed* are used in the following to describe the precipitate structures and the influence of minor Cu and Zn additions. A *Pure* denotes that the Cu and/or Zn enter the β″ precipitates and partially occupy different Si and/or Al columns without altering their structures. *Interface* refers to the structure in the precipitate at the border between the precipitate and the surrounding Al matrix. *Interfacial* Cu and/or Zn describes a precipitate where, e.g., Cu and/or Zn occupy Al matrix columns at the precipitate-matrix interface without entering the precipitate crystal structure. In a *fragmented* precipitate Cu and/or Zn atoms occupy specific local atomic configurations such as in U1, U2, B′, β'_{Cu} Q′/C phases [39,44]. Therefore, one such precipitate comprises fragments of different phases in the same needle cross-section. *Mixed* precipitates are defined as containing Cu and/or Zn in their bulk (*fragmented*), at the precipitate/matrix interface (*Interfacial*), as well as disordered areas that cannot be identified as belonging to known precipitate structures, for example with 2-fold symmetry and/or mirror symmetries.

11.3.1 Influence of Cu on the precipitate structures in the peakaged condition

Starting with Fig. 11.2(a, c) acquired from alloy O1 (0.05 wt% Cu) in the PA condition, β″ precipitates show abnormally brighter columns inside their structures and at the β″/Al interface than neighbor columns. Fig. 11.2a shows brighter columns β″ unit structure, namely Si_1, Si_2, and Si_3/Al columns, indicating that Cu partially occupied these sites, see Fig. 11.2b. The systematic higher intensity observed at β″/Al matrix interface corresponds with the Si_3/Al columns along [3 -2 0] Al, see Fig. 11.2(c, d).

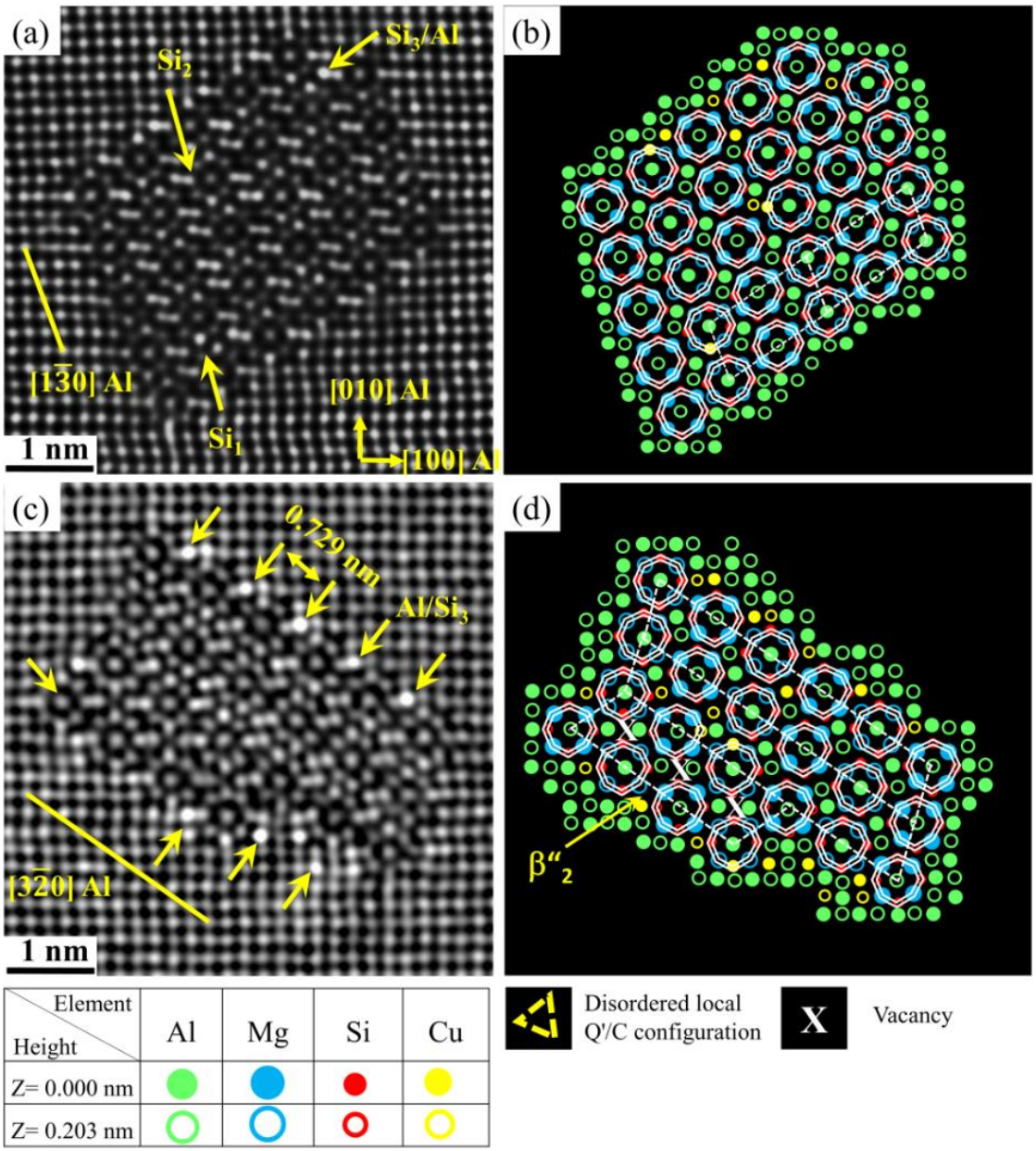

Fig. 11.2. HAADF-STEM lattice images of the cross-section of β″ precipitates found in the Al-Mg-Si alloy with 0.05 wt% Cu in the PA condition (a, c), and their suggested atomic overlay (b, d), respectively.

Fig. 11.3(a, c) shows fragmented β″ precipitates that contains at least one unit ('eye') configuration different from the common monoclinic β″ structural unit. The β″ and fragmented β″ phases are the primary hardening precipitates observed in alloy O1 in the PA condition. Due to the partial occupancy of Cu to specific columns in the crystal structure of almost all investigated precipitates, those columns exhibit a higher intensity than other equivalent columns. Interestingly, an unexpectedly significant influence of 0.05 wt% Cu addition on the precipitate structures is observed in Al-Mg-Si alloys in the PA condition.

Several local atomic configurations (e.g., β'_{Cu}, Q′/C, and U2) appeared in the β″ crystal structures, modifying its structure and leading to more complex precipitate structures, as seen in Fig. 11.3(a-d). Furthermore, the U2 phase is observed in the disordered part of the fragmented precipitate without Cu showing a distinct tendency to occupy the Si and/or Al sites in the U2 region, see Fig. 11.3(a, b).

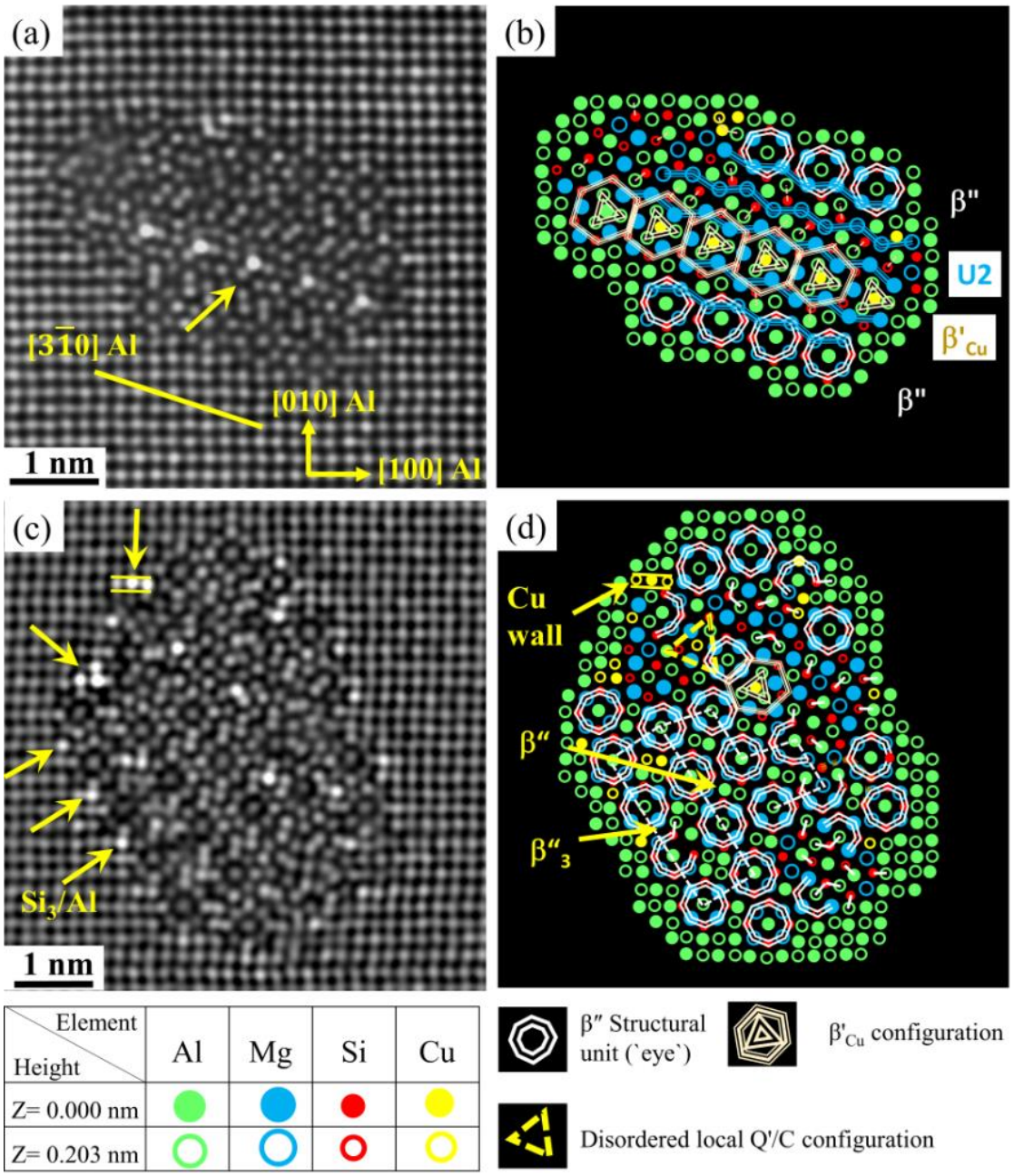

Fig. 11.3. HAADF-STEM lattice images of fragmented and mixed precipitate cross-sections found in Al-Mg-Si alloy with 0.05 wt% Cu in the PA condition (a, c), and (b, d) their suggested atomic overlay, respectively.

Based on the observation of several precipitates found in the microstructure of alloy O1, the influence of 0.05 wt% Cu on the Al-Mg-Si bulk precipitates can be summarized as

follows: ~22.5 % of the acquired precipitates are found to be pure β″ precipitates, ~23.9 % are β″ precipitates with a Cu-interface enrichment, and ~53.5 % are fermented and mixed precipitates, see Table 11.2. In the fragmented and mixed precipitates Cu atoms are incorporated into the crystal structure and led to the emergence of a sub-unit of different phases.

Table 11.2. Effect of 0.05 wt% Cu and 0.06 wt% Zn, individually and in combinations, on the precipitate crystal structures existing in the microstructure of the studied 6082-Al-Mg-Si alloys in the PA (O1, O2, and O3) and OA (O4) conditions.

Cu/Zn addition	Pure β″ *(%)*	Interface (%)	Fragmented & Mixed (%)	Number of investigated cross-sections
O1	22.5	23.9	53.5	68
O2	39.8	-	60.2	74
O3	21.8	3.7	74.5	52
O4	-	-	100	33

11.3.2 Influence of Zn on the precipitate structures in the peakaged condition

Fig. 11.4a shows FFT-filtered images of one mixed precipitate from Zn-containing alloy O2 in the PA condition. The atomic overlay shows that it consists of a combination of β″, Q′/C, β'_{Cu} (iso-structural to β'_{Ag}), and U2 structural configurations. Interestingly, one area containing a mirror plane and many arrow configurations (drawn in orange) are observed. Atomic columns with abnormally high Z contrast can be noticed inside and at the Al matrix/precipitate interface, see Fig. 11.4(a, c). Furthermore, extended areas with 2-fold symmetry, mirror plane, and arrow configurations are observed in the disordered regions in-between β″ phase in the precipitates shown in Fig. 11.5(a-d). It is interesting to note that many of the areas with mirror plane symmetry are related to the arrow configurations, which is believed (based on the current results) to be triggered by the strong Zn tendency to occupy all atomic columns in β″ unit structure except for Mg_2 and Mg_3 sites. Interestingly, unlike Cu containing alloy, Zn shows a strong tendency to occupy Al and Si columns in the U2 structure.

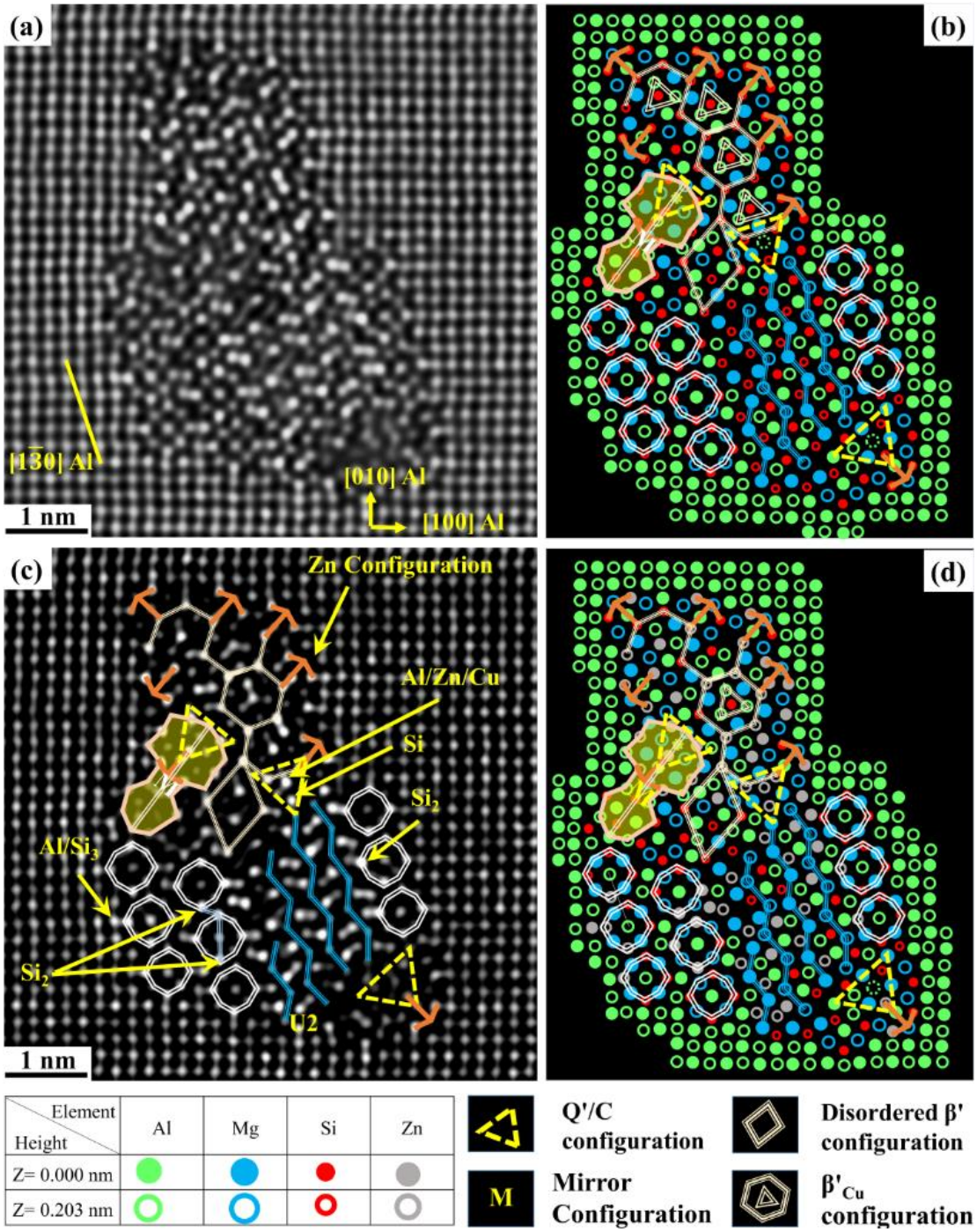

Fig. 11.4. HAADF-STEM image of a Zn containing β" mixed precipitate cross-section taken from alloy O2. (a) FFT Filtered image, (b) suggested atomic overlay based on the construction rules for Al, Mg and Si, (c) enhanced contrast/brightness image showing different sites and configurations found in this precipitate, and (d) suggested overlay by considering Zn based on Z contrast.

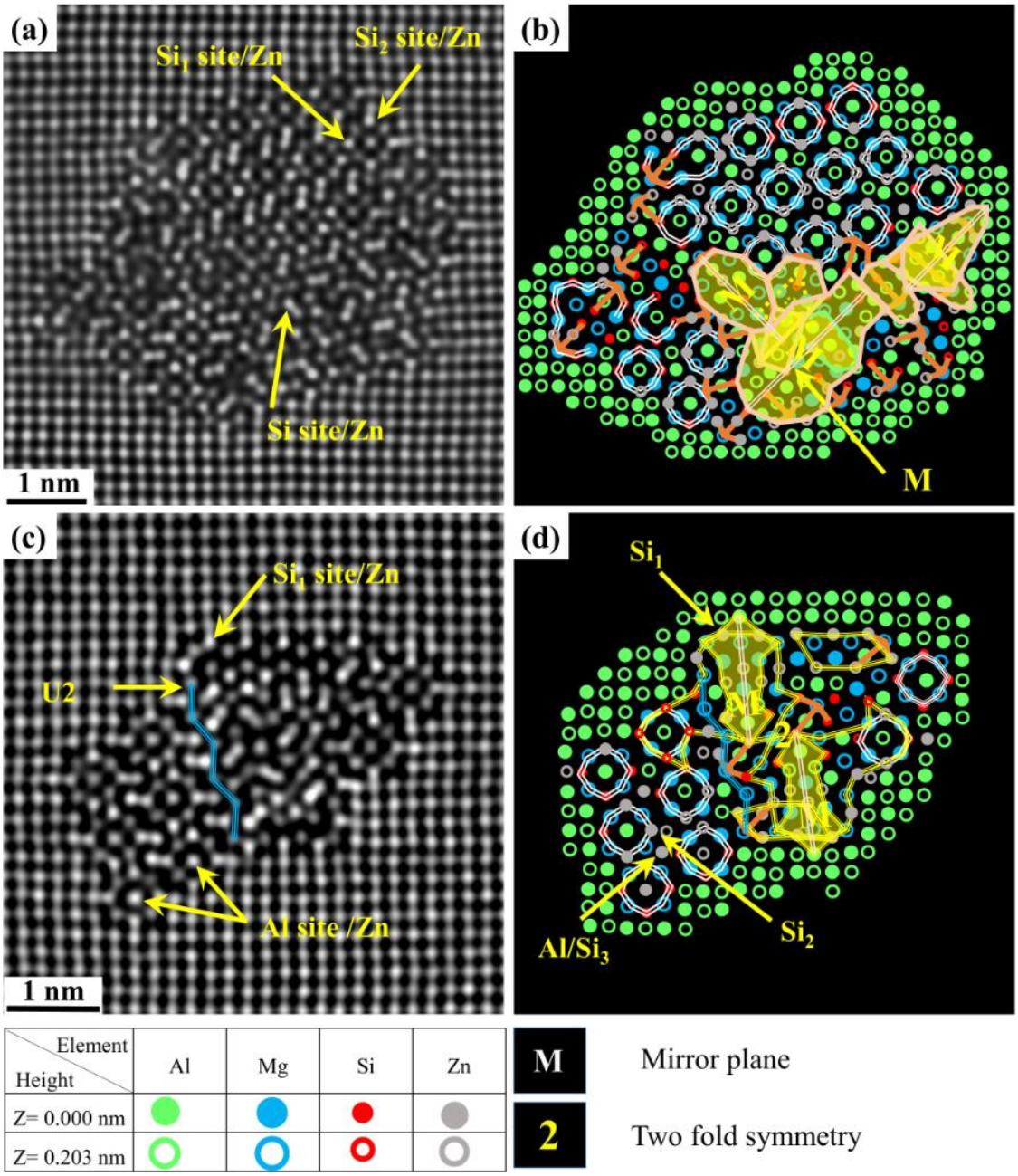

Fig. 11.5. Side-by-side HAADF-STEM images of Zn containing β" mixed precipitates and their suggested atomic overlay (a-d). Yellow arrows show different atomic sites, e.g., Al, Si_1, Si_2, and Si_3, that are partially occupied by Zn. Two-fold symmetry and mirror plane configurations are shown in (b) and (d).

The precipitates in Fig. 11.6 confirm that Zn can enrich Si and Al atomic columns in a multitude of local atomic configurations of β″, U2, Q'/C, and $β'_{Cu}$ phases. In Fig. 11.6(a), most of the columns in the U2/$β'_{Cu}$/U2 part of the precipitate are Zn-enriched, forming a band of brighter contrast. In addition, Fig. 11.6(b, c, d) clearly shows that Zn can be found at the β″/Al matrix interface occupying Si_3/Al columns and inside the precipitates, occupying different atomic columns in the β″ unit cell.

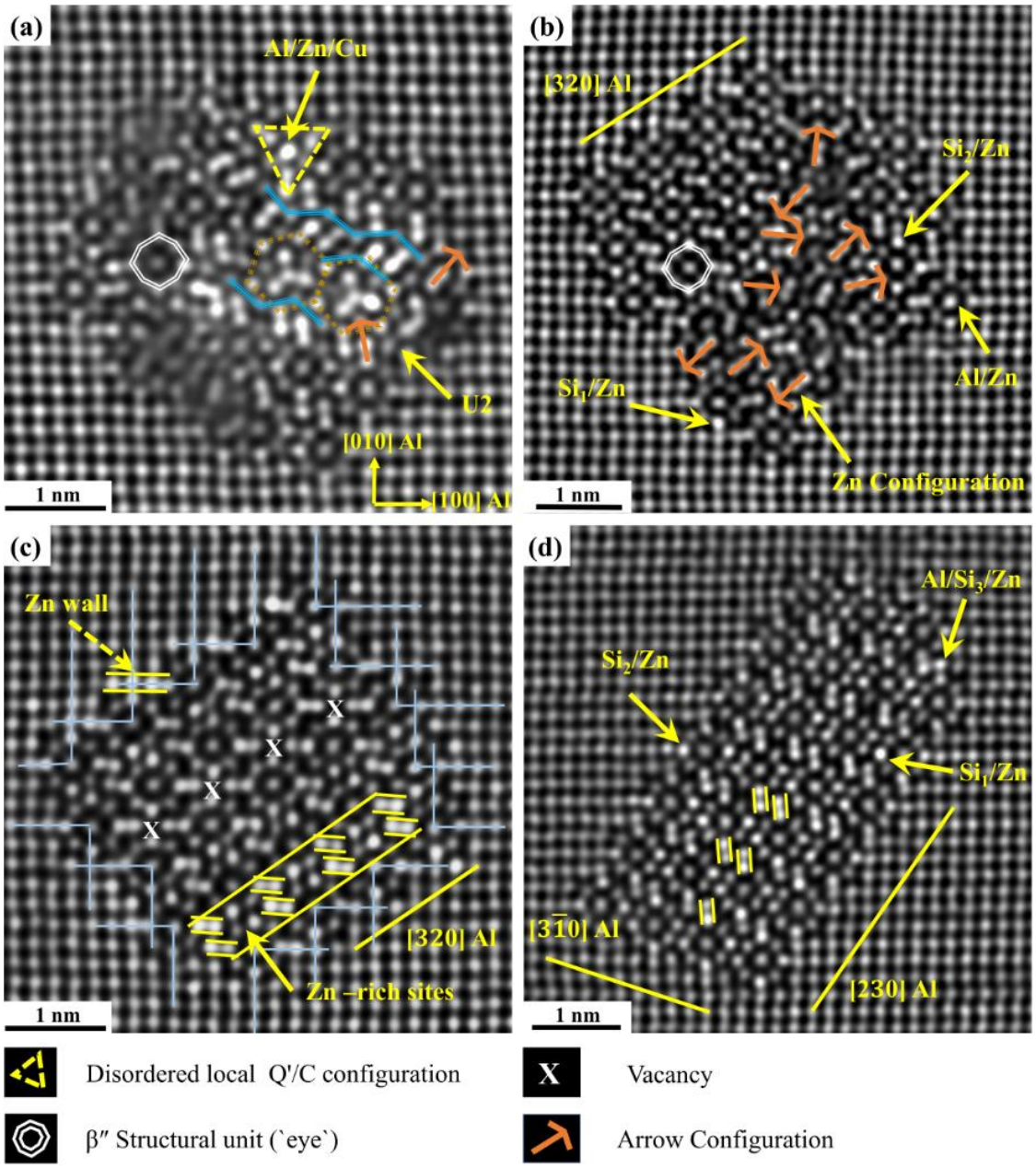

Fig. 11.6. (a, b) HAADF-STEM image of Zn containing β" fragmented and mixed precipitates respectively, indicating the local configurations found in their structures, i.e., β", U2, Q′/C, and β'_{Cu}. (c, d) HAADF-STEM images of Zn containing pure β" precipitates with yellow arrows showing the atomic sites that Zn has occupied. The dashed-yellow arrow shows Zn-occupied Si_2, Si_3/Al, and Al sites at the interface forming a Zn wall usually found in Al-Mg-Zn-Cu alloys.

11.3.3 Influence of Cu and Zn on the precipitate structures in the peakaged condition

Precipitates in alloy O3 revealed evident differences concerning their structures and the fraction of fragmented and mixed precipitates compared to alloys O1 and O2, as shown in Table 11.2 and Figs. 11.7(a, c) and 11.8(a, c). Similar to the precipitates in alloys O1 and O2, alloy O3 contained precipitates having a number of atomic columns with higher

intensity than other corresponding columns owing to a partial occupancy of either Zn and/or Cu. It is worth mentioning that the minor Zn and Cu additions lead to the appearance of β'_{Cu}, Q′/C, and U2 configurations in the β″ crystal structure, see Figs. 11.7d and 11.8(b, d). Also, interestingly, mirror planes and arrow configurations are observed in alloy O3, see Figs. 11.7d and 11.8(b, d). Since these atomic arrangements have not been observed in alloy O1, it directly indicates the effect of Zn incorporation that has not been previously documented in the literature. The effect of 0.05 wt% Cu and 0.06 wt% Zn additions on the precipitate structures of alloy O3 can be summarized as follows: ~21.8 % of the recorded precipitates are identified as pure β″ precipitates, ~3.7 % are β″ precipitates with Cu/Zn-interface enrichment, and ~74.5 % are incorporated and mixed precipitates, see Table 11.2. Therefore, it can be inferred that significant changes in the fraction of pure and fragmented/mixed precipitates are observed in alloy O3 as compared to alloys O1 and O2. Furthermore, the complexity of fragmented/mixed precipitates was observed to be higher in the Zn-added alloys (O2 and O3) compared to only Cu-added alloy (O1), see Figs. 11.3, 11.4, 11.5, 11.6(a, b), 11.7(c, d), 11.8.

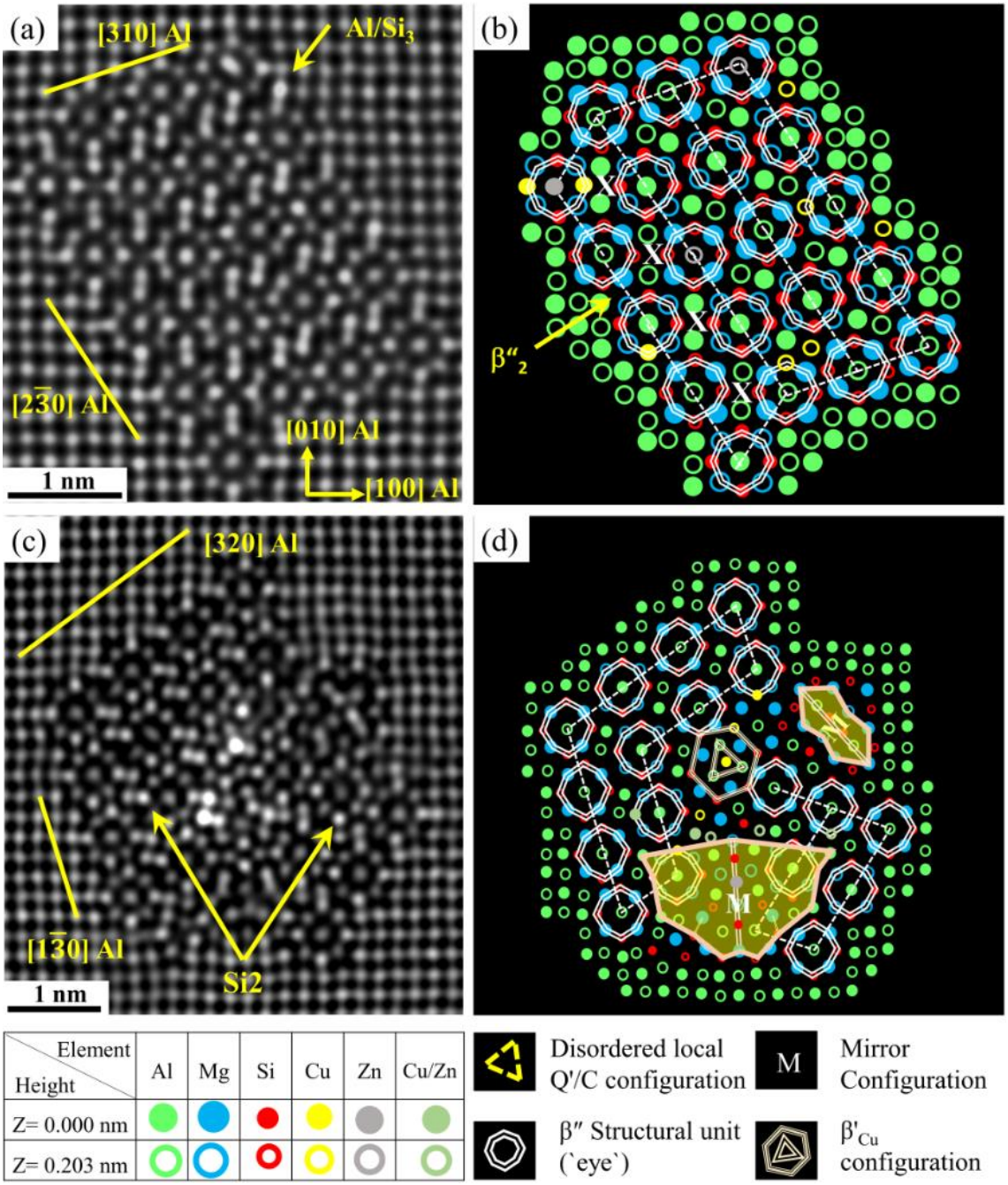

Fig. 11.7. HAADF-STEM lattice images (a, c) of precipitate cross-sections from Al-Mg-Si alloy with 0.05 wt% Cu and 0.06 wt% Zn (alloy O3) in the PA condition with the corresponding suggested atomic overlay (b, d), respectively.

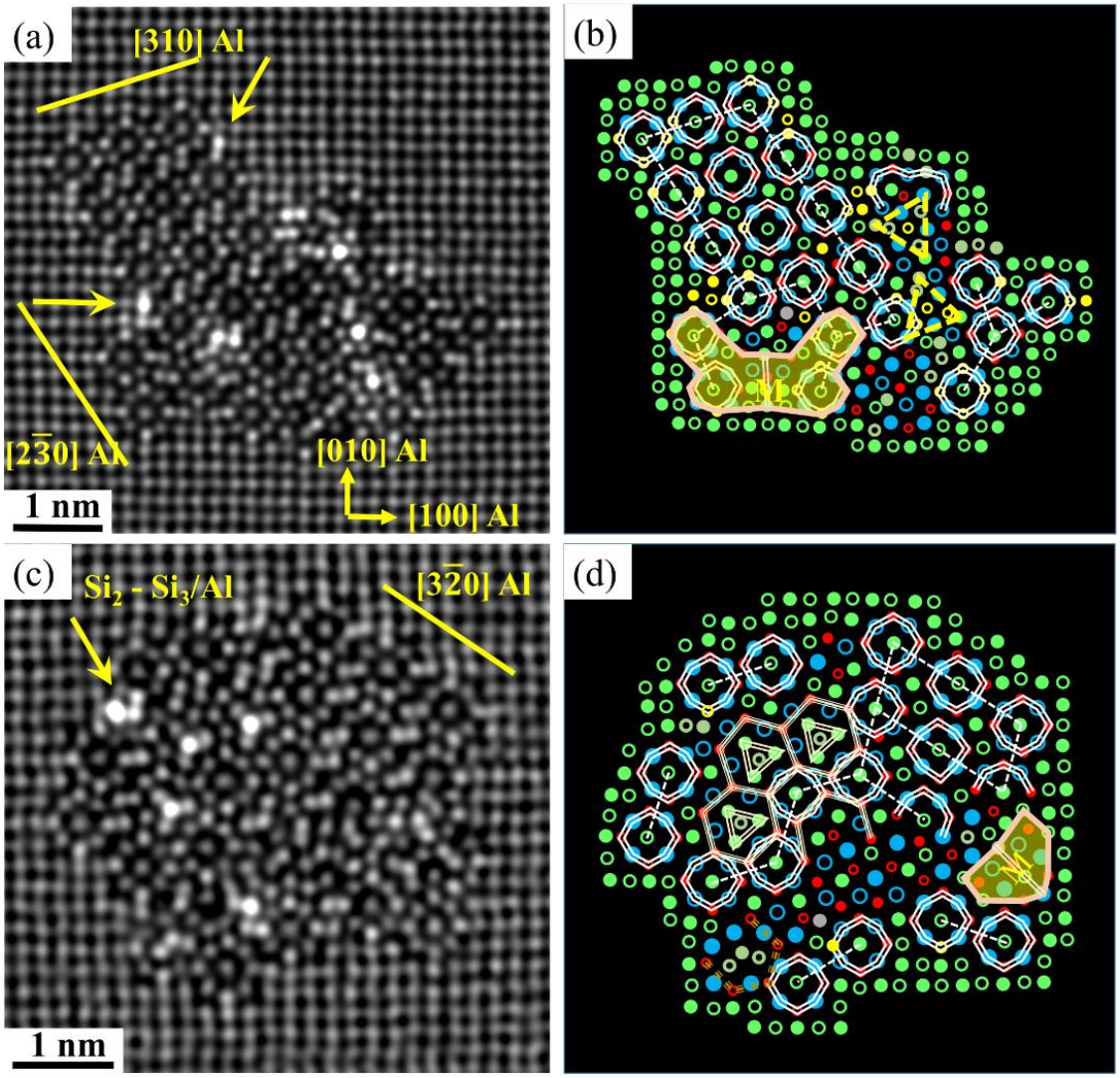

Fig. 11.8. HAADF-STEM lattice images (a, c) of the fragmented precipitate observed in the microstructure of alloy O3 in the PA condition along with the corresponding suggested atomic overlay (b, d), respectively. See legend in Fig. 11.7.

11.3.4 Influence of Cu and Zn on the precipitate structures in the overaged condition

Fig. 11.9a shows the atomic resolution of one of the mixed precipitates observed in the microstructure of alloy O4 in the OA condition along with the suggested atomic overlay considering the construction rules for the Al, Mg and Si, see Fig. 11.9b. The suggested overlay after considering the Z contrast can be seen in Fig. 11.9d. Determination of Zn site is not self-evident based on the Z contest, but brighter atomic sites are usually noticed inside the precipitate structures without clear structural preferences. Moreover, mirror planes and several arrow configurations are observed in precipitates in this condition, see Fig. 11.9(b, c). The amount of Cu and Zn incorporated into precipitate structures vary. However, all

investigated precipitates exhibited a few atomic columns with higher intensity than the other corresponding sites, see other examples in Fig. 11.10. In general, the precipitates in alloy O4 with 0.06 wt% Cu and 0.06 wt% Zn in the OA condition showed the presence of U1, U2, β'_{Cu}, Q′/C, β″, and B′ sub-unit configurations, see Figs. 11.9b and 11.10.

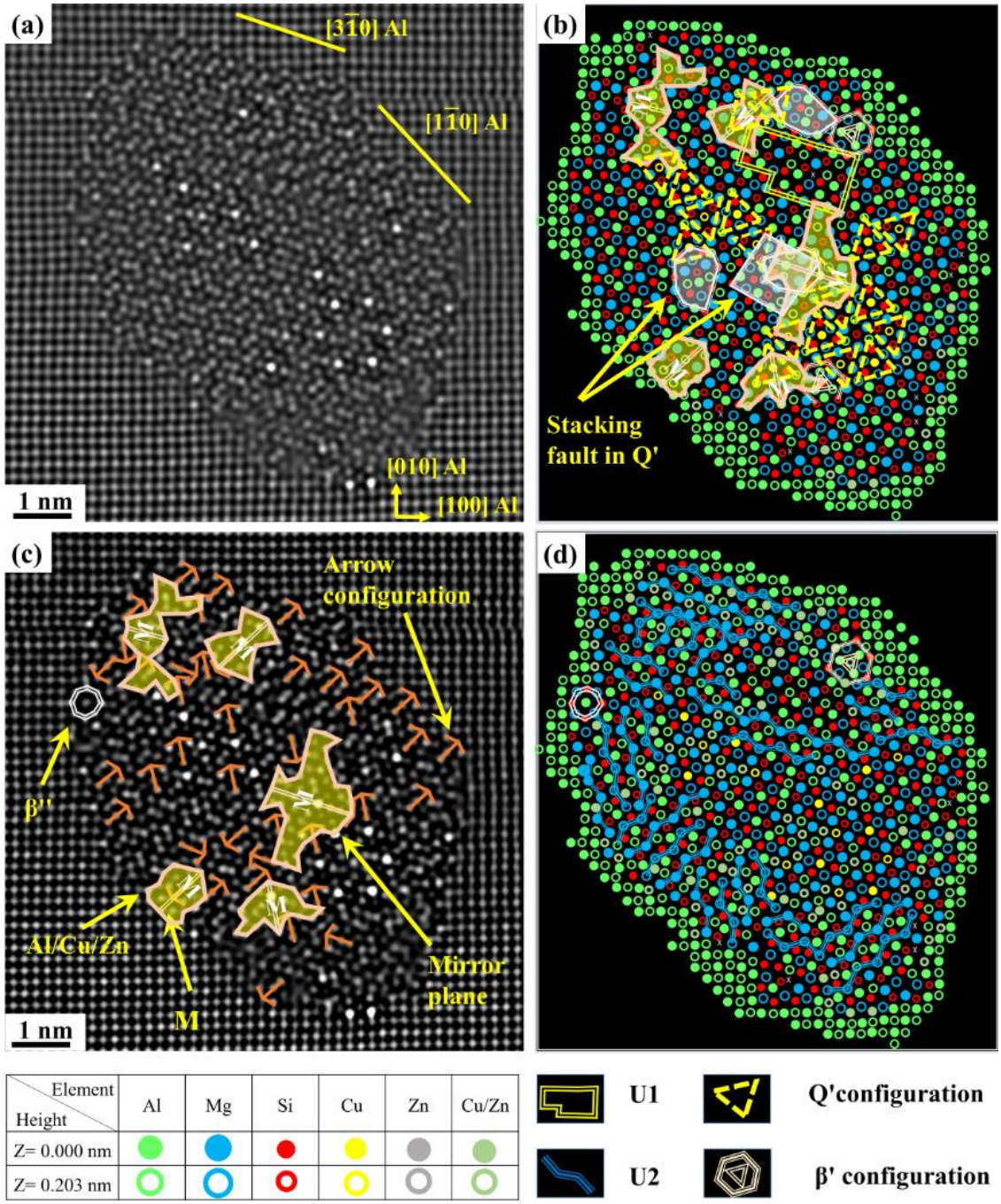

Fig. 11.9. HAADF-STEM image of a mixed precipitate cross-section found in alloy O4 in the OA condition. (a) FFT Filtered image, (b) suggested overlay based on the construction rules considering Al, Mg, and Si, (c) Enhanced contrast/brightness image illustrating different mirror planes and arrow configurations noticed in the precipitate, and (d) suggested overlay by additional consideration of Cu and Zn based on known sites that Cu can occupy, and Z contrast.

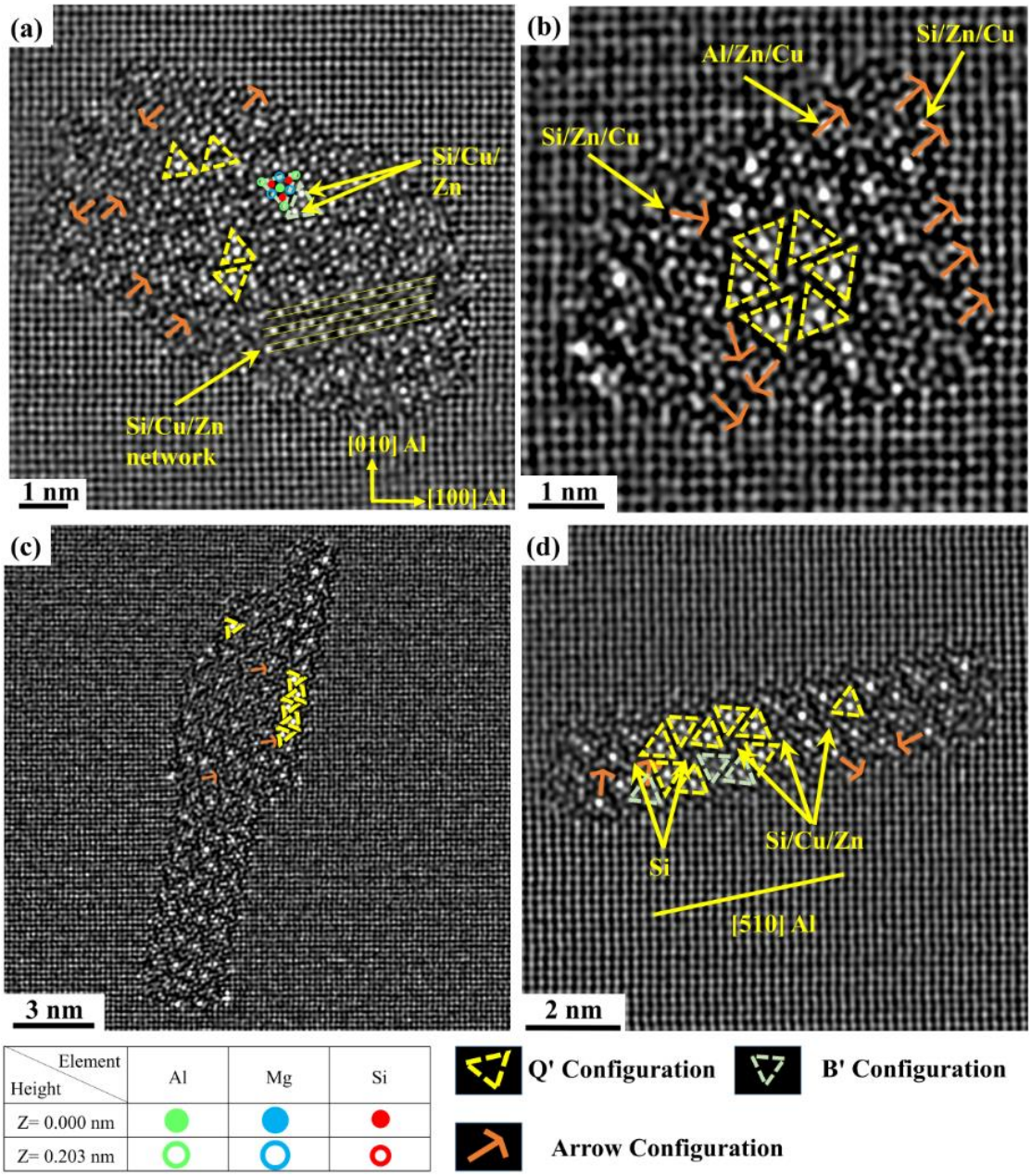

Fig. 11.10. HAADF STEM images of typical precipitate cross-sections observed in the microstructure of alloy O4 (a, b, c, d), showing the presence of Q'/B' and arrow configurations.

11.3.5 Atom probe tomography results

Three samples of alloys O2 and O3 sectioned from the top surface layer of the extruded profiles were investigated by APT, and an example of the volume containing the hardening precipitates is presented in Fig. 11.11. Microstructural features with low volume density such as constituent intermetallic particles, dispersoids and GB particles are not observed in the evaporated samples from alloy O3. By coincidence one sample from alloy O2 incorporated a dispersoid (see supplementary chapter Fig. S.3). The output from the

APT investigations are the distribution of solutes (including Cu and/or Zn) in the microstructure, the average composition of the hardening precipitates (β″ and disordered β″) and the solid solution concentration (in-between the needles). Concerning the composition of the bulk precipitates observed in alloy O2, the proximity histogram in Fig. 11.11b demonstrates that in addition to Mg and Si they also contain Zn, see Table 11.3. The latter observation is in agreement with the atomic resolution HAADF-STEM results obtained from alloy O2, as Zn is evidently incorporated into the precipitate crystal structures. The APT results indicate that the bulk precipitates contain ~0.1 at% Zn, and their Mg/Si ratio is ~1.38 ± 0.11. Concerning the composition of the hardening precipitates in alloy O3, the proximity histogram in Fig. 11.11.d clearly shows that in addition to Mg and Si they contain Cu and Zn, see also Table 11.3. The average concentration of Zn in precipitates is ~0.1 at%, similar to the alloy O2 case, but the amount of Cu is almost ten time higher, at ~0.9 at% Cu. Compared to the measured solute concentrations left in-between needles in the matrix and the nominal alloy composition, these results show that most of the Zn in the alloy stays in solid solution, while the hardening precipitates consume approximately 44 % of the Cu added to the alloy O3. The APT results also show that the Mg/Si ratio in the precipitates in the alloy O3 in the PA condition with 0.05 wt% Cu and 0.06 wt% Zn is 1.77 ± 0.11.

Table 11.3. Nominal, matrix, and average hardening precipitate compositions (at%). The measurement uncertainties of the nominal and matrix composition is lower than 0.01 at%. Traces (i.e., < 0.01 at%) of Ag, Ga, Cr, V, and Ti are also observed.

Alloy O2 (at%)				Alloy O3 (at%)			
Element	Nominal	Matrix	Precipitate	Element	Nominal	Matrix	Precipitate
Mg	0.72	0.29	39.0 ± 1.4	Mg	0.60	0.19	47.3 ± 1.2
Si	0.58	0.31	28.3 ± 1.3	Si	0.44	0.15	26.8 ± 1.0
Zn	0.02	0.02	0.1 ± 0.1	Zn	0.02	0.02	0.1± 0.1
Mn	0.02	0.02	n.s.	Cu	0.09	0.05	0.9 ± 0.2

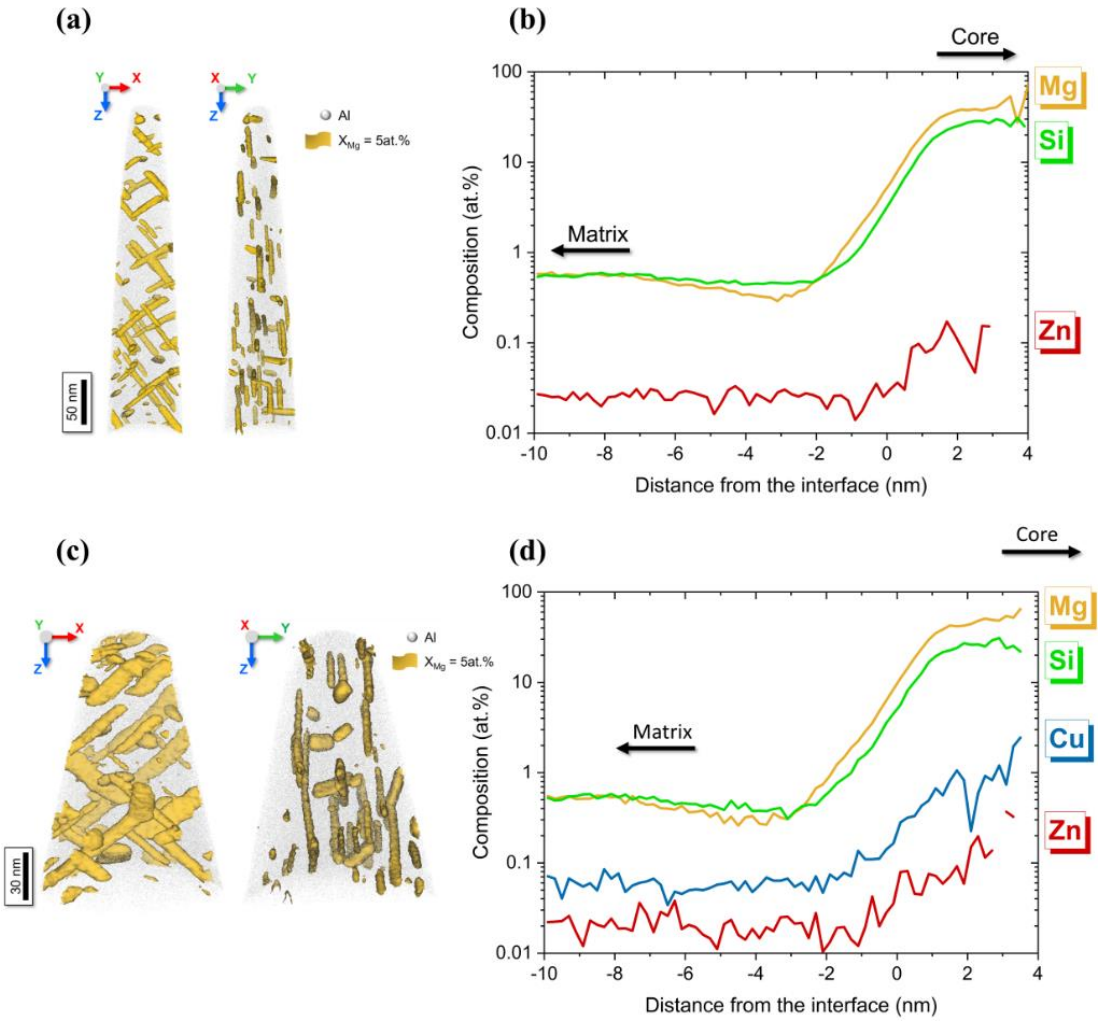

Fig. 11.11. APT analysis of samples from the alloys O2 and O3: (a) Atomic reconstruction of the analysed volumes displaying the precipitates by Mg iso-concentration surface at 5 at% from alloy O2, (b) Proximity histogram of all hardening precipitates in the two volumes of the alloy O2, (c) Atomic reconstruction displaying the precipitates by Mg iso-concentration surface at 5 at% from alloy O3, and (d) Proximity histogram of all precipitates found in the two volumes of the alloy O3.

11.4 Discussion

The focus in the current work has been to investigate the influence of minor additions of Cu (≤ 0.05 wt%) and/or Zn (≤ 0.06 wt%) on the precipitate structures in the PA and OA conditions. Such concentrations can be expected in the final recycled Al-Mg-Si alloys due to the presence of relatively low-quality post-consumer scraps in the recycling process, which drives the need to understand the impact of such elements in low concentration on the precipitate structures. Because the HAADF-STEM images display atomic number Z-contrast, Si atomic columns will have a slightly higher contrast than the Al and Mg columns. It is, therefore, possible to infer the presence of Cu and Zn by

observing which atomic columns have abnormally high contrasts in alloys O1 and O2, respectively. In addition, it is possible to observe the atomic arrangement near these areas to understand if or how Zn and Cu are altering the local crystal structure in such concentrations. According to literature, Cu incorporates into the crystal structure of the hardening precipitates in the Al-Mg-Si-Cu system by occupying certain atomic columns [13,39,45]. Consequently, the abnormally brighter columns that do not belong to the solved Cu configurations are presumed to be occupied fully or partially by Zn atoms in the alloys containing both elements (O3 and O4). This assumption is also based on the results obtained from the alloy O2 with only 0.06 wt% Zn addition and on the limited work reported from alloys with a high Zn concentration (1 wt%) [10]. The precipitates presented in the current work are representative of the phases observed in 6082-Al-Mg-Si alloy in the PA condition alloys (O1, O2, and O3) and OA condition alloy (O4) with minor addition of Cu and/or Zn as they are selected from a series of randomly recorded atomically-resolved HAADF-STEM images.

11.4.1 Influence of Cu on the precipitate structures in the peakaged condition

Despite the low Cu concentration in alloy O2, Cu incorporated into the structure of β″ and fragmented/mixed precipitates occupying certain atomic sites, e.g., Si_3/Al and Si_1 in β″ precipitates [44,46], see Fig. 11.2(a, b). The fragmented and mixed precipitates show a complex structure as at least two of the following sub-unit configurations are observed in their crystal structures: β″, β'_{Cu}, Q'/C and/or U2, see Fig. 11.3(b, d). These outcomes clearly demonstrate the impact of 0.05 wt% Cu on the precipitate structure in Al-Mg-Si alloy in the PA condition. The influence of Cu on reducing the misfit dislocations at β″/Al matrix interface has been investigated in Al-Mg-Si alloy with 0.09 wt% Cu in the PA condition by Saito et al. [47]. It is claimed that the periodic distribution of Cu at the β″/Al matrix interface along [230] Al can suppress the misfit dislocation observed in Cu-free alloys. Interestingly, a similar effect is noticed in the current work with low Cu content as the periodic distribution of brighter columns at the β″/Al matrix interface along [3-20] Al suppresses misfit dislocations, see Fig. 11.2c. In a separate work, Sunde et al. [44] studied the influence of 0.03 and 0.09 wt% Cu addition on the precipitate structures in Al-0.7Mg-0.9Si (wt%) alloy in different aging conditions. The results showed that most of the precipitates in the PA condition were β″ precipitates. Also, the incorporation of Cu into β″ structure was higher in the 0.09 wt% Cu added alloy than in the one with 0.03 wt% Cu,

leading to the formation of β'_{Cu} sub-unit configurations in the former. The β'_{Cu}, Q'/C, and U2 sub-unit configurations are observed in this study in the alloy O1, extending the critical Cu concentration that can influence the precipitate structure in the PA condition. Saito et al. [48,49] reported that Cu was never observed inside disordered part of β″ precipitate, as it was only observed within the non-β″ disordered parts or at the β″/matrix interface. In the current work it is evident that Cu partially occupies Si_3/Al inside the β″ structure found within the mixed/fragmented precipitates and at the β″/Al matrix interface, see Fig. 11.3(c, d).

11.4.2 Influence of Zn on the precipitate structures in the peakaged condition

Saito et al. [10] investigated the effect of high Zn concentration (1.02 wt%) on the precipitate structure in leaner Al-0.47Mg-0.39Si (wt%) alloy. The results showed that low amounts of Zn was incorporated into precipitate structures led to the formation of disordered precipitates. In the current work, approximately 60.2 % of the recorded precipitates are fragmented and mixed, which comprised of β″ sub-unit structures in combination with sub-unit structures of other precipitate phases normally found in Al-Mg-Si-Cu alloys, such as U2, β'_{Cu}, and Q′/C, see Figs. 11.4b, 11.5c, and 11.6a. The remainder, 39.8 %, are pure β″ precipitates, showing brighter atomic columns in the core part or at the Al matrix/precipitate interface as a result of Zn incorporation, see Fig. 11.6(c, d). Z-contrast of atomic columns in such precipitates indicate that Zn concentration is low, however, Zn atoms show a tendency to randomly and partially occupy Mg_1/Al, Si_1, Si_2, and Si_3/Al atomic sites, see Figs. 11.4, 11.5, and 11.6. Incorporation of Zn in the Si_3/Al sites is experimentally supported by Saito et al. [50], who investigated the influence of high Zn concentration on the precipitate structures in Al-0.52Mg-0.38Si-0.42Zn (wt%) alloy. The incorporation of Zn into Si_3/Al, Si_2, and Si_1 columns of the β″ unit cell is also supported by density functional theory (DFT) calculations. It has been predicted that Zn atoms are preferentially incorporated in the bulk of the β″ structure, i.e., not close to the interface. In the same work, Saito et al. [50] reported that no Zn on the Si_1 atomic sites was observed experimentally, and Si_2 has slightly higher intensity attributing it to cross-talk artifacts or electron channeling [50]. The current work evidently shows that the Zn can occupy Si_1 and Si_2 columns in the bulk of the β″ structure, but no Zn was found in the Mg_1 and Mg_2 sites, confirming the DFT calculations. Based on this work, it is believed that the affinity of Zn to occupy Mg_1/Al, Si_1, Si_2, and Si_3/Al sites in the β″ unit cell, caused the formation of an

increased number of two-fold and mirror symmetries in disordered precipitates, related to the arrow configuration which is part of the pure (ordered) β″ and U2 phases, see Fig. 11.12. Interestingly, Zn is also found to occupy Al and Si sites in U2 configuration.

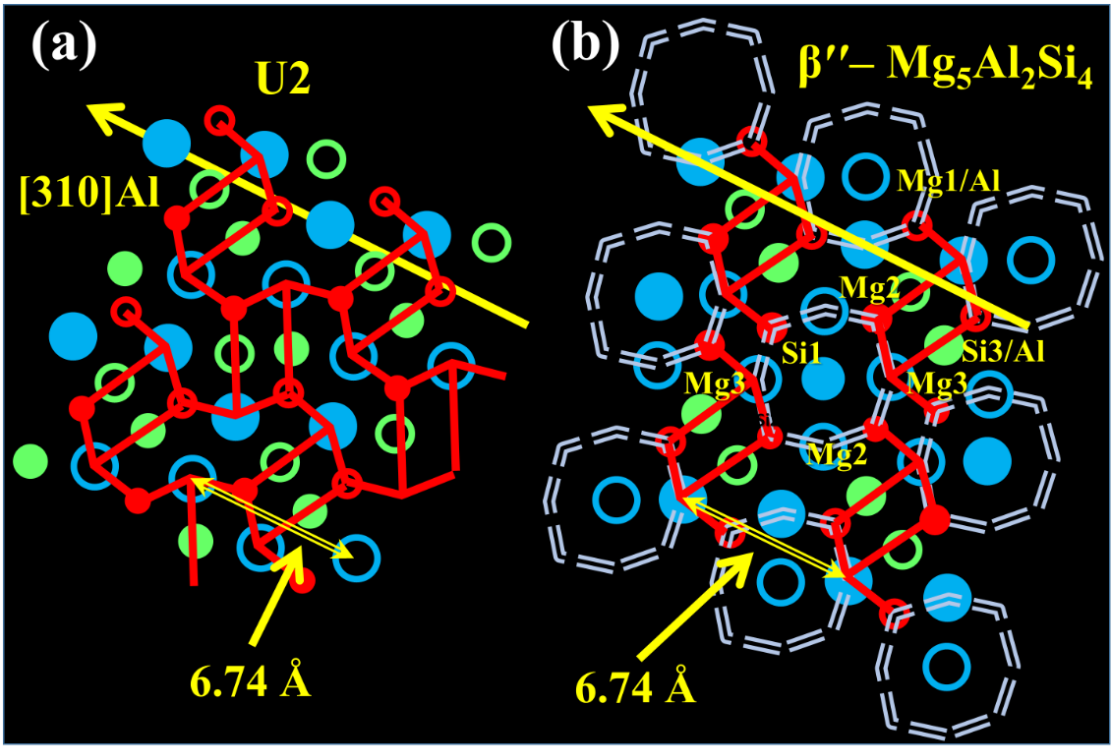

Element / Height	Al	Mg	Si	Zn
Z= 0.000 nm	●	●	●	●
Z= 0.203 nm	○	○	○	○

Fig. 11.12. Schematic image showing the arrow configuration as a part of pure β″ and U2 phases.

The gradual incorporation of Cu into Si_3/Al and Si_1 columns of the β″ unit cell has been thought to be the starting point of the formation of Q′/C and $β'_{Cu}$ structural sub-units [44]. The observation of $β'_{Cu}$ and Q′/C sub-structures without the presence of Cu indicates that Zn atoms can have a similar effect to that of Cu on Al-Mg-Si precipitate crystal structures. Therefore, the observations made in the present study suggest that Zn could partially occupy the columns that are normally associated with Cu occupancy in the Q′/C and $β'_{Cu}$ structures. Interestingly, the current results also indicate that Zn could be (partially) occupying Al columns in the $β'_{Cu}$ unit cell, Si columns in Q′/C, and Al and Si columns in the U2 unit cell (found in the fragmented precipitates), see Figs. 11.4c, 11.5c, and 11.6a. In

addition to the above-mentioned, Zn can partially occupy various atomic sites in sub-structures of the Q′/C, β'_{Cu}, and U2 phases and in β″ precipitates. Zn is also observed to have a more unique subtle effect on precipitate crystal structures that to the best of the authors' knowledge have not been described previously, see Figs. 11.4c, 11.5(b, d), and 11.9(a, b). It promotes the formation of defects with extended two-fold symmetry and mirror plane configurations, which is not observed in precipitates nucleated in pure Al-Mg-Si alloys or with Ag, Li, and Cu additions [10,39,41,47,48,50–57]. Moreover, Zn did not show the same tendency as Cu to occupy β″/Al matrix interface periodically, but evidently, Zn incorporates into β″ structure grown along [320] and [230] Al and preferentially occupies the Si_2, Si_3/Al sites, which also suppresses the misfit dislocation, see Fig. 11.6(c, d). It is interesting to note that Zn suppressed the misfit dislocation even in the precipitate comprised of β″ and β''_2 structures, see Fig. 11.6a. Furthermore, based on the suggested atomic overly and unlike Cu, once Zn enters the precipitate structure, it can occupy all atomic columns except for Mg sites, which is believed the reason behind disturbing the Si network leading to more complex structures, see Figs. 11.4, 11.5, and 11.6.

11.4.3 Influence of Cu and Zn on the precipitate structures in the peakaged and overaged conditions

By studying 0.1 wt% Cu and ~1 wt% Zn additions in Al-Mg-Si alloy separately, Saito et al [54] showed that the majority of the hardening precipitates lacked an overall periodicity. Zn and Cu columns, cannot be distinguished in this alloy based on Z-contrast, formed certain local symmetries connected with the Si-network. It is also reported that the Zn and Cu columns were detected to occupy the Al sites at the precipitate/matrix interface. The presence of Zn in the precipitate structures in alloy O3 is not obvious using Z-contrast also, but brighter atomic columns are observed without any clear site preference. This is most likely related to the partial incorporation of Zn, as Cu has not been reported to occupy such columns, see Figs. 11.7 and 11.8 [44,47,48,54,58]. In spite of the very low Zn concentrations, the current work provides deep understanding of the influence of Zn on the precipitate structures as brighter atomic columns, which do not belong to a known unit configuration, are observed in the core part of the precipitates, see Figs. 11.7c and Figs. 11.8c. Furthermore, a noticeably higher number of brighter Si_2 atomic columns (in the β″ structural unit) are observed after Zn additions, indicating that Zn partially occupies such columns, see Fig. 11.7c. Therefore, the present study shows that Cu and Zn atoms in

combination can have a considerable influence on precipitation in Al-Mg-Si alloys. Interestingly, the quantitative APT measurements of the chemistry of the bulk precipitates in alloy O3 indicates that the affinity of Cu to enter the crystal structure of the hardening precipitates is higher than that for the Zn. Therefore, the amount of Cu in the hardening precipitates is found to be notably higher than that for Zn, even though Zn has a slightly higher concentration in the alloy, see Fig. 11.11d. The Z contrast of the atomic resolution HAADF-STEM images performed on alloys O1 and O2 shows high tendency for Cu and Zn to incorporate into a precipitate structure. Based on these two observations, it can be concluded that the occupancy level (fraction of Cu and Zn atoms in the columns) for Cu is higher than that for Zn.

The transformation of the precipitate structures after 5 h aging at 240 °C (OA condition) in alloy O4 is demonstrated in Figs. 11.9 and 11.10. The results clearly show abnormal high Z contrast inside the precipitate structures, which indicates that the Cu and/or Zn are incorporated into their structures, see Figs. 11.9c and 11.10. The suggested atomic overlay in Fig. 11.9(b, d) shows a more complicated structure compared to precipitate structures found in alloy O3 (PA condition) as several mirror-plane configurations, arrow, U1, Q′/C, β'_{Cu}, U2, and interestingly β″ unit structures are observed. In addition, it is noticed that the Si network in disordered part of the precipitates in this condition is remarkably disordered. The presence of mirror plane configurations in the disordered area is believed to be due to the presence of Zn in this alloy as to the best author's knowledge, such configurations are not reported previously in the presence of Cu in the OA condition [58,59].

11.5 Conclusions

The influence of 0.05 wt% Cu and 0.06 wt% Zn, individually and in combinations, on the precipitate crystal structures were investigated using aberration-corrected HAADF-STEM and APT. The main findings of the current work are summarized as follows:

- Minor addition of Cu and/or Zn has a significant influence on the precipitate structures in Al-Mg-Si alloys in the peakaged and overaged conditions.
- Cu is found to occupy Si_3/Al sites inside β″ structure found within the mixed precipitates as well as periodically occupying the mixed precipitate/Al matrix interface.

- Zn noticeably disturbs the Si network within the fragmented/mixed precipitate containing mirror plane symmetry, which is not observed in the case of only Cu addition.
- Zn shows a high tendency to incorporate into precipitate structure leading to introducing different resolved sub-configurations found in the Al-Mg-Si-Cu system. Also, it is evident that Zn has a strong tendency to occupy all atomic sites inside the β″ structure except for Mg_2 and Mg_3 sites, which is believed to be the reason behind the formation of extended areas with two-fold symmetry and mirror plane configurations in the mixed precipitates.
- The suggested atomic overlays indicate that Zn didn't show periodic distribution inside the fragmented/mixed precipitate crystal structures, as once entering the structure, it can partially occupy all atomic columns (Al, Si, Cu) except for Mg sites.
- Cu and Zn additions to the alloy's composition had a significant impact on the precipitate structures in the overaged condition, as U1, U2, Q′/C, β'_{Cu}, and β″ configurations are observed, in addition to the tendency of the two elements to partially occupy atomic columns of the Si network.
- APT results indicate that Zn has less tendency to incorporate into precipitate structures than Cu, with most of the Zn still found in the solid solution.

CRediT authorship contribution statement

Emad H. Bartawi: Conceptualization, Methodology, Investigation, Formal analysis, Writing - Original Draft, **Calin D. Marioara:** Writing - Review & Editing, Formal analysis, **Ghada Shaban:** Writing - Review & Editing, Formal analysis, **Constantinos Hatzoglou:** Formal analysis, **Randi Holmestad:** Writing - Review & Editing**, Rajan Ambat:** Conceptualization, Supervision, Writing - Review & Editing, Project administration, Funding acquisition.

Acknowledgements

EHB and RA would like to thank Hydro Aluminium, Norway, for providing the material. The first author also thank Dr. Ruben Bjørge from SINTEF Industry for his assistance during STEM experiments. EHB and RA acknowledge funding from the Independent Research Fund Denmark (grant number 9041- 00240A). Also, this project has received funding from the European Union's Horizon 2020 research and innovation programme under grant agreement No 823717 – ESTEEM3. The Research Council of Norway (RCN) is acknowledged for funding the NTNU atom probe facility through the Norwegian Laboratory for Mineral and Materials Characterization (MiMaC) project number: 269842. The HR-STEM work was conducted on the NORTEM (Norwegian Research Council project number: 197405) infrastructure at the TEM Gemini Centre, Trondheim, Norway.

Data Availability

The raw/processed data required to reproduce these findings cannot be shared at this time as the data also forms part of an ongoing study.

References

[1] J. Hirsch, Recent development in aluminium for automotive applications, Trans. Nonferrous Met. Soc. China. 24 (2014) 1995–2002.

[2] J.R. Davis, Corrosion of aluminum and aluminum alloys, ASM international, 1999.

[3] J. Hirsch, Aluminium in innovative light-weight car design, Mater. Trans. 52 (2011) 818–824.

[4] D. Raabe, D. Ponge, P.J. Uggowitzer, M. Roscher, M. Paolantonio, C. Liu, H. Antrekowitsch, E. Kozeschnik, D. Seidmann, B. Gault, F. De Geuser, A. Deschamps, C. Hutchinson, C. Liu, Z. Li, P. Prangnell, J. Robson, P. Shanthraj, S. Vakili, C. Sinclair, L. Bourgeois, S. Pogatscher, Making sustainable aluminum by recycling scrap: The science of "dirty" alloys, Prog. Mater. Sci. 128 (2022) 100947.

[5] S.K. Das, J.A.S. Green, G. Kaufman, Aluminum recycling: Economic and environmental benefits, Light Met. Age. 68 (2010) 42–46.

[6] M.X. Guo, Y.D. Zhang, G.J. Li, S.B. Jin, G. Sha, J.S. Zhang, L.Z. Zhuang, E.J. Lavernia, Solute clustering in Al-Mg-Si-Cu-(Zn) alloys during aging, J. Alloys Compd. 774 (2019) 347–363.

[7] X.P. Ding, H. Cui, J.X. Zhang, H.X. Li, M.X. Guo, Z. Lin, L.Z. Zhuang, J.S. Zhang, The effect of Zn on the age hardening response in an Al-Mg-Si alloy, Mater. Des. 65 (2015) 1229–1235.

[8] M.X. Guo, X.K. Zhang, J.S. Zhang, L.Z. Zhuang, Effect of Zn addition on the precipitation behaviors of Al–Mg–Si–Cu alloys for automotive applications, J. Mater. Sci. 52 (2017) 1390–1404.

[9] J. Man, L. Jing, S.G. Jie, The effects of Cu addition on the microstructure and thermal stability of an Al–Mg–Si alloy, J. Alloys Compd. 437 (2007) 146–150.

[10] T. Saito, S. Wenner, E. Osmundsen, C.D. Marioara, S.J. Andersen, J. Røyset, W. Lefebvre, R. Holmestad, The effect of Zn on precipitation in Al-Mg-Si alloys, Philos. Mag. 94 (2014) 2410–2425.

[11] G. Svenningsen, M.H. Larsen, J.C. Walmsley, J.H. Nordlien, K. Nisancioglu, Effect of artificial aging on intergranular corrosion of extruded AlMgSi alloy with small Cu content, Corros. Sci. 48 (2006) 1528–1543.

[12] G. Svenningsen, J.E. Lein, A. Bjørgum, J.H. Nordlien, Y. Yu, K. Nisancioglu, Effect of low copper content and heat treatment on intergranular corrosion of model AlMgSi alloys, Corros. Sci. 48 (2006) 226–242.

[13] C.D. Marioara, S.J. Andersen, T.N. Stene, H. Hasting, J. Walmsley, A.T.J. Van Helvoort, R. Holmestad, The effect of Cu on precipitation in Al-Mg-Si alloys, Philos. Mag. 87 (2007) 3385–3413.

[14] Z. Jia, L. Ding, L. Cao, R. Sanders, S. Li, Q. Liu, The influence of composition on the clustering and precipitation behavior of Al-Mg-Si-Cu alloys, Metall. Mater. Trans. A. 48 (2017) 459–473.

[15] J.F. Nie, Physical metallurgy of light alloys, Fifth Edit, Elsevier, 2014.

[16] E.H. Bartawi, O. V. Mishin, G. Shaban, J.H. Nordlien, R. Ambat, Electron microscopy analysis of grain boundaries and intergranular corrosion in aged Al-Mg-Si alloy doped with 0.05 wt% Cu, Corros. Sci. 209 (2022) 110758.

[17] X. Zhang, X. Zhou, J.O. Nilsson, Corrosion behaviour of AA6082 Al-Mg-Si alloy extrusion: The influence of quench cooling rate, Corros. Sci. 150 (2019) 100–109.

[18] G.A. Edwards, K. Stiller, G.L. Dunlop, M.J. Couper, The precipitation sequence in Al–Mg–Si alloys, Acta Mater. 46 (1998) 3893–3904.

[19] C.D. Marioara, S.J. Andersen, H.W. Zandbergen, R. Holmestad, The influence of alloy composition on precipitates of the Al-Mg-Si system, Metall. Mater. Trans. A. 36 (2005) 691–702.

[20] M. Murayama, K. Hono, W. Miao, D.E. Laughlin, The effect of Cu additions on the precipitation kinetics in an Al-Mg-Si alloy with excess Si, Metall. Mater. Trans. A. 32 (2001) 239–246.

[21] S. Esmaeili, D.J. Lloyd, Effect of composition on clustering reactions in

AlMgSi(Cu) alloys, Scr. Mater. 50 (2004) 155–158.

[22] M. Liu, J. Banhart, Effect of Cu and Ge on solute clustering in Al-Mg-Si alloys, Mater. Sci. Eng. A. 658 (2016) 238–245.

[23] Q. Xiao, H. Liu, D. Yi, D. Yin, Y. Chen, Y. Zhang, B. Wang, Effect of Cu content on precipitation and age-hardening behavior in Al-Mg-Si-xCu alloys, J. Alloys Compd. 695 (2017) 1005–1013.

[24] S. Zhu, Z. Li, L. Yan, X. Li, S. Huang, H. Yan, Y. Zhang, B. Xiong, Effects of Zn addition on the age hardening behavior and precipitation evolution of an Al-Mg-Si-Cu alloy, Mater. Charact. 145 (2018) 258–267.

[25] X. Zhang, L. Yan, Z. Li, X. Li, G. Gao, H. Yan, K. Wen, Y. Zhang, B. Xiong, Effects of Cu addition on age hardening behavior and mechanical properties of high-strength Al-1.2Mg-1.2Si alloy, Materials (Basel). 16 (2023).

[26] W.F. Miao, D.E. Laughlin, Effects of Cu content and preaging on precipitation characteristics in aluminum alloy 6022, Metall. Mater. Trans. A. 31 (2000) 361–371.

[27] C. Cayron, L. Sagalowicz, L. Sagalowicz, P.A. Buffat, Structural phase transition in Al-Cu-Mg-Si alloys by transmission electron microscopy study on an Al-4 wt% Cu-1 wt% Mg-Ag alloy reinforced by SiC particles, Philos. Mag. A. 79 (1999) 2833–2851.

[28] D.J. Chakrabarti, D.E. Laughlin, Phase relations and precipitation in Al–Mg–Si alloys with Cu additions, Prog. Mater. Sci. 49 (2004) 389–410.

[29] X. Wang, M. Guo, J. Zhang, L. Zhuang, Effect of Zn addition on the microstructure, texture evolution and mechanical properties of Al-Mg-Si-Cu alloys, Mater. Sci. Eng. A. 677 (2016) 522–533.

[30] A. qin Tian, X. hong Xu, L. Sun, Y. lai Deng, Effects of interrupted ageing and asymmetric rolling on microstructures, mechanical properties, and intergranular corrosion behavior of Al-Mg-Si-Zn alloy, J. Cent. South Univ. 29 (2022) 821–835.

[31] X. Xu, W. Zhu, M. Yuan, C. Liang, Y. Deng, The effect of Zn content on the

microstructure and mechanical properties of the Al-mg-Si alloy, Mater. Charact. 198 (2023) 112714.

[32] Y.-H. Cai, C. Wang, J.-S. Zhang, Microstructural characteristics and aging response of Zn-containing Al-Mg-Si-Cu alloy, Int. J. Miner. Metall. Mater. 20 (2013) 659.

[33] L. Yan, Y. Zhang, X. Li, Z. Li, F. Wang, H. Liu, B. Xiong, Effect of Zn addition on microstructure and mechanical properties of an Al–Mg–Si alloy, Prog. Nat. Sci. Mater. Int. 24 (2014) 97–100.

[34] S. Zhu, Z. Li, L. Yan, X. Li, S. Huang, H. Yan, Y. Zhang, B. Xiong, Natural aging behavior in pre-aged Al–Mg–Si–Cu alloys with and without Zn addition, J. Alloys Compd. 773 (2019) 496–502.

[35] W. Lefebvre, F. Vurpillot, X. Sauvage, Atom probe tomography: put theory into practice, Academic Press, 2016.

[36] B. Gault, M.P. Moody, J.M. Cairney, S.P. Ringer, Atom Probe Microscopy and Materials Science, Springer Ser. Mater. Sci. 160 (2012) 299–311.

[37] C. Hatzoglou, S. Rouland, B. Radiguet, A. Etienne, G. Da Costa, X. Sauvage, P. Pareige, F. Vurpillot, Preferential evaporation in atom probe tomography: An analytical approach, Microsc. Microanal. 26 (2020) 689–698.

[38] Atom Probe Tomography (APT) - Department of Materials Science and Engineering - NTNU, (2022).

[39] T. Saito, E.A. Mørtsell, S. Wenner, C.D. Marioara, S.J. Andersen, J. Friis, K. Matsuda, R. Holmestad, Atomic structures of precipitates in Al–Mg–Si alloys with small additions of other elements, Adv. Eng. Mater. 20 (2018) 1800125.

[40] S.J. Andersen, H.W. Zandbergen, J. Jansen, C. Træholt, U. Tundal, O. Reiso, The crystal structure of the β″ phase in Al–Mg–Si alloys, Acta Mater. 46 (1998) 3283–3298.

[41] S.J. Andersen, C.D. Marioara, R. Vissers, A. Frøseth, H.W. Zandbergen, The structural relation between precipitates in Al–Mg–Si alloys, the Al-matrix and

diamond silicon, with emphasis on the trigonal phase U1-MgAl2Si2, Mater. Sci. Eng. A. 444 (2007) 157–169.

[42] S.J. Andersen, C.D. Marioara, A. Frøseth, R. Vissers, H.W. Zandbergen, Crystal structure of the orthorhombic U2-Al4Mg4 Si4 precipitate in the Al-Mg-Si alloy system and its relation to the β′ and β″ phases, Mater. Sci. Eng. A. 390 (2005) 127–138.

[43] S.J. Andersen, C.D. Marioara, J. Friis, R. Bjørge, Q. Du, I.G. Ringdalen, S. Wenner, E.A. Mørtsell, R. Holmestad, T. Saito, J. Røyset, O. Reiso, Directionality and column arrangement principles of precipitates in Al-Mg-Si-(Cu) and Al-Mg-Cu linked to line defect in Al, Mater. Sci. Forum. 877 (2017) 461–470.

[44] J.K. Sunde, C.D. Marioara, R. Holmestad, The effect of low Cu additions on precipitate crystal structures in overaged Al-Mg-Si(-Cu) alloys, Mater. Charact. 160 (2020) 110087.

[45] C.D. Marioara, S.J. Andersen, J. Røyset, O. Reiso, S. Gulbrandsen-Dahl, T.E. Nicolaisen, I.E. Opheim, J.F. Helgaker, R. Holmestad, Improving thermal stability in Cu-containing Al-Mg-Si alloys by precipitate optimization, Metall. Mater. Trans. A. 45 (2014) 2938–2949.

[46] R. Vissers, M.A. van Huis, J. Jansen, H.W. Zandbergen, C.D. Marioara, S.J. Andersen, The crystal structure of the β′ phase in Al–Mg–Si alloys, Acta Mater. 55 (2007) 3815–3823.

[47] T. Saito, F.J.H. Ehlers, W. Lefebvre, D. Hernandez-Maldonado, R. Bjørge, C.D. Marioara, S.J. Andersen, E.A. Mørtsell, R. Holmestad, Cu atoms suppress misfit dislocations at the β″/Al interface in Al-Mg-Si alloys, Scr. Mater. 110 (2016) 6–9.

[48] T. Saito, C.D. Marioara, S.J. Andersen, W. Lefebvre, R. Holmestad, Aberration-corrected HAADF-STEM investigations of precipitate structures in Al-Mg-Si alloys with low Cu additions, Philos. Mag. 94 (2014) 520–531.

[49] T. Saito, S. Muraishi, C.D. Marioara, S.J. Andersen, J. Røyset, R. Holmestad, The effects of low Cu additions and predeformation on the precipitation in a 6060 Al-

Mg-Si alloy, Metall. Mater. Trans. A Phys. Metall. Mater. Sci. 44 (2013) 4124–4135.

[50] T. Saito, F.J.H. Ehlers, W. Lefebvre, D. Hernandez-Maldonado, R. Bjørge, C.D. Marioara, S.J. Andersen, R. Holmestad, HAADF-STEM and DFT investigations of the Zn-containing β'' phase in Al-Mg-Si alloys, Acta Mater. 78 (2014) 245–253.

[51] S.J. Andersen, C.D. Marioara, J. Friis, S. Wenner, R. Holmestad, Precipitates in aluminium alloys, Adv. Phys. X. 3 (2018) 790–814.

[52] E.A. Mørtsell, C.D. Marioara, S.J. Andersen, I.G. Ringdalen, J. Friis, S. Wenner, J. Røyset, O. Reiso, R. Holmestad, The effects and behaviour of Li and Cu alloying agents in lean Al-Mg-Si alloys, J. Alloys Compd. 699 (2017) 235–242.

[53] L. Ding, Z. Jia, J.F. Nie, Y. Weng, L. Cao, H. Chen, X. Wu, Q. Liu, The structural and compositional evolution of precipitates in Al-Mg-Si-Cu alloy, Acta Mater. 145 (2018) 437–450.

[54] T. Saito, C.D. Marioara, S.J. Andersen, W. Lefebvre, R. Holmestad, Structural investigation of precipitates with Cu and Zn atomic columns in Al-Mg-Si alloys by aberration-corrected HAADF-STEM, in: J. Phys. Conf. Ser., 2014: p. 12030.

[55] S. Wenner, C.D. Marioara, S.J. Andersen, M. Ervik, R. Holmestad, A hybrid aluminium alloy and its zoo of interacting nano-precipitates, Mater. Charact. 106 (2015) 226–231.

[56] M. Gazizov, C.D. Marioara, J. Friis, S. Wenner, R. Holmestad, R. Kaibyshev, Unique hybrid precipitate structures forming in an Al–Cu–Mg–Si alloy, J. Alloys Compd. 826 (2020) 153977.

[57] M. Gazizov, C.D. Marioara, J. Friis, S. Wenner, R. Holmestad, R. Kaibyshev, Precipitation behavior in an Al–Cu–Mg–Si alloy during ageing, Mater. Sci. Eng. A. 767 (2019) 138369.

[58] M. Torster, F.J.H. Ehlers, C.D. Marioara, S.J. Andersen, R. Holmestad, Applying precipitate-host lattice coherency for compositional determination of precipitates in Al-Mg-Si-Cu alloys, Philos. Mag. 92 (2012) 3833–3856.

[59] J.K. Sunde, C.D. Marioara, A.T.J. van Helvoort, R. Holmestad, The evolution of precipitate crystal structures in an Al-Mg-Si(-Cu) alloy studied by a combined HAADF-STEM and SPED approach, Mater. Charact. 142 (2018) 458–469.

12. Overall discussion

This chapter presents a general discussion from the appended papers (Chapters 5-11), which provide detailed results and discussions on the influence of minor addition of Cu (≤ 0.05 wt%) and/or Zn (≤ 0.06 wt%) on the microstructure and intergranular corrosion (IGC) resistance of Al-Mg-Si alloys. Such concentration of Cu and Zn is of vital importance in the topic of recycling Al alloys. Therefore, understanding the influence of such low Cu and Zn on the microstructure and IGC resistance might lead to attempts toward more impurity-tolerant alloys, hence maximizing the use of Al scrap. In addition, it should be emphasized that the scrap quality determines the amount of primary Al that should be added to keep the alloy composition within the standard composition. This section presents a brief discussion covering the most important findings related to the influence of Cu and/or Zn on the microstructure, precipitates structures, and IGC resistance in Al-Mg-Si alloys in different aging conditions.

The IGC resistance of the 16 variants of 6080-Al-Mg-Si alloys (as received condition) with different minor additions of Cu and Zn (see Chapter 3) was investigated in acidified solution according to BS ISO 11846 method B [1], see Fig. 12.1. The IGC test after 24 h demonstrated localized IGC in alloys containing low Cu ≤ 0.03 and Zn ≤ 0.02 wt%. With increasing Cu and Zn content, the number of the affected grain boundaries (GB) noticeably increases as moving toward uniform IGC is noticed, see Fig. 12.1(a, o, p). However, alloys 16 and 7 demonstrate improvement in their IGC resistance compared to alloys (4, 13) and (3, 9), respectively, see Fig. 12.1. The STEM results obtained from alloy 1 clearly showed two groups of GBs. The first group showed no GB particles, while the second group showed β particles along its investigated boundaries. Moreover, Cu-thin film was also observed in a limited number of the investigated GBs. The presence of Cu film and β particles along some GBs is considered the driving force for IGC to take place in this alloy [2–5]. Increasing only Cu content in these alloys (1, 2, 3, and 4) increases the number of the affected GBs. Since all received alloys were subjected to the same thermomechanical process and the alloying composition was kept constant (precisely controlled), it can be concluded that the observed degradations can be directly linked to a rise in Cu concentrations. Further, to ensure that the fractions of high angle (HABs), low angle (LABs), and coincident site lattice (CSL) boundaries did not exhibit noticeable changes

and thus affecting the role of Cu, Electron backscatter diffraction (EBSD) was utilized. The EBSD results indicated that the fraction of LABs and HABs in all investigated alloys is ~10 % and 90 %, respectively. This clearly indicates that any improvements or degradations in the IGC resistance after adding Cu and/or Zn are directly caused by introducing Cu and/or Zn. In this particular case, the noticeable degradation in the IGC resistance is primarily linked to the introduction of Cu into alloys 2, 3, and 4 compared to alloy 1.

As seen in Fig. 12.1, the IGC invaded the surface of alloy 4. However, the susceptibility to IGC evidently decreased by adding Zn (alloys 8, 12, and 16). The EBSD results revealed that the fraction of the LABs and HABs in these alloys was ~10 % and 90 %, respectively. Thus, the improvement observed in the mentioned alloys was directly attributed to the Zn additions. The STEM results obtained from alloy 4 showed the presence of Cu-rich film along some investigated GBs. Moreover, Q/Q′, along with β particles, were also observed along the investigated GBs. However, the TEM results obtained from alloy 16 revealed the presence of Cu/Zn-rich films along some investigated GBs. Furthermore, Q/Q′ and Zn-containing Q/Q′ particles were detected along the GBs. The presence of Zn-rich film is believed to reduce the negative effect of Cu film, as Cu will shift the GB potential positively, while Zn will balance that effect by shifting it toward negative values. The presence of Zn in Q/Q′ particles will also reduce their electrochemical potential. The optimal electrochemical potential of GB and GB particles is to be as much as close to the electrochemical potential of PFZ and its adjacent region. However, the aging parameter and the Zn concentrations will play a critical role in determining the amount of Zn incorporated into such particles, hence the final electrochemical potential. In alloy 16, the IGC results clearly indicated that the heat treatment, two-step aging after water-quenching (WQ), and Zn/Cu ratio are satisfactory, resulting in a noticeable improvement in the IGC resistance compared to alloy 4. However, changing the heat treatment conditions by applying WQ after the solutionizing, alloy 16 did not demonstrate a good IGC resistance as in the two-step aging condition (as receive condition), see Chapters 9 and 10.

The impact of Zn on the microstructure and IGC resistance in Al-Mg-Si alloys (alloys 1, 5, 9, and 13) were also considered in this work, see Fig. 12.1. The susceptibility to IGC increased by increasing Zn content. Alloy 1 demonstrates relatively high IGC resistance while shifting toward more uniform IGC was observed by increasing the Zn concentrations. It is relevant to mention that Zn addition has a noticeably more significant

impact on the IGC extension (lateral attach) than penetration depth (vertical attack). However, Cu addition showed different behavior, heavily influencing both the IGC extension and the penetration depth, see Chapters 6 and 8.

Concerning the influence of Cu and Zn additions on the precipitate structures, alloys 4, 16, and 13 in the peakaged (PA) condition were subjected to STEM. Moreover, the precipitate structures in the overaged (OA) condition were also investigated in alloy 16. The atomic resolution high-angle annular dark-field STEM (HAADF-STEM) indicated that Cu and Zn have a relatively high affinity to incorporate into hardening precipitate structures β″. However, atom probe tomography (APT) results indicated that Cu has a higher affinity to enter the precipitate structure than Zn, see Chapter 11. Although very low Cu and Zn concentrations, the results showed that Cu and Zn can significantly influence the precipitate structures of the investigated alloys in the PA and OA conditions. U2, Q′/C, and β'_{Cu} subunit structures were observed in the precipitate structures in alloy 4 (only Cu). The Zn addition showed a distinctly unique influence on the precipitate structure in Al-Mg-Si alloys as in addition to the presence of U2, Q′/C, β'_{Cu} subunit structures, Zn promoted the formation of 2-fold symmetry and mirror planes configurations, see Chapter 11.

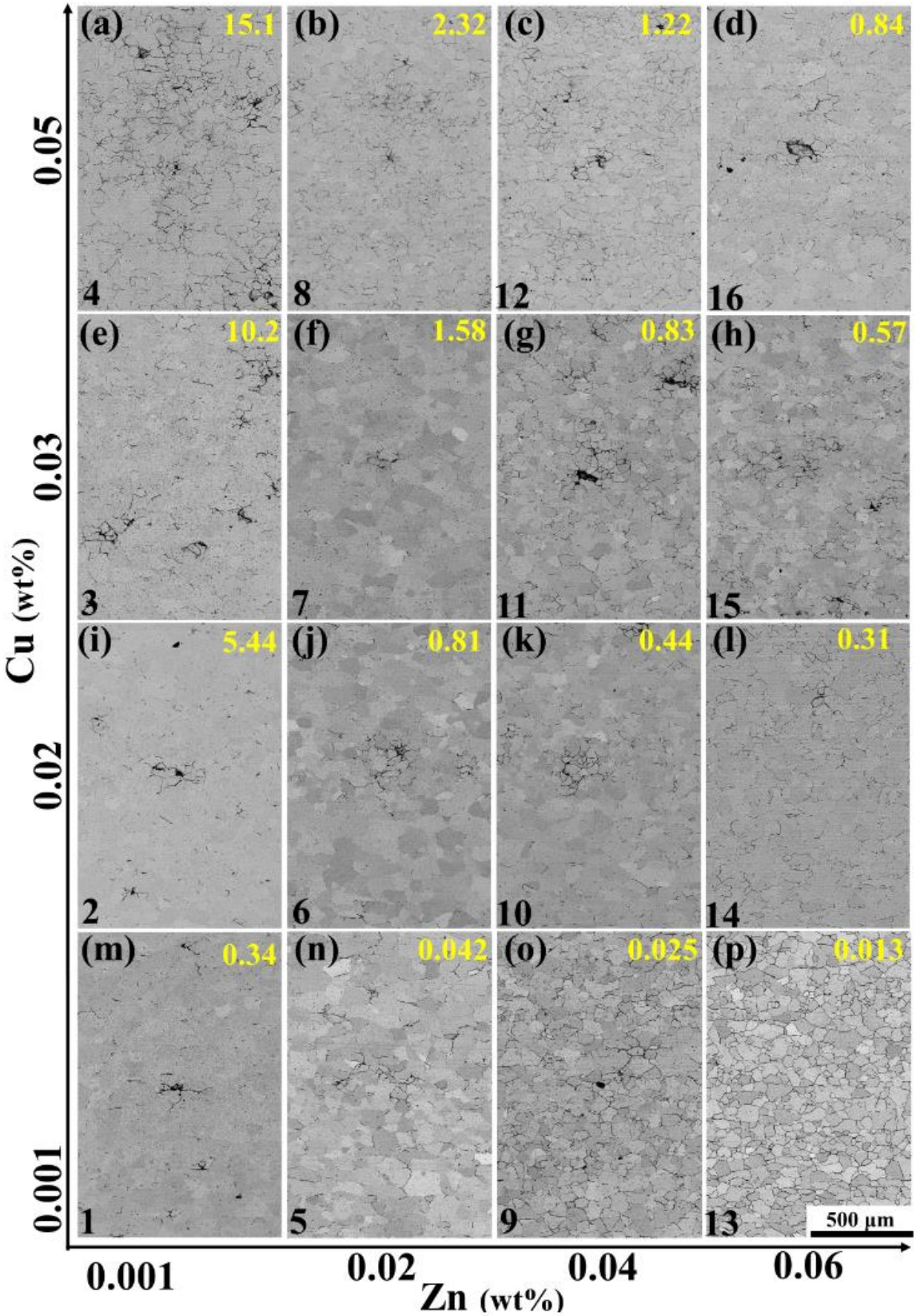

Fig. 12.1. SEM-BSE images of the surface morphology of the 16 investigated alloys after 24 h of exposure. The yellow numbers placed in the top left corners indicate the Cu/Zn ratio. The numbers on the lower left side indicate the alloy number.

References

[1] E.N. ISO, Corrosion of metals and alloys. Determination of resistance to intergranular corrosion of solution heat-treatable aluminium alloys, Br. Stand. Inst. (2005).

[2] G. Svenningsen, J.E. Lein, A. Bjørgum, J.H. Nordlien, Y. Yu, K. Nisancioglu, Effect of low copper content and heat treatment on intergranular corrosion of model AlMgSi alloys, Corros. Sci. 48 (2006) 226–242.

[3] G. Svenningsen, M.H. Larsen, J. Lein, J. Nordlien, K. Nisancioglu, Intergranular corrosion of extruded AA6000-series model alloys, Proc. 9th Int. Conf. Alum. Alloy. (2004) 818–824.

[4] M.H. Larsen, J.C. Walmsley, O. Lunder, R.H. Mathiesen, K. Nisancioglu, Intergranular corrosion of copper-containing AA6xxx AlMgSi aluminum alloys, J. Electrochem. Soc. 155 (2008) C550.

[5] H. Zhan, J.M.C. Mol, F. Hannour, L. Zhuang, H. Terryn, J.H.W. De Wit, The influence of copper content on intergranular corrosion of model AlMgSi(Cu) alloys, Mater. Corros. 59 (2008) 670–675.

13. Overall conclusions

This chapter presents overall conclusions drawn from the findings of the research papers (Chapters 5-11) resulting from the current Ph.D. work. In summary, the main findings are as follows:

1- Al-Mg-Si alloy with 0.05 wt% Cu content in the peakaged condition was highly susceptible to IGC. The driving force for the IGC to take place is the presence of Cu-rich film and the formation of Q/Q′ and β particles along the grain boundaries (GBs).
2- Random and coincident site lattice (CSL) high-angle grain boundaries showed nearly the same susceptibility to intergranular corrosion (IGC). However, some CSL grain boundaries, i.e., Σ5, Σ13, Σ17, and Σ19, exhibited relatively good IGC resistance. Only low angle grain boundaries with misorientation of less than 10 ° displayed greater IGC resistance than any other grain boundaries.
3- The extent (lateral attack) and the penetration depth of the IGC were observed to increase with increasing the Cu concentration, even in a very low amount (0.001-0.05 wt%).
4- The IGC resistance in Al-Mg-Si with 0.05 wt% in the peakaged condition can be improved by introducing a proper amount of Zn. Based on our results, the 0.06 wt% Zn in Al-Mg-Si with 0.05 wt% Cu noticeably reduced the susceptibility to IGC. However, the mentioned Cu/Zn ratio (0.05/0.06 wt%) might not give the desired results if unfavorable heat treatment is applied.
5- Zn-rich Q/Q′ particles and Cu/Zn-rich films were detected along some grain boundaries in Al-Mg-Si alloys containing 0.05 wt% and 0.06 wt% Zn. The presence of Zn is believed to lower the difference in the electrochemical potential between the cathodic and anodic sites along the GB regions and thus reducing the driving force for the IGC to take place.
6- Tiny Zn concentration (0.06 wt%) was noticed to have a considerable negative influence on the IGC resistance of Al-Mg-Si alloy. In this scenario, the Zn addition influenced the extension (lateral attack) of the IGC considerably more than the penetration depth (vertical attack).

7- In alloy containing 0.06 wt% Zn, Zn-rich Mg-Si particles were detected along some investigated GBs. Furthermore, No Mg-Zn particles, usually found in the microstructure of Al-Zn-Mg alloys, were detected along the GBs in Al-Mg-Si alloys in the peakaged condition.

8- Scanning Kelvin probe force microscope (SKPFM) findings demonstrated lower electrochemical potential along the GBs compared to its adjacent region in Al-Mg-Si alloy containing 0.06 wt% Zn, indicating that the GB will act as anode while its adjacent area as a cathode.

9- The IGC results indicated that the Cu/Zn ratio of 1.58 is an outstanding balance leading to a noticeable reduction in the susceptibility to IGC in Al-Mg-Si alloys containing minor Zn and Cu amounts. However, the results indicated that the susceptibility to IGC slightly increased in peakaged condition.

10- Atomic resolution high-angle annular dark-field scanning transmission electron microscope (HAADF-STEM) results indicated that minor addition of Cu (0.05 wt%) and Zn (0.06 wt%) can significantly influence the hardening precipitate structures.

11- The HAADF-STEM findings revealed that once Cu entered the precipitate structures, preferably occupied certain atomic columns leading to the formation of Cu-sub unit structures such as Q′/C, β'_{Cu}.

12- The atomic resolution HAADF-STEM results revealed that once Zn incorporated into precipitate structures, it has a tendency to occupy all atomic sites except for Mg_2 and Mg_3 in the β″ structure.

13- Atom probe tomography (APT) results showed that Zn has less affinity to enter the hardening precipitate structures than Cu.

14. Future work

The impact of minor additions of Cu and Zn on the microstructure, precipitate structures, and IGC resistance in Al-Mg-Si alloys has been studied in depth. However, further work can be conducted in pursuit of further understanding and enhancing the IGC resistance of Al-Mg-Si alloys with minor Cu/Zn additions:

- Statistical analysis on the effect of grain boundary misorientation on the IGC resistance of Al-Mg-Si alloys with 0.05 wt% Cu was conducted. Based on our results, increasing the Cu content (low amount) in Al-Mg-Si can increase the lateral (extension) and vertical (penetration depth) attacks. At the same time, the Zn has much more influence on the lateral than the vertical attack. Therefore, it would be interesting to investigate the impact of grain boundary misorientation on the IGC resistance in Al-Mg-Si alloys in the presence of very low Zn content (e.g., 0.06 wt%).
- In the current study, one-step aging was conducted on the heat treated alloys, and an in-depth investigation was performed. However, our preliminary results on the two-step aged alloys demonstrated encouraging IGC results without sacrificing the mechanical properties. Therefore, more work can be conducted investigating the influence of two-step aging on the microstructure and IGC resistance of Al-Mg-Si with minor addition of Cu and Zn.
- For the heat treatment work, the studied alloys were water-quenched after the solutionizing. Therefore, different cooling rates can be conducted for the purpose of improving the IGC resistance.
- In the present study, the atom probe tomography (APT) results was performed on two alloys with Zn (0.06 wt%) and Cu (0.05 wt%)+Zn (0.06 wt%) to investigate the composition of the bulk hardening precipitates in the peakaged condition. However, studying the precipitate free zone (PFZ) and grain boundary (GB) compositions in the underaged, peakaged, and overaged conditions would be beneficial for a deeper understanding the influence of Cu and Zn concentration in the PFZ on the IGC resistance of Al-Mg-Si alloys.

15. Supplementary chapter

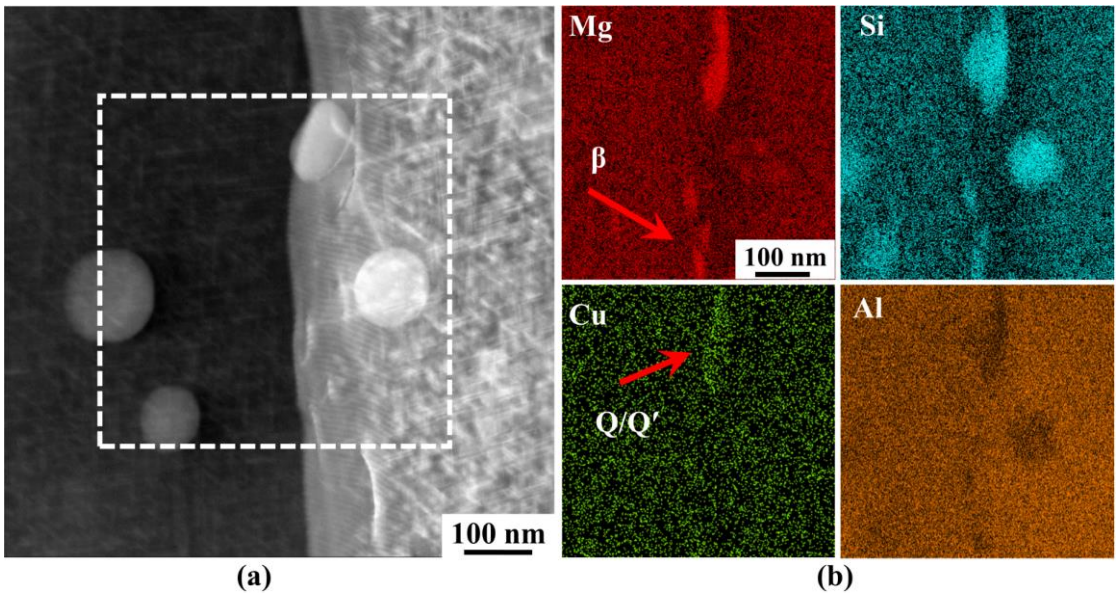

Fig. S.1. HAADF-STEM image of grain boundary of alloy A1 along with the corresponding EDS elemental maps, see Chapter 7.

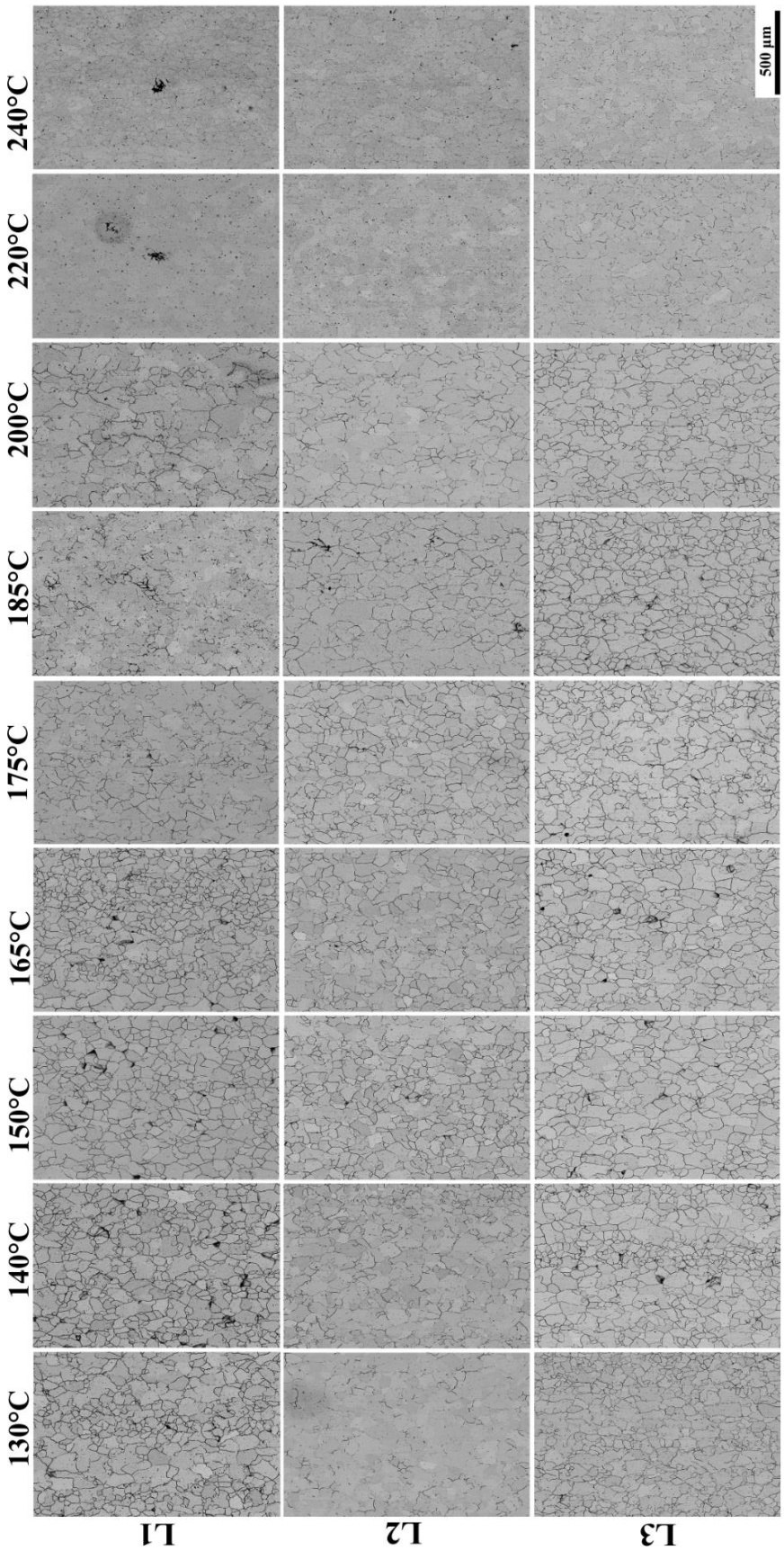

Fig. S.2. BSE-SEM showing the surface morphology of the corroded alloys, see Chapter 9.

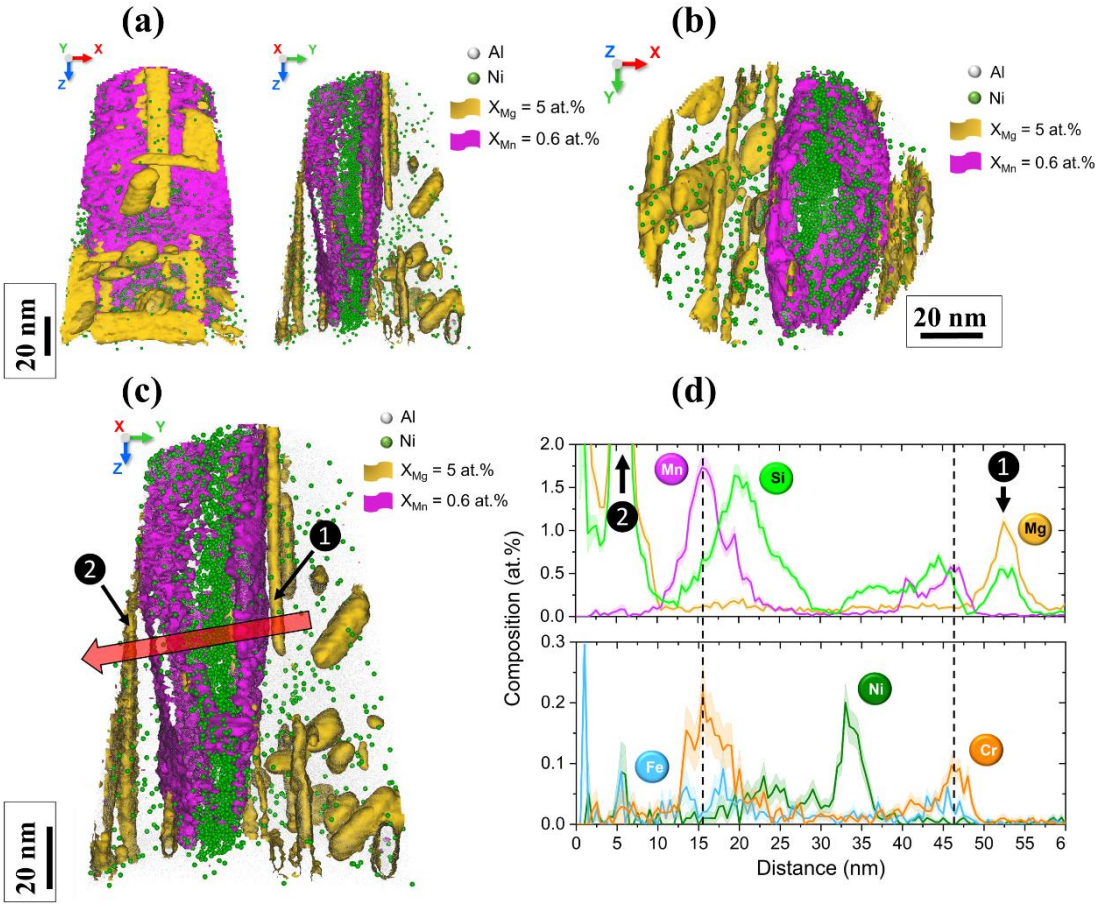

Fig. S.3 APT analysis of alloy O2: (a), (b), and (c) Atomic reconstruction displaying the precipitates by Mg iso-concentration surface at 5 at.% and dispersoid by Mn iso-concentration surface at 0.6 at.%. (d) Concentration profile of dispersoid type precipitate along the red arrow in (c), see Chapter 11.

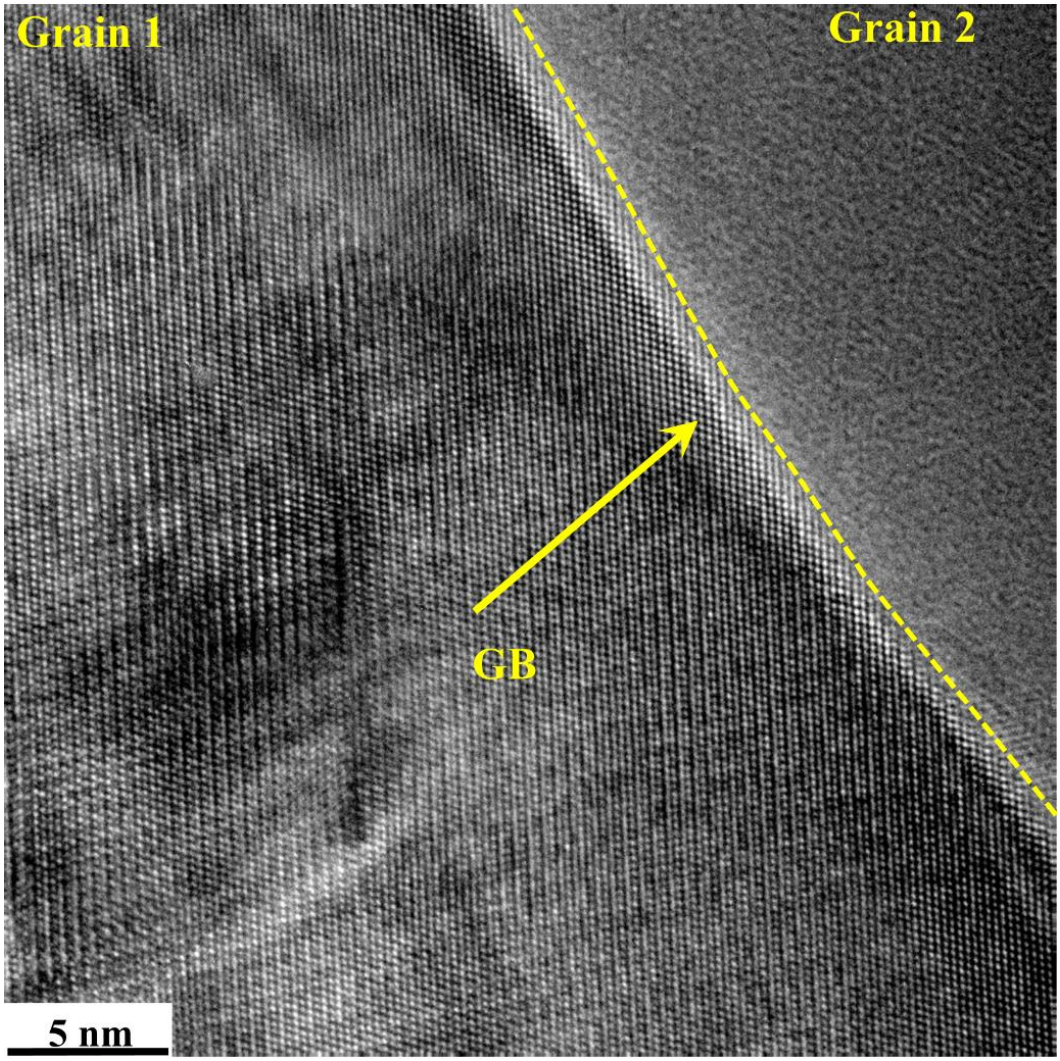

Fig. S.4. High resolution TEM image of grain boundary observed in alloy Al.1, see Table 3.1.

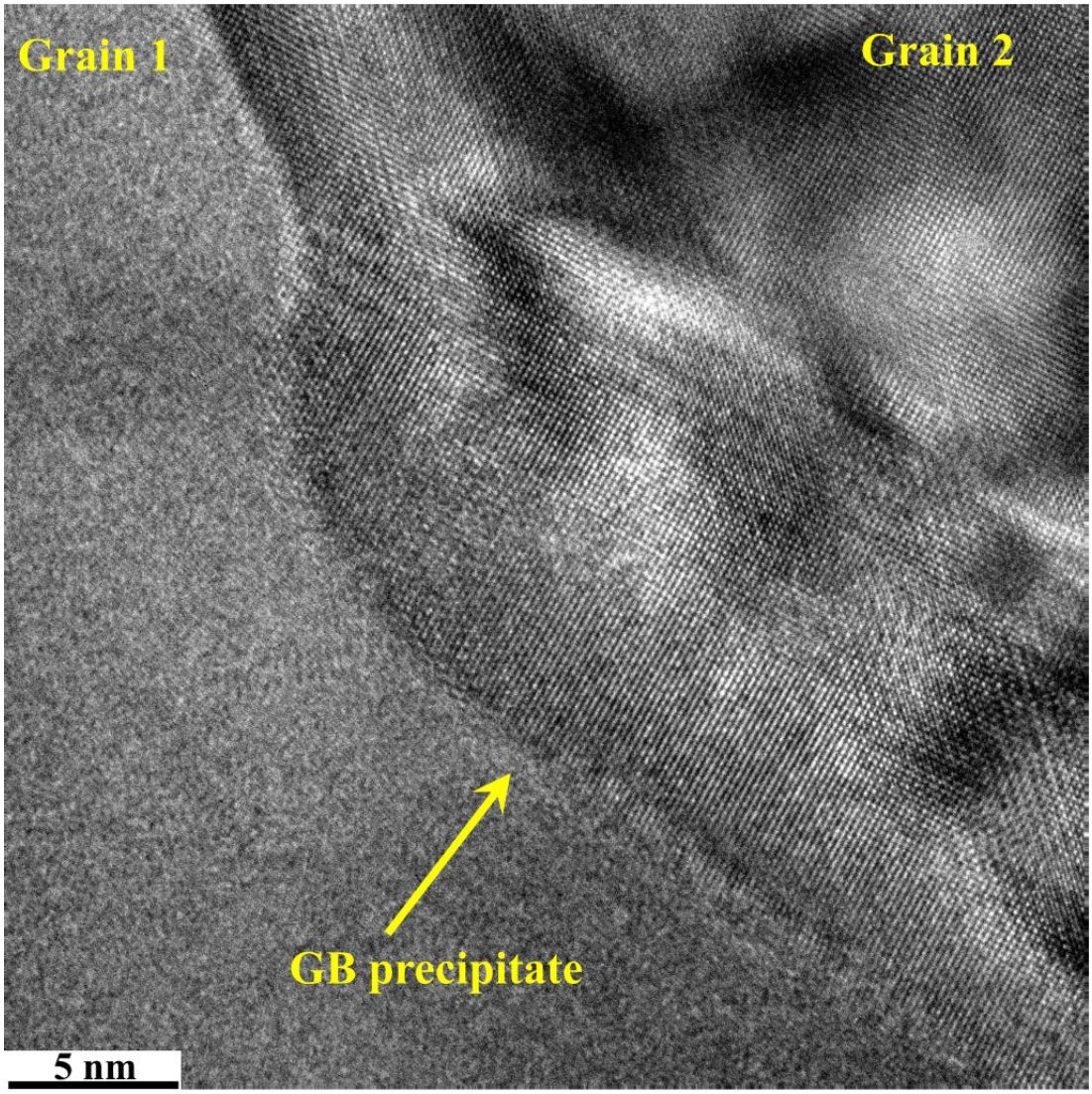

Fig. S.5. High resolution TEM image of Mg-Si grain boundary particle observed in alloy Al.1, see Table 3.1.

DTU Construct

Section of Materials and Surface Engineering
Koppels Allé 404
2800 Kongens Lyngby

978-87-7475-763-4